NEW MATERIALS FOR THE IMMOBILIZATION, GENERATION, AND CHARACTERIZATION OF REACTIVE INTERMEDIATES

A Dissertation

by

ANDREW A. EZAZI

Submitted to the Graduate and Professional School of
Texas A&M University
in partial fulfillment of the requirements for the degree of

DOCTOR OF PHILOSOPHY

Chair of Committee,	David C. Powers
Committee Members,	Sarbajit Banerjee
	Hongcai Zhou
	Manish Shetty
Head of Department,	Simon W. North

August 2023

Major Subject: Chemistry

ABSTRACT

Reactive intermediates invoked in the functionalization of strong C-H bonds are difficult to characterize. The high energy required to break C-H bonds often means the lifetime of the intermediates is fleeting due to opportunities to engage in undesired reactivity. One method of suppressing undesired reactivity pathways is to immobilize the reactive intermediate in a solid. While doing so may result in longer-lived intermediates, ensconcing a molecule in a material introduces other issues, namely several homogeneous characterization methods are unavailable in the context of heterogeneous materials.

This dissertation will present efforts to develop new materials to immobilize and characterize reactive nitride intermediates. The first chapter discusses strategies to synthesize Metal-Organic Frameworks (MOFs) based on kinetically inert ions. In the second chapter, we leverage the metalloligand strategy advanced in the first chapter to synthesize new MOFs based on Ru_2 paddlewheel molecules, which we hope will serve as platforms to interrogate nitrogen atom transfer in confined environments. The third chapter discusses the synthesis of optically transparent thin films of Ru_2 paddlewheel molecules, their photochemistry, and attempts at apical ligand metathesis to introduce photoprecursor groups. The fourth chapter builds upon the synthesis of porous, optically transparent thin films demonstrated in the third chapter, but instead with porphyrin molecules. We explored the growth mechanism of our polyelectrolyte films and explore solid-state photochemistry of our films. The final chapter presents a prospectus of future film targets for solid-state photochemistry.

ACKNOWLEDGEMENTS

The following list of people I wish to thank is wholly inadequate in scope and depth, but I endeavor to try anyway. I would like to thank my mentors and friends in the Powers Group who have preceded me – Drs. Wen-Yang Gao, Ashley Cardenal, Sung-Min Hyun, Chen-Hao Wang, Anuvab Das, and Asim Maity. This talented group of former senior students and postdoc taught me everything I know (almost literally) and I was honored to stand on the shoulders of such industrious and intelligent giants. I would also like to thank my contemporaries in the Powers Group – Drs. Richard Thompson, Gerard Van Trieste III, and Mario Cosio for being the best group of friends, supporters, and labmates anyone could ask. Never was there a dull day or dull debate when we were all together. I would also like to thank the junior students in the Powers Group for keeping me young (in spirit) and always in practice when it comes to mentoring. I would particularly like to thank Ms. Aishanee Sur and Mr. Subham Sarkar for entertaining my preposterous ideas about polyelectrolyte film possibilities and for providing me so much practice and material to continue forward.

I would like to extend additional thanks to Texas A&M University and the Department of Chemistry for providing me a place to conduct research and call home. I would like to thank all the departmental support staff for their training and expertise and patience: Drs. Greg Wiley and Doug Elliot in the NMR Facility for always laughing with me and letting me quench an NMR, Dr. Yohannes Rezenom in the Mass Spec facility for always being kind and for running my samples first regardless of the salt content, and Dr. Nattami Bhuvanesh in the X-Ray facility for answering my after hours emails about PXRD parameters. Additionally, a lot of my work would

have been impossible or significantly more expensive without the talented hands of Bill Merka in the Glass Shop, Will Seward in the Machine Shop, and Tim Pehl in the Electronics Shop.

I would like to thank Dr. Simon North for being a supportive department head, Dr. Tamara Powers for being a wonderful teaching advisor and providing me the freedom and opportunity to grow as an educator of young chemists, Dr. Edward Lee for providing mentorship and support both inside and outside of the teaching lab, and finally Ms. Sandra Horton and Ms. Valerie McLaughlin along with all the other front office staff for supporting the graduate student mission and putting up with my constant shenanigans and questions.

I would like to thank all of the other graduate students in the department of chemistry for being excellent neighbors and abiding by my random requests for chemicals or advice. I would particularly like to thank all my friends in the Ozerov, Gabbaï, and Nippe labs for being great friends and always willing to talk with me about science and life in between borrowing chemicals. I would especially like to thank the friends I made in my cohort. Most of us are scattered across the country now, but I will always take a part of you with me in the memories that we all share and the struggles we all persevered through.

I would also like to thank my collaborators: Kyle Korman, Joe Simms, and Dr. Eric Bloch from the Bloch group at IU have been a fantastic help with launching the films project and running needed measurements as well as providing materials. A significant portion of this dissertation would not have been possible without their existence and scientific expertise. Another significant portion of this dissertation would not have been possible without Mr. Ethan Iverson in the Grunlan Group at TAMU. His endless enthusiasm and energy have been infectious and his expertise was sorely needed to bring this project to where it now stands.

Chief amongst the people I wish to thank is my advisor, Dr. David Powers. Dave refused to give up on my development, no matter how depressed the slope of my progress graph was. His careful tutelage has taught me the value of interpersonal communication in scientific endeavors and in life, and also the value of always doing the easy experiments first. His willingness to engage with new chemistry has allowed me the freedom and opportunity to explore an incredible amount of chemical space. For even partly removing the veil of my own ignorance, I am eternally grateful.

CONTRIBUTORS AND FUNDING SOURCES

Contributors

This work was supervised by a dissertation committee consisting of my advisor Professor David C. Powers, Professor Sarbajit Banerjee, and Professor Hongcai Zhou of the Department of Chemistry and Professor Manish Shetty of the Department of Chemical Engineering.

Yohannes Rezenom collected the MALDI-MS in Chapter II. Ethan Iverson and Hudson Legendre collected the profilometry data in Chapters III and IV. Ethan Iverson collected the AFM data in Chapter IV. Kyle Korman collected the SEM images in Chapter III. Subham Sarkar synthesized **III-1** in Chapter III and Chapter IV and collected the ^{1}H and ^{19}F NMR data for that compound. Wen-Yang Gao synthesized **III-6** in Chapter III. Matthew Figgins synthesized **IV-1** in Chapter IV and collected the ^{1}H NMR data for that compound. Aishanee Sur synthesized **MnTCPPCl** thin films in Chapter IV, performed the photolysis, and collected the UV-Vis data. Sarah Fisher collected QCM data for a film of **IV-1** in Chapter IV. Subham Sarkar synthesized **V-1** and the film of **V-1** in Chapter V and collected UV-Vis data.

Funding Sources

This work was funded by Texas A&M University, the Welch Foundation (A-1907), the U.S. Department of Energy (DOE), Office of Science, Office of Basic Energy Sciences, Catalysis Program under Award Number DE-SC0018977, and the National Science Foundation under Award Number 2154976 - Collaborative Research: Porous Molecules as a Platform for Solid-State Organometallic Chemistry.

TABLE OF CONTENTS

Page

LIST OF FIGURES

Page

LIST OF TABLES

Page

CHAPTER I

INTRODUCTION: LEVERAGING EXCHANGE KINETICS FOR THE SYNTHESIS OF ATOMICALLY PRECISE POROUS CATALYSTS[1]

I.1. Introduction

Systematic control of the structure of molecular catalysts, via modulation of the ligand donicity and geometry, enables evaluation of structure-activity relationships and optimization of catalyst selectivity in homogeneous catalysis.[1-5] While heterogeneous catalysts often display enhanced stability and recyclability in comparison to their homogeneous counterparts, similar systematic variation of the local chemical structure of catalyst sites is not routinely possible.[6] The potential to merge the structure-dependent selectivity of molecular catalysis with the durability of heterogeneous systems has motivated extensive efforts to develop molecularly addressable solid-state catalysts.[7, 8]

Covalent tethering (*i.e.*, grafting) of molecular catalysts to solid supports has been widely investigated as a strategy to control the structure of active sites in heterogeneous catalysis. Grafting relies on covalently attaching an appropriately functionalized molecular catalyst onto solid supports, such as siliceous, aluminous, and graphitic materials (Figure I-1a).[9, 10] Heterogenizing molecular catalysts via grafting enables the local catalyst structure to be controlled by judicious selection of molecular grafting precursors. Challenges inherent to molecular grafting, such as controlling catalyst loading and the heterogeneity of local catalyst microenvironments, complicate

[1]Text in this chapter was adapted with permission from reference 123: Ezazi, A. A.; Gao, W,.-Y.; Powers, D. C. *ChemCatChem*, **2021**, *13*, 2117–2131. Copyright John Wiley and Sons.

analysis of the structure-function relationships that underpin systematic catalyst development and optimization.[11, 12]

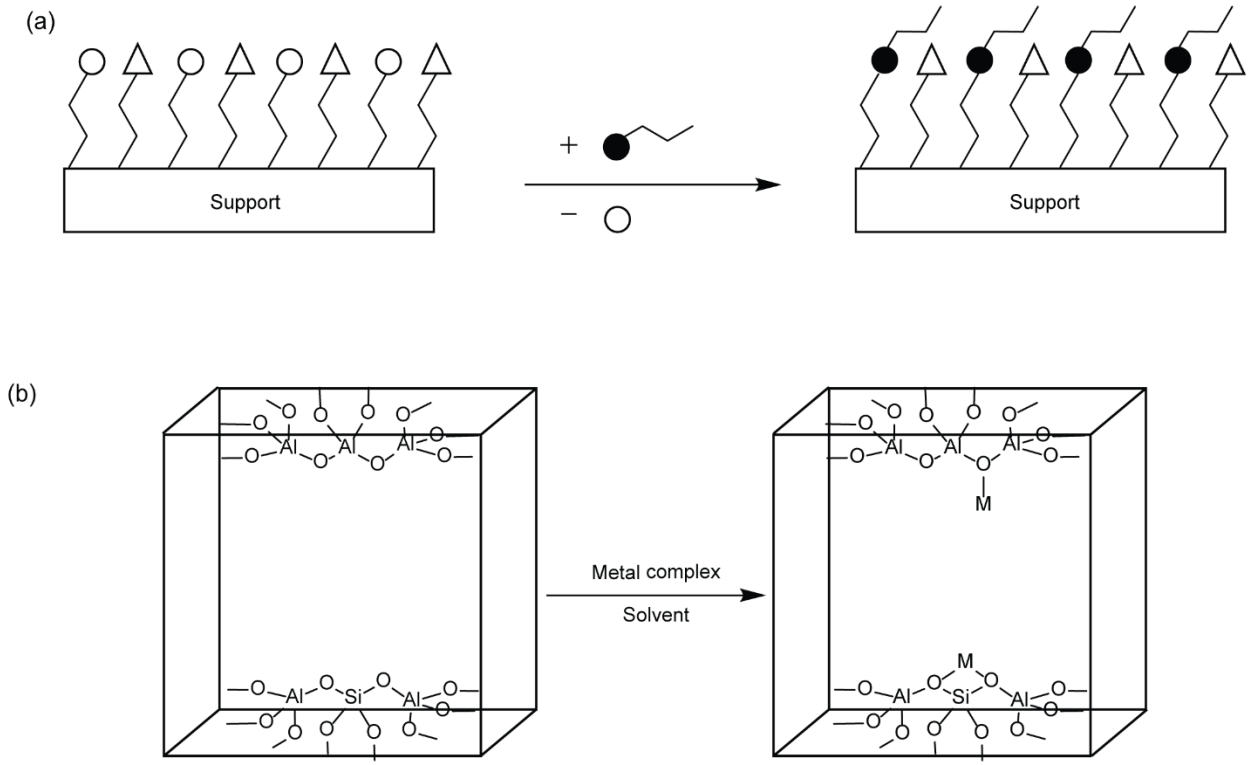

Figure I-1. General strategies for incorporating catalysts in solid supports include (a) grafting of molecular catalysts or (b) doping of a solid material with soluble catalysts. Grafting of molecular catalysts to heterogeneous materials provides a strategy to control the active sites of heterogeneous catalysts. Grafting is accomplished by coupling functionalized ligands with surface functional groups of the solid support. A similar strategy involves the doping of solid supports i.e., zeolites. Transition metal-doped zeolites have been pursued as catalysts for a wide variety of transformations. While doping increases the diversity of reactions that can be achieved with zeolite catalysts, challenges associated with active site heterogeneity complicate delineation of structure-function relationships. Reprinted with permission from reference 123. Copyright John Wiley and Sons.

Zeolites are a family of porous aluminosilicate materials. Transition-metal-doped zeolites bind transition metal cations with an all-oxygen donor sets at anionic aluminum sites in the lattice. [13, 14] These materials have found widespread application as highly active catalysts in an array of reactions.[15-17] Because the local catalyst structure is defined by the aluminosilicate support, and

because the aluminum sites are randomly distributed within the zeolite framework, challenges related to active site heterogeneity, and attendant variability of coordination modes of bound metal dopants, can render these materials challenging to optimize (Figure I-1b).

Metal-organic frameworks (MOFs) are a class of porous materials composed of metal nodes (secondary building units, SBUs) and polytopic organic ligands. Reticular synthetic logic, which affords isostructural frameworks by replacement of either metal nodes or organic linkages by a topologically analogous moieties, underpins the rational synthesis of MOFs (*i.e.*, isoreticular MOFs) (Figure I-2a).[18, 19] Reticular synthetic logic allows the material properties to be varied independently from the local structure of lattice-confined active sites. Combined with the crystallinity and uniform porosity that is characteristic of MOFs, the ability to rationally manipulate materials properties has stimulated significant interest in the development of MOFs as platforms for selective catalysis.[20]

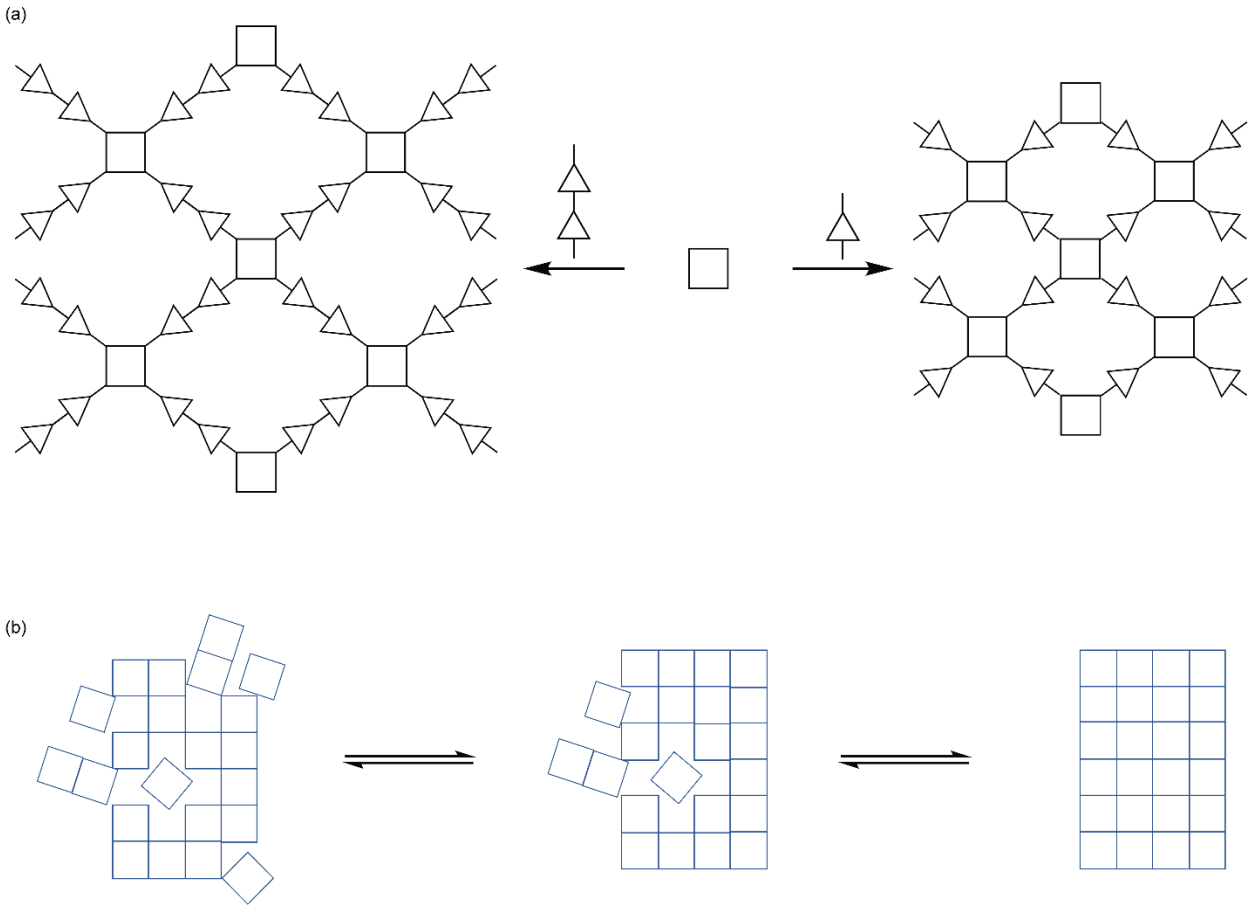

Figure I-2. (a) Reticular synthetic logic enables rational modification of material structure, for example by elongation of the linker structure, while the overall material topology is unchanged. (b) Reversible M–L bond formation allows for defect annealing and the growth of extended crystalline frameworks. Reprinted with permission from reference 123. Copyright John Wiley and Sons.

Access to crystalline MOFs requires reversible M–L bond construction in order to provide a mechanism to anneal crystallization defects (Figure I-2b).[21] This requirement is manifest in an abundance of MOFs based on metal ions that participate in rapid ligand exchange reactions but a relative dearth of materials based on metal ions featuring slow ligand-exchange kinetics.[22, 23] Those MOFs that have been reported based on kinetically inert ions such as Ru^{3+} or Cr^{3+} are typically available only as microcrystalline powders, which underscores the challenge of generating large

crystallite domains with slowly exchanging ions. Similarly, the ligands on which MOFs are constructed — and thus which comprise the primary ligand sphere of lattice ions — also must participate in reversible M–L reversible bond formation. As a result, weak-field ligands, such as carboxylates and azolates, are commonly encountered in MOFs; access to materials based on strong-field ligands is less well developed. Further, the need for M–L reversibility can render controlling the distribution of individual metal ions in multimetallic MOFs challenging. Construction of these materials with metal ions that display different M–L substitution kinetics often leads to phase segregation or metal ion scrambling.

To unlock the full potential of MOFs as molecularly addressable platforms for heterogeneous catalysis, synthetic tools that enable systematic variation of the chemical and electronic structure, as well as the distribution, of the lattice ions are required. Methods to access atomically precise materials based on arbitrary metal ions and primary ligand sets would enable systematic evaluation of catalyst selectivity and the potential to couple catalyst-controlled and confinement-induced selectivities. Access to such methods would naturally result in the ability to control the distribution of metal ions in multimetallic systems.

This dissertation discusses strategies relevant to the construction of porous polymer architectures from kinetically incompetent metallomonomers. In this context, this chapter summarizes emerging synthetic strategies that leverage relative rates of M–L substitution to access atomically precise MOF catalysts. Chemical strategies that enable incorporation of metal ions with intrinsically slow exchange kinetics as part of the connecting linker or within the SBU are discussed. Extension of these methods to the preparation of materials in which the primary coordination sphere of immobilized organometallic moieties are systematically modulated and the distribution of metals in multimetallic MOFs is controlled are presented.

I.2. Metallopolymerization as a Strategy to Control the Primary Coordination Sphere of Lattice-Confined Catalysts

The requirement for reversible M–L bond construction to access crystalline MOFs implies that lattice ions are most often supported by weak-field ligands that readily undergo exchange chemistry.[24, 25] In contrast, a much more diverse array of primary coordination spheres are encountered in molecular catalysis, including strong-field donors such as carbenes, phosphines, and basic nitrogen donors. To control the electronic structure of the catalyst active site, and thus the catalyst activity and selectivity, access to MOF catalysts with more diverse primary coordination spheres is necessary. The synthetic approaches described in this section rely on metallopolymerization of pre-synthesized organometallic linkers or SBUs to access MOF catalysts that feature lattice ions supported by systematically addressable primary coordination spheres.

The polymerization of appropriately functionalized organometallic complexes, such as functionalized metallosalens or metalloporphyrins, is a classic strategy towards the synthesis of MOF catalysts.[26-35] For example, Nguyen and Hupp *et al.* reported the synthesis of $[Zn_2(BPDC)_2(Mn\mathbf{L_1})Cl]\cdot 10DMF\cdot 8H_2O$ (**I-3**) via the polymerization of pyridine-decorated Mn salen **I-1** with biphenyldicarboxylic acid (**I-2**) in the presence of zinc nitrate (Figure I-3).[36] Material **I-3** was demonstrated to be an effective catalyst of enantioselective olefin epoxidation. While **I-3** was the first report of incorporation of a metallosalen in a framework material, reticular replacement of the metallosalen linker has enabled access to families of isostructural frameworks.[37, 38]

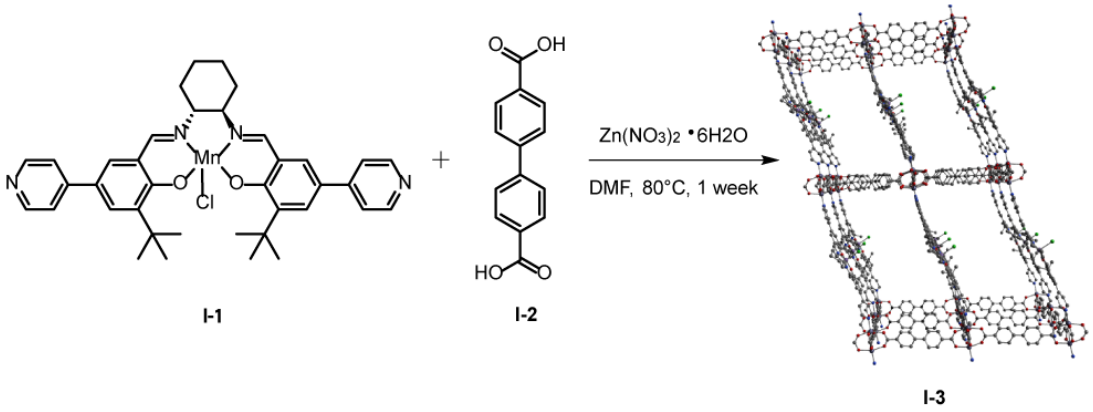

Figure I-3. Synthesis of Mn salen MOF I-3 by solvothermal combination of I-1, I-2, and $Zn(NO_3)_2$ in DMF. Reprinted with permission from reference 123. Copyright John Wiley and Sons.

I.2.1. Incorporation of Strong-Field Donors.

Because metallopolymerization strategies rely on catenation of substituents that are peripheral to the organometallic unit being incorporated, these strategies have been applied to the incorporation of lattice ions that are supported by strong-field, slowly exchanging ligands.

Pincer Ligands

Pincer ligands are meridionally coordinating, tritopic ligands that have found broad application in coordination chemistry and homogeneous catalysis.[39] Similar to the preparation of metallopophyrin and metallosalen-based materials, extensive efforts have been directed towards the preparation of porous materials based on transition metal pincer sites. Metallopolymerization of pincer complexes featuring peripheral donors enables incorporation of the diversity of available pincer complexes to be incorporated into MOFs.[40-42] For example, Humphrey demonstrated that palladation of carboxylated pincer **I-4** followed by polymerization in the presence of Co^{2+} provides access to a MOF, PCM-36, based on Pd pincer linkers (Figure I-4a).[43]

The advantage of metallopolymerization is that the materials properties, which are in part dictated by the structure of the SBUs, can be varied independently of the local structure of the pincer site. For example, polymerization of Pd-pincer **I-4** with combinations of Zn^{2+} or Co^{2+} resulted in 1-D chains, 2-D sheets, and 3-D MOFs that all contained the Pd pincer moiety (Figure I-4b, I-4c).[44] In addition to providing topological control, metallopolymerization provides a strategy to incorporate metal ions that may be incompatible with solvothermal chemistry: The conditions described for the polymerization of **I-4** — DMF, water, and ethanol at 50 °C — would likely effect reduction of Pd^{2+} to Pd^{0} via b-hydride elimination pathways. Due to the kinetic stabilization afforded by the strongly bound pincer ligands, the Pd^{2+} sites become compatible with solvothermal reaction conditions.

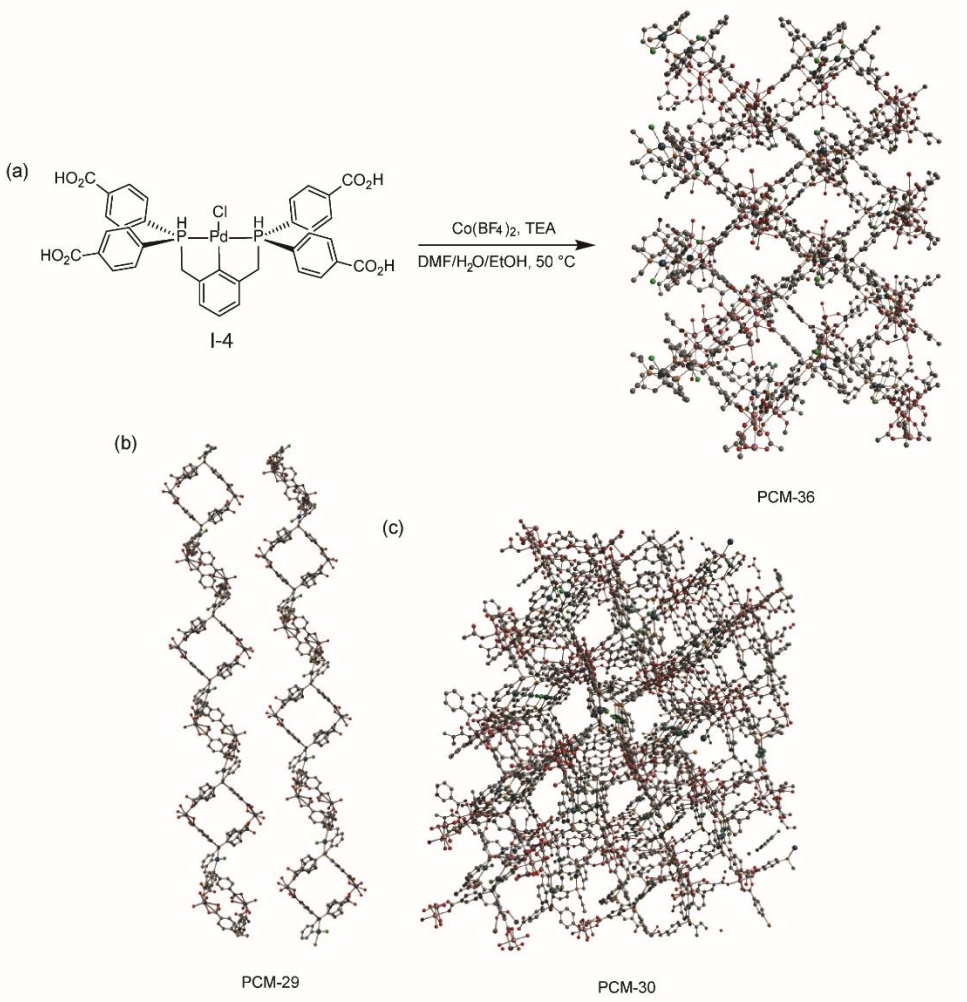

Figure I-4. Stabilization of Pd^{2+} in a pincer ligand prevents undesired reduction during solvothermal material synthesis. Reprinted with permission from reference 123. Copyright John Wiley and Sons.

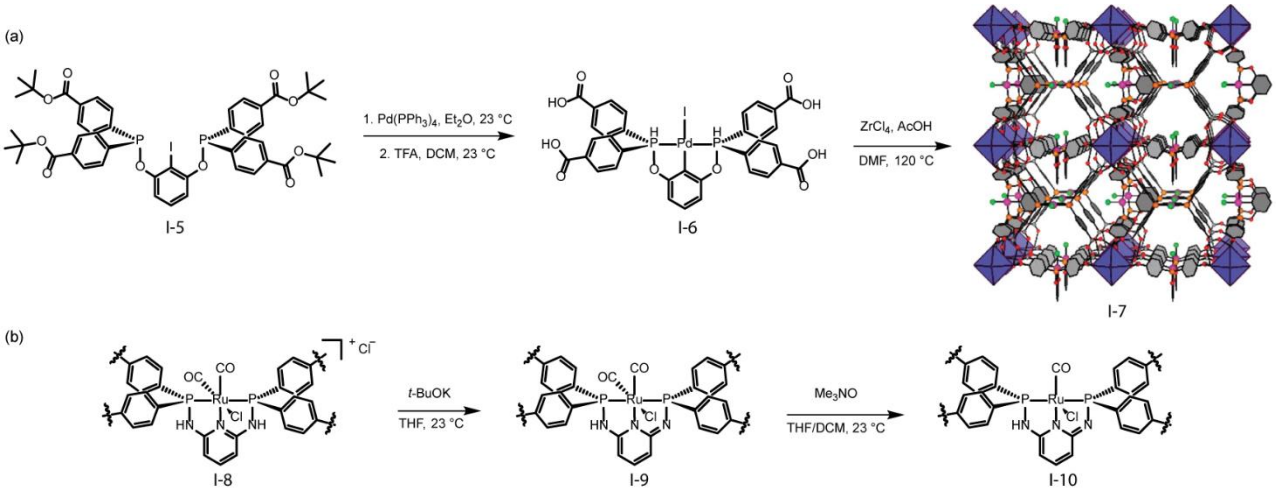

Figure I-5. Synthesis routes for Pd-pincer containing MOFs. (a) A two-step metalation-deprotection sequence affords pincer complex I-6. Metallopolymerization with $ZrCl_4$ affords MOF I-7. (b) The stability of the M–C bond in I-8 enables post-synthetic modification to access the neutral monodecarbonyl I-9, which is an active catalyst for aldehyde hydrosilylation. Figure I-5b reprinted with permission from reference 123. Copyright John Wiley and Sons.

Wade *et al.* demonstrated metallopolymerization to access isostructural materials in which the donor of the pincer ligand are varied between PCP and PNP (Figure I-5).[45, 46] Metallation of the *tert*-butyl ester-protected proligand **I-5** with Pd followed by trifluoroacetic acid-promoted ester hydrolysis provided access to metallomonomer **I-6**. Solvothermal polymerization with $ZrCl_4$ at 120 °C afforded **I-7**, in which the pre-synthesized metal pincer complex was incorporated into the extended MOF lattice. This strategy was subsequently utilized to synthesize the isostructural Ru-PNP pincer-based material **I-8**. In addition to enabling the synthesis of an isostructural pair of materials, the kinetic inertness of the metallomonomers allows for post-synthetic modification of the catalyst sites. For example, the CO ligands of **I-9** were removed by treatment with trimethylamine *N*-oxide to yield an open coordination site with which to bind substrates (Figure 5b). The impact of heterogenation is evidenced by the observation that while **I-10** promotes catalytic hydrosilylation of benzaldehydes (~80% yield), the homogeneous analogue is ineffective

(<5% yield). The modularity of metallopolymerization strategies has enabled the synthesis of additional pincer-based MOFs based on a diverse set of primary coordination spheres.[47-49]

Carbene Ligands

N-heterocyclic carbenes (NHCs) are a class of strong sigma-donor ligands that are frequently encountered in homogeneous catalysis.[50, 51] Direct synthesis of uncoordinated NHCs is often challenging because NHCs strongly coordinate to available metal centers, thus limiting reversibility necessary for materials synthesis.[52, 53] Hupp *et al.* demonstrated that this challenge could be overcome by synthesis of imidazolate-based frameworks, which could be post-synthetically deprotonated to generate lattice-bound mesoionic NHCs.[54] Following synthesis of TIF-1, a Co^{2+}-imidazolate framework, deprotonation with *n*-BuLi yielded free mesoionic NHCs. The strong bases utilized to deprotonate the lattice imidazolate units can lead to framework degradation, which has limited broad implementation of this synthetic strategy.[55] Additional stategies based on *in situ* metalation of NHCs,[56-58] polymerization of metallocarbene linkers,[59, 60] and post synthetic metalation/exchange have been developed[61-63] to overcome these limitations.

Selectively programming metal content at NHC vs. at SBU in one-pot synthesis is a significant synthetic challenge.[56, 64] Sumby, Doonan, and coworkers reported synthesizing a M-NHC containing MOF where the node and M-NHC are composed of Zn and Cu respectively.[57] Heating a solution of DMF, **I-11**, Zn^{2+}, and Cu^{+} yielded **I-12**, in which Cu^{+} forms a bis-NHC complex and is connected by Zn_4O nodes (Figure I-6a). This material was used as a catalyst for CO_2 hydroboration. In a follow-up report, these authors demonstrated that analogous synthetic conditions with ligand **I-13**, in which the angle between carboxylates is reduced, only produces *mono*-NHC complexes (Figure I-6b).[58]

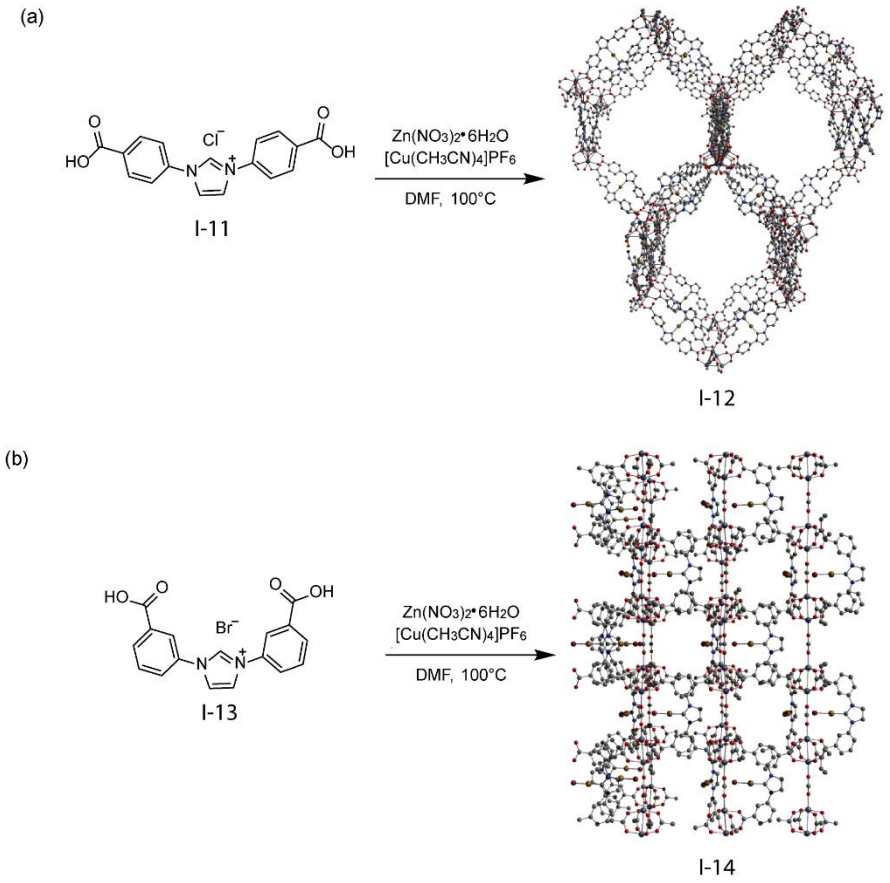

Figure I-6. (a) One pot synthesis of I-12 from ligand I-11 yields bis-NHC ligated Cu sites. (b) Replacement of ligand I-11 with ligand I-13, which features meta-carboxyates rather than para-carboxylates, affords I-14, which features mono-NHC ligated Cu sites. Reprinted with permission from reference 123. Copyright John Wiley and Sons.

Yaghi *et al.* demonstrated metallopolymerization as a strategy to access NHC-based MOFs.[59] Metallomonomer **I-15** was prepared by palladation of carboxylated imidizolium-based linker followed by deprotection of the peripheral *tert*-butyl esters (Figure 7). Polymerization of **I-15** with $Zn(NO_3)$ in a mixture of DEF and pyridine afforded IRMOF-77, which is isostructural with MOF-5. The addition of pyridine to the polymerization medium was necessary to suppress the formation of *bis*-carbene Pd complexes. Elemental analysis, ^{13}C SS-NMR, and IR data indicate exclusive NHC metallation with Pd, with no metathesis to Zn-NHC sites occuring. Importantly,

attempts to access IRMOF-77 via post-synthetic metalation of the imidazolium containing analog, IRMOF-76, resulted in framework decomposition.

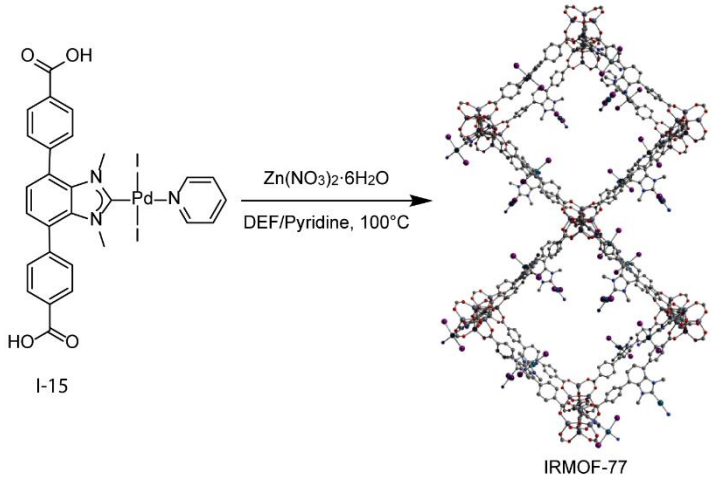

Figure I-7. Metallopolymerization of Pd carbene complex I-15 enables synthesis of IRMOF-77, which features palladated NHC sites. Reprinted with permission from reference 123. Copyright John Wiley and Sons.

Post-synthetic exchange of linkers is a widely utilized technique in MOF synthesis and has been used to install sensitive functional groups.[29, 65] Martín-Matute and coworkers utilized post-synthetic exchange to introduce an iridium NHC linker, **I-16**, into UiO-68-2CH_3.[62] **I-16** was substituted into UiO-68-2CH_3 by soaking the as synthesized MOF in a methanolic solution of **I-16** at 60°C for 24 hours (Figure I-8). ^{1}H NMR, energy dispersive X-ray spectroscopy (EDS), and inductively coupled plasma optical emission spectroscopy (ICP-OES) data indicate metallolinker loadings of 27-36%, and IR measurements indicate the presence of free carboxylic acid motifs, which suggests that some linker may reside in the pore space (it is unknown if one or both carboxylates are uncoordinated to the Zr cluster). EDS data additionally suggest a homogeneous

distribution of **I-16** in the MOF. The substituted UiO-68-2CH_3 platform was competent as a catalyst for the isomerization of 1-octen-3-ol to octan-3-one.

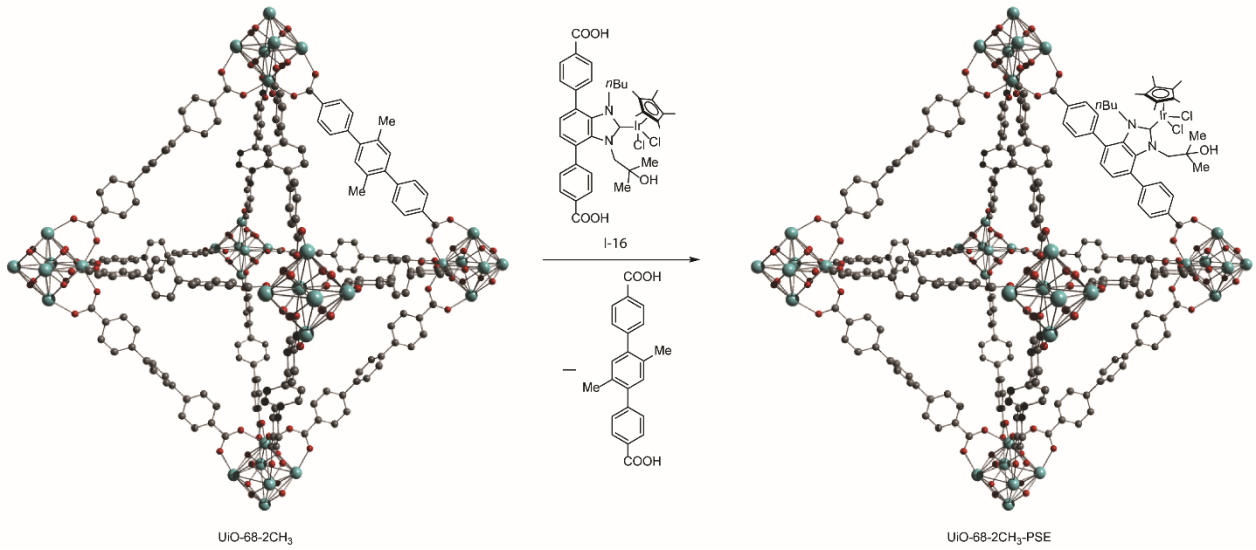

Figure I-8. Post-synthetic exchange of metalloligand I-16 into UiO-68-2CH_3 affords UiO-68-2CH_3-PSE. Methyl groups are ommitted for clarity. Reprinted with permission from reference 123. Copyright John Wiley and Sons.

Phosphine Ligands

Similar to NHCs, phosphines are strongly sigma donating ligands that are often encountered in homogeneous catalysis.[66] Humphrey and co-workers demonstrated the solvothermal combination of Co^{2+} or Ni^{2+} with tris(p-carboxylato)triphenylphosphine (**I-17**) and 4,4'-bipyridine (**I-18**) afforded PCM-101, a 3-dimensional MOF in which the phosphine ligand forms 2-dimensional sheets with an M_3O cluster, which are spanned by bipyridine struts (Figure 9).[67] PCM-101 features two open phosphine binding sites that point into the pore space between layers and are arranged *trans* to each other. Subsequent metallation with either (Me_2S)AuCl or

CuBr·(MeSMe) provided phosphine-supported Au_2 and Cu_2 sites, respectively. Both materials were used to catalyze the hydroalkoxylation of 4-pentyn-1-ol to 2-hydroxy-2-methyl-hydrofuran.

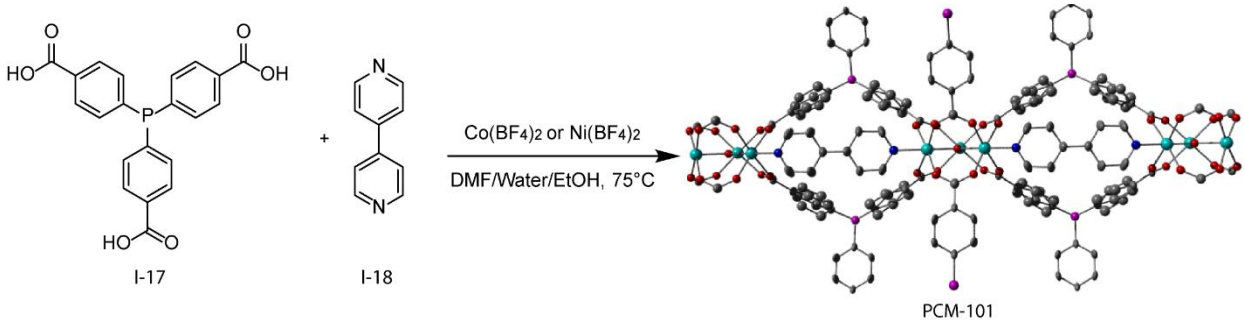

Figure I-9. Synthesis of PCM-101, which features free phosphine sites, was achieved by polymerization of I-17 and I-18 with either Co^{2+} or Ni^{2+}. Reprinted with permission from reference 123. Copyright John Wiley and Sons.

Lin and coworkers reported the synthesis of phosphine-containing MOF, $Zr_6(OH)_4O_4\mathbf{L}_6$ (L= 4,4-bis(4-carboxyphenylethynyl)-BINAP).[68] In this synthesis, the uncoordinated phosphines were preserved during polymerization due to the selection of Zr^{4+} as the metal ion for SBU construction; the hard acid Zr^{4+} does not strongly coordinate with phosphines, which are soft bases according to hard-soft acid-base (HSAB) theory.[69] Post-synthetic metalation of the lattice-bound phosphines with either Ru^{2+} or Rh^{2+} provided materials that were applied to asymmetric group-transfer reactions.[68]

I.2.2. Isostructural Materials with Systematically Varied Primary Ligand Sets.

Strong donors such as amides and amidinate ligands are rarely encountered in MOF chemistry due to the irreversibility of M–L bond formation under many conditions. Metallopolymerization strategies offer an attractive approach to generating isostructural materials with systematically varied primary coordination spheres because the coordination sphere is

installed during the synthesis of molecular monomers and is not directly involved in the polymerization chemistry. Powers *et al.* reported the synthesis of a family of Ru_2 complexes in which the bridging ligands included amide, hydroxypyridinate, aminopyridinate, and carboxylate functional groups (Figure I-10a).[70] The ligands were decorated with peripheral iodide substituents, which enabled polymerization via Sonogashira cross-coupling with polyalkynes (Figure I-10b). The resulting porous materials featured Ru_2 units in which the bridging ligands of the metallomonomers were incorporated into the porous material. This family of materials displayed ligand-dependent nitrene-transfer selectivity (*i.e.*, allylic amination vs. olefin aziridination) that was similar to that observed with analogous soluble molecular catalysts (Figure I-10c). Because the C–C coupling reactions used to generate these materials is irreversible, the generated heterogeneous catalysts were amorphous.

Metallopolymerization of Ru_2 metallomonomers was extended to the synthesis of crystalline materials by changing the peripheral functional group from iodo- to cyano- and thus the polymerization protocol from Sonogashira coupling to Ag^+ coordination (Figure I-10d).[71] The weak Ag–N coordination bond allows for reversible M–L bond formation, thus yielding crystalline materials, but also comes at the expense of material stability: the generated coordination polymers are unstable to desolvation.

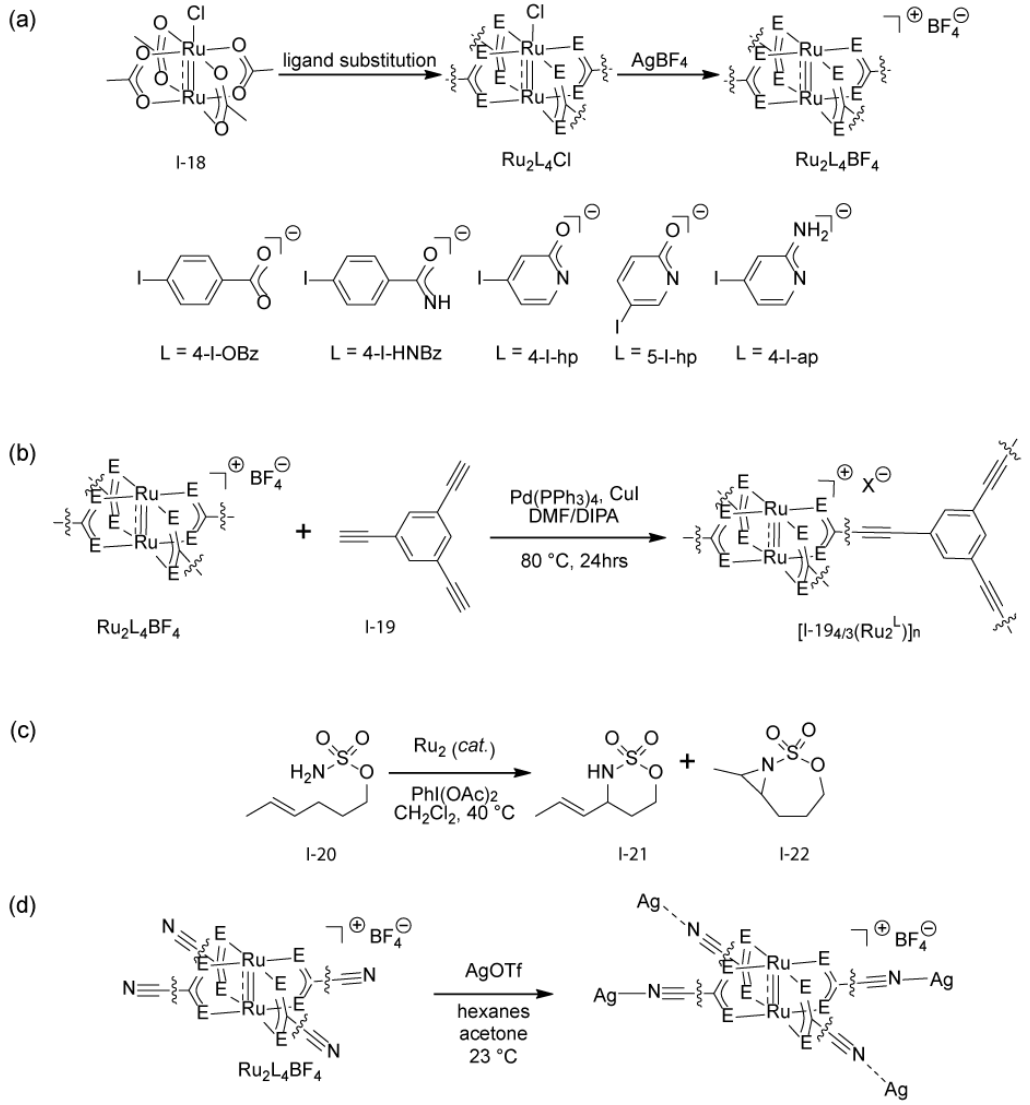

Figure I-10. Synthesis strategies to produce metallopolymers containing Ru_2 units. (a) Ligand exchange on $Ru_2(OAc)_4Cl$, followed by anion exchange, affords access to a family of Ru_2 precursors with diverse primary coordination spheres. (b) Sonogashira cross-coupling with polyalkynes allowed access to Ru containing polymers. (c) The Ru_2-based polymers displayed similar nitrene transfer selectivity in the cyclization of sulfonamide 20 as compared with analogous molecular catalysts. (d) Metallopolymerization of Ru_2 complexes via Ag–N coordination affords a family of crystalline Ru_2 metallopolymers with varied coordination spheres.

I.3. Lattice-Ion Lability Enables Post-Synthetic Cation Exchange

The exchange of lattice ions in MOFs can provide a strategy to generate new materials in which the lattice structure in maintained but the ion content is altered. Post-synthetic modification of template MOFs can provide access to framework materials that are inaccessible or challenging to make by direct synthesis.[65] Similar to the post-synthetic linker exchange illustrated in Figure 8, cation exchange can provide homogeneously distributed materials. One of the particular advantages of cation methathesis is that it can afford access to mixed-metal materials which are comprised of slowly exchanging metal ions.[72, 73] While predictive models for the rate and extent of ion exchange continue to be delineated,[74, 75] rational exchange has been demonstrated based on geometric considerations, alteration of ligand exchange rates by control of solvation environment, and through use of redox strategies to access kinetically labile oxidation states.

I.3.1. Differential Exchange Rates of Cation Metathesis as a Tool to Access Bimetallic Materials

Cation exchange within a MOF lattice was first demonstrated by Dincă and Long , who described exchanging the Mn^{2+} ions in the MOF $Mn_3[(Mn_4Cl)_3(BTT)_8(CH_3OH)_{10}]_2$ (**I-23**, BTT = 1,3,5-benzenetristetrazole) with a variety of other mono- and divalent cations to generate a family of materials that were evaluated for H_2 binding.[76] Material **I-23** features two inequivalent Mn sites, one which is 5-coordinate (and part of the SBU) and the other which is 2-coordinate (and is not part of the SBU). Soaking the parent MOF in solutions of Li^+, Cu^+, Fe^{2+}, Co^{2+}, Ni^{2+}, Cu^{2+}, or Zn^{2+} resulted in the selective exchange of the 2-coordinate Mn site. The extent of exchange depended on the exchanging ion: the greatest extent of exchange was achieved with Cu^{2+} and Zn^{2+}, which exchanged 5 Mn^{2+} cations and a minimum with Cu^+ not exchanging any Mn^{2+} ions. For Cu^{2+} and

Zn^{2+}, the observed number of exchanged cations per formula unit is higher than 3, indicating partial exchange of the higher coordinate, cluster Mn sites.

The discrimination of positional exchange is likely a result of increased kinetic lability of the lower coordinate site, but it is not clear if the degree and extent of exchange has significant thermodynamic considerations. Such ion segregation is not trivial to accomplish and highlights the potential of cation exchange to provide discrete heterobimetallic materials with selective exchange of particular sites.

Dincă *et al.* demonstrated cation exchange chemistry to prepare heterobimetallic Co/Zn MOF-5 with greater Co content than had been available from direct solvothermal methods. Direct solvothermal access to mixed Co/Zn MOF-5 materials had been shown to afford a maximum of 21% Co, regardless of the stoichiometric excess.[77] This is an unexpected result based on exchange rate analysis: the exchange rates of Co^{2+} and Zn^{2+} are similar, therefore it might be anticipated that the ion incorporation would match the stoichiometry of the reaction mixture. Soaking Zn-MOF-5 in a solution of anhydrous DMF and $CoCl_2$ resulted in mono, di, and tri substitutions of Co for Zn after 1 day, 2 weeks, and 1 month, respectively (Figure I-11).[78] This strategy has been further advanced by the Dincă group to prepare a family of ion-exchanged, metastable MOF-5 derivatives which are not accessible by direct solvothermal synthesis.[79]

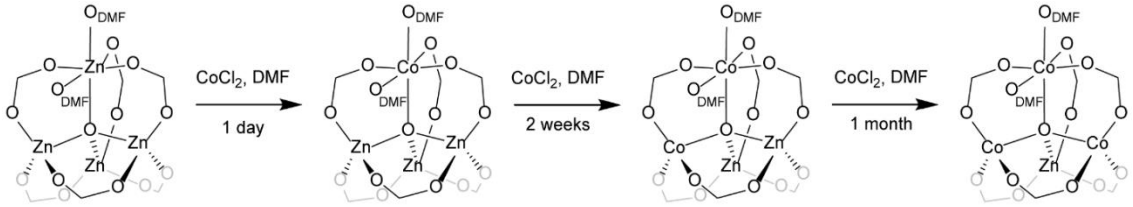

Figure I-11. Stepwise substitution of Zn^{2+} for Co^{2+} in MOF-5 is promoted by binding of DMF to fill the coordination sphere of Co. Reprinted with permission from reference 123. Copyright John Wiley and Sons.

Exchange of Mn^{2+} into MOF-5 has been demonstrated to provide competent group-transfer catalysts: by exchanging a single Zn^{2+} for Mn^{2+}, catalytic epoxidation of cyclopentene can be realized using an iodosylarene oxidant to generate a putative Mn^{IV}-oxo.[80] Similar partially exchanged materials have been developed for highly efficient ethylene polymerization and allylic oxidation of cyclohexene from Mn and Cr exchanged nodes in MFU-4l, respectively.[80-82] Both CFA-1 and MFU-4l feature a pentanuclear Zn SBUs with the central Zn in a trigonal prismatic geometry and the peripheral Zn atoms in a Td or trigonal pyramidal geometry (depending on counterion, Figure I-12a). The outer Zn ions are able to be exchanged readily exchanged by Mn^{2+}, Cr^{2+}, Cr^{3+}, Ti^{3+}, and Ti^{4+} to yield catalytically active MOFs.[83] The introduction of Ti and Cr ions, very oxophilic species, into an azolate framwork is noteworthy in that few materials exist based on these ions continaing an all nitrogen ligand set. With the exception of Cr^{3+}, all the exhanged ions have fast ligand exchange rates.

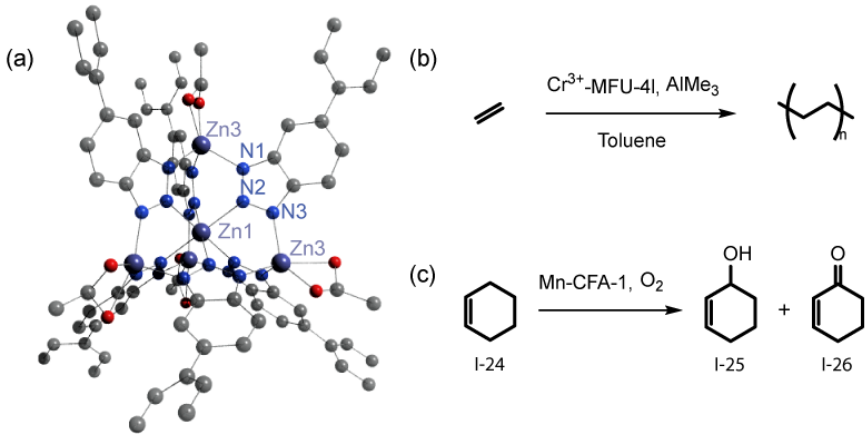

Figure I-12. Post-synthetically metalated SBUs which enable hydrocarbon functionalization. (a) The pentanuclear Zn SBU present in both CFA-1 and MFU-4l. (b) Gas-phase ethylene polymerization with Cr^{3+}-substituted MFU-4l. (c) Mn-CFA-1 will catalyze the oxidation of I-24 under O_2 to give I-25 and I-26. Reprinted with permission from reference 123. Copyright John Wiley and Sons.

As described above, disparities in the exchange rates between inequivalent metal binding sites have been utilized to access materials that display site-specific metal-ion exchange.[84] Ma *et al.* demonstrated cation metathesis of Co for Cd within the porphyrinic linker of MMPF-5, which is a MOF based on $Cd(CO_2R)_3$ SBUs.[85] During synthesis from tetrakis(3,5-dicarboxyphenyl)porphyrin with $Cd(NO_3)_2$ in DMSO at 135 °C for 24 hours, both Cd SBUs and Cd porphyrin units were obtained (Figure I-13b). The porphyrinic binding site cannot accommodate the Cd^{2+} ion, which is thus weakly bound above the porphyrin plane.[86] Soaking as-synthesized MMPF-5 in a DMSO solution of Co^{2+} at 85°C resulted in metathesis of only porphyrinic cadmium with cobalt, generating a bimetallic MOF material comprised of cadmium nodes with cobalt metalloligands. This strategy is predicated on the coordinately saturated Cd at the node exchanging much more slowly than the weakly bound porphyrinic Cd.

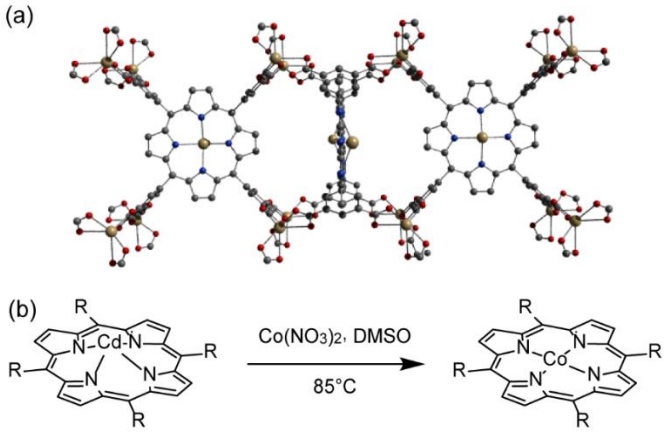

Figure I-13. Cd-based porphyrin MOFs. (a) 3-Dimensional structure of MMOF-5 in which $Cd(CO_2)_3$ SBUs connect octatopic Cd porphyrins. (b) Post-synthetic metathesis of Cd with Co is accomplished by soaking MMOF-5 in a DMSO solution of $Co(NO_3)_2$ and heating at 85°C. Reprinted with permission from reference 123. Copyright John Wiley and Sons.

I.3.2. Solvation Environment Modulates Exchange Rate

Exchange of any ion in a cluster involves making and breaking of M–solvent bonds and it has been postulated that the rate of ion metathesis is governed by the strength of the M–solvent bond.[87] Factors such as coordination geometry, coordination number, and rigidity of linker can affect M–solvent bond strength, thus affecting the ultimate degree of transmetallation. In support of this model, while transmetallation of Co^{2+} into MOF-5 afforded tris-substitution, transmetallation of Ni^{2+} into MOF-5 yielded only mono-substitution.[88] The difference between the Ni^{2+} and Co^{2+} experimental results is proposed to arise from the relative kinetic accessibility of subsequent metathesis events. In the aforementioned example, exchange of solvent molecules is rapid due to fast exchange rates on Zn^{2+} and Co^{2+} in either T_d or O_h geometry but incorporation of a single Ni^{2+} ion significantly increases the barrier to further substitution in the SBU. Ni^{2+} in a strong field environment prefers to be octahedral and therefore will bind two DMF molecules. However there can only be a maximum of two DMF molecules bound at a time (the cluster can only accommodate one O_h ion), meaning that further substitution of Ni^{2+} will be disfavored.[89] Therefore, when Co^{2+} is substituted, the rate of subsequent metal exchange is retarded; for Ni^{2+}, which has a slower aqua exchange rate, the opportunity for further exchange is completely eliminated.

Powers *et al.* demonstrated that careful control of the solvation environment enabled control of exchange kinetics during the synthesis of Pd_2 carboxylate-based materials.[90] In a variety of organic solvents, Pd carboxylates assemble in carboxylate-bridged trinuclear arrays. Exchange of Pd^{2+} into a Zn_3btei template lattice, which features M_2 tetracarboxylate nodes, provided access to Pd_3btei. Significant exchange (79% Pd incorporation into the Zn sites of Zn_3btei) was achieved over the course of 112 days. The extent of substitution as a function of time displayed sigmoidal

kinetics, with exchange displaying a significant induction period (Figure I-14a). Loss of coordinated DMF was observed during this induction period, with the rate of exchange being significantly accelerated following exchange of DMF for $CHCl_3$ (Figure I-14b).[91] The rate of Pd-for-Zn exchange is significantly retarded by coordinated DMF at Zn. By substituting the tightly bound apical solvent molecule for the weakly coordinating $CHCl_3$, the rate of Zn exchange and extent of cation exchange was increased, thus enabling facile ion exchange.

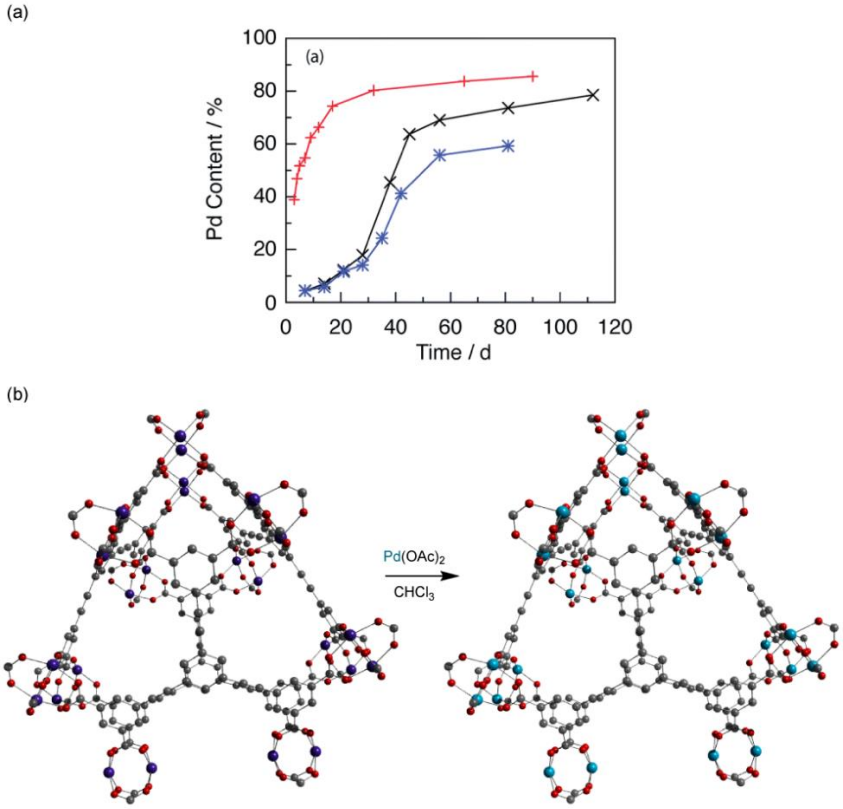

Figure I-14. Pd exchange into Zn_3btei. (a) Incorporation of Pd into Zn_3btei follows sigmoidal behavior. Solvent exchange eliminates the observed induction period(b) The rate of Pd exchange for Zn in Zn_3btei is sensitive to the solvation environment of the parent lattice ions. Figure 14b reprinted with permission from reference 123. Copyright John Wiley and Sons.

I.3.3. Controlling Exchange Chemistry via Redox Processes.

Reductive labilization, in which redox chemistry of lattice ions is utilized to promote exchange, has been developed to circumvent the challenge of incorporating kinetically inert ions within crystalline materials. This strategy is predicated on utilizing redox chemistry to transiently generate metal ions that participate in facile exchange chemistry. Zhou *et al.* reported reductive labilization of framework Fe^{3+} to enable synthesis of crystalline PCN-333-Cr^{3+}.[92] Attempts to generate PCN-333-Cr^{3+} via direct solvothermal synthesis all yielded amorphous powder. Based on analysis of water exchange rates, Cr^{3+} is classified as kinetically inert; any attempt to introduce (or displace) Cr^{3+} must deal with the very slow ligand exchange rate.[93] To achieve the desired exchange chemistry, Cr^{2+} was employed: reduction of Fe^{3+} to Fe^{2+} by Cr^{2+} occurs under N_2 in DMF and enables dissociation of Fe^{2+} to occur, exchanging with additional Cr^{2+}. The framework Cr^{2+} was then oxidized by exposure to air to yield Cr^{3+} (Figure I-15). Complete replacement of Fe^{3+} with Cr^{3+} was evidenced by both ICP-MS and EDS measurements.

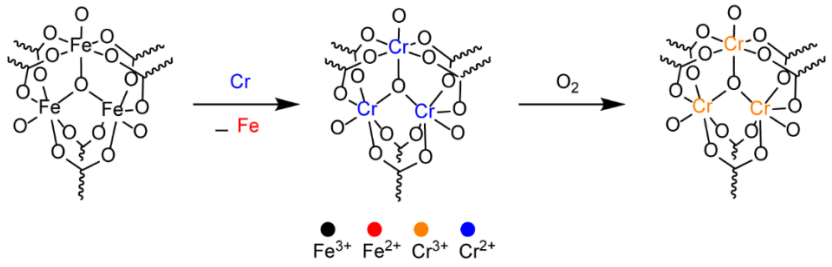

Figure I-15. Reductive labilization of Fe^{3+} to Fe^{2+} allows for facile and rapid ion metathesis with Cr^{2+}. Reprinted with permission from reference 123. Copyright John Wiley and Sons.

I.4. Synthesis of Multimetallic SBUs with Atomic Precision

Homogeneously distributed bi- or multimetallic materials in which metals occupy symmetry equivalent positions are desirable for the ability to tune chemical and physicochemical properties for applications in gas separation, heterogeneous catalysis, and conductivity,[94-98] but

can be challenging to prepare by self-assembly due to differences in M–L bond exchange rates.[99] The distribution of metal ions in a simple bimetallic system is bounded by completely homogeneous distribution and total ion segregation. A homogeneous distribution would be expected for ions with well-matched exchange rates, as the probability of incorporation of each ion to a growing crystallite is the same (Figure I-16a). The latter would be expected to occur when exchange rates are dissimilar, with first nucleation and growth of crystallites comprised mostly or entirely of the faster exchanging metal and then subsequent growth of the slower exchanging metal (Figure I-16b).[100] In the previous section, we examined a number of examples in which differential exchange rates enabled access to multimetallic materials, but cation exchange methods do not provide a general solution to atomically precise distribution of metal ions. To overcome the intrinsic biases arising from metal ion exchange rates, strategies based on polymerization of pre-formed clusters or polyfunctional ligands can be used to enforce ion segregation. These strategies can also be used to install metal clusters which do not form under direct synthesis conditions; either because of mismatched exchange rates or unfavorable reaction conditions.

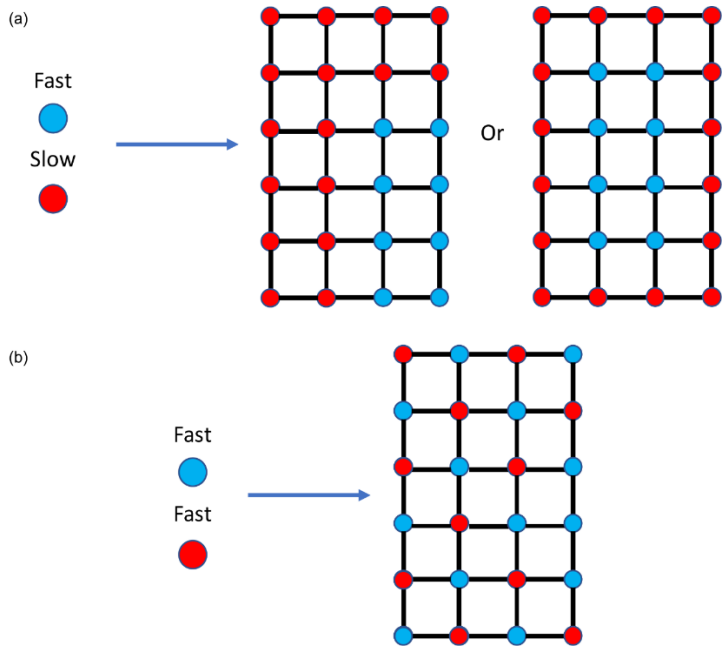

Figure I-16. Impact of ion exchange rates on ion distribution in multimetallic MOFs. Reprinted with permission from reference 123. Copyright John Wiley and Sons.

A number of experimental results have been reported that support the critical role of M–L exchange rates on the distribution of metal ions in multimetallic materials prepared by solvothermal synthesis. Deng *et al.* highlighted the challenge of controlling the composition and distribution of metal clusters during assembly of materials during an investigation of the synthesis of MOFs based on metalloporphyrin linkers connected by heterobimetallic M_3O SBUs.[101] The mixed metal MOFs were synthesized by combination of Fe^{3+}, Mn^{2+}, and Ni^{2+} metal salts with metalloporphyrins in DMF at 150 °C. X-ray photoelectron spectroscopy (XPS) provided a probe to evaluate the ion distribution; the binding energy of component ions is shifted in heterometallic clusters when compared to their homometallic analogs. They observed two different ion distribution paradigms: the first being homogeneously distributed mixed-metal clusters of the composition $M'_xM_{3-x}O$, and the second being isolated domains consisting of homometallic clusters of the composition M_3O. In the synthesis of mixed Fe/Ni MOFs, the exchange rates of Fe^{3+} and

Ni^{2+} are well matched and give mixed-metal nodes of the formula $Fe_xNi_{3-x}O$. When Fe^{3+} and Mn^{2+}, ions with disparate exchange rates, were combined, domain segregation resulted with clearly defined areas consisting of only Mn_3O or only Fe_3O clusters (Figure I-17).

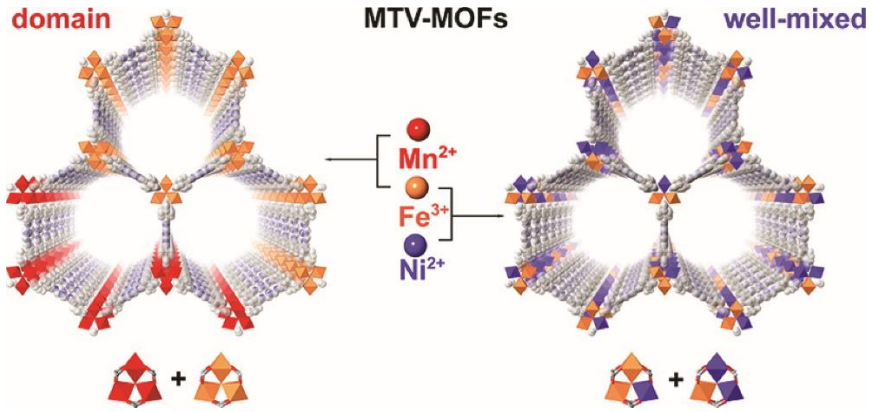

Figure I-17. Segregation of metal ions in a material will occur if the disparity in exchange rates is large. Homogeneous distribution of metals will occur if their exchange rates are well-matched.

Yaghi *et al.* further expounded on the issue of metal ion distribution in samples of MOF-74 that contained two different metal species: Co^{2+} with Pb^{2+}, Cd^{2+}, or Mn^{2+}.[102] Based on relative exchange rates, the material comprised of Co and Mn should be the most homogeneously distributed (most similar ligand exchange rates) and the material comprised of Co and Pb should be the most segregated (most disparate ligand exchange rates). Yaghi *et al.* used APT, Atom Probe Tomography, to characterize the local heterogeneity of their mixed-metal MOF-74. By utilizing APT, 3D models of the SBU were created that allow for exact spatial mapping of the metal contents of their mixed metal MOFs. It was observed that Co-Mn MOF-74 showed a local homogeneous metal distribution pattern which consisted of little ion segregation and that Co-Pb MOF-74 exhibited long chains of the same atom, indicating a high degree of segregation. The described APT experiments were critical because bulk techniques like XRD or EDS do not provide

information about the local heterogeneity of a material. While UV-Vis, XAS, and magnetic techniques are widely utilized in the PSM literature as reporters for successful ion incorporation and local structure, these techniques have been less widely adopted for the polymerization of preformed metal clusters.[77, 79, 103-105]

I.4.1. Strategies to circumvent exchange rate disparities.

Zou *et al.* examined the rates on the growth of, and ion distribution within, isostructural MOF materials, ZIF-8 and ZIF-67.[106] These MOFs are constructed by polymerization of 2-methylimidiazole (**I-27**) with either Zn^{2+} or Co^{2+}, respectively (Figure I-18a). Using sample turbidity (measured by absorbance at 360 nm) as a proxy for the extent of MOF formation, growth rates were measured for homometallic ZIF-8 and ZIF-67 (Figure I-18b). The obtained data indicate that ZIF-67 forms rapidly after a short induction period and then ceases additional growth. In contrast, ZIF-8 growth displays two distinct kinetic regimes, which correspond first to the nucleation of small particles (10-20 nm radius) followed by growth of these crystallites into larger nanocrystals.

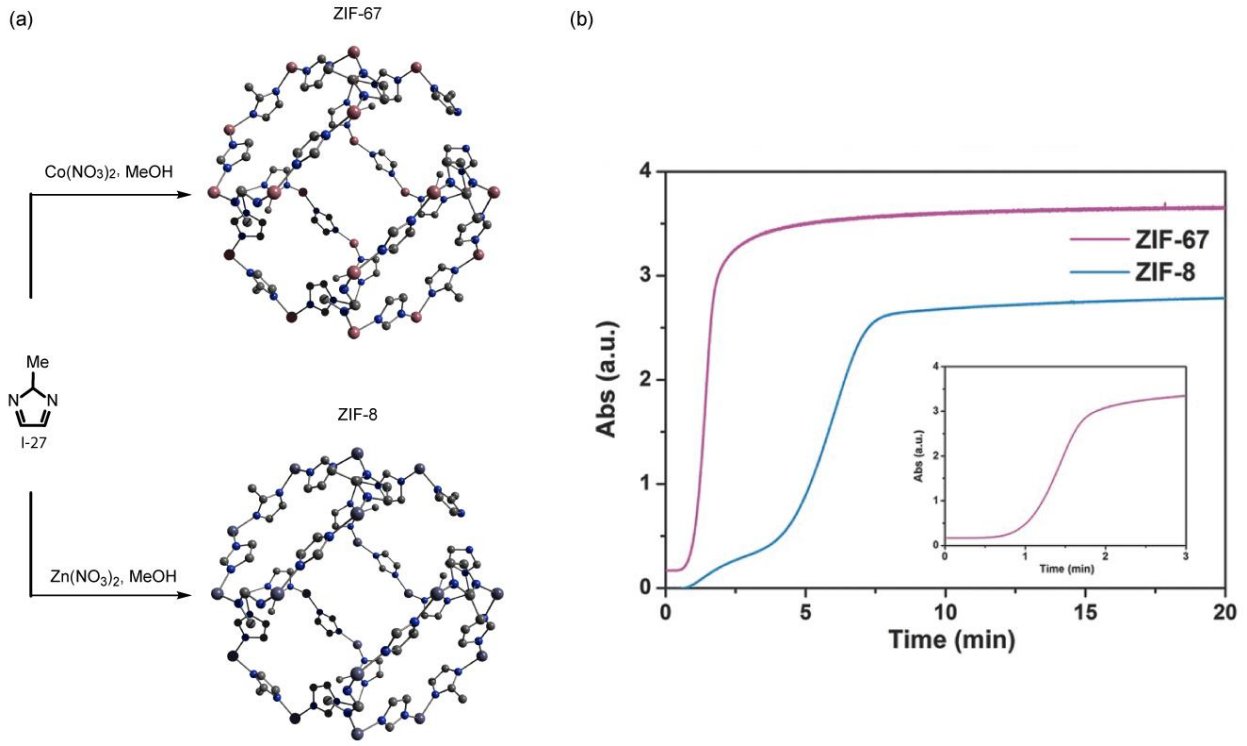

Figure I-18. Core-shell structures resulting from disparity in metal exchange rate. (a) Synthesis of ZIF-8 and ZIF-67 is accomplished by combination of either $Zn(NO_3)_2$ or $Co(NO_3)_2$ with I-27 in methanol. (b) Plot of sample absorbance at 360 nm (measure of sample opacity) *vs.* time for the polymerization of 2-methylimidazole with Zn^{2+} (blue) and Co^{2+} (pink) to afford ZIF-67 (pink) and ZIF-8 (blue), respectively. Figure 18a reprinted with permission from reference 123. Copyright John Wiley and Sons.

A series of experiments were undertaken to examine the impact of varying the proportions of the two metal ions on the distribution of ions within the resulting bimetallic materials. A 4:1 mixture of Zn and Co resulted in core-shell particles, with a ZIF-67 core and a ZIF-8 shell, which is consistent with rapid nucleation of Co^{2+} material and slower growth of the Zn^{2+} material proceeding in a kinetic regime. Increasing the Co^{2+} proportion to 1:1 or greater resulted in the formation of a homogeneous solid-state solution, which was attributed to the rapid formation of small ZIF-8 crystallites being absorbed within rapidly growing ZIF-67. Modifying the timing of metal ion introduction allowed for more precise control over the distribution of ions. First, cobalt and ligand were mixed and allowed to react, then zinc was added. This resulted in a core of ZIF-

67, with the shell being a homogeneous mixture of ZIF-67 and ZIF-8. The time of second component addition dictated the size of the core. The reverse addition, Co to Zn, resulted in amorphous products which is most likely the result of relatively slower formation of ZIF-8 compared to ZIF-67.

I.4.2. Metallopolymerization of heterometallic clusters.

In chapter **I.2.** we encountered metallopolymerization as a strategy to control the primary coordination sphere of lattice ions and to incorporate kinetically inert ions into crystalline materials. Similar strategies have been applied to the synthesis of materials based on heterometallic SBUs that can be difficult to access via self-assembly due to ion scrambling. Synthesis of kinetically stable heterometallic clusters, followed by polymerization enables programmed assembly of materials with defined node composition. For example, Zhou *et al.* prepared a series of Fe_2MO (**I-28**, M= $Fe^{2+,3+}$, Co^{2+}, Ni^{2+}, Mn^{2+}, Zn^{2+}) clusters supported by acetate ligands.[107] Subsequent treatment of these clusters with polytopic carboxylic acids led to polymerization (Figure I-19). Judicious linker selection enabled control over SBU connectivity and thus material topology. Attempts to prepare this family of MOFs by one-pot solvothermal methods resulted polycrystalline or amorphous phases. By pre-forming the metal clusters, precise control over the composition and distribution the clusters were achieved. This example of metallopolymerization differs from those previously described in that the primary M–L bonds are exchanged and the structural integrity of the SBU is maintained by the templating oxide ligand. Lan *et al.* applied this strategy towards the formation of NNU-31-M (M= Zn^{2+}, Co^{2+}, or Ni^{2+}), a set of materials comprised of **I-28** and 4,4′,4″-tricarboxytriphenylamine as the ligand.[108] The fidelity of the clusters

post polymerization was ascertained by UV-Vis and Ultraviolet Photoelectron Spectroscopy (UPS), which validated that no ion scrambling occurred under the synthetic conditions.

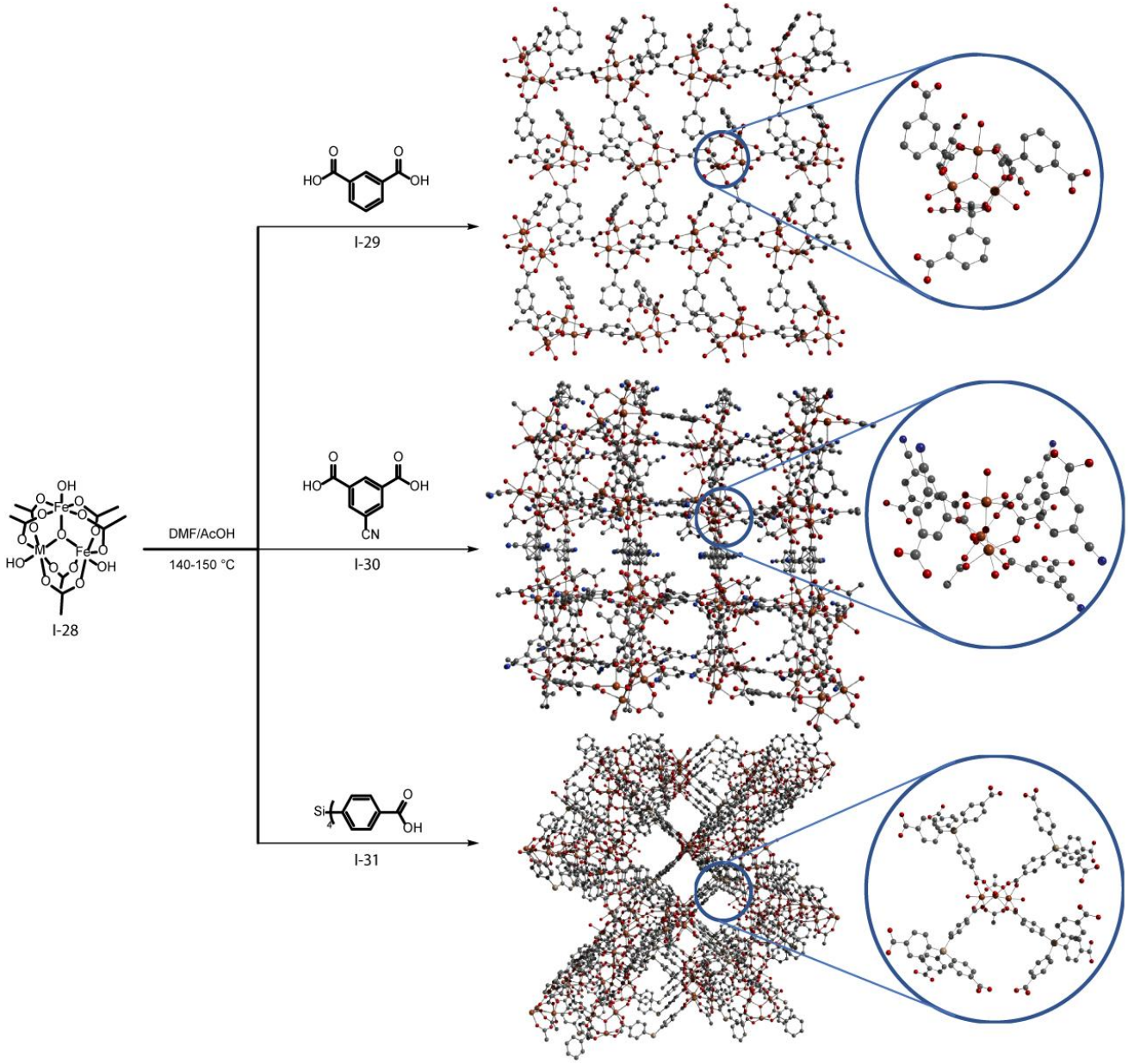

Figure I-19. Preformed Fe_2M clusters adopt a variety of connectivities depending on the steric bulk of the ligand. Use of a preformed metal cluster allows access to node connectivity that is not possible via self-assembly. Reprinted with permission from reference 123. Copyright John Wiley and Sons.

The metallopolymerization of pre-formed heterometallic clusters has been extended to incorporate clusters that are not readily available by self assembly. Zhou *et al.* prepared PCN-415 and PCN-416, which are materials comprised on $Ti_8Zr_2O_{12}$ nodes and either terephthalate (**I-32**), or 2,6-napthalenedicarboxylate linkers (**I-33**), respectively, via polymerization of pre-formed clusters (Figure I-20).[109] Self-assembly of the mixed metal cluster under PCN-415 synthesis conditions yielded poorly crystalline material with UiO-66 (a $Zr_6O_4OH_4$-based material) as an impurity, indicating that formation of Zr_6 clusters competed with the formation of Ti_8Zr_2 clusters. Thus, use of the pre-formed cluster enables access to crystalline, phase pure, bimetallic materials which are otherwise inaccessible. In general, synthesis conditions are not conducive to the self-assembly of Ti clusters (*i.e.*, in acetonitrile or methanol).[110-112]

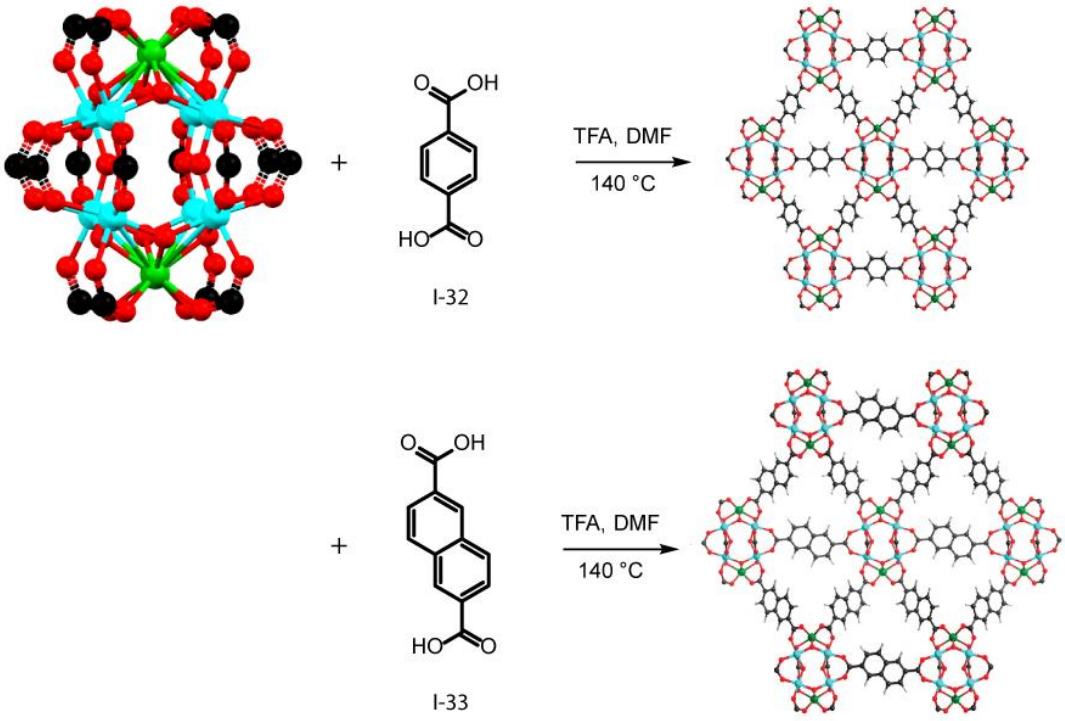

Figure I-20. Synthesis of PCN-415 and PCN-416 utilize the preformed cluster, $Ti_8Zr_2O_{12}(CH_3COO)_{16}$, with I-33 or I-34 in TFA and DMF at 140 °C to make PCN-415 and PCN-416 respectively.

Due to slow ligand-exchange kinetics, there are only a few MOFs comprised of kinetically inert ions such as Ru^{3+} or Rh^{2+}.[113, 114] Fischer *et al.* reported M_3btc_2 analogs with Ru_2 and Rh_2 paddlewheels as the nodes, prepared via exchange of acetate ligands with H_3btc (BTC = benzene tricarboxylate) at pre-formed dimers **I-18** and **I-34** (Figure I-21a).[115] Due to the similarity of ligand exchange kinetics at these two metal ions, using mixed-metal feeds enabled access to solid-solutions of mixed Ru_2-/Rh_2-based $M_3(btc)_2$ in which the ultimate metal composition was roughly equal to the feed composition. The homogeneity of metal paddlewheel distribution was confirmed by depth profiling experiments where layers of the material were ablated and the metal contents of the exposed surface were probed by XPS (Figure I-21b). The M_2 structures in these experiments are likely maintained under solvothermal conditions due to the presence of M–M bonding, which prevents the ion scrambling that can plague solvothermal syntheses of mixed-metal materials.

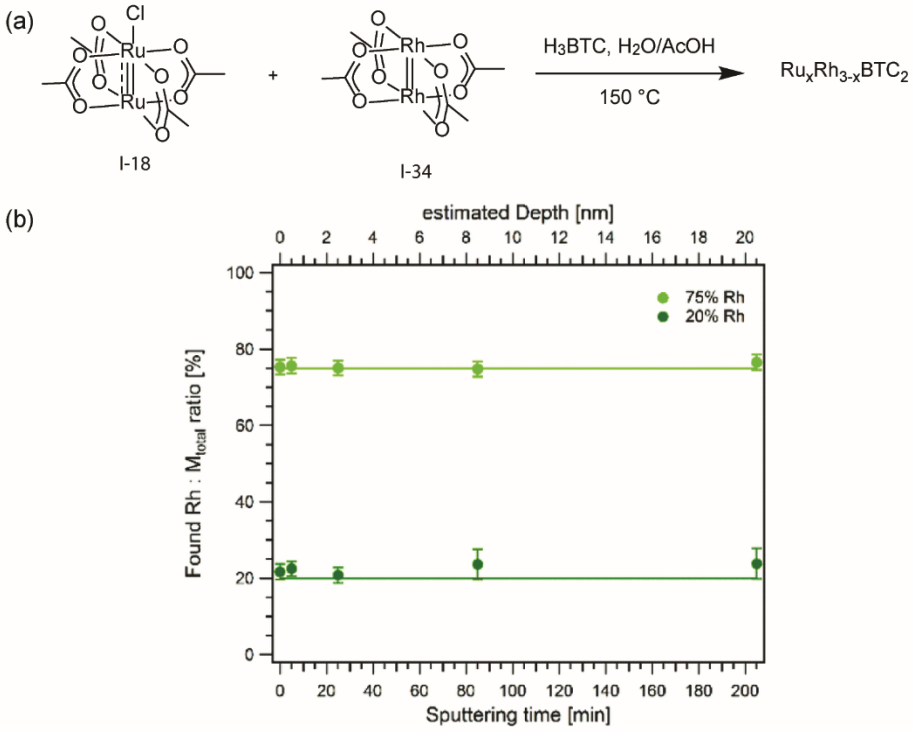

Figure I-21. Mixed-metal HKUST-1 phases from solvothermal synthesis. (a) Synthesis of mixed metal M_3btc_2 takes place between $Ru_2(OAc)_4Cl$ (I-18), $Rh_2(OAc)_2$ (I-34), and H_3BTC

in a water/acetic acid mixture at 150 °C. (b) Metal ratios in mixed metal M_3btc_2 phases as a function of depth. Reprinted with permission from reference 123. Copyright John Wiley and Sons.

I.4.3. Templating ion distribution in heterometallic MOFs.

In chapter **I.2.**, we introduced HSAB theory as a strategy to access materials with free phosphines. Using similar HSAB theory concepts, Li *et al.* described a strategy to control metal ion distribution in the synthesis of BUT-52. BUT-52 consists of $In(COO)_4$ sites and Cu_6S_6 clusters and is synthesized by combination of Cu^+, a soft Lewis acid, and In^{3+}, a hard Lewis acid, with a difunctional ligand, 6,6′-dithiodinicotinic acid (Figure I-22). This results in a material in which Cu^+ preferentially complexes the soft Lewis basic thiol group while In^{3+} preferentially complexes the hard Lewis basic carboxylate group.[116] BUT-52 can only be synthesized through the slow introduction of 2-mercaptonicotinic acid, which is generated by slow decomposition of compound **I-35**; addition of 2-mercaptonicotinic acid to In^{3+} and Cu^+ in DMF yields an amorphous phase. No data is available on the ligand exchange rate of Cu^+, but it can be assumed to be similar to Zn^{2+} as both are d^{10} meaning that the exchange rate for In^{3+} and Cu^+ should be similar. Despite the assumed similarity in exchange rates, BUT-52 still forms with distinct alternating In and Cu nodes, which are bound to carboxylate and sulfur respectively. HSAB enables this template effect through thermodynamic preferences, which overcome the exchange rate similarity.

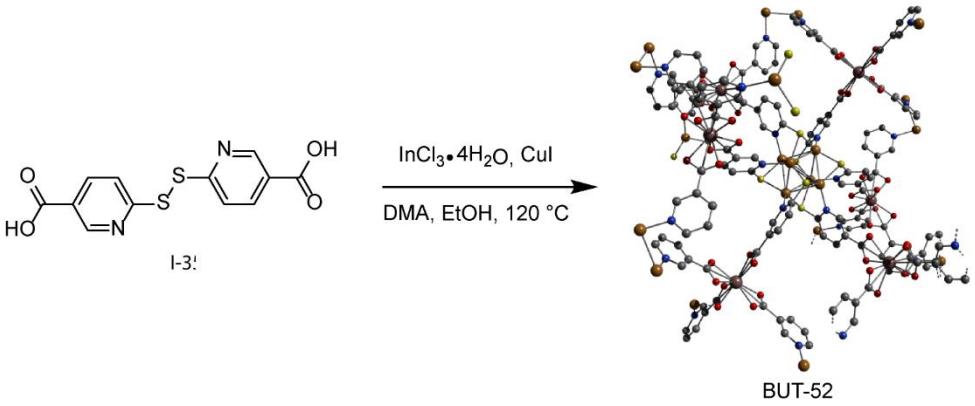

Figure I-22. BUT-52 is synthesized via the slow decomposition of I-35. Reprinted with permission from reference 123. Copyright John Wiley and Sons.

Powers *et al.* reported a mechanochemical synthesis of mixed Ru/Cu HKUST-1 material in which the distribution of Ru and Cu were precisely controlled by the polymerization conditions.[117] Using a strategy similar to that described in Section 2 for the metallopolymerization of a Ru_2 units (Figure I-10), polymerization of ruthenium paddlewheel complexes featuring peripheral 3,5-dicarboxylate substituents provided a step-wise strategy to assemble M_3btc_2 materials (Figure I-23). Mechanochemical polymerization of monomer **I-38** with $Cu(OAc)_2$ afforded mixed-metal M_3btc_2 phases in which the relative positions of the two ions were precisely controlled.[118] Bulk measurements using wavelength dispersive spectroscopy (WDS) and PXRD confirmed the homogeneous distribution of Ru and Cu paddlewheels. Additionally, extended X-ray absorption fine structure (EXAFS) and UV-Vis measurements confirmed the lack of ion scrambling. This result is contrasted by a report from Kleist and coworkers in which they attempted to make a mixed metal HKUST-1 with Cu^{2+} and Ru^{2+} by direct synthesis using metal salts.[119] Although the starting metal ratio was 4:1 Cu:Ru, the final metal ratio of the obtained material was 11:1 Cu:Ru. Under those conditions, the insignificant incorporation of the Ru ions is most likely due to the large disparity in ion exchange rates between the two metal ions.

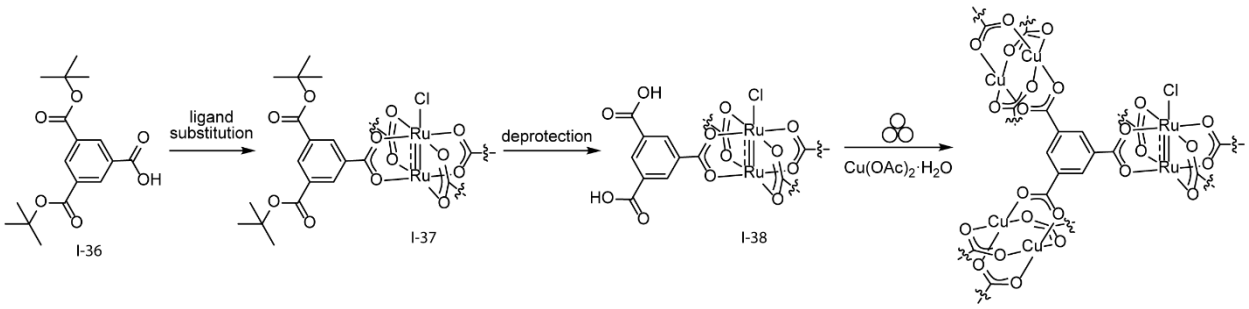

Figure I-23. Mechanochemical synthesis of Ru/Cu HKUST-1 analogs by polymerization of Ru_2 SBUs featuring pendent carboxylate substituents. Reprinted with permission from reference 123. Copyright John Wiley and Sons.

I.5. Conclusion

Inherent differences in ligand exchange rate determine the ultimate structure and homogeneity of materials, and thus limit the potential of direct synthesis methods to synthesize complex materials. This has motivated much research into strategies that allow for installation of slower exchanging ions, strategies such as pre-polymerization synthesis of designer organometallic linking struts, post-synthetic metathesis methods, and polymerization of preformed clusters to control end distribution of ions.

The utility of these synthetic strategies becomes apparent in the ability to tune physical properties of materials and in the wide variety of catalytic reactions that are enabled through site-selective insertion of active metal ions. Selective gas separation has been a longstanding challenge in the MOF community, and the strategies articulated in this review provide an opportunity to introduce chemical complexity that enables cooperative binding opportunities, such as those espoused in the cation metathesis literature. Additionally, the ability to incorporate additional metal ions provides the opportunity for dual catalysis or enables catalysis which is prohibitive to accomplish in the solution phase, such as polymerization of alkene feedstocks.

One of the major challenges of attempting to make multimetallic materials in which constituent ions have disparate exchange rates is the verification of material homogeneity. Bulk measurements like XRD and EDS are necessary in determining bulk structure and distribution, but determining local homogeneity requires more sophisticated techniques like APT. The use of pre-formed metal clusters is an attractive alternative to one-pot methods because there is no ambiguity about the constituents of the cluster, however ion scrambling is still a concern. Techniques like EXAFS, UV-Vis, and photoelectron spectroscopy can be utilized to ascertain the fidelity of mixed-metal clusters post-polymerization.

In response to the need to incorporate diverse organometallic catalysts in MOFs, other techniques have been developed. Grafting techniques, like those employed in siliceous and aluminous materials, have been adapted to MOF materials to incorporate molecules which do not have functional groups that are necessary for incorporation into MOFs using the metalloligand method, such as tungsten alkylidenes.[120-122] Along with the techniques described in this introduction,[123] the incorporation of catalytically relevant ions and motifs through kinetic control has enabled advanced materials synthesis for heterogeneous catalysis. This thesis will discuss additional elaborations of strategies discussed previously, and a potential new method of heterogenization useful for *in operando* optical spectroscopy of immobilized catalysts.

CHAPTER II

SYNTHESIS OF NEW RUTHENIUM PADDLEWHEEL BASED MATERIALS

II.1 Introduction

Sustainable and efficient methods for nitrogen incorporation into organic substrates, whether they be simple or complex, is an outstanding challenge in transition metal mediated C–H amination. Buchwald-Hartwig amination accomplishes this task but requires pre-functionalized substrates, which can add significant synthetic effort and derivatization.[124] Trying to directly functionalize unactivated C–H bonds is challenging due to challenges associated with selectivity between multiple chemically similar C–H bonds that are present in many molecules and the necessity of generating highly energetic reagents.[125] Highly reactive intermediates, such as nitrides, nitrenes, carbenes, and oxos are difficult to utilize and study. The high reactivity predisposes them to a variety of decomposition pathways. For instance, nitrides and carbenes may engage in dimerization, solvent oxidation, or ligand functionalization (Figure II-1).[126-128]

One of the goals of this thesis is to study platforms which can accomplish selective substrate functionalization without catalyst decomposition. To this end, we have pursued site immobilization of Ru_2 paddlewheel complexes which are competent in nitrogen-atom transfer (NAT) reactions. Paddlewheel complexes are of particular interest for two reasons: 1) The facility of ligand exchange amongst reported complexes can provide ready access to a family of molecules with slight perturbations to electronic structure,[129] and 2) The ability of the distal metal atom to act as an electron reservoir, which aids in the cycling of oxidation states necessary for facile transfer nitrogen atom (or group) transfer.[130] We endeavored to develop NAT from Ru_2,

particularly intermolecular NAT, as there are few examples in the literature of this reactivity mode.[131, 132] NAT must be affected from a Ru_2N intermediate, which we generate from the corresponding azide precursor via thermolysis or photolysis. The generated Ru_2[II,III] nitride is a reactive molecule and reported to undergo bimolecular decomposition to produce N_2 and a Ru_2[II,II] byproduct. We hypothesized that site immobilization in a MOF would allow us to prevent this decomposition mode and instead engage with substrate to afford aminated products.

Molecular immobilization can be accomplished through several methods such as grafting onto solid supports or polymerization reactions, which often result in amorphous materials.[29, 123, 133] While incorporation in polymeric materials can extend the lifetime and activity of immobilized catalysts, it presents additional challenges to the study of catalysts. Unambiguous characterization of the active site is challenging for amorphous materials because of the variety of chemical environments present. The suite of spectroscopic tools for characterization is limited to solid state NMR, X-ray absorption/scattering techniques, and diffuse reflectance UV-Vis.[134, 135]

Several of the characterization issues can be remedied by incorporation within a crystalline framework, such as a MOF.[48, 136, 137] Crystalline frameworks are generated by reversible bond-forming reactions which allow for sequential bond-forming and bond-breaking processes to occur. This process allows for defect removal and eventual crystallization in the thermodynamically least energetic phase, which is ostensibly identical across the material.[138-140]

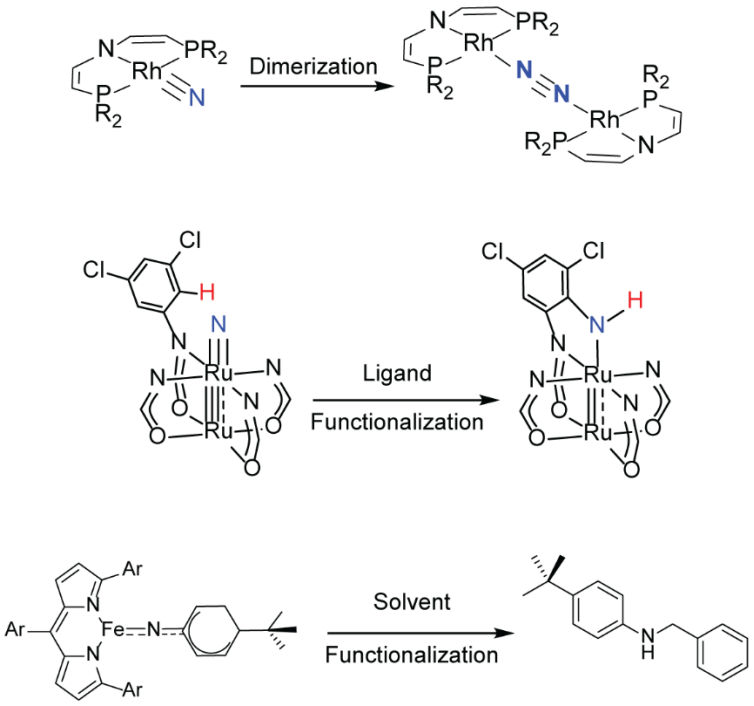

Figure II-1. Common decomposition pathways of energetic intermediates include dimerization, deleterious ligand functionalization, or solvent functionalization.

One method to utilize MOFs to generate crystalline porous materials as catalyst scaffolds is via post-synthetic modification (Figure II-2a). Post-synthetic modification strategies rely on incorporating coordination sites within a framework material to tether molecules. This can be accomplished using condensation reactions, acyl transfer, or metalation of open tethers.[141] This strategy is particularly attractive for functional groups which may not survive the synthesis conditions required to make MOFs.[142] Some potential drawbacks of utilizing post-synthetic incorporation techniques are as follows: successful incorporation of a tether, fidelity of the tether during synthesis, and access to internal sites.[143]

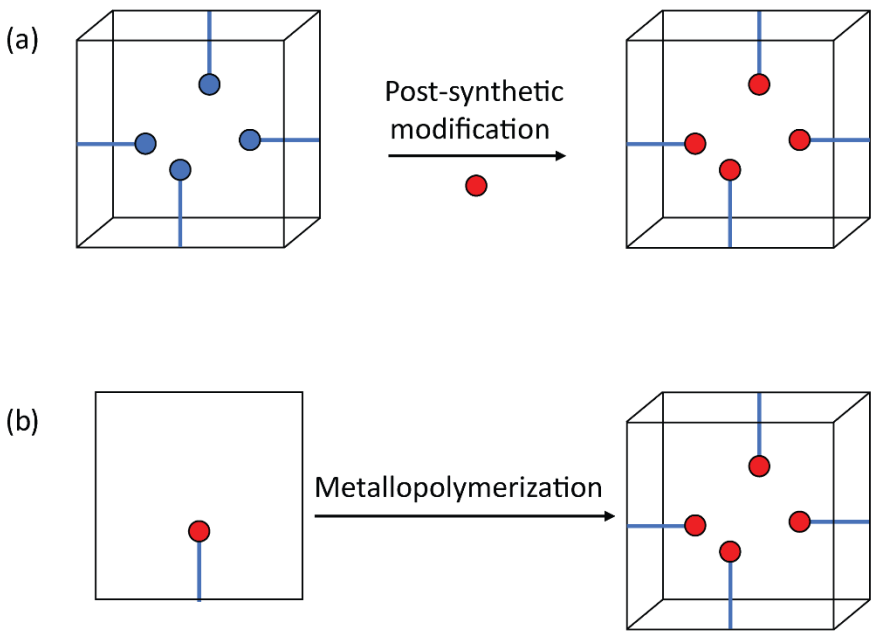

Figure II-2. (a) Post-synthetic modification strategies are predicated on using frameworks with already included functional handles to enable changes. (b) Metallopolymerization strategies are predicated on the polymerization of the desired ligand.

An alternate strategy is to create MOFs with metalloligands, which are linking elements comprised of a coordination complex (Figure II-2b).[26, 144] Controlled metallopolymerization allows incorporation of the desired moiety under a common set of synthetic conditions. Additionally. this strategy allows precise synthetic control over the primary coordination sphere of the metalloligand and a high degree of modularity among linking struts. Some examples of metalloligand moieties successfully polymerized include metalloporphyrins, bulky pincers, and salen complexes.[27, 30, 145, 146]

We viewed metallopolymerization as a strategy that would allow for atomistic control over the electronic structure of supported metal ions within a conserved framework topology, thus making it an ideal synthetic strategy for incorporation of Ru_2 complexes in a material. Site immobilization of Ru_2 moieties has been achieved before by solvothermal methods to make 3D

structures, however the majority of these strategies result in materials catenated through the apical coordination sites thereby excluding catalysis as no open metal sites remain.[147-153] In addition, direct solvothermal strategies do not allow for any synthetic tuning of the primary coordination sphere or the topology, as they rely on *in situ* self-assembly.

Our group has previously developed a family of metallomonomers based on Ru_2 units with peripheral functional groups designed to enable various polymerization modes. Polymerization of iodinated metallomonomers via irreversible Sonogashira cross-coupling yielded porous non-crystalline materials.[70] This method allowed explicit control over the primary coordination sphere of the Ru_2 unit, and thus tuning the product selectivity for an intramolecular C–H amination reaction, but characterization of the active site is rendered virtually impossible due to the amorphous nature of the resultant polymer. Subsequently, we reported metallopolymerization via mechanochemical combination of carboxylated metallomonomers with $Cu_2(OAc)_4$ which provided access to a crystalline mixed Ru_2/Cu_2 HKUST-1 phase (Figure II-3).[117]

In this chapter, further advancements to our metallopolymerization strategy involving synthons of Ru_2 units with open carboxylic acids are discussed. Access to new Ru_2 monomers and attempts to synthesize a variety of MOFs using carboxylated Ru_2 metallomonomers are described.

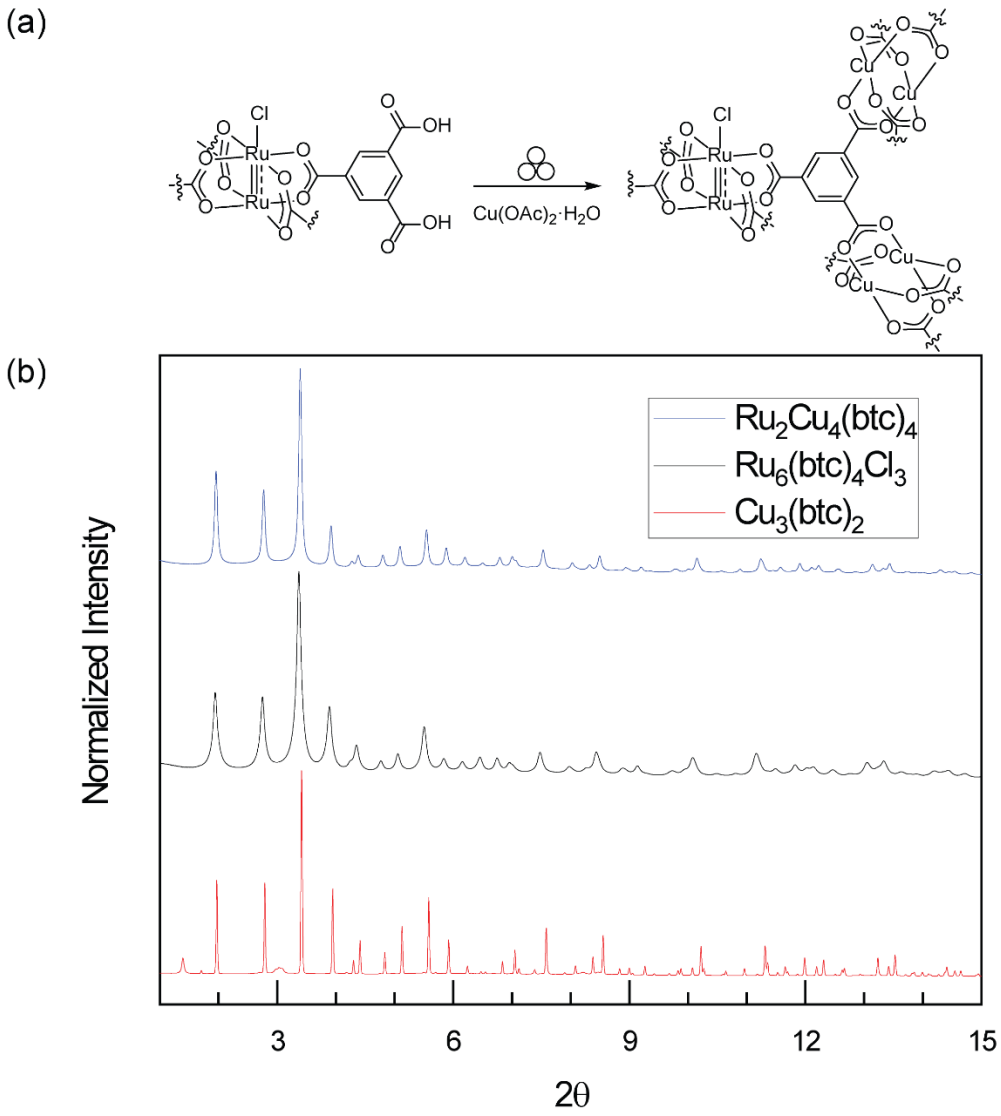

Figure II-3. (a) Polymerization of a Ru_2 molecule with Cu_2OAc_4 yields a mixed metal HKUST-1 structure. (b) PXRD patterns of the mixed metal HKUST-1, Ru-HKUST-1, and Cu-HKUST-1

II.2 Results and Discussion

In this section, we describe the synthesis and characterization of ruthenium complexes **II-3** and **II-6**. The synthesis of these complexes and related protection/deprotection strategies are

discussed. Attempts to utilize these complexes to synthesize MOFs are discussed and potential opportunities in alternate modes of materials assembly are suggested.

II.2.1 Synthesis and Characterization

Synthesis of carboxylated metallomonomers is conceptually challenging because conditions must be developed that enable access to the molecular complexes and not subsequent polymerization. For example, combination of 1,4-BDC with Ru_2OAc_4Cl only yields amorphous polymeric Ru_2 material[154, 155] and none of the desired metallomonomer **II-3** (for a review on metal-organic polyhedra including those synthesized using 1,3-BDC, see the following[156]).To accomplish this goes, we pursued the synthesis of compounds **II-3** and **II-6** via the synthetic strategy illustrated in Figure II-4.

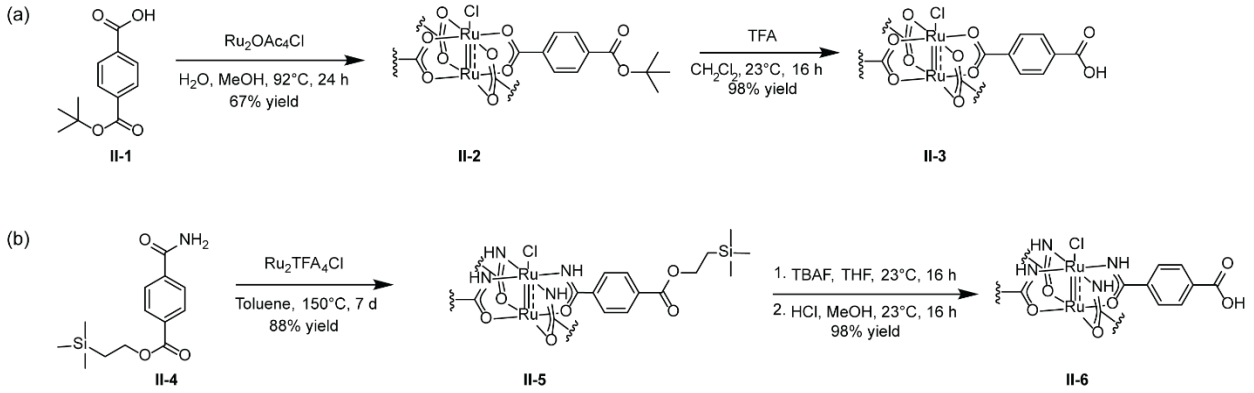

Figure II-4. (a) Synthesis procedure for II-3. Ligand exchange of $Ru_2(OAc)_4Cl$ with II-1 proceeds in 67% yield to give II-2, which is deprotected with TFA to give II-3. (b) Synthesis procedure for II-6, which is similar to the strategy in II-4a.

Synthesis of **II-2** was accomplished by combination of **II-1** and Ru_2OAc_4Cl in a 1:1 water/MeOH mixture at 92 °C for over a period of 24 h. Above this temperature, the thermal decomposition of **II-1** into 1,4-BDC and isobutylene becomes rapid; additionally longer synthesis times lead to slight deprotection of **II-2**. To assay reaction progress, NMR spectroscopy was used

to identify a peak at δ = –45ppm (s, $CDCl_3$), which corresponds to residual Ru_2-bound acetate ligands. Treatment of isolated complex **II-2** with TFA in CH_2Cl_2 afforded a quantitative yield of **II-3**. We chose to *tert*-butyl esters as protecting groups for **II-1** because of their ease of deprotection with TFA.[157] Other ester deprotection conditions, namely those involving hydroxide bases, are incompatible with the paddlewheels, presumably due to the formation of apical hydroxides which are insoluble.[158, 159]

Synthesis of **II-6** required a different protecting group strategy, as the *tert*-butyl esters were incompatible with the acidic conditions required for synthesis of ligand **II-4**. Additionally, ligand **II-4** is stable at 150 °C for over 7 d, unlike **II-1**, making it suitable for extended ligand exchange reactions.[160] Complex **II-5** was prepared in 88% yield from **II-4** and freshly prepared $Ru_2(TFA)_4Cl$ by refluxing in toluene for 7 d at 150 °C. The reaction vessel was fit with a Soxhlet extractor containing potassium carbonate to scrub produced TFA.[161] Deprotection of **II-5** is accomplished by treatment with TBAF in THF, to afford the tetra-TBA salt of **II-6**. Ultimately, protonation with HCl afforded **II-6** in quantitative yield.

*II.2.2 Synthesis attempts for **II-3***

II.2.2.1 DMOF-1

Attempts to synthesize analogs of DMOF-1 with **II-3** solvothermally resulted in complete exclusion of **II-3**; if a ligand exchange event occurs at Ru, liberated ligand will polymerize with other metal ions. Based on metal ion exchange rates, ligand exchange at other metals is much greater than at Ru, and thereby result in its exclusion whenever there are fast exchanging metal ions present.[22] Thus, solvothermal synthesis of DMOF-1 with **II-3**, Cu_2OAc_4, and DABCO yielded single crystals of all Cu DMOF-1.

Additional attempts to incorporate **II-3** into crystalline materials centered around mechanochemical synthesis strategies; we hypothesized that by dramatically reducing solvent amounts, there would be reduced opportunities for ligand exchange to occur at Ru. Ball-milling of **II-3** with Cu_2OAc_4, DABCO, and ethanol as an additive yielded a PXRD consistent with that observed for DMOF-1 (Figure II-5), a material which could not be accessed solvothermally. The material was porous with a surface area of 300 m^2/g. Neat milling (without additive) also yielded a PXRD consistent with that of DMOF-1, albeit significantly less crystalline. Attempts to substitute the pillaring DABCO with bipyridine or pyrazine yielded poorly crystalline material that could not be indexed. Exposure of Ru-DMOF-1 to aqueous NaN_3 resulted in dissolution of the solid material.

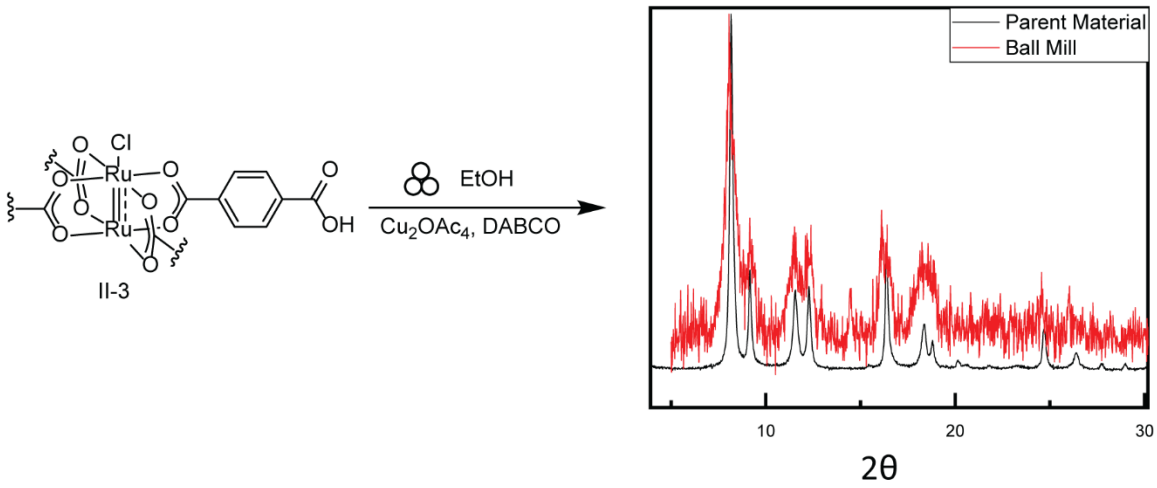

Figure II-5. Ball milling of II-3 with $Cu_2(OAc)_4$ and DABCO with EtOH (η=0.66) as an additive produces the PXRD shown. Overlaying with parent material DMOF-1 indicates several peaks which overlap exactly.

Efforts to improve crystallinity centered around solvent additives. It has been reported that small amounts of solvent additives can increase the yield of solid-state reactions and enable

formation of crystalline phases.[162-164] We screened several commonly reported solvent additives in varying ratios (represented as η, defined as uL of solvent per mg of reactant) (Figure II-6). MeOH proved to be the best solvent additive, with little change observed by slight variations in η. Having a large η value (>1) lead to a decrease in crystallinity. Adding water to the reaction led to slight decreases in crystallinity as compared to just solvent.

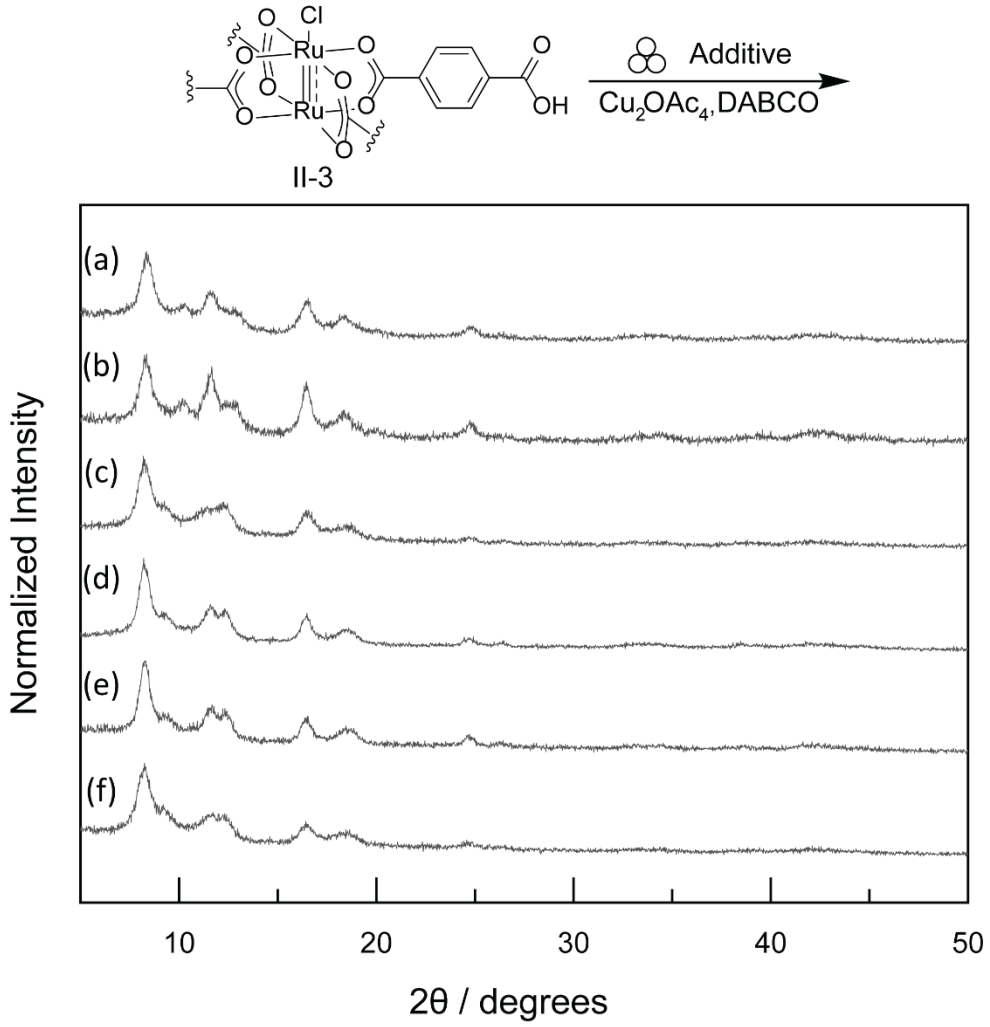

Figure II-6. Ball milling of II-3 with Cu_2OAc_4, DABCO, and various solvent additives: (a) 1:1 DMF/H_2O η=0.66 (b) 1:1 MeOH/H_2O η=0.66 (c) MeOH η=2 (d) MeOH η=0.66 (e) MeOH η=0.33 (f) EtOH η=0.66

Additionally, we screened a variety of alcohol and amide solvents at a fixed ratio of η = 0.68 to explore whether solvent identity was important towards improving crystallinity (Figure II-7). 2-phenylethanol and *N*,*N*-diethylacetamide (DEA) gave the highest crystallinity of all additives, however the attained results still feature large FWHM (full-width at half maximum) and subsequently broad peaks with poor resolution.

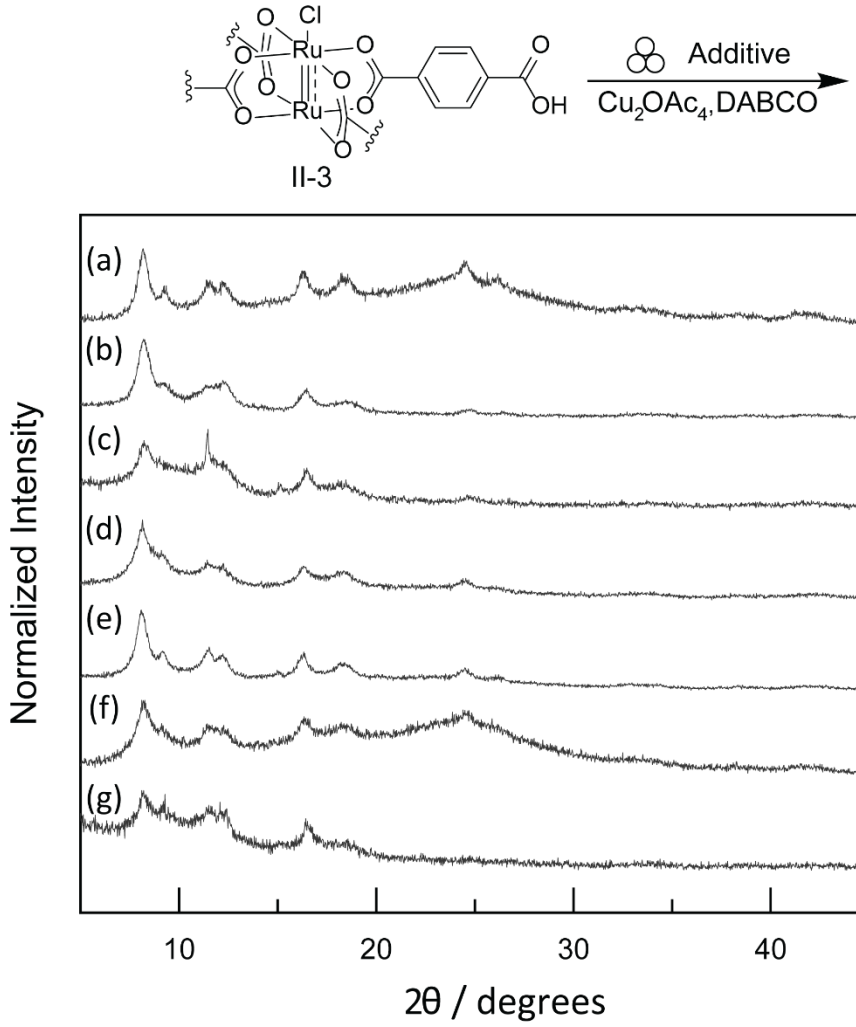

Figure II-7. Ball milling of II-3 with Cu_2OAc_4, DABCO, and various solvent additives at η=0.68: (a) 2-phenylethanol (b) HFIP (c) DMF (d) tBuOH (e) DEA (f) iPrOH (g) DEF.

II.2.2.2 Zr based attempts

During studies of the mechanochemically derived Ru_2/Cu_2-HKUST-1 materials, we noted material dissolution upon exposure to sodium azide, presumably due to the formation of soluble copper polyazide complexes.[165] This chemical incompatibility with NaN_3 prompted us to explore the synthesis of more robust materials, namely Zr-based materials.

Zr-based materials are widely reported in the literature as being robust to a variety of harsh conditions.[166] We hypothesized that access to Zr-based materials would solve issues of chemical stability and, following literature reports of mechanochemical MOF formation using preformed Zr clusters, we attempted to incorporate **II-3** in a Zr MOF (Figure II-8).[167-169] Table **II-1** contains synthesis conditions attempted for synthesizing mixed Zr/Ru materials; variables examined included the identity of the Zr cluster, reaction time, milling frequency, base additive, stoichiometry, and solvent additives. For all of the examined conditions, the resulting materials were amorphous. Ligand exchange did occur under reaction conditions at ruthenium: when **II-7** was used as the cluster, acetic acid was liberated in the reaction mixture. Washing the generated solid with methanol yielded a colored solution. When assayed by NMR, the solution showed peaks at δ = -45 ppm, which corresponds to Ru_2 compounds with varying degrees of acetate substitution, originating from the Zr cluster. Figure II-8 shows a representative PXRD after washing and drying; all reactions feature a large peak centered around 8° 2θ and no other peaks.

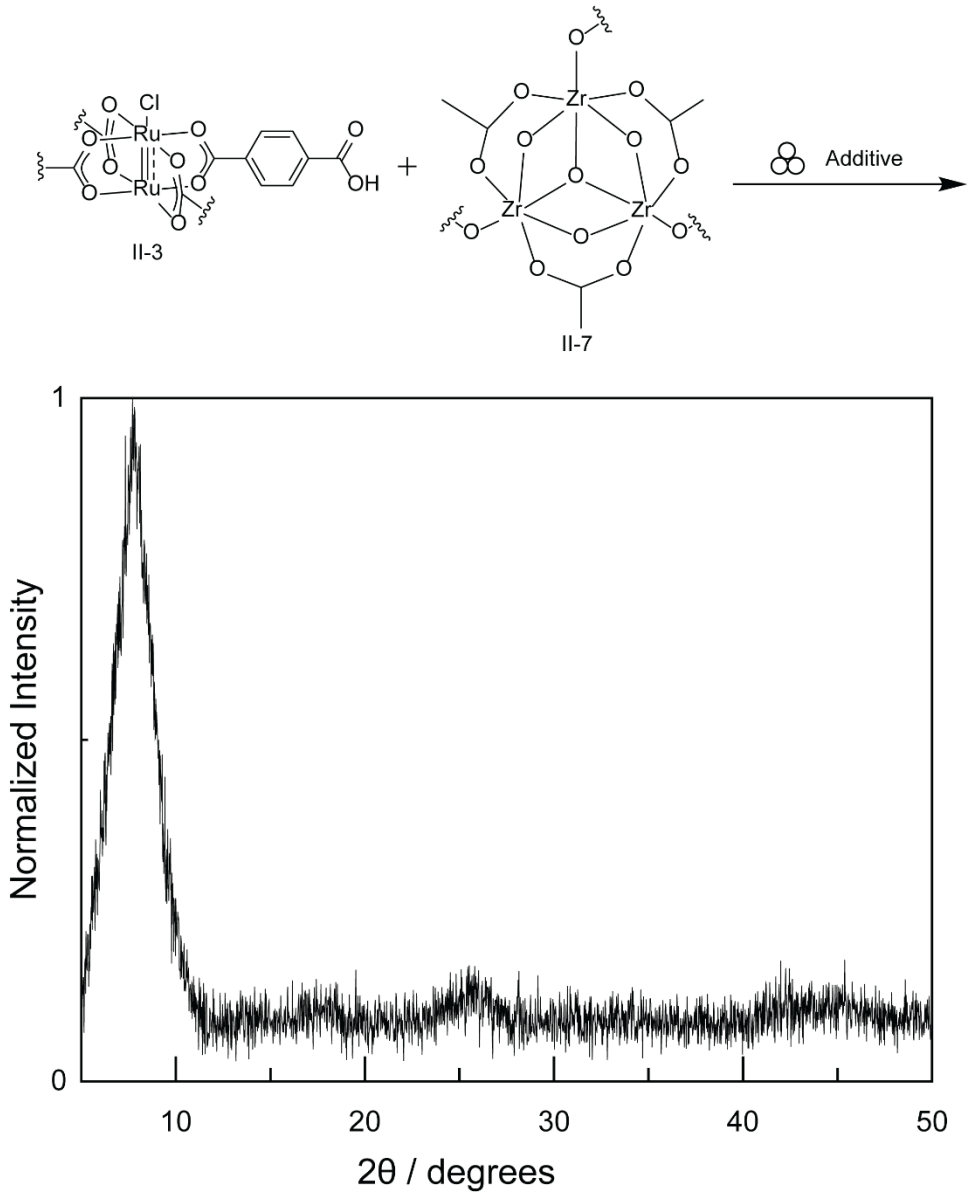

Figure II-8. Ball milling of II-3 with Zr clusters (shown in this case II-7) yielded powder patterns consistent with that displayed above, regardless of additive used or milling conditions.

Table II-1. **Comparison of mechanochemical synthesis conditions utilized to synthesize mixed Zr/Ru MOFs with II-3.** ^ = Molar ratio of 4:1 Ru:Zr * = Molar ratio of 3:1 Ru:Zr

Zr Cluster	Additive	Freq / Time
II-7 ^	DMF (η=0.56)	30 Hz, 90 min
	MeOH (η=0.56)	30 Hz, 90 min
	EtOH (η=0.56)	30 Hz, 120 min
	DMF/TEA (η=0.56)	30 Hz, 60 min
II-8 ^	DMF/TEA (η=0.68)	30 Hz, 60 min
	MeOH (η=0.78)	30 Hz, 60 min
	DMF (η=0.50)	30 Hz, 60 min
	DMF (η=0.78)	50 Hz, 60 min
	MeOH (η=0.78)	50 Hz, 60 min
II-9 *	-	30 Hz, 60 min
	MeOH(η=0.75)	30 Hz, 60 min
	DMF(η=0.75)	30 Hz, 60 min
	DMF (η=0.75)	50 Hz, 60 min

*II.2.3 Synthesis attempts for **II-6** and **II-10***

II.2.3.1 Solid-state

In addition to the attempts reported in the previous section, we also endeavored to synthesize Ru/Zr MOFs with **II-6** as the Ru_2 motif via ball-milling. Table II-2 contains the list of synthetic conditions assayed. Similarly to previous attempts with **II-3**, all resultant materials were amorphous, yielding PXRDs identical to that seen in Figure II-8. No color was observed in washes of the material, indicating that Ru_2 was indeed incorporated structurally in the material, in contrast to the earlier described ball milling conditions with **II-3**.

Table II-2. **Comparison of mechanochemical synthesis conditions utilized to synthesize mixed Zr/Ru MOFs with II-6.** All molar ratios 4:1 Ru:Zr. All samples milled at a frequency of 50Hz.

Zr Cluster	Solvent additive (η=0.2)	Time	Additive
II-7	DMF	120 min	-
	DEF	120 min	-
	MeOH	120 min	-
	MeOH	120 min	NaOAc
	MeOH	120 min	K_2CO_3
	-	120 min	-
II-8	DMF	90 min	-
	MeOH	90 min	-

II.2.3.2 Solution state

Our group demonstrated that solvothermal synthesis could be utilized when the primary coordination sphere motif was changed from carboxylate to amidate (Figure I-10). We hypothesized this outcome was due to the kinetic stability of the Ru–N bond under the polymerization conditions. This feature enabled the use solvothermal synthesis conditions for the synthesis of **II-6**, which is the direct congener of **II-3**. Solvothermal synthesis attempts at incorporating **II-6** were initially focused on reported conditions for the PCN series of MOFs.[170, 171] Table II-3 contains synthesis attempts for utilizing **II-6** as the metallolinker. Combining **II-7** with **II-6** yielded amorphous solids, regardless of acid modulator addition or Zr source used.

Table II-3. Comparison of solvothermal synthesis conditions utilized to synthesize mixed Zr/Ru MOFs with II-6.

Entry #	Zr Source	Solvent	Acid modulator
1	$ZrCl_4$	DMF	-
2			AcOH (0.25 mL)/Benzoic Acid (0.05 g)
3			AcOH (0.25 mL)
4			AcOH (0.5 mL)
5			AcOH (0.75 mL)
6			AcOH (1 mL)
7			AcOH (2 mL)
8			Benzoic Acid (0.120 g)
9			Formic Acid (0.5 mL)
10			Formic Acid (0.50 mL)/Benzoic Acid (0.020 g)
11			TFA (0.05 mL)
12			TFA (0.10 mL)
13			TFA (0.15 mL)
14			TFA (0.30 mL)
15			TFA (0.60 mL)
16		DEF	-
17			AcOH (0.25 mL)
18			AcOH (0.25 mL)/Benzoic Acid (0.05 g)
19			AcOH (0.5 mL)/Benzoic Acid (0.05 g)
20	$ZrOCl_2$	DMF	Benzoic Acid (0.100 g)
21			Benzoic Acid (0.270 g)
22			TFA (0.10 mL)
23			TFA (0.10 mL)/Benzoic Acid (0.100 g)
24			HBF_4 (0.10 mL)
25			HBF_4 (0.10 mL)/Benzoic Acid (0.100 g)
26	**II-8**	DMF	-
27			AcOH (0.25 mL)
28			AcOH (1 mL)
29			HBF_4 (0.05 mL)
30			TFA (0.05 mL)
31	**II-9**	DMF	TFA (0.04 mL)

Solvothermal synthesis attempts utilizing **II-10** are summarized in Table II-4 for the formation of Zr-containing MOFs. Conditions for MOF-808 were adapted (Table II-4) and yielded

an insoluble orange powder; the resulting PXRD is displayed in Figure **II-9**.[172] The obtained powder pattern did not correspond to any known material available; no structural models based on a Zr_6/paddlewheel exist and a model crystal structure could not be generated as data quality was too poor. Zr_6OAc_{12} was chosen as the model with which to compare diffraction patterns as no zirconium formate cluster has been reported in the literature.[173-176] Based on analysis of the PXRD for MOF-808, we tentatively assign the material generated via the solvothermal combination of **II-10**, $ZrOCl_2$, and formic acid (Table II-4, entry 1) as a mixed Ru_2/Zr MOF.

Table II-4. Comparison of solvothermal synthesis conditions utilized to synthesize mixed Zr/Ru MOFs with II-10. All reactions performed in DMF.

Entry #	Zr Source	Acid modulator
1	$ZrOCl_2$ (2.70 equiv)	Formic Acid (2 mL)
2		TFA(0.08 mL)
3		Benzoic Acid (0.5 g)
4	**II-7** (1.00 equiv)	Acetic Acid (2 mL)
5		HBF_4 (0.01 mL)
6	$ZrCl_4$ (9.15 equiv)	TFA (0.06 mL)
7	**II-8** (1.00 equiv)	TFA (0.08 mL)

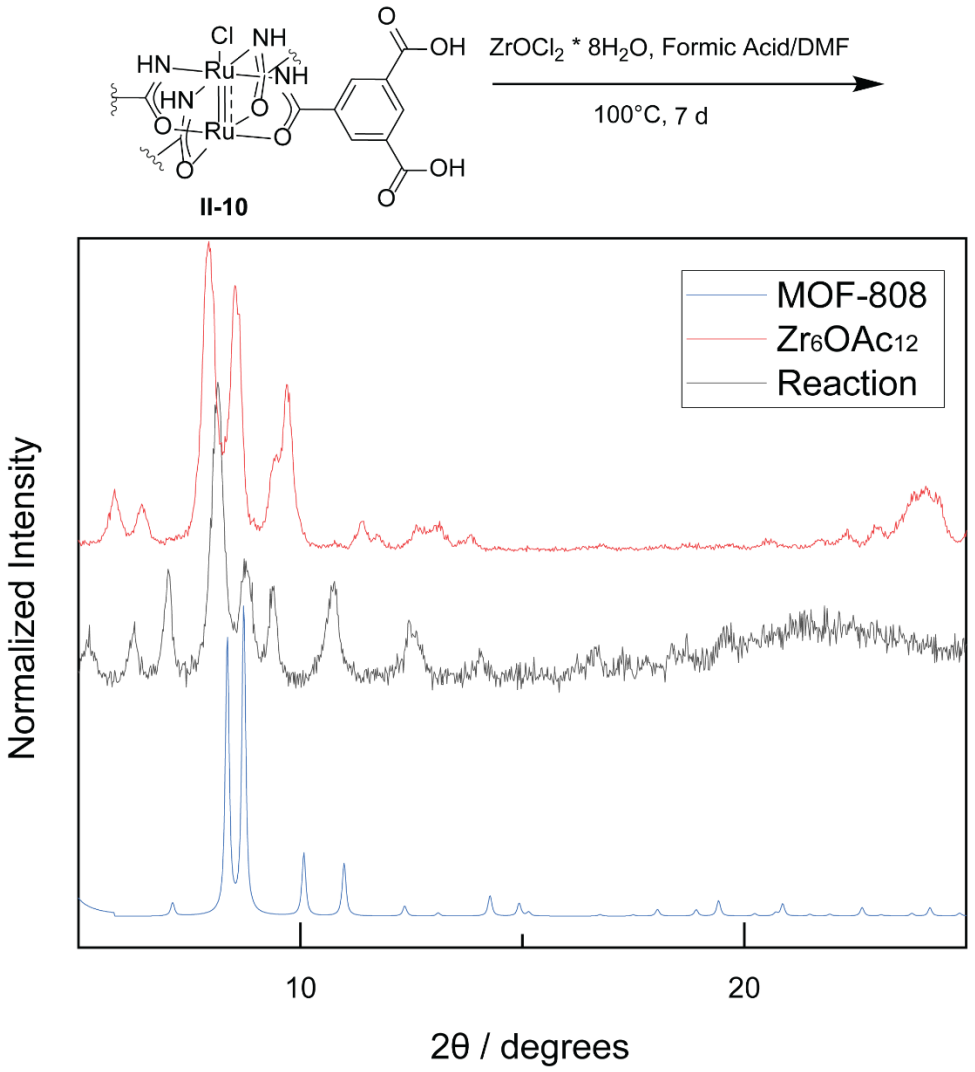

Figure II-9. Solvothermal combination of II-10 with $ZrOCl_2$ in Formic Acid/DMF at 100°C for 7 days produces the powder pattern seen above. Overlaying with MOF-808 and a model Zr_6OAc_{12} cluster indicates that successful incorporation of II-10 into a material occurred.

II.3. Conclusions

Sequestration of reactive compounds into porous, crystalline architectures is a strategy to harness productive reactivity pathways and allow further spectroscopic interrogation. In this chapter, we endeavored to use Ru_2 based metalloligands to generate new materials which could be used to generate reactive intermediates competent in C-H functionalization. Our original strategy

was predicated on mixed Cu/Ru HKUST-1 like materials, but these materials suffered from being incompatible with the sodium azide, which is necessary to generate reactive nitrides. Our efforts turned then to attempting to make materials which would be more robust in our reaction conditions.

Switching to Zr-based materials would offer us this robustness, still in a crystalline matrix. Initial ball milling experiments trying to synthesize DMOF-1 with **II-3** yielded poorly crystalline materials which dissolved upon exposure to NaN_3. Instead, we switched to **II-6** and **II-10** as the change to a more basic primary coordination sphere (amide vs carboxylate) would allow us to also explore solvothermal methods, instead of just limiting ourselves to mechanochemical synthesis techniques. Unfortunately, no attempt to generate Zr based materials using **II-6** generated crystalline material. Out of all reaction conditions screened using **II-10**, only the conditions adapted from syntheses of MOF-808 yielded a crystalline material. The generated PXRD is of an unknown phase and data quality was too poor to attempt to build a 3D model from the powder pattern, but we tentatively assign this material as a new Ru_2/Zr MOF.

Additional screening experiments to generate single-crystalline material using the previously identified condition should be engaged, and digestion followed by ^{1}H NMR is necessary to prove successful incorporation of **II-10** into the material framework. Overall, this provides a reasonable platform upon which to build crystalline frameworks from metalloligands to examine reactive intermediates.

II.4. Experimental Details

II.4.1 General Considerations

Materials

All reactions were carried out under ambient conditions unless stated otherwise. Solvents were obtained as ACS reagent grade. All chemicals and solvents were used as received unless noted otherwise. 1,3,5-Benzenetricarbonyl trichloride, 2-phenylethanol, and tetrabutylammonium fluoride (TBAF; 1 mol/L in THF) were obtained from TCI. Diethyl ether (Et_2O), ethyl acetate (EtOAc), dichloromethane, methanol (MeOH), tetrahydrofuran (THF), hexanes, chloroform, tetrafluoroboric acid (HBF_4) solution, acetic anhydride, sodium bicarbonate, zirconium isopropoxide (70% in IPrOH), zirconium tetrachloride, pyrazine, 2,2'-bipyridine, and acetic acid (AcOH) were obtained from Sigma Aldrich. Ammonium hydroxide, *N*,*N*-dimethylformamide, sodium chloride, *N*,*N*-diethylformamide, and thionyl chloride (DMF) were obtained from VWR Chemicals BDH. EtOH (KOPTEC 200 proof) was purchased from Decon Labs. Silica gel (0.063–0.200 mm, 60 Å for column chromatography), *tert*-butyl alcohol, pyridine, terephthaloyl chloride, potassium carbonate, trifluoroacetic anhydride, and trifluoroacetic acid were obtained from EMD Millipore. Copper acetate monohydrate, 1,3,5-benzenetricarboxylic acid, and LiCl were purchased from Alfa Aesar. Oxalyl chloride, zirconyl chloride, and DABCO were purchased from Bean Town Chemical. Hydrochloric acid and sodium sulfate were obtained from Macron Chemicals. 2-(Trimethylsilyl)ethanol was purchased from Matrix Scientific. Ruthenium chloride ($RuCl_3 \cdot xH_2O$) was obtained from Pressure Chemical. Trifluorotoluene, *N*,*N*-diethylacetamide, and formic acid were obtained from Alfa Aesar. Methacrylic acid was obtained from Acros Organics. NMR solvents were purchased from Cambridge Isotope Laboratories and were used as received.

Mechanochemical Synthesis

Mechanochemical synthesis was conducted using a Spex Certiprep 5100 mixer mill (60 Hz). Starting materials were loaded into a 2.5 mL polystyrene grinding vial (with a slip-on cap) with 10 methacrylate grinding balls (3.2 mm diameter).

Characterization Details

NMR spectra were recorded on a Bruker Ascend 400 operating at 400.13 MHz for ^{1}H and 376.36 MHz for ^{19}F or a Varian NMRS 500RM operating at 500.13 MHz for ^{1}H and 470.41 MHz for ^{19}F. Spectra were referenced against solvent signals: $CDCl_3$ (7.26 ppm, ^{1}H), CD_2Cl_2 (5.32 ppm, ^{1}H), D_2O (4.79 ppm, ^{1}H), CD_3OD (3.31 ^{1}H), DMSO-d_6 (2.50 ppm, ^{1}H), and benzotrifluoride (–63.72ppm, ^{19}F).[177] ^{1}H and ^{19}F NMR data are reported as follows: chemical shift (δ, ppm), (multiplicity: s (singlet), d (doublet), t (triplet), m (multiplet), br (broad), integration). Matrix-assisted laser desorption ionization (MALDI) data were obtained using a Bruker Microflex LRF MALDI-TOF using reflectron-TOF modes.

Powder X-ray Diffraction (PXRD)

In-house PXRD measurements were carried out on a Bruker D8 Advance Eco X-ray diffractometer (Cu Kα, 1.5418 Å; 40 kV, 25 mA) fitted with a LynxEye detector. The angular range was measured from 5.00 to 50.00° (2θ) with steps of 0.010° and a measurement time of 0.3 second per step. Simulated PXRD patterns were calculated using Mercury 3.9.[178]

II.4.2 Synthesis and Characterization

Synthesis of di-*tert*-butyl terephthalate

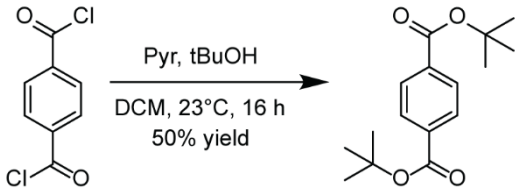

A 250-mL round-bottomed flask was charged with terephthaloyl chloride (5.00 g, 24.6 mmol, 1.00 equiv) and 100 mL of CH_2Cl_2. A mixture of *t*-BuOH (4.70 mL, 49.5 mmol, 2.00 equiv) and pyridine (4.10 mL, 49.5 mmol, 2.00 equiv) was added to the flask via an additional funnel over 30

min. The reaction mixture was stirred at 23 °C for 16 h. The solvent was removed under reduced pressure. The residue was dissolved in Et_2O and washed with 75 mL of saturated aqueous $NaHCO_3$ and brine (50 mL × 2) before being purified by SiO_2 gel column chromatography (1:4 EtOAc:Hex eluent) to afford di-*tert*-butyl benzene-1,4-dicarboxylate (3.38 g, 50% yield) as a white solid. ^{1}H NMR (δ, 23 °C, $CDCl_3$): 8.01 (s, 4H), 1.60 (s, 18H). The reported data is in agreement with literature values.[179]

Synthesis of II-1

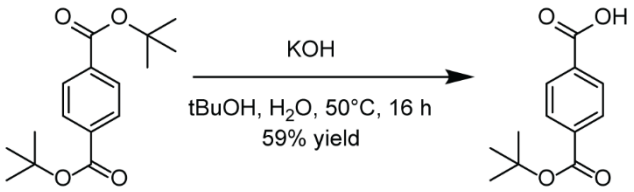

II-1

A 100-mL round-bottomed flask was charged with potassium hydroxide (0.351 g, 6.22 mmol, 1.00 equiv) and a 40 mL of a 1:1 mixture of *t*-BuOH/Water. The mixture was heated at 50 °C and stirred until the solids dissolved. Di-*tert*-butyl terephthalate (1.73 g, 6.22 mmol, 1.00 equiv) was added to the reaction mixture in one portion and the reaction mixture was stirred at 50 °C for 16 h. The reaction mixture was partitioned between EtOAc and 50 mL 2M HCl and further washed with brine (2 × 100 mL) then water (1 × 100mL). The organic layer was dried over Na_2SO_4 and dried *in vacuo*. The residue was purified by SiO_2 gel column chromatography (1:4 EtOAc:Hex eluent) to afford **II-1** (0.813 g, 59% yield) as a white solid. ^{1}H NMR (δ, 23 °C, $CDCl_3$): 8.14 (d, J = 8.2 Hz, 2H), 8.07 (d, J = 8.2 Hz, 8H), 1.61(s, 9H).

Synthesis of Ru_2OAc_4Cl

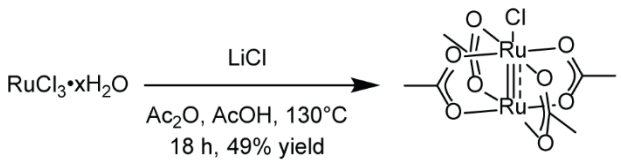

$Ru_2(OAc)_4Cl$ was prepared according to the following modification of literature methods.[180] A 100-mL three neck round-bottomed flask was charged with $RuCl_3 \cdot xH_2O$ (0.517 g, 2.49 mmol, 1.00 equiv) and anhydrous LiCl (0.761 g, 17.7 mmol, 7.27 equiv). A mixture of glacial acetic acid (25mL) and acetic anhydride (10mL) was added to the reaction vessel. The resulting solution was heated at 130 °C for 18 h with N_2 bubbled through the solution via a metal needle for the duration of the reaction. The reaction was cooled to 23 °C and a red-brown precipitate was observed. The precipitate was isolated via vacuum filtration, washed with copious amounts of MeOH and Et_2O and dried *in vacuo* to afford the title compound (0.297 g, 49% yield) as an orange solid. ^{1}H NMR (δ, 23°C, D_2O): –45.0 (br s, 12H).

Synthesis of II-2

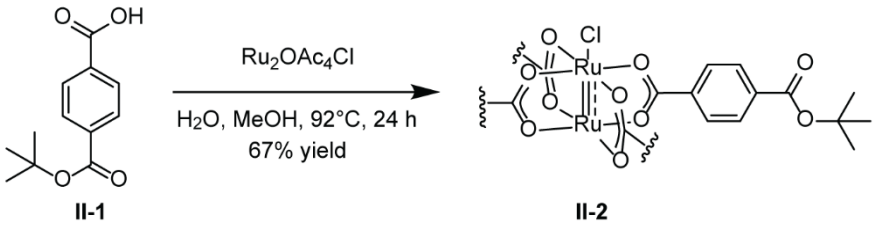

II-1 **II-2**

A 100-mL round-bottomed flask was charged with Ru_2OAc_4Cl (0.124 g, 0.262 mmol, 1.00 equiv), **II-1** (0.438 g, 1.57 mmol, 6.00 equiv), and 40 mL of a 1:1 mixture of MeOH/H_2O. The reaction mixture was heated to 92 °C and stirred for 24 h. The solvent was removed *in vacuo* to afford a brown solid. The residue was dissolved in CH_2Cl_2 and filtered. The filtrate was concentrated *in vacuo* and triturated with Et_2O and the solid was isolated via vacuum filtration. The solids were dried under reduced pressure to afford **II-2** (0.196 g, 67% yield) as a brown solid. ^{1}H NMR (δ, 23

°C, DMSO-d_6): 31.07 (br s, 8H), 7.83 (d, 8H), 3.05 (s, 36H). Mass spectrometry (MALDI, positive) data: calc $[Ru_2(C_{12}H_{13}O_4)_4]^+$: 1088.1, expt m/z = 1088.0

Synthesis of II-3

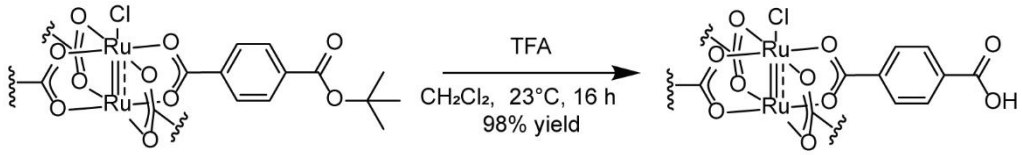

II-2 **II-3**

A 50-mL round-bottomed flask was charged with **II-2** (0.196 g, 0.175 mmol, 1.00 equiv) and CH_2Cl_2 (25 mL). To this reaction mixture was added TFA (300 µL, 3.92 mmol, 22.4 equiv). The mixture was stirred at 23 °C for 16 h. The obtained brown solids were collected by vacuum filtration and washed with CH_2Cl_2 (2 × 20 mL) to afford **II-3** (0.157 g, 98% yield) as a brown solid. ^{1}H NMR (δ, 23 °C, DMSO-d_6): 31.23 (br s, 8H), 15.79 (s, 4H), 7.82 (d, 8H). Mass spectrometry (MALDI, positive) data: calc $[Ru_2(C_8H_4O_4)_4]^+$: 863.9, expt m/z = 863.8

Synthesis of *bis*(2-(trimethylsilyl)ethyl) terephthalate

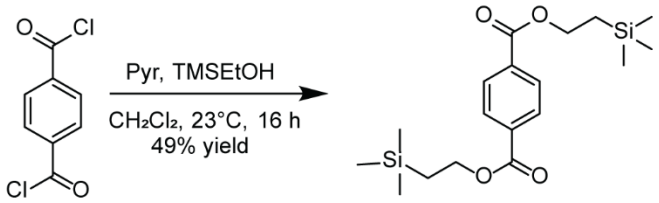

A 250-mL round-bottomed flask was charged with terephthaloyl chloride (5.00 g, 24.6 mmol, 1.00 equiv) and 100 mL of CH_2Cl_2. A mixture of 2-(trimethylsilyl)ethanol (5.00 mL, 51.3 mmol, 2.08 equiv) and pyridine (6.00 mL, 77.2 mmol, 3.14 equiv) was added to the flask slowly through an additional funnel over 30 min. The reaction mixture was stirred at 23 °C for 16 h. The solvent was removed under reduced pressure. The residue was dissolved in EtOAc and washed with 75 mL of

water and saturated aqueous NH_4Cl (50 mL × 2). The organic layer was dried over Na_2SO_4 and dried *in vacuo*. The resultant white residue was purified by SiO_2 gel column chromatography (1:9 EtOAc:Hex eluent) to afford the title compound (4.41 g, 49% yield) as a white solid. ^1H NMR (δ, 23 °C, $CDCl_3$): 8.09 (s, 4H), 4.44 (t, *J* = 8.4 Hz, 4H), 1.15 (t, *J* = 8.5 Hz, 4H), 0.09 (s, 18H).

Synthesis of 2-(trimethylsilyl)ethoxycarbonyl benzoic acid

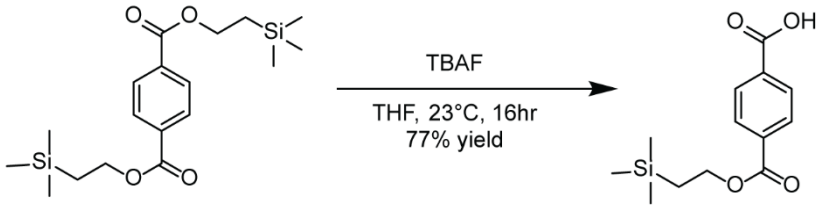

A 250-mL round-bottomed flask was charged with *bis*(2-(trimethylsilyl)ethyl) terephthalate (3.25 g, 8.87 mmol, 1.00 equiv) and of THF (100 mL). TBAF (1M in THF, 8.87 mL, 8.87 mmol, 1.00 equiv) was added dropwise over 30 min, and the resulting reaction mixture was stirred at 23 °C for 16 h. Solvent was removed *in vacuo* and the resulting residue was partitioned between Et_2O (50 mL) and 1M HCl (20 mL). The aqueous layer was extracted with Et_2O (2 × 50mL). The combined organic layers were washed with NH_4Cl (2 × 50mL) and dried over Na_2SO_4. Solvent was removed *in vacuo* and the residue was purified by SiO_2 gel column chromatography (1:9 MeOH:CH_2Cl_2 eluent) to afford the title compound (1.82 g, 77% yield) as a white solid. ^1H NMR (δ, 23 °C, $CDCl_3$): 8.14 (dd, *J* = 8.6, 5.0 Hz, 4H), 4.46 (t, *J* = 8.5 Hz, 4H), 1.15 (t, *J* = 8.5 Hz, 4H), 0.09 (s, 18H).

Synthesis of II-4

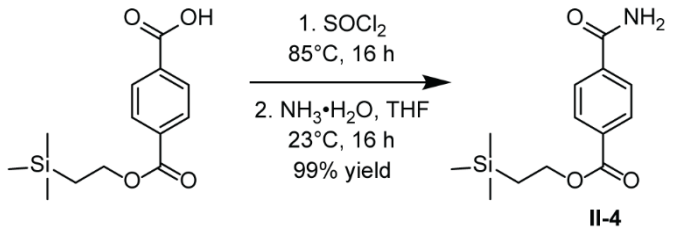

A 100-mL round-bottomed flask was charged with 2-(trimethylsilyl)ethoxycarbonyl benzoic acid (2.00 g, 7.51 mmol, 1.00 equiv) and $SOCl_2$ (30 mL). The reaction mixture was heated to 85 °C and stirred for 16 h under N_2. The solvent was removed *in vacuo*. To the yellow residue was added THF (50 mL) and $NH_3 \cdot H_2O$ (2.00 mL, 50.2 mmol, 6.69 equiv) was added dropwise and the reaction was stirred for 16 h at 23 °C. Solvent was removed *in vacuo* to give an off-white solid. The solid was triturated with H_2O and isolated via vacuum filtration to give **II-4** (1.99 g, 99% yield) as a white solid. ^{1}H NMR (δ, 23 °C, DMSO-d_6): 8.13 (s, 1H), 8.00 (dd, J = 8.7, 3.8 Hz, 4H), 7.55 (s, 1H), 4.40 (t, J = 8.2 Hz, 2H), 1.11, (t, J = 8.3 Hz, 2H), 0.06 (s, 9H).

Synthesis of Ru_2TFA_4Cl

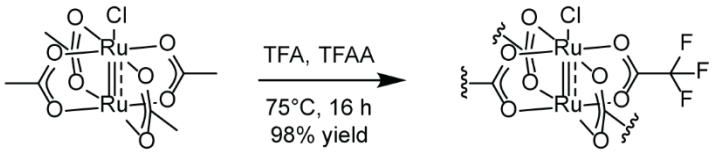

A 100-mL round-bottomed flask was charged with $Ru_2(OAc)_4Cl$ (0.100 g, 0.211 mmol, 1.00 equiv). A mixture of trifluoroacetic acid (20 mL) and trifluoroacetic anhydride (2 mL) was added to the reaction vessel. The resulting solution was heated at 75 °C for 16 h under N_2. The solution was dried *in vacuo* to afford Ru_2TFA_4Cl (0.108 g, 98% yield) as a purple-red solid. ^{19}F NMR (δ, 23°C, DMSO-d_6): –73.1 (s, 12F).

Synthesis of II-5

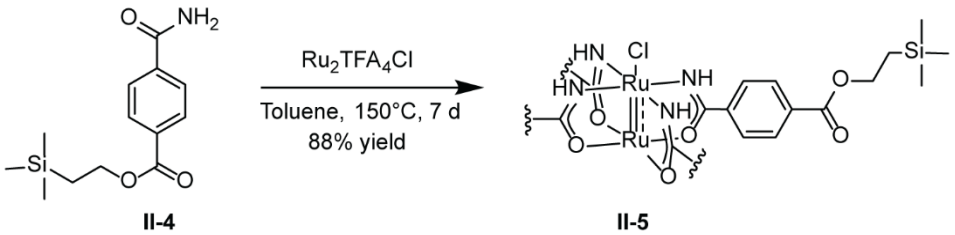

II-4 **II-5**

A 100-mL Schlenk flask was charged with freshly prepared Ru_2TFA_4Cl (0.065 g, 0.0942 mmol, 1.00 equiv) and **II-4** (0.250 g, 0.942 mmol, 10.0 equiv) under N_2. To this was added dry and degassed toluene (50 mL), and the reaction vessel was equipped with a micro Soxhlet extractor containing K_2CO_3. The reaction mixture was heated to 150 °C and stirred under N_2 for 7 d. The solvent was removed *in vacuo* and the resulting dark brown residue was triturated with CH_2Cl_2 and isolated via vacuum filtration. The dark brown solid was further washed with CH_2Cl_2 (1 × 15mL) and Et_2O (2 × 15 mL) to afford **II-5** (0.108 g, 88% yield) as a brown/purple solid. ^{1}H NMR (δ, 23 °C, DMSO-d_6): 27.32 (br s, 8H), 8.62 (8H), 8.06 (s, 4H), 7.49 (s, 4H), 5.62 (s, 8H), 0.96 (s, 36H). Mass spectrometry (MALDI, positive) data: calc $[Ru_2(C_{13}H_{18}O_3NSi[)_4]^+$: 1260.2, expt m/z = 1260.3

Synthesis of II-6

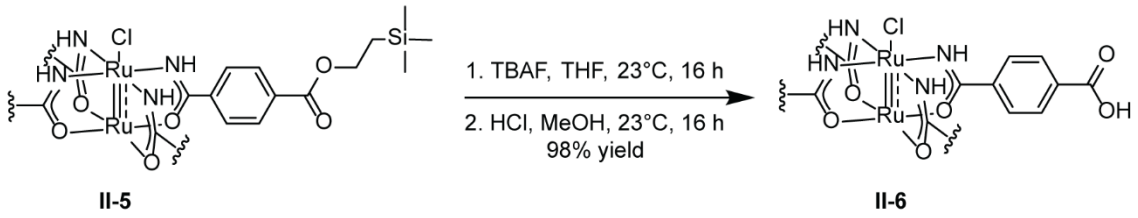

II-5 **II-6**

A 25-mL round-bottomed flask was charged with **II-5** (0.025 g, 0.019 mmol, 1.0 equiv) and THF (15 mL). To this, TBAF (1M in THF, 0.16 mL, 0.16 mmol, 8.3 equiv) was added and the reaction mixture was stirred at 23 °C for 16 h. Solvent was removed *in vacuo*. MeOH (10 mL) was added to the resulting green residue. Upon dissolution, 1M HCl (0.25 mL, 0.25 mmol, 13.0 equiv) was

added and the solution was stirred at 23 °C for 16 h. The resulting solid was isolated by vacuum filtration to yield **II-6** (0.017 g, 98% yield) as a yellow solid. ^{1}H NMR (δ, 23 °C, DMSO-d_6): 28.81 (br s, 2H), 28.12 (br s 6H), 15.49 (s, 4H), 8.57 (br s, 4H), 8.48 (br s, 2H), 8.36 (br s, 2H). Mass spectrometry (MALDI, positive) data: calc $[Ru_2(C_8H_6O_3N)_4]^+$: 859.9, expt m/z = 859.9

Synthesis of II-7

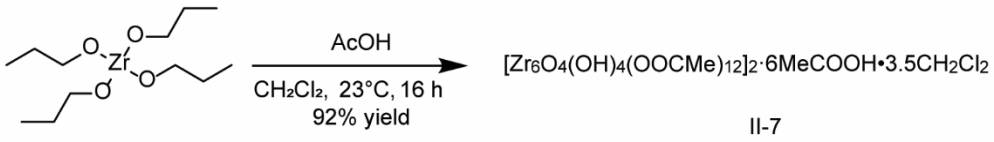

A 50-mL Schlenk flask was charged with $Zr(OPr)_4$ (70% in 1-propanol, 1.00 g, 3.05 mmol, 1.00 equiv). Solvent was removed *in vacuo* to give a white powder. To this powder was added dry and degassed AcOH (3.68 g, 61.2 mmol, 20.1 equiv) and CH_2Cl_2 under N_2. The reaction mixture was stirred at 23 °C for 16 h. The resulting white solid was isolated via vacuum filtration and washed with AcOH (30 mL). The solid was dried under reduced pressure to afford **II-7** (0.761 g, 92% yield based on Zr) as a white solid. ^{1}H NMR (δ, 23 °C, CD_2Cl_2): 10.37 (br s), 2.08 (br s, 6H), 2.01 (br s, 1H), 1.97 (br s, 2H), 1.92 (br s, 1.5H), 1.83 (br s, 1.5H). The obtained spectral data and integrations are in good agreement with those reported in literature.[181]

Synthesis of II-8

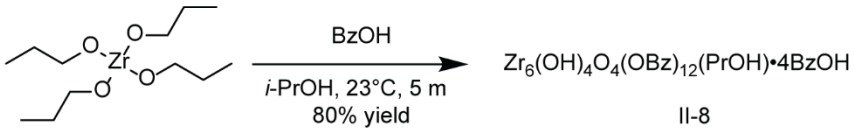

A 250-mL Schlenk flask was charged with *i*-PrOH (94 mL) and BzOH (16.0g, 131 mmol, 80.4 equiv). The solution was degassed via three freeze-pump-thaw cycles and put under N_2. $Zr(OPr)_4$ (70% in 1-propanol, 0.762 g, 1.63 mmol, 1.00 equiv) was added to the reaction mixture and white precipitate was immediately observed. The precipitate was isolated via vacuum filtration and

washed with *i*-PrOH (150 mL) to afford **II-8** (532 mg, 80% based on Zr) as a white powder. The obtained PXRD are in good agreement with those reported in literature.[182]

Synthesis of II-9

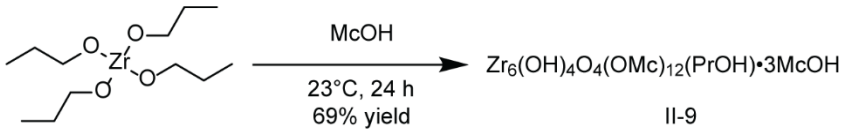

A 25-mL Schlenk flask was charged with $Zr(OPr)_4$ (70% in 1-propanol, 1.04 g, 2.23 mmol, 1.00 equiv) and methacrylic acid (1.00 mL, 11.8 mmol, 5.30 equiv). The reaction mixture was degassed via three freeze-pump-thaw cycles and put under N_2. The reaction mixture was left to sit at 23 °C for 24 h at which point white precipitate was observed. The solid was isolated via vacuum filtration and used without further purification to give **II-9** (1.03 g 69% yield) as a white powder. The obtained PXRD are in good agreement with those reported in literature.[182]

Synthesis of tris(2-(trimethylsilyl)ethyl) benzene-1,3,5-tricarboxylate

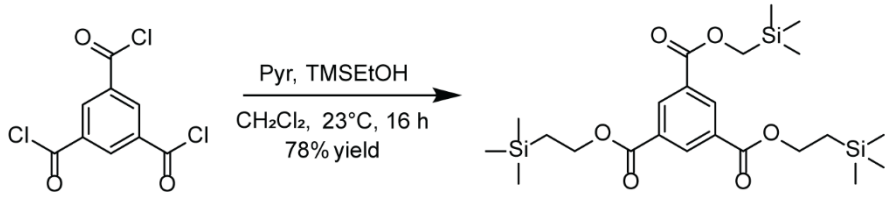

A 250-mL round-bottomed flask was charged with 1,3,5-benzenetricarbonyl trichloride (5.00 g, 18.8 mmol, 1.00 equiv), 2-(trimethylsilyl)ethanol (9.00 mL, 62.8 mmol, 3.34 equiv), and CH_2Cl_2 (100 mL). A mixture of pyridine (7.60 mL, 94.4 mmol, 5.02 equiv) and CH_2Cl_2 (20 mL) was added dropwise to the flask over 15 min. The reaction mixture was stirred at 23 °C for 16 h. Saturated aqueous NH_4Cl (100 mL) was added and the mixture was extracted with CH_2Cl_2 (100 mL × 3). The combined organic layers were evaporated under vacuum. The residue was dissolved in

hexanes (150 mL) and filtered. Solvent was removed *in vacuo* to afford the title compound (7.32 g, 78% yield) as a white solid. ^{1}H NMR (δ, 23 °C, $CDCl_3$): 8.83 (s, 3H), 4.46 (t, *J* = 8.5 Hz, 6H) 1.16 (t, *J* = 8.5 Hz, 6H), 0.09 (s, 27H). The obtained spectral data are in good agreement with those reported in literature.[117]

Synthesis of 3,5-bis((2-(trimethylsilyl)ethoxy)carbonyl)benzoic acid

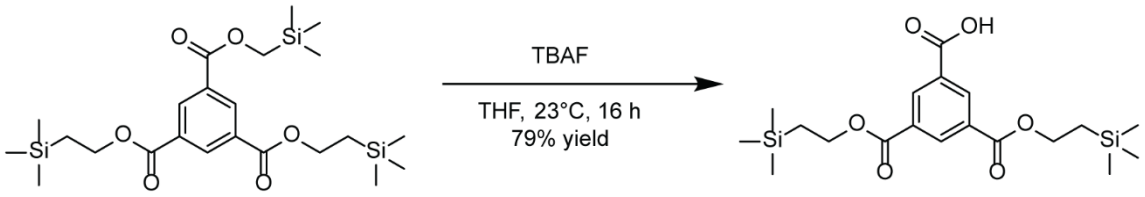

A 500-mL round-bottomed flask was charged with tris(2-(trimethylsilyl)ethyl) benzene-1,3,5-tricarboxylate (5.22 g, 10.5 mmol, 1.00 equiv) and THF (100 mL). TBAF (1 M in THF, 10.5 mL, 10.5 mmol, 1.00 equiv) was diluted with THF (90 mL) and the entire solution added rapidly, with vigorous stirring, to the reaction mixture. The reaction mixture was stirred at 23 °C for 16 h. Diethyl ether (100 mL) and 1M HCl (20 mL) were added to the reaction mixture. The layers were separated, and the aqueous layer was extracted with diethyl ether (50 mL × 3). The combined organic layers were washed with brine (2 × 100 mL) and 2M NaOH (10 mL). A white gel was observed to be formed, which was isolated via vacuum filtration and washed with hexanes (200 mL). The residue was suspended in CH_2Cl_2 (100 mL) and 8M HCl (15 mL) was added. The organic layer was washed with brine (2 × 100 mL), filtered to remove undissolved precipitate, and concentrated *in vacuo* to yield the title compound (3.43 g, 79% yield) as a white solid. ^{1}H NMR (δ, 23°C, $CDCl_3$): 8.92 (d, *J* = 1.5 Hz, 2H), 8.90 (t, *J* = 1.5 Hz, 1H), 4.49 (m, 6H), 1.18 (m, 6H), 0.10 (s, 18H). The obtained spectral data are in good agreement with those reported in literature.[117]

Synthesis of bis(2-(trimethylsilyl)ethyl) 5-carbamoylisophthalate

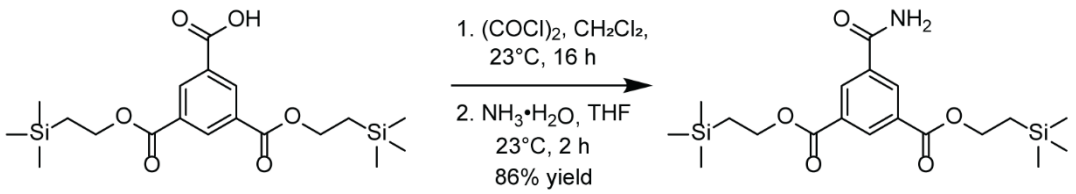

A 250-mL round-bottomed flask was charged with 3,5-bis((2-(trimethylsilyl)ethoxy)carbonyl)benzoic acid (3.43 g, 8.32 mmol, 1.00 equiv), DMF (0.10 mL, 1.3 mmol, 0.156 equiv), and CH_2Cl_2 (60 mL). Oxalyl chloride (1.5 mL, 17.3 mmol, 2.08 equiv) was added dropwise to the flask over 10 min. The reaction mixture was stirred at 23 °C under N_2 for 16 h. The solvent was removed *in vacuo*. THF (60.0 mL) was added to the obtained yellow solid. $NH_3 \cdot H_2O$ (28%, 6.2 mL, 44 mmol, 5.29 equiv) was added dropwise over 10 min. The reaction mixture was stirred at 23 °C for 2 h. The solvent was removed under vacuum to afford a white solid. H_2O (150 mL) was added to the flask and the obtained solid was collected by vacuum filtration. The solid was washed with additional H_2O (200 mL) and dried under reduced pressure to yield the title compound (2.95 g, 86% yield) as a white solid. H NMR (δ, 23 °C, $CDCl_3$): 8.80 (t, *J* = 1.5 Hz, 1H), 8.67 (d, *J* = 1.0 Hz, 2H), 6.50 (br, 1H), 6.21 (br, 1H), 4.46 (m, 4H) 1.16 (m, 4H), 0.09 (s, 18H). The obtained spectral data are in good agreement with those reported in literature.[117]

Synthesis of II-S1

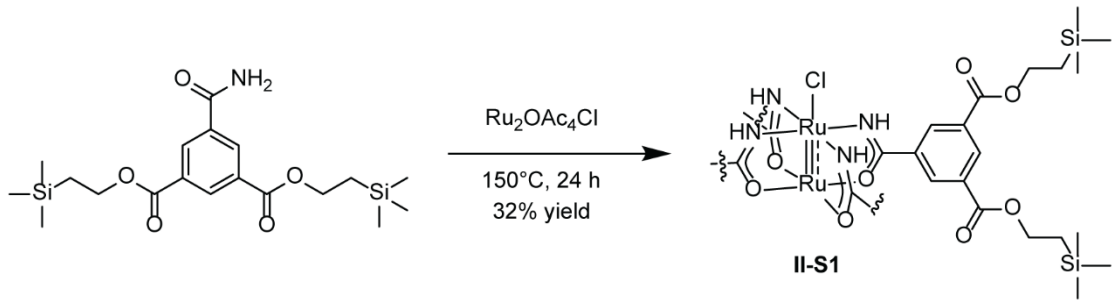

A 25-mL Schlenk flask was charged with $Ru_2(OAc)_4Cl$ (0.127 g, 0.270 mmol, 1.00 equiv) and bis(2-(trimethylsilyl)ethyl) 5-carbamoylisophthalate (1.07 g, 2.62 mmol, 9.7 equiv). The headspace of the flask was evacuated. The reaction mixture was heated to 150 °C under N_2. The reaction mixture was observed to melt and was stirred at 150 °C for 24 h. The reaction mixture was cooled to 23 °C and hexanes (75 mL) was added to the residue. The obtained suspension was sonicated and filtered to give a dark red filtrate. This process was repeated until the filtrate received was colorless. The combined filtrate was concentrated under reduced pressure to afford dark brown solids. The solids were washed with MeOH (75 mL) and dried under reduced pressure to afford **II-S1** (0.161 g, 32% yield) as a red solid. ^{1}H NMR (δ, 23 °C, DMSO-d_6): 28.23 (br s, 8H), 19.24 (br s, 4H), 5.68 (br s, 16H), 1.80 (br s, 16H), 0.49 (s, 72H). The obtained spectral data are in good agreement with those reported in literature.[117]

Synthesis of II-10

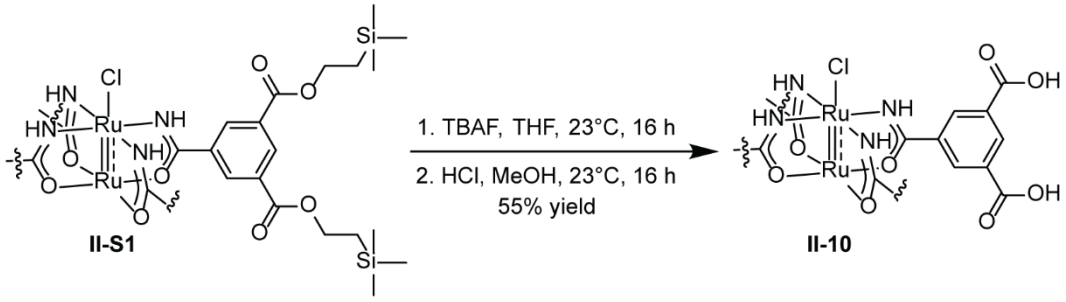

A 50-mL round-bottomed flask was charged with **II-S1** (0.150 g, 0.080 mmol, 1.00 equiv), TBAF (1 M in THF, 1.6 mL, 1.6 mmol, 20 equiv), and THF (20 mL). The reaction mixture was stirred at 23 °C for 16 h. The obtained yellow solids were collected by vacuum filtration and washed with THF (20 mL × 2) to afford a light-yellow solid. The solid was transferred to a 50-mL round-bottomed flask, and subsequently was charged MeOH (20 mL) and 1M HCl (1.0 mL). The reaction mixture was stirred at 23 °C for 2 h. The obtained yellow solids were collected by vacuum filtration

and washed with H_2O (20 mL) to afford **II-10** (0.047 g, 55% yield) as a yellow solid. ^{1}H NMR (δ, 23 °C, CD_3OD): 28.2 (br s, 8H), 19.2 (br s, 4H), 3.18 (m, 12), 1.64 (m, 12H), 1.44 (m, 12H), 1.09 (t, 16H). The obtained spectral data are in good agreement with those reported in literature.[117]

General procedure for mechanochemical synthesis of Ru-DMOF-1

The reaction vessel was charged with **II-3** (0.020 g, 0.022 mmol, 1.0 equiv), Cu_2OAc_4 (0.0045 g, 0.022 mmol, 1.0 equiv), and DABCO (0.005 g, 0.05 mmol, 2 equiv). Solvent additive was added to the reaction mixture, and the reaction vessel was sealed. The reaction was milled at 60 Hz for 30 min. The vessel was then filled with MeOH and briefly sonicated to form a suspension. The suspension was transferred to a centrifuge and centrifuged at 6000 RPM for 5 min. The solvent was decanted and the obtained solid was washed with MeOH (2 × 15 mL) to yield dark green powder (0.023 g).

General procedure for mechanochemical synthesis of binary structures

The reaction vessel was charged with **II-3** (0.050 g, 0.056 mmol, 4.0 equiv), **II-7** (0.039 g, 0.014 mmol, 1.0 equiv), and solvent additive. The reaction vessel was shaken at either 30 or 50 Hz for 60, 90, or 120 min. The obtained black solids were suspended in MeOH and transferred to a centrifuge tube. Solvent was separated by centrifugation at 6000 RPM for 7 min. The solvent was decanted and the obtained solid was washed with MeOH (2 × 15 mL) to yield black powder (0.047 g). The same conditions were applied to samples containing **II-8** (0.032 g, 0.019 mmol, 1.00 equiv) or **II-9** (0.024 g, 0.014 mmol, 1.0 equiv).

General procedure for solvothermal synthesis using II-6

A 20-mL scintillation vial was charged with **II-6** (0.015 g, 0.017 mmol, 1.0 equiv), Zr source (0.25 equiv), and DMF (2 mL). The reaction mixture was sonicated until all solids were dissolved and acid modulator was added. The vial was placed into a 120 °C oven for 3 d. No solid was observed except for entry #'s 14, 15, and 21 from Table II-3, in which case a black precipitate was observed.

General procedure for solvothermal synthesis using II-10

A 20-mL scintillation vial was charged with **II-10** (RuBTCNH2, 0.020 g, 0.019 mmol, 1.0 equiv), Zr source, and DMF (2 mL). The reaction mixture was sonicated until all solids were dissolved and acid modulator was added. The vial was placed into a 100 °C oven for 7 d and orange solids were observed upon cooling. The solid was isolated via vacuum filtration and washed with DMF (2 × 10 mL).

NMR Spectra

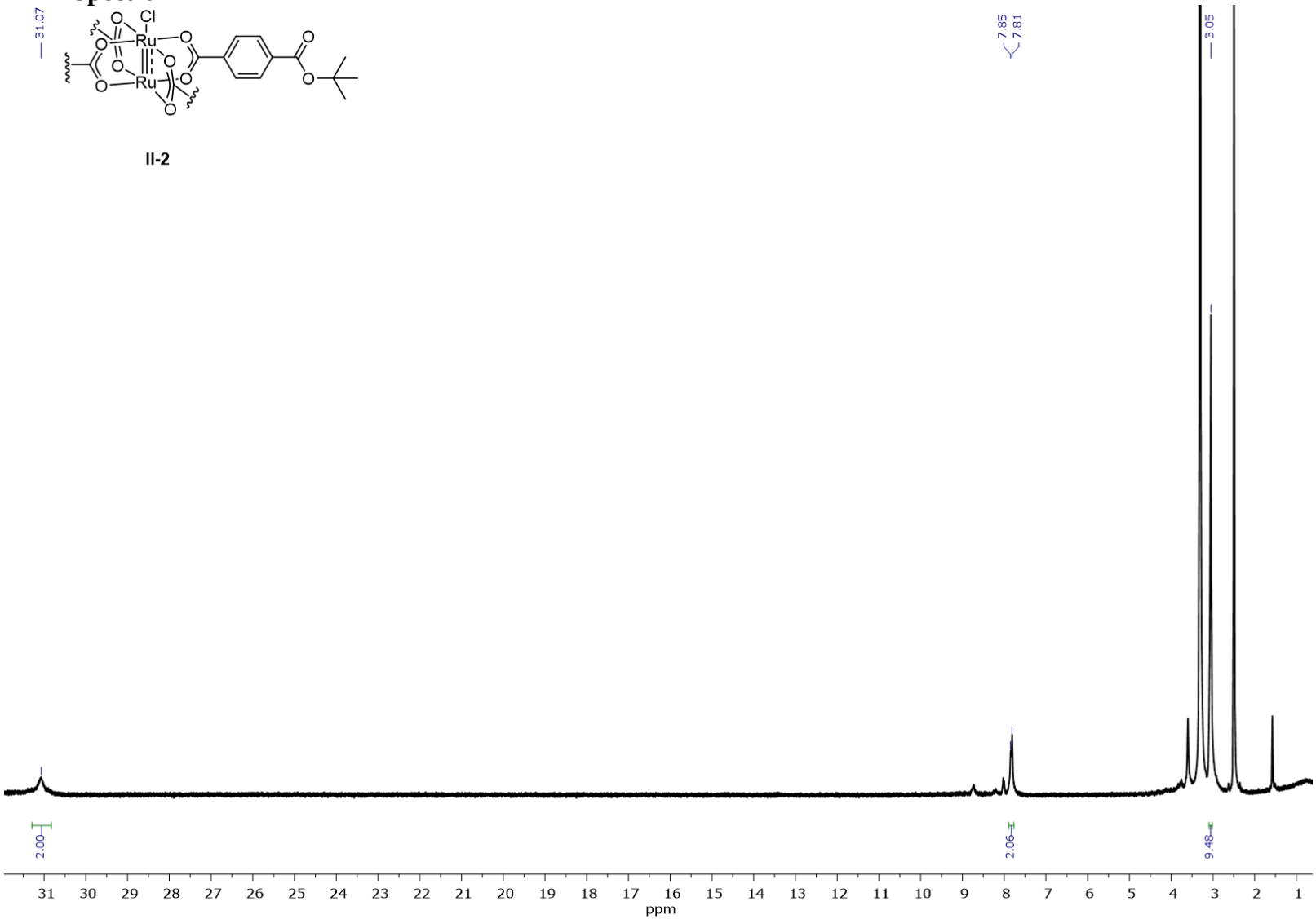

Figure II-10. NMR of II-2 in DMSO-d_6 at 23°C.

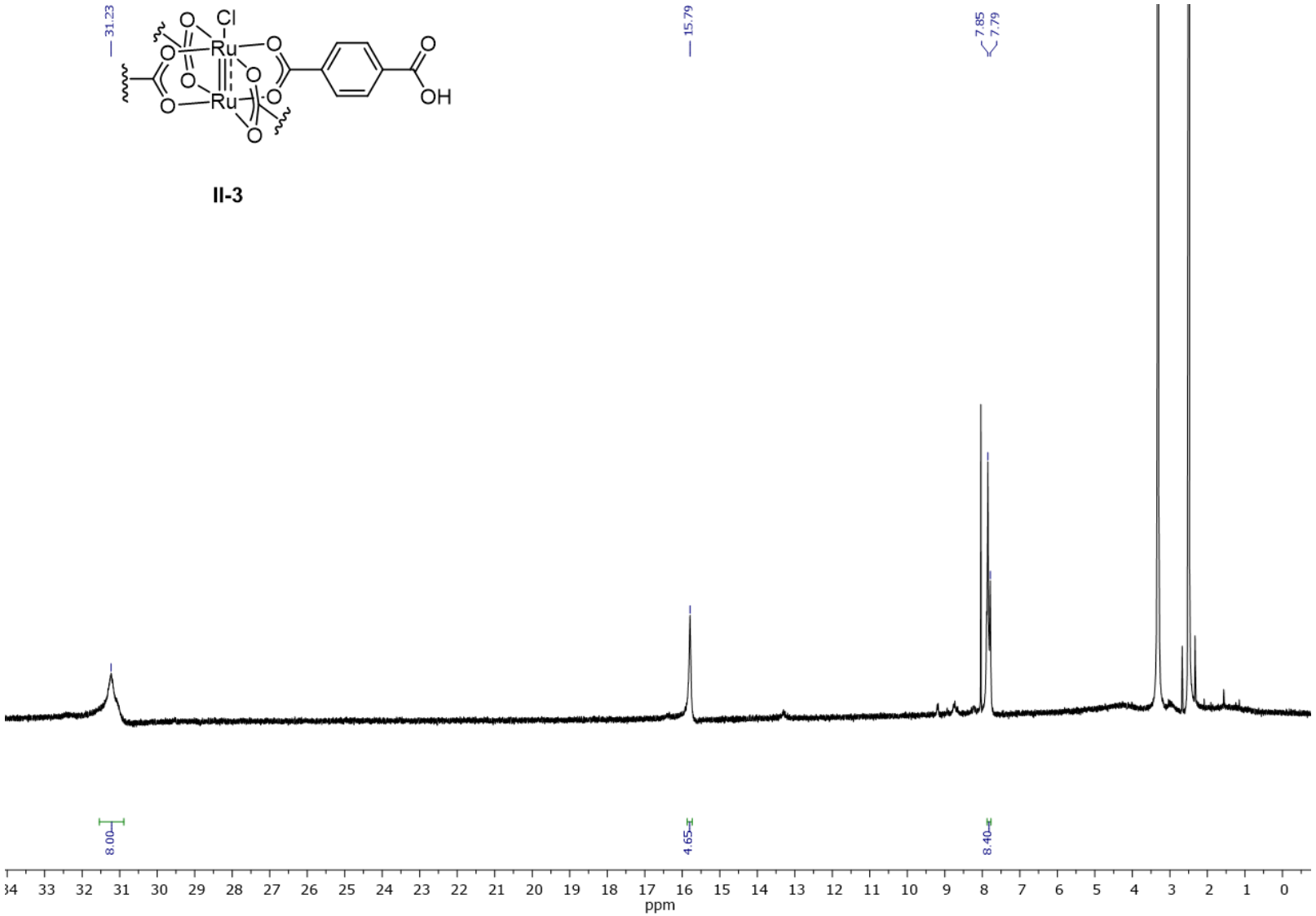

Figure II-11. NMR of II-3 in DMSO-d_6 at 23°C. Peaks at δ = 8.01 and 13.23 indicate free BDC. II-3 decomposes over time in DMSO.[117]

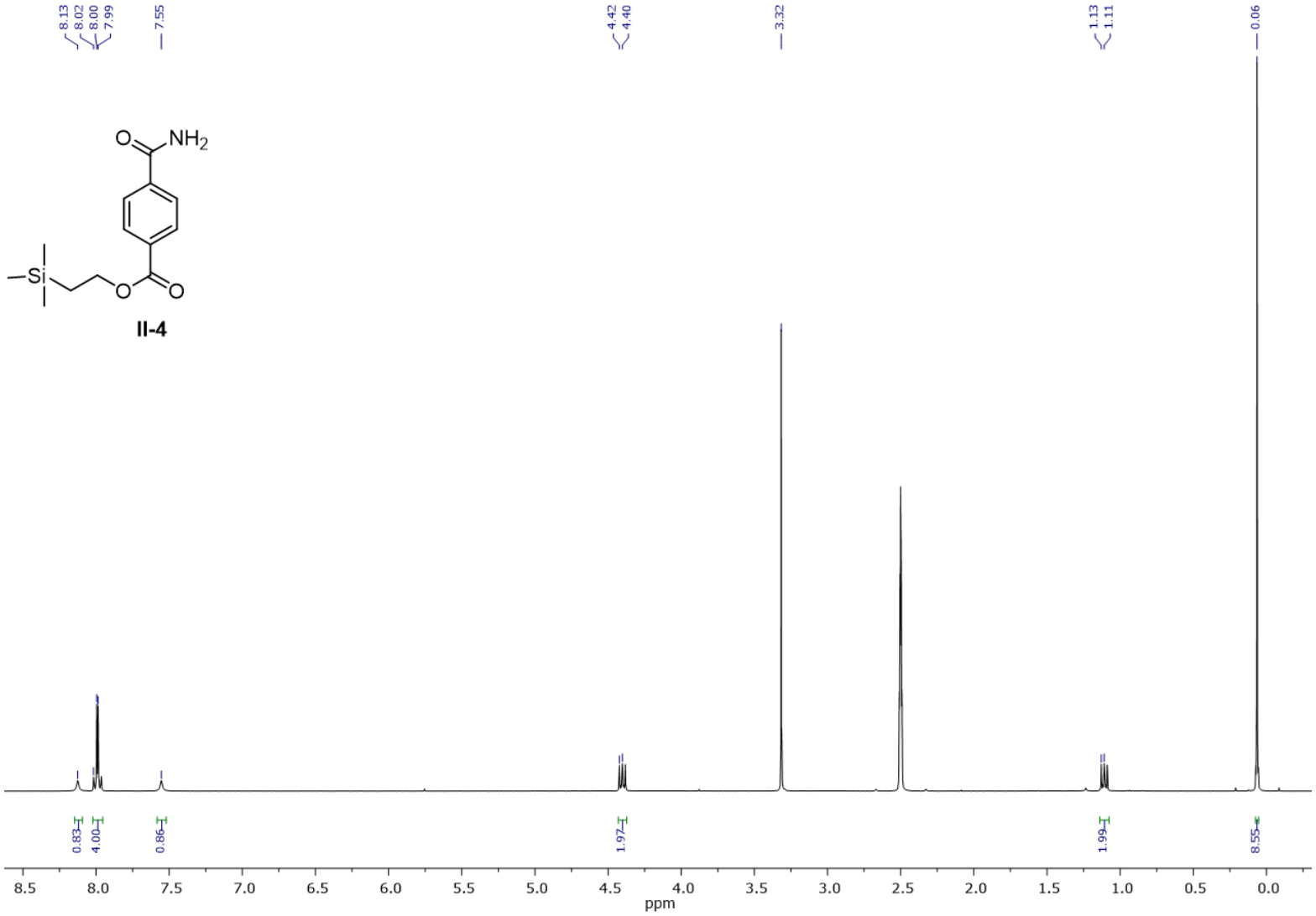

Figure II-12. NMR of II-4 in DMSO-d_6 at 23°C.

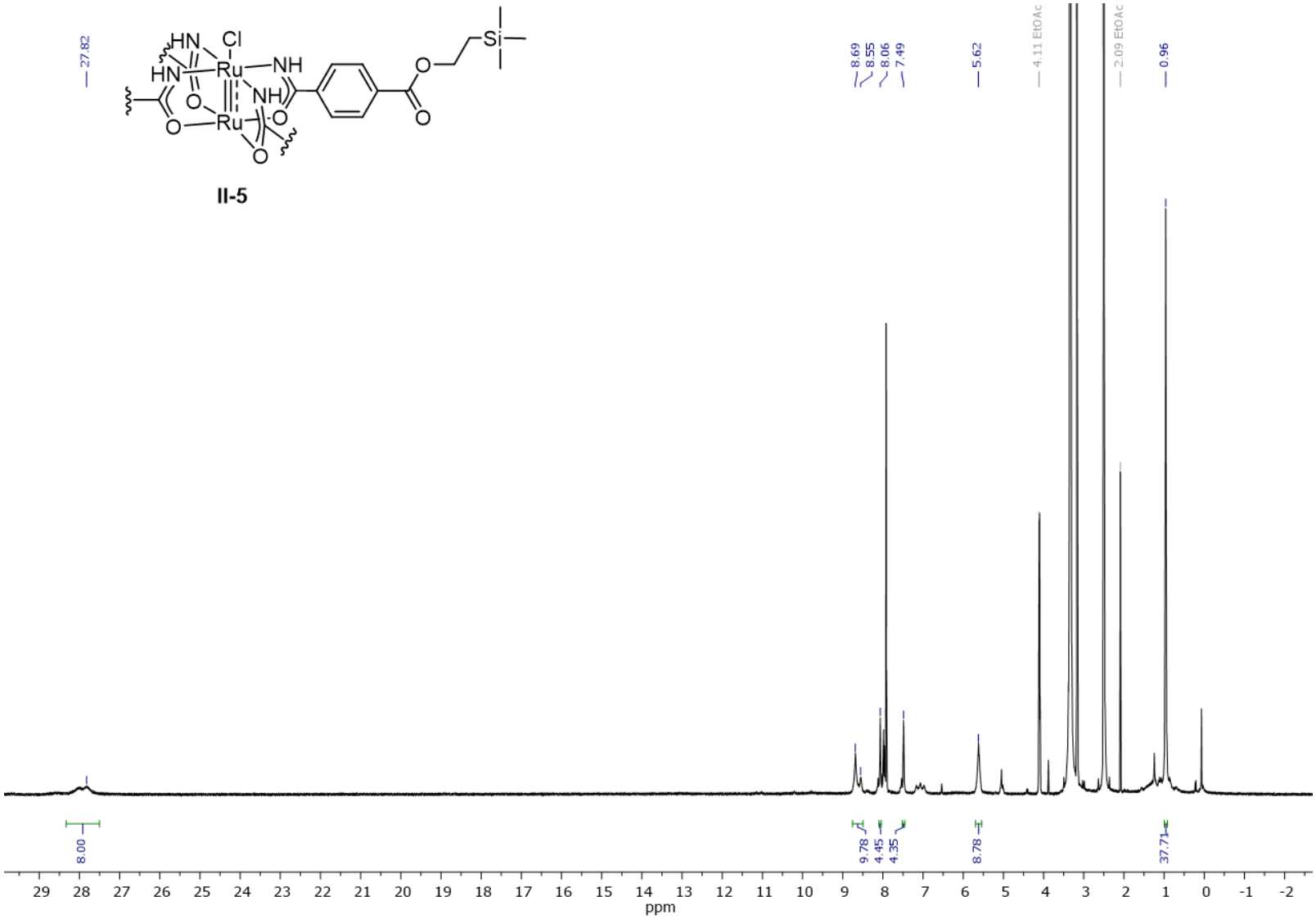

Figure II-13. NMR of II-5 in DMSO-d_6 at 23°C.

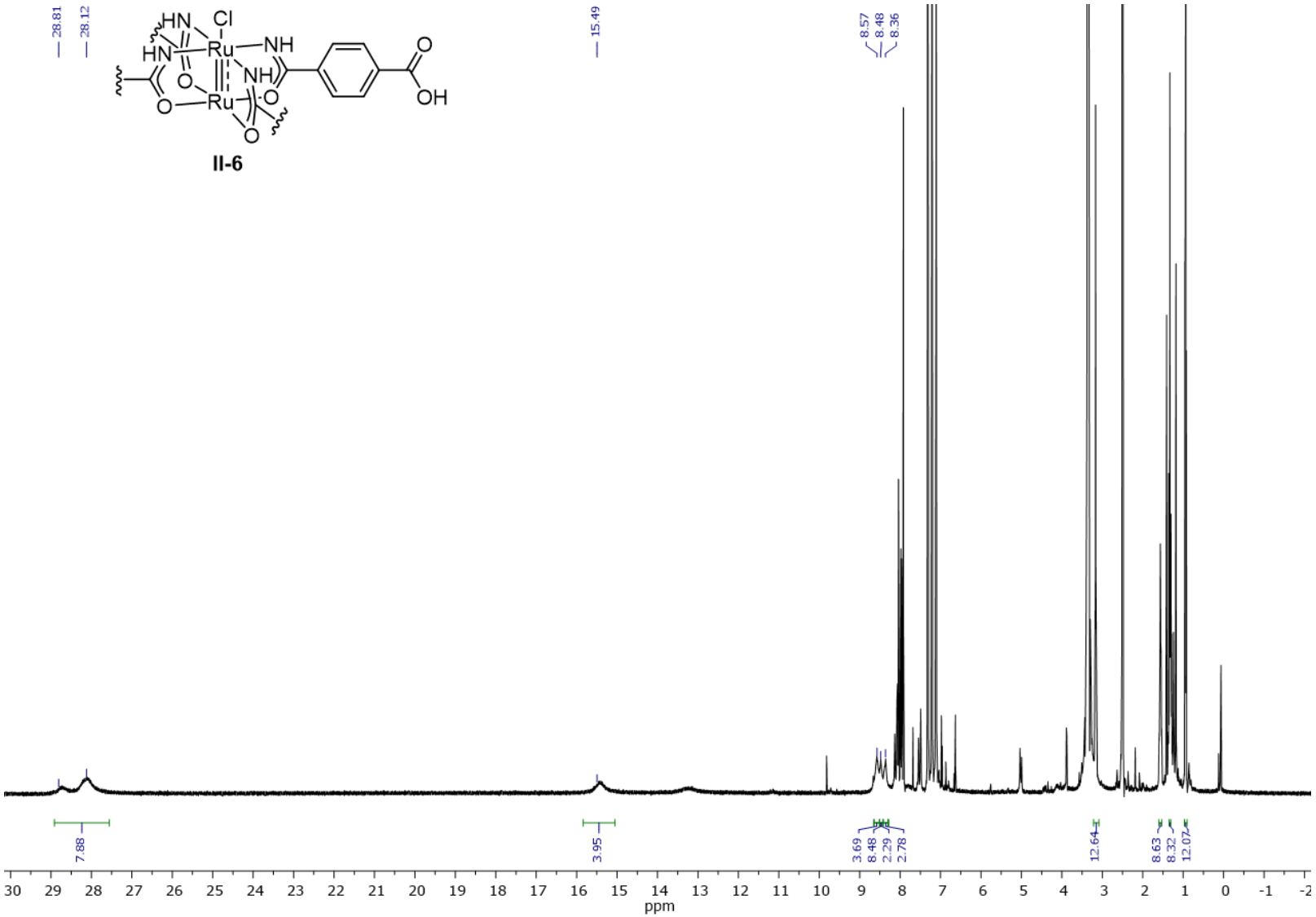

Figure II-14. NMR of II-6 in DMSO-d_6 at 23°C.

CHAPTER III

SYNTHESIS AND PHOTOCHEMISTRY OF RUTHENIUM PADDLEWHEEL BASED THIN FILMS

III.1. Introduction

In the last chapter, we described new heterogeneous platforms to confine reactive intermediates and avoid undesired and unproductive reaction pathways. The evidence for the success of this strategy is circumstantial: While we were not able to directly observe and characterize the putative Ru_2 nitrides generated in these systems,[131, 183, 184] we inferred their intermediacy based on the observations of aminated products and lack of N_2 evolution (Figure III-1).[185, 186] Both of these observations contrast corresponding results with molecular analogues. Unambiguous spectroscopic and structural characterization of lattice-confined Ru_2N species has not yet been accomplished.

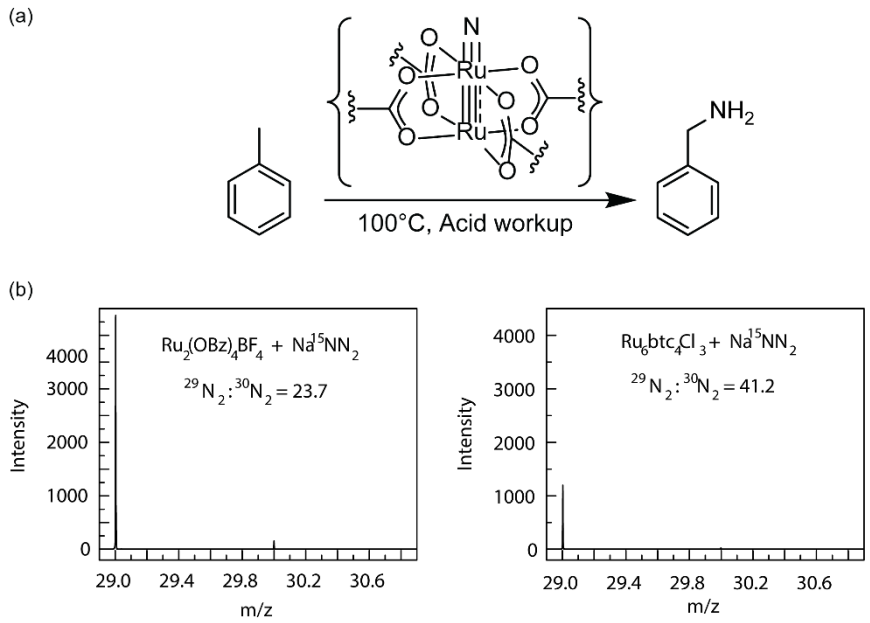

Figure III-1. (a) Reaction scheme for turning toluene into benzylamine via a putative Ru_2 nitride. (b) GC-MS head space analysis of reactions between Ru_2 molecule (left) or Ru_2 material (right) and $Na^{15}NN_2$ shows different $^{29}N_2$:$^{30}N_2$ ratios – $^{30}N_2$ can only be produced via bimolecular combination of ^{15}N. Immobilization in a MOF clearly retards the amount of bimolecular combination of Ru_2N. Data reprinted with permission from reference 186. Copyright John Wiley and Sons.

Dincă and coworkers demonstrated the potential to fully characterize reactive intermediates by isolation within extended lattices by during studies of NO disproportionation at an iron site in Fe-MOF-5.[187, 188] Using diffuse reflectance infrared fourier transform spectroscopy (DRIFTS) they were able to characterize various Fe-NO adducts in the solid state, for which there exists no homogeneous analog. One of the key assumptions made here however is that the surface of the material is acting the same as the bulk of the material, which cannot be assayed by diffuse reflectance techniques. Their assignments are bolstered by additional XAS and Mössbauer data, which were enabled by the relatively long lifetimes of the intermediates of interest. In the case of shorter-lived species (or materials for which Mössbauer is not available), techniques to probe the electronic structure are limited to diffuse reflectance UV-vis (DRUV).

Application of optical methods (both photochemistry and optical spectroscopic tools) is challenging. Penetration depth of visible light into solids is dependent on many factors such as thickness of material, roughness, molar absorptivity, and the wavelength of light.[189-191] For instance, in ZnO the penetration depth of 280–360 nm light ranges from 50 nm to 65 nm.[192, 193] (DRUV) is often used to characterize heterogeneous materials, but the depth to which the material is interrogated is assumed to only be in the immediate vicinity of the surface of the material as the technique inherently relies on scattering.[194] Other methods of spectroscopic interrogation, including X-ray absorption spectroscopy, are available to assay lattice-confined species.[195] As for XAS probes, the lifetimes of reactive intermediates present a significant time mismatch challenge with the time required to obtain a data set.[196]

Chemical vapor deposition is a widely used technique to prepare optically addressable inorganic materials, but the synthetic programmability of these techniques is often limited to *simpler* materials than one can generate via solvent phase self-assembly and is also constrained by the requirement of appropriately volatile precursors.[197-202]

Metal-organic layers offer optically addressable porous architectures with high synthetic programmability.[203] Metal-organic layers (MOLs) can be synthesized via a top-down or bottom-up approach.[204] The top-down methodologies involve synthesizing a MOF via normal solvothermal methods and then breaking the linking elements between layers through some exfoliation procedure. This method can be quite harsh and gives materials of varying thickness and quality. The bottom-up methodologies involve using either capping agents, surfactants, or interfacial synthesis to produce layers of tunable thickness and high quality, but potentially with surface modification of the metal sites due to the presence of capping agents and surfactants.[205] The clear advantages of these techniques are that they produce thin films of materials which are

optically addressable and assayable whereas the bulk materials generated from more traditional solvothermal synthesis conditions are not.

Combining the explicit control over thickness of the bottom-up approach and the bulk fidelity of material provided by the top-down approach would provide a powerful platform to systematically control the thickness and optical transparency of porous thin films. We hypothesized that layer-by-layer (LbL) film growth, based on porous molecular cages and organometallic complexes featuring complementary charge could provide a strategy to access such thin films. LbL growth has been demonstrated for MOFs synthesis, but control over nucleation is an outstanding issue, or the need for anchoring to self-assembled monolayers (which are often not robust under solvothermal conditions) have prevented their broader adoption.[206-208] Many early iterations of LbL platforms involved charged polymers as one component (or both) and a small molecule inorganic complex as the counter ion component (Figure III-2); the resultant films are referred to as polyelectrolyte films.[209-211] Extension to two small molecule components has naturally to give thin films of oppositely charged organometallic complexes.[212]

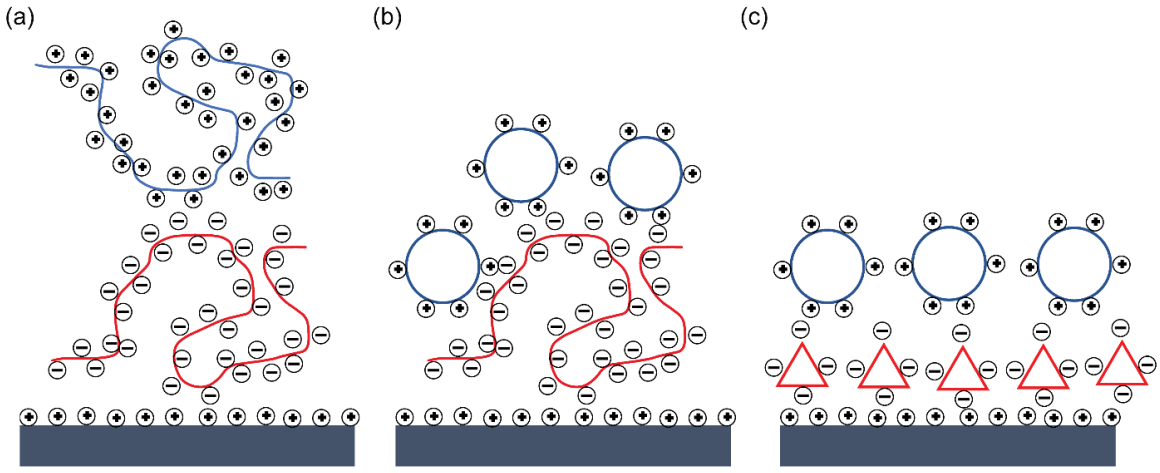

Figure III-2. The LbL synthesis method on a charged substrate. (a) LbL deposition of two charged polymers. (b) LbL deposition of one charged polymer and charged small molecule. (c) LbL film synthesis consisting of two charged small molecules.

In order to address the issue of lack of spectroscopic characterization of our hypothesized Ru_2N unit, we endeavored to synthesize thin films based on the Ru_2 units discussed in the previous chapter. Those molecules contained a carboxylic acid, which after deprotonation, would be a perfect fit for the layer-by-layer film growth using our polyelectrolyte complexes. We chose to use the cage molecule ZrFDCOTf (**III-1**) as the initial material because it is chemically robust and does not absorb in the visible region.[213] Additionally, the cage molecules are inherently porous and thus we hypothesize will allow substrate ingress and egress from the active sites – which is critical to our azide metathesis strategy of accessing Ru_2N intermediates. Herein we describe the synthesis and optical characterization of Ru_2-based thin films from **III-1** and **III-2**. We also demonstrate the optical addressability of these films by performing photoreduction reactions *in situ* and discuss attempts at ligand metathesis inside the materials.

III.2. Results

III.2.1 Synthesis and characterization of Ru_2 thin films

Synthesis of thin films containing **III-2** was accomplished using the layer-by-layer (LbL) deposition method of film growth.[214, 215] Glass slides were initially subjected to plasma treatment in order to clean them, and provide a charged surface from which to anchor charged molecules.[216-222] Starting from solutions of **III-1** and **III-2**, the treated glass slide was first dipped in a MeOH solution of **III-1**, followed by MeOH as a wash, and then the cycle repeated with the corresponding solution of polyelectrolyte (Figure III-3). This generates the film in Figure III-4a, with corresponding UV-vis in Figure III-4b. An overlay of **III-2** in MeOH with the film **III-1-2** shows good spectral agreement with peaks at λ = 373 nm and 435 nm. Wavelength dispersive

spectroscopy measurements indicate a ratio **III-1:III-2** ratio of 2:1, exactly what is expected based on the charge ratio of the two compounds (4^+ charge for **III-1**, and 8^- charge for **III-2**).

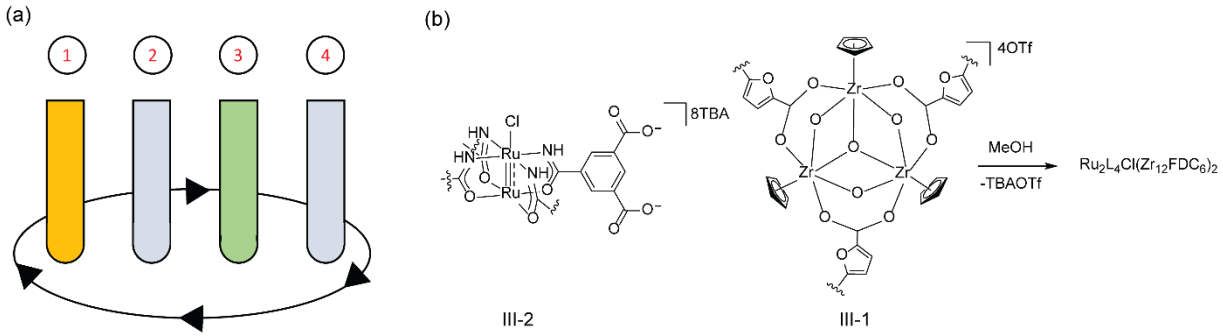

Figure III-3. (a) Schematic of the layer-by-layer synthesis method; a sample is dipped into solutions 1-4 where 1 is a solution of III-1, 3 is a solution of III-2, and 2 and 4 are wash solutions of MeOH. A complete dip sequence of 1-4 is one bilayer. (b) Reaction scheme for synthesizing thin films.

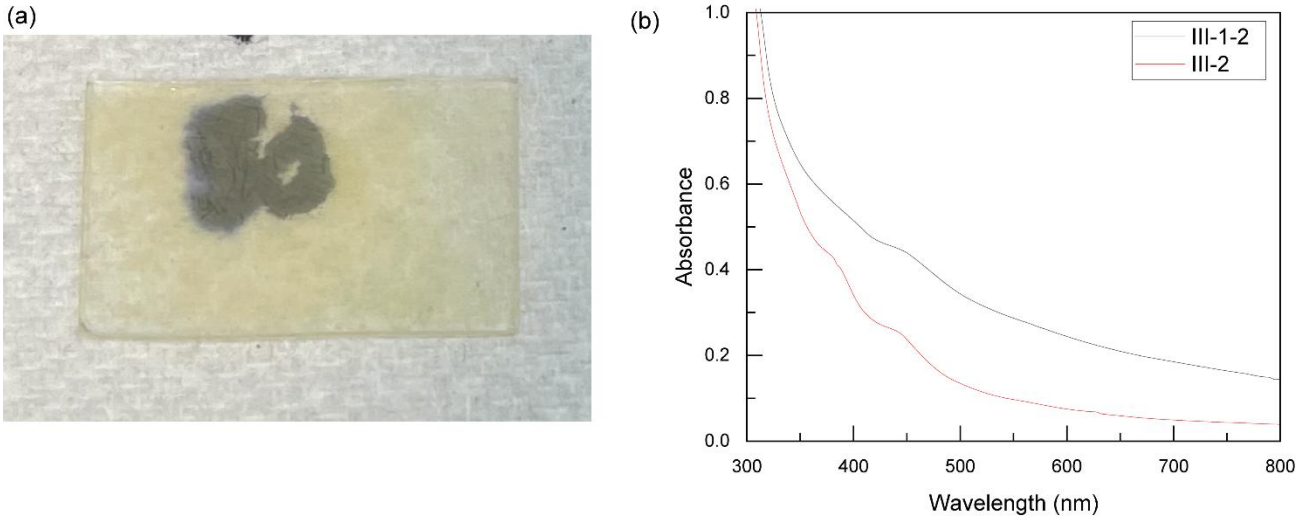

Figure III-4. (a) Optical photograph of thin film III-1-2 after 50 BL at 3 second dips. The film is yellow in color and optically transparent. (b) UV-vis of III-2 and the thin film of III-1-2.

Our goal was to develop thin films which would still be optically addressable; in order to accomplish this, we screened a system of variables including concentration of polyelectrolyte, dip time per solution, bilayer number (BL #), and presence of a drying step.

To assess the effect of time in solution on thickness, ellipsometry was employed on thin films of **III-1-2** (Table III-1) which were synthesized by hand. The times screened were 3, 10, and 15 seconds per solution with samples measured at 50 bilayers and solution concentrations of 2 mg/mL. The average thickness for 3 s dips was 208 ± 43 nm and average roughness was 12 nm. For 10 s dips the average thickness was 156 ± 4 nm and the average roughness was 17 nm. For 15 s dips the average thickness was 154 ± 5 nm and the average roughness was 4 nm. This data suggests that 3 s dip times led to the thickest films while increased dip time led to less rough films. An additional film was made with 3 s dip time at 50 bilayers, but the concentration was increased to 10 mg/mL and the resulting film thickness was 345 ± 102 nm.

Table III-1. Thickness measurements on films of III-1-2, varying by dip time measured at 50 bilayers and solution concentrations of 2 mg/mL. Error is reported as standard error; measurements are repeated 20 times to generate error.

Time of dip	Spot #	Thickness (nm)	Roughness (nm)
3 s	1	247 ± 2	9
	2	243 ± 3	178
	3	217 ± 2	14
	4	229 ± 2	17
	5	194 ± 2	9
	6	119 ± 2	4
10 s	1	159 ± 30	17
	2	152 ± 64	18
	3	148 ± 52	15
	4	151 ± 58	18
15 s	1	158 ± 4	3
	2	158 ± 6	7
	3	152 ± 6	4
	4	159 ± 4	3
	5	145 ± 12	4

Our goal was to synthesize films which would be desirable for use in photochemistry. We speculated that the optimal samples of **III-1-2** for photochemistry would have thicknesses of, or about, 500 nm based on the optical density and be as smooth as possible; we hypothesized that the

large baseline observed in the UV-vis profiles in these systems were a direct result of light scattering due to roughness in the sample (Figure III-4b). To meet these metrics, greater understanding of the film growth process was needed, and as such we carried out a striping experiment. We synthesized two films, one with drying and one without, using **III-1** and **III-2** on a robot platform to generate well-defined zones to characterize.[223]

Figure III-5a shows the two striping samples. The samples were prepared with 5 dipping zones, ranging from 10-50 bilayers. Each of the dipping zones of interest is separated by a yellow band, which is a mixing layer known as the wetting zone where the wet film starts but is not of a constant thickness.[224] The bands seen in Figure III-5a appear brown visually upon aging; when initially synthesized they appeared yellow, which is consistent with **III-2** in solution (see Figure III-4b). Profilometry data on the two samples is displayed in Table III-1. Including a drying step between dips led to increased thickness of bilayers and increased roughness as compared to the absence of a drying step. For the sample with an included drying step, the growth trend is linear with a slope of 13 nm/BL (Figure III-5b).

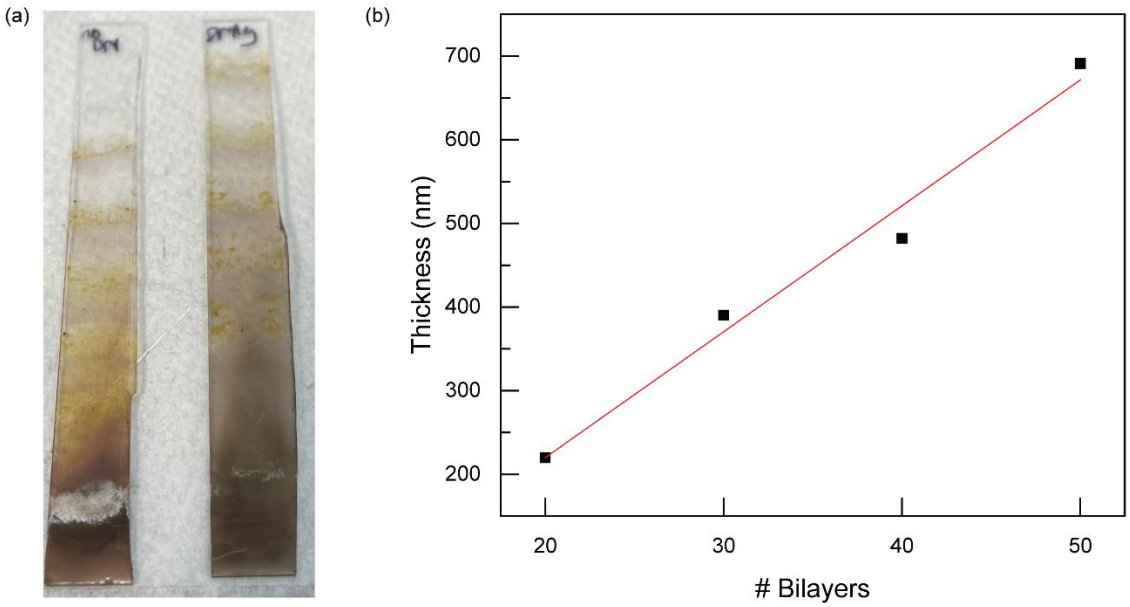

Figure III-5. (a) Samples produced via striping experiment from 0–50 bilayers at 15 s dips. Solution concentration was 10 mg/mL. Sample produced without drying is on the left, with drying is on the right. (b) Plot of thickness vs. Bilayer count for sample with drying.

Table III-2. Thickness and roughness measurements of thin films produced from striping experiment – with and without drying.

	Without Drying		With Drying	
# Bilayers	Thickness (nm)	Roughness avg. (nm)	Thickness (nm)	Roughness avg. (nm)
20			220	72
30	119	37	390	58
40	215	30	482	67
50	366	38	691	53

We sought to further characterize the surface of the films to gain insight into the growth mechanism and obtained SEM images of both films synthesized in Figure III-5a. Figure III-6

shows the SEM images obtained on both samples; images were taken of areas of 10 and 40 bilayers.

25× magnification images of 10 bilayers with drying (Figure III-6a) shows smooth surface features with small clusters of nucleation. Figure III-6b shows an image of the sample with drying and shows slight cracking in the surface. Figure III-6c shows a still relatively smooth surface at 40 bilayers at 100× magnification. Figure III-6d shows the image of 40 bilayers with drying and indicates significant surface clusters and surface defects which is consistent with higher surface roughness observed (Table III-2). These images suggest that even at 10 BL, there is little island growth and the film is growth in a layer-by-layer fashion. Also with drying the cracking appears to be a long-range phenomenon and not visible on the ~10 nm scale; visible cracks are large however, appearing to be 100s of microns in length.

25× magnification images of 10 bilayers without drying (Figure III-6e) show several small clusters of nucleation, consistent with our inability to obtain reliable profilometry data from these samples. An image (Figure III-6f) reveals a virtually featureless surface. 50× magnification images of the same sample at 40 bilayers show small cracks (Figure III-6g) without major features, and an image (Figure III-6h) of the same spot showcases a largely smooth surface with clusters of elevated growth or imperfections, which is consistent with the data in Table III-2. The samples produced without drying are significantly smoother, with far less imperfections in the surface, but are thinner. We hypothesize that the drying step is physisorbing material to the surface, thereby resulting in greater thickness, and also greater roughness as nucleation is not uniform.[225-227] In films where drying is excluded, this physisorption process is less significant, leading to thinner and smoother films.

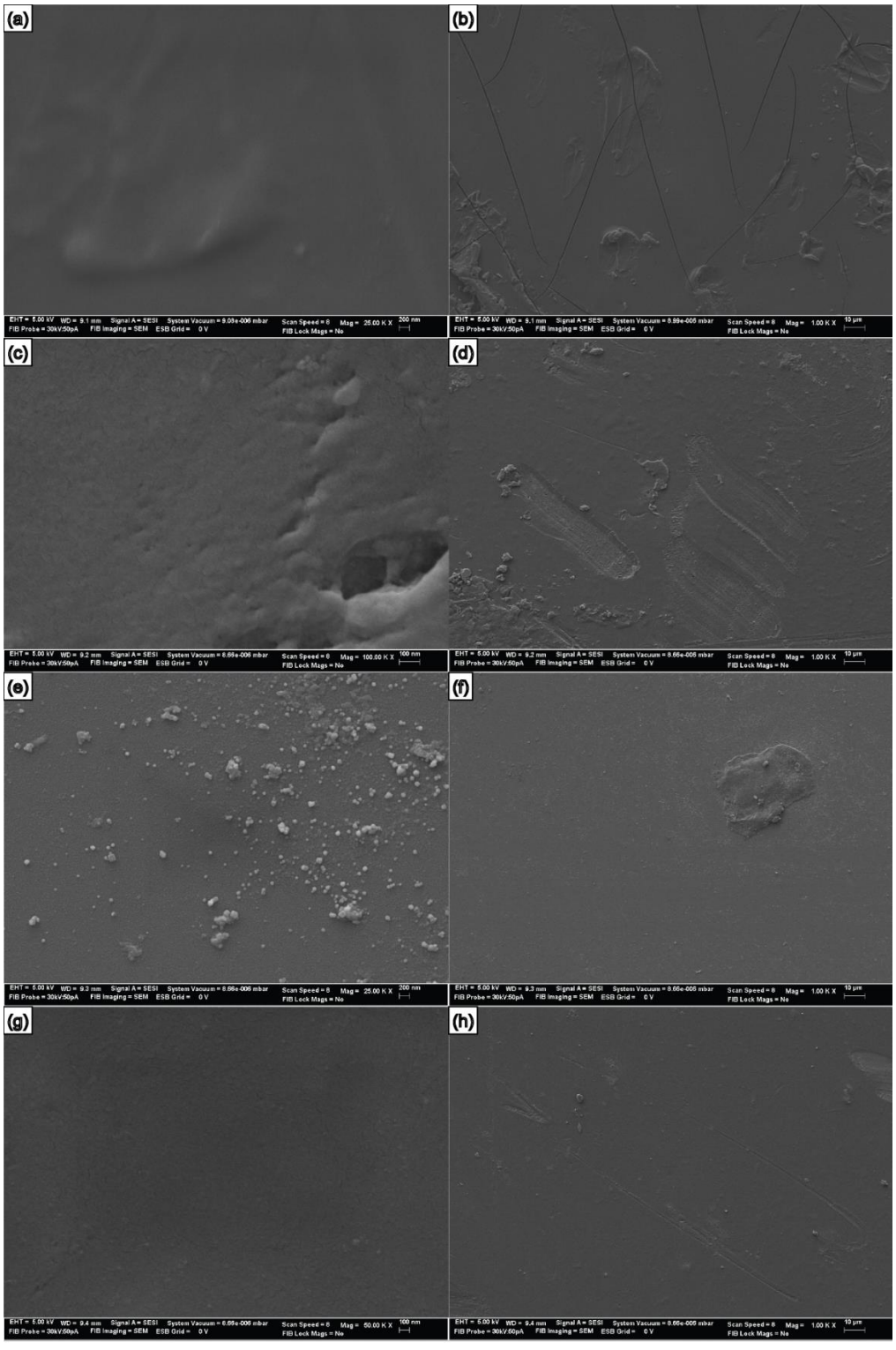

Figure III-6. (a) 10 BL with drying at 200 nm scale bar. (b) 10 BL with drying at 10 µm scale bar. (c) 40 BL with drying at 100 nm scale bar. (d) 40 BL with drying at 10 µm scale bar. (e)

10 BL without drying at 200 nm scale bar. (f) 10 BL without drying at 10 µm scale bar. (c) 40 BL without drying at 100 nm scale bar. (d) 40 BL without drying at 10 µm scale bar.

We additionally synthesized two samples of 20 bilayers each with washing time extended to 1 min (with and without drying) and of 50 bilayers which was aged before imaging to examine how the film topography would be affected. Figures III-7a and III-7b show the samples at 20 bilayers with greater wash time and shows significant surface buildup, indicating that increased washing time is not affecting film growth. Figure III-7c shows the thin film with drying at 50 bilayers, aged at 3 days, which shows large and varied surface buildup, and figure III-7d showcases the significant cracking of the surface. This cracking phenomenon leads to the increased scatter and darkening of color observed in the samples in Figure III-6a.

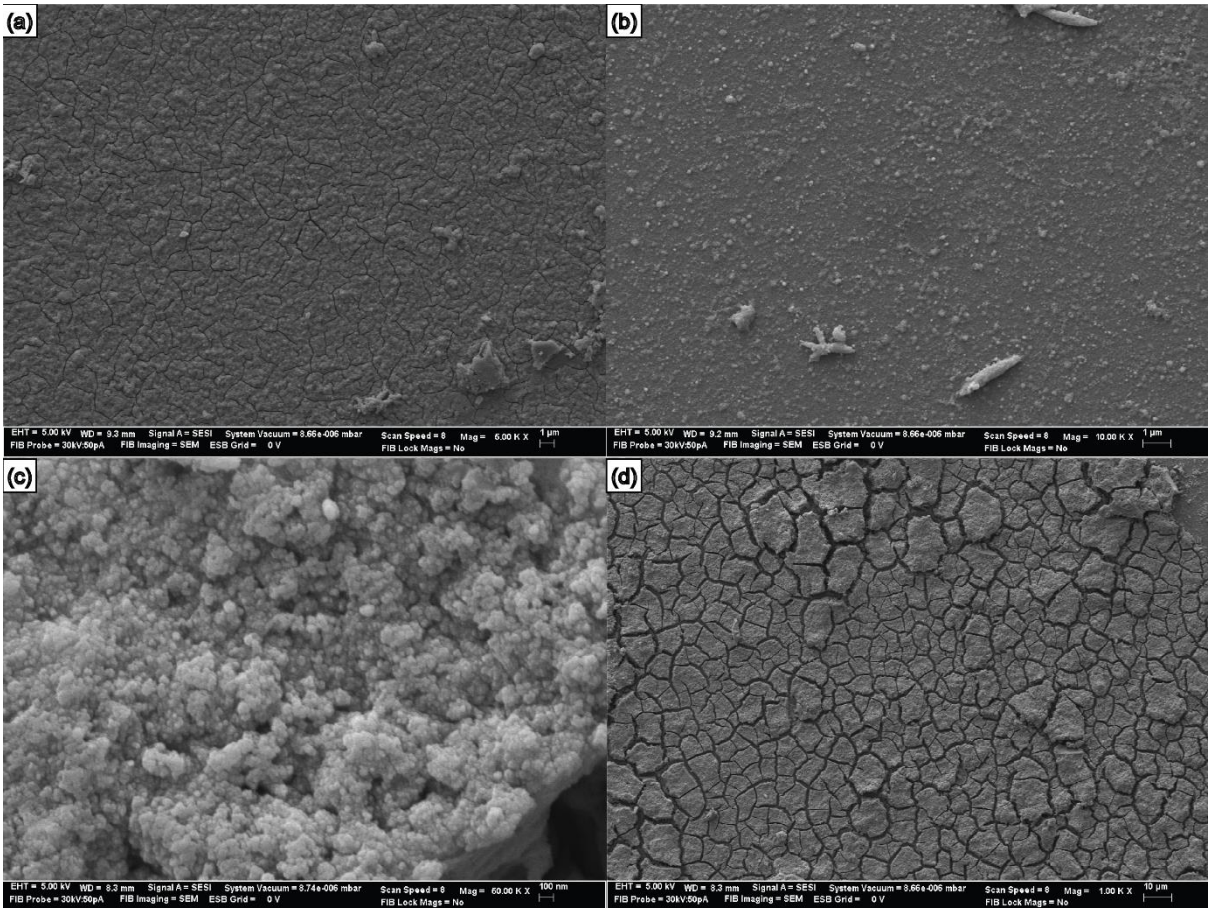

Figure III-7. (a) 20 BL with extra wash time and drying at 1 µm scale bar. (b) 20 BL with extra wash time and without drying at 1 µm scale bar. (c) 50 BL with drying at 100 nm scale bar. (d) 50 BL with drying at 10 µm scale bar.

III.2.2 Ligand metathesis of Ru_2 based thin films and photolysis attempts

We sought to investigate the potential for ion metathesis within optically transparent thin films (*i.e.*, **III-2-Cl**) to access Ru_2N_3-containing thin films. To this end, we soaked thin films of **III-2-Cl** in aqueous solutions of NaN_3; the resulting UV-vis traces are pictured in Figure III-8a. The only change observed in the UV-vis is an increase in the baseline of the sample. Apical ligand metathesis in Ru_2 systems is known to affect changes in the UV-vis spectrum;[131] the observation that no significant spectral changes were observed suggested that no reaction occurred. N_3^- for Cl^-

exchange could also be evaluated by IR spectroscopy, however the SiO_2 substrate the films are grown on absorbs light in the infrared region completely, preventing IR measurements of films grown on this substrate.

We opted for an alternate synthesis route to attempt azide metathesis and synthesized a film of **III-2-BF_4**. We soaked the film in a THF solution of $TMSN_3$; Figure III-8b shows the spectral change over 5 h. The spectral changes are subtle, being characterized by slight increases in ε and a broad hump extending from ~430 nm to ~460 nm. Photolysis of this sample with a 335 nm long pass filter in THF for extended periods of time yields no change in the UV-vis (Figure III-8c). We hypothesize that these results indicate that instead of metathesis, the Ru_2 center is reduced by 1 electron to generate a Ru_2(II,II). An overlay of the photoreduction of a film of **III-2-Cl** with the $TMSN_3$ treatment of a film of **III-2-BF_4** indicates the product of these reactions is the same (Figure III-8d).

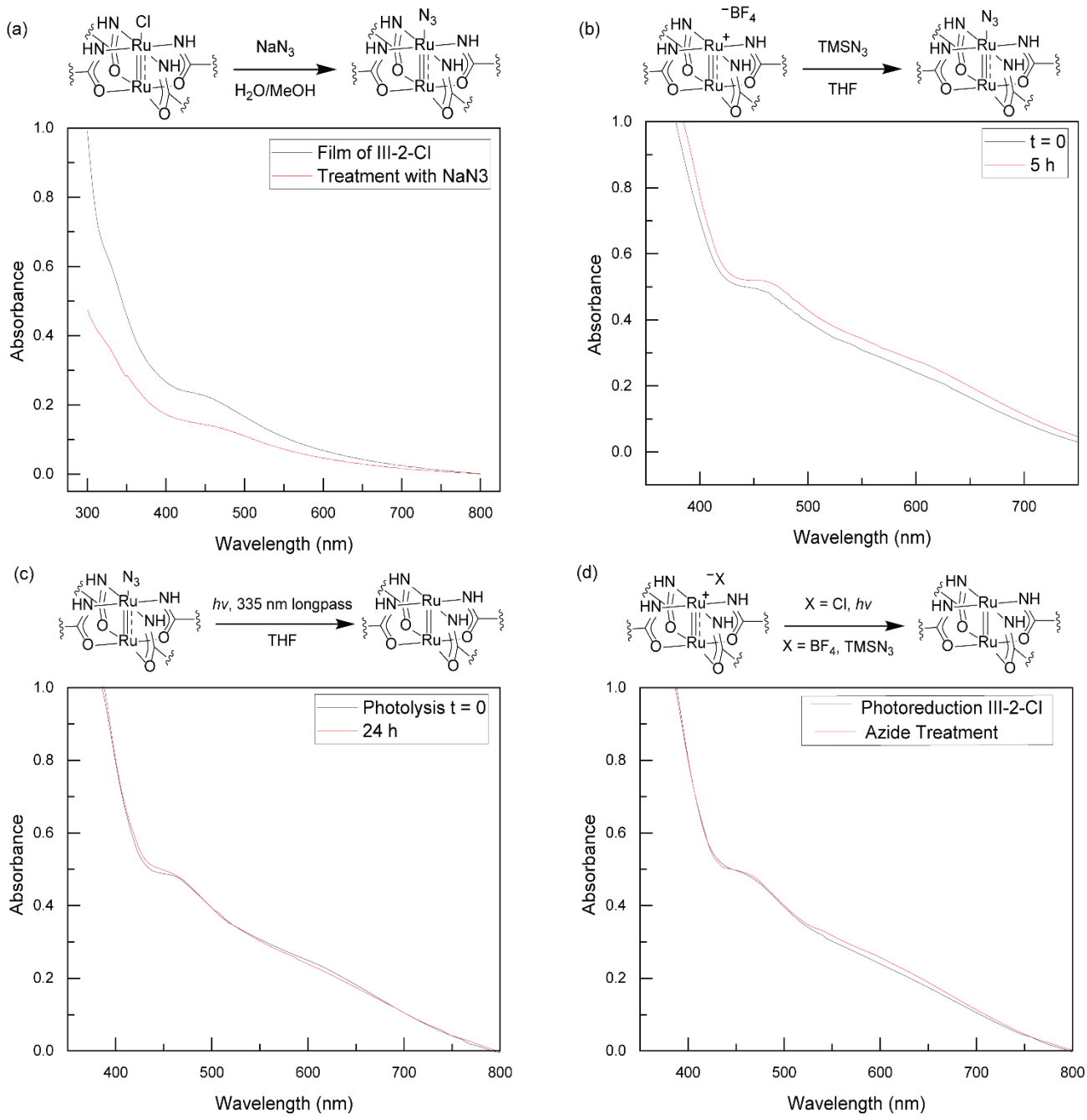

Figure III-8. (a) Treatment of III-2-Cl with a solution of NaN_3 yields minimal spectral changes except for a decrease in background, which could be indicative of leaching into solution. (b) Treatment of III-2-BF_4 with $TMSN_3$ shows only a slight broadening of the peak at 437 nm. (c) Photolysis of azidated films yields no change. (d) Overlay of spectra of the photoreduction of III-2-Cl and the $TMSN_3$ reaction with III-2-BF_4 indicates the product is the same.

III.3. Discussion

In order to understand the photoreduction chemistry of our Ru_2 films, we turned to the precursor complex **III-3** to observe its photochemical behavior. Photolysis of **III-3** in THF (Figure III-9a) shows little change in the spectral profile except for an increase in absorbance and a broadening of the absorbance feature centered around 463 nm. It was hypothesized that the spectral change can be attributed to photoreduction of the Ru_2 unit to give **III-4**, concomitant with extrusion of $Cl^{\bullet}$. Additionally, the photogenerated solution of **III-4** was exposed to O_2 to reoxidize **III-4**; the transformation is shown in Figure III-9b. The peaks at 452 nm are consistent with a II,II oxidation state at Ru_2, indicating that O_2 does not reoxidize the photoreduced compound **III-4**. **III-4** was independently synthesized, and the spectra are compared in Figure III-9c.

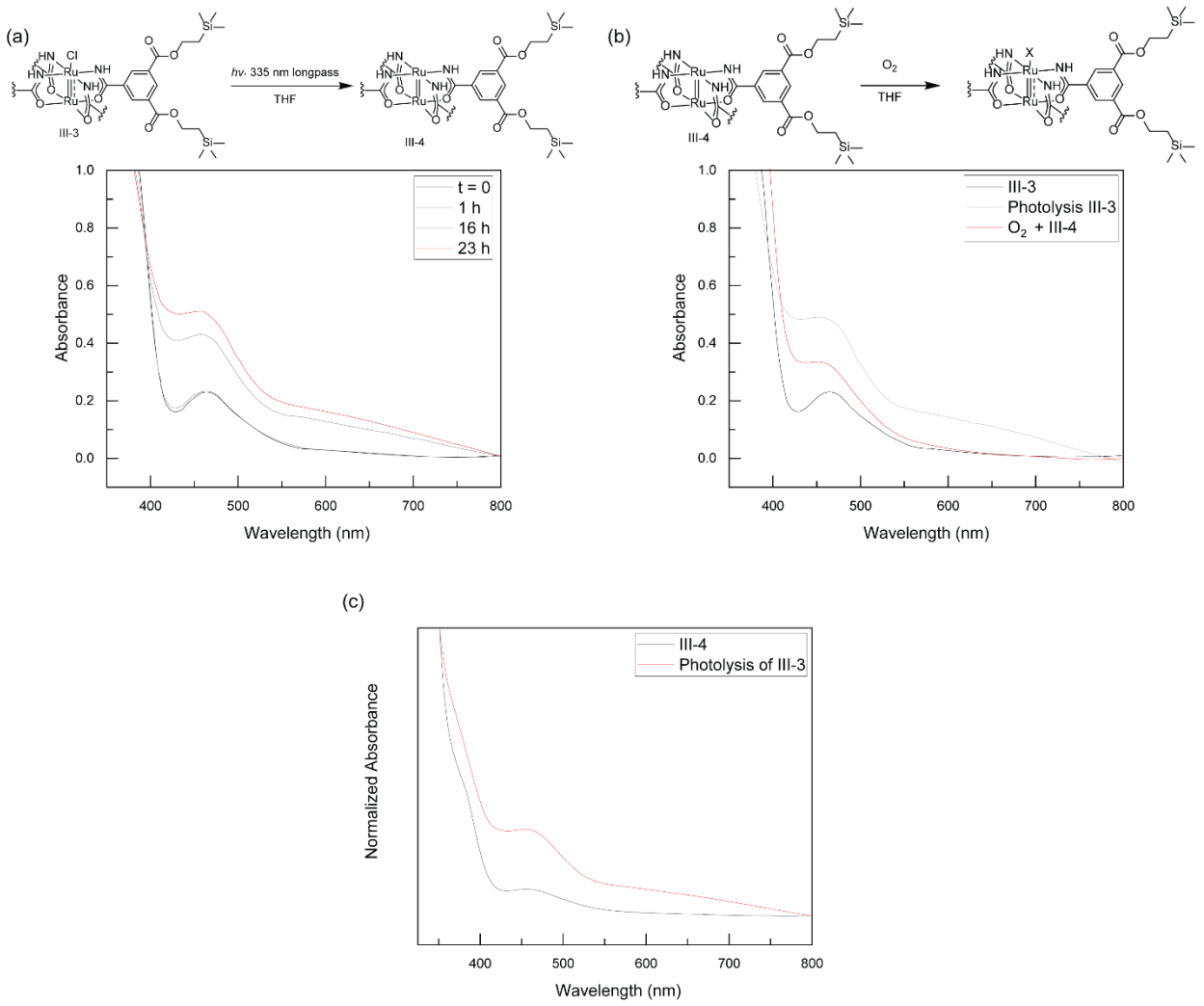

Figure III-9. (a) Time resolved photoreduction of compound III-3 in THF. (b) Exposure of III-4 to O_2 results in the spectral changes observed, which we hypothesize is consistent with oxidation from a (II,II) to a (II,III) system. (c) Overlay of photoreduction of III-3 and independently synthesized III-4. Peak positions at 456 nm match.

We performed analogous photochemistry with complex Ru_2esp_2Cl to ascertain the effect that changing the primary coordination sphere would have on the photochemical behavior. Photolysis of a THF solution of Ru_2esp_2Cl yields the one-electron reduced **III-5** (Figure III-10a). The obtained UV-vis spectrum overlays that of independently synthesized **III-5**, with peaks at 300 nm and 443 nm (Figure III-10b). Exposure of **III-5** to O_2 shows a regaining of spectral features

associated with Ru_2esp_2Cl, but does not overlay, indicating the identity of the apical anion is not Cl but instead maybe OH (Figure III-10c). This behavior is also observed for Ru_2OPiv_4Cl (Figure III-10d).

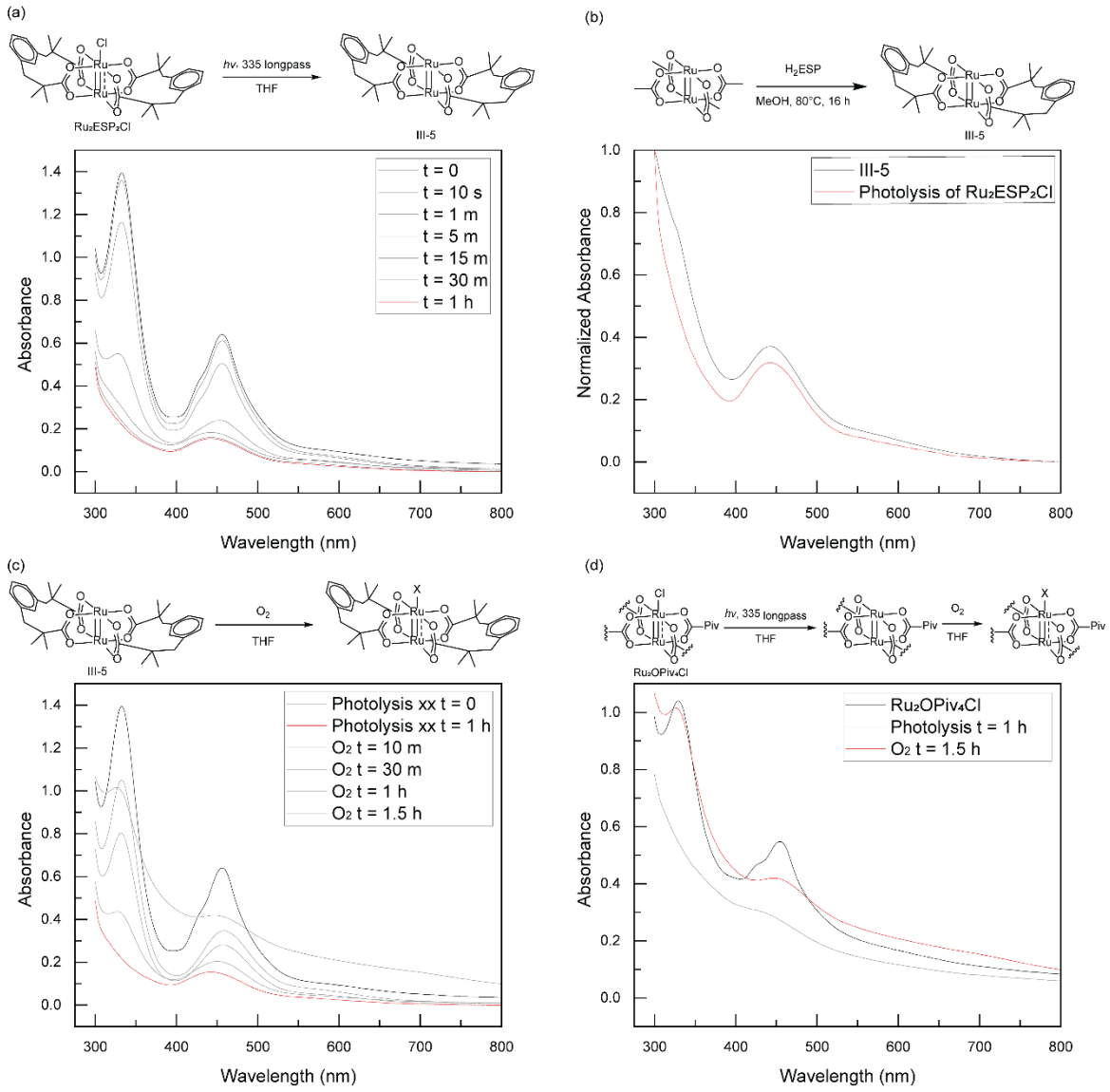

Figure III-10. (a) Photolysis of Ru_2esp_2Cl using a 335 nm long pass filter in deoxygenated THF affords III-5. (b) Independently synthesized III-5 shows excellent spectral agreement with the product of photoreduction of III-5. (c) Reaction of III-5 with O_2 leads to spectral evolution consistent with 1 e^- oxidation. The apical ligand after oxidation is unknown. (d) Analogous experiments with Ru_2OPiv_4Cl show similar behaviors.

We also sought to synthesize films of **II-3** and **III-6** with **III-1**. Attempts to deprotonate **II-3** with either TBAOH or NEt_3 resulted in decomposition of the dimer unit as evidenced by the disappearance of peak centered at δ = 31.3 ppm in the ^1H NMR, which is diagnostic for carboxylate-bridged Ru_2[II,III] complexes (Figure III-11). Attempts to deprotonate **III-6** with TBAOH in MeOH resulted in the evolution of absorbances centered at 331 nm and 476 nm (Figure III-12). Over 4 h the feature at 476 nm disappears while the peak at 331 nm increases in intensity, which we interpreted as slow decomposition of the Ru_2 core as the low energy feature is attributed to M–M transitions in the M–M bonding manifold. We also synthesized a film from **III-6** using NEt_3 as a base (Figure III-13) but the film generated is broad and featureless, which does not give any information as to the integrity of the Ru_2 unit.

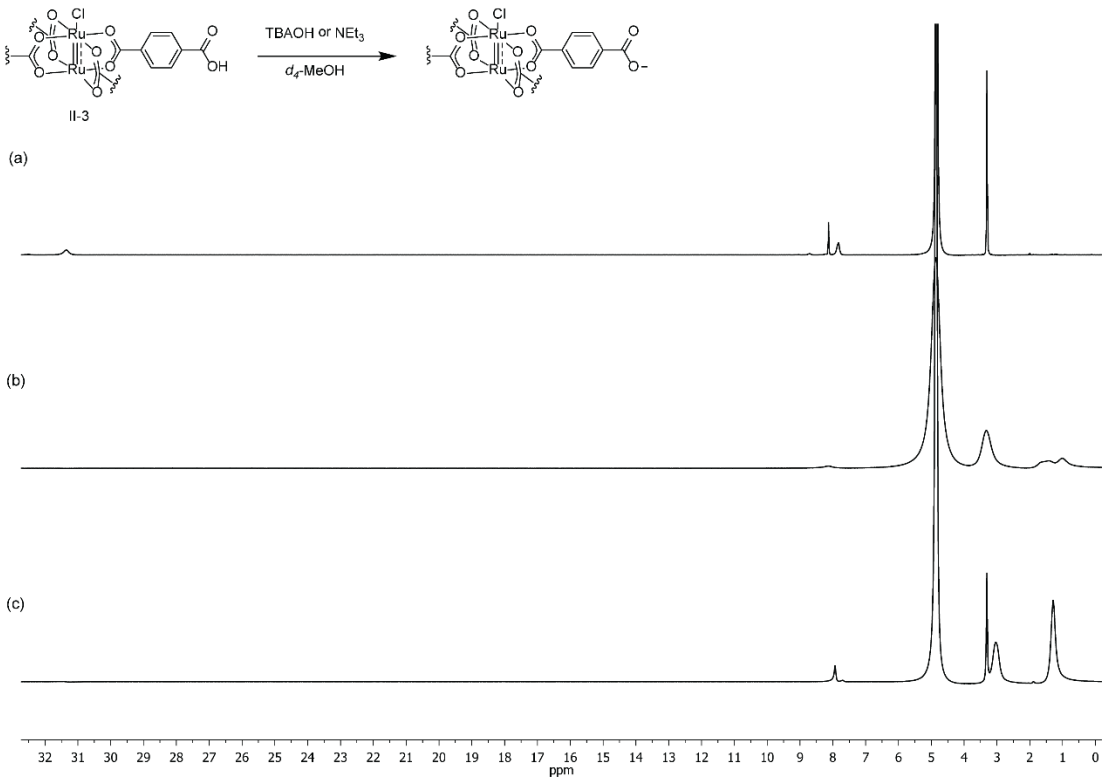

Figure III-11. Deprotonation of compound II-3 using either TBAOH or NEt_3 in d_4-MeOH results in decomposition of II-3 as ascertained by the disappearance of the reported peak at δ = 31.3 ppm, which corresponds to the ortho protons of the phenyl ring. (a) No base added. (b) TBAOH (4 eq.) added, spectrum recorded 2 m after injection. (c) NEt_3 (4 eq.) added, spectrum recorded 5 m after injection.

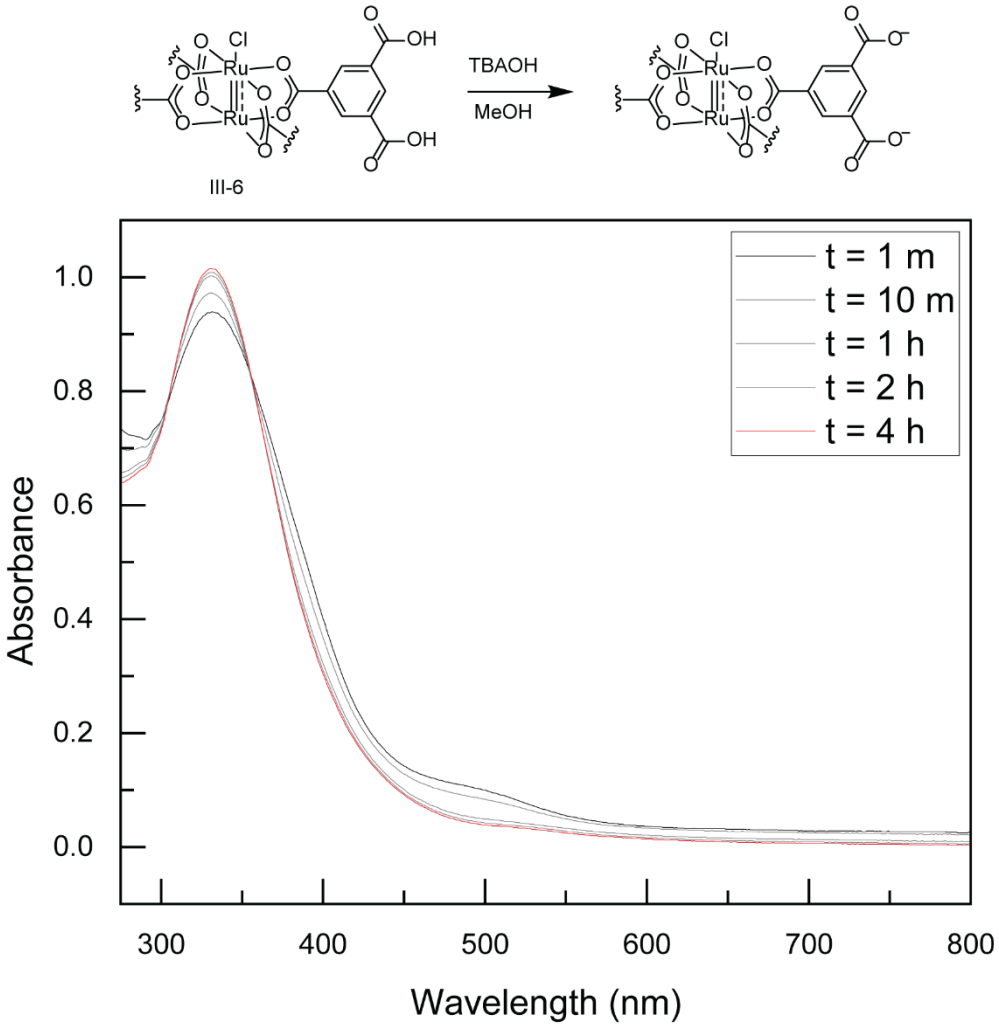

Figure III-12. Time-dependent UV-vis of reaction between *III-6* and TBAOH in MeOH. The spectral feature at 331 nm increases over a 4 h period, while the feature at 476 nm disappears. We attribute this to decomposition of the paddlewheel motif, in conjunction with observed NMR data in Figure III-11.

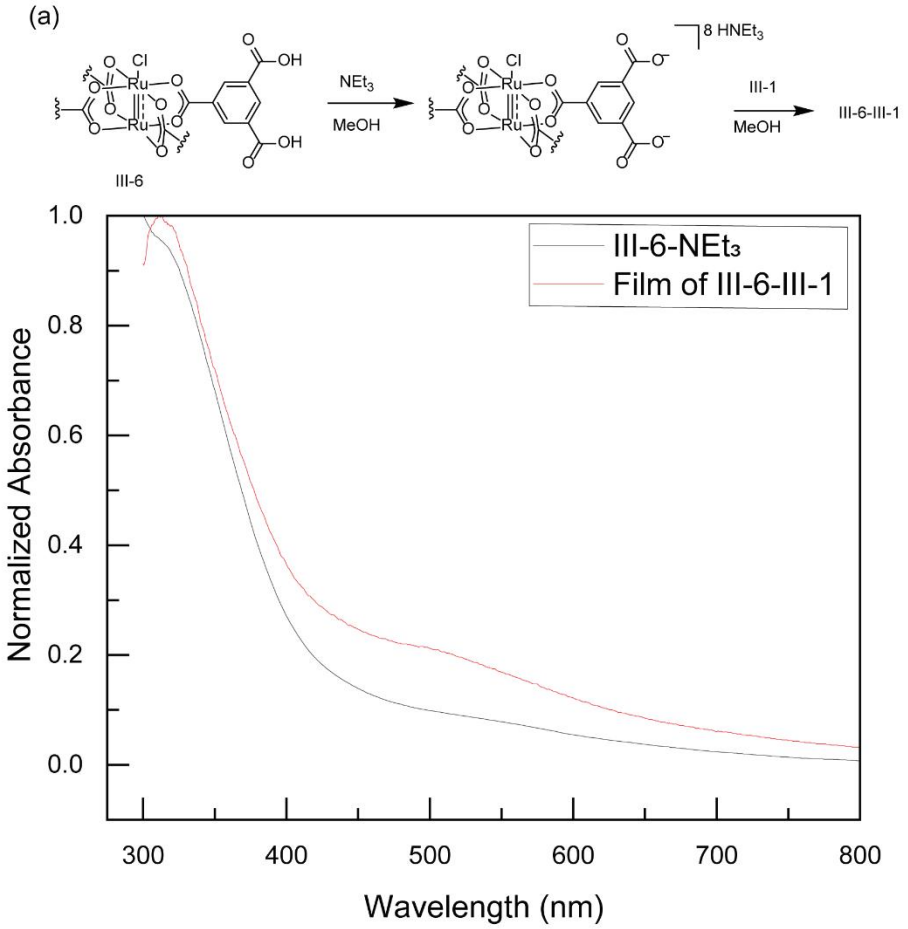

(b)

Figure III-13. (a) Reaction scheme to produce films of III-6 and UV-vis with III-6 and III-6-III-1 overlaid. (b) Optical photograph of film of Ru_2BTC_4Cl after 50 bilayers.

III.4. Conclusion

In this section we demonstrated the synthesis and characterization of thin films of **III-1** and **III-2**, synthesized by the LbL method. This resulted in films with programmable thicknesses which were optically transparent. The films are also chemically addressable, as evidenced by the sequential photoreduction and aerobic re-oxidation, which leveraged but the optical transparency and the porosity, respectively. We had originally developed these films to characterize a hypothesized transient Ru_2 nitride which was competent for C–H insertion, but the specific Ru_2 molecules (**III-2-Cl and III-2-BF$_4$**) we utilized were either unreactive towards substitution when using NaN_3 or reduced when using $TMSN_3$.

We used these molecules because they provided facile synthetic access to a deprotonated carboxylic acid motif, which is required for synthesizing films. NMR and UV-vis data presented in this chapter demonstrate that access to deprotonated carboxylic acids of our Ru_2 molecules is highly structure dependent. Efforts are still ongoing in our labs to find amenable synthetic conditions to produce thin films from **II-3** and **III-6**. We hypothesize that access to films of these molecules will give different results upon apical ligand metathesis with azide and further allow access to the nitride we invoke in reaction chemistry.

We are also interested in using these platforms for low temperature UV-vis spectroscopy. The electronic configuration of Ru_2^{5+} systems is dependent on the ambient temperature (Figure 14), and magnetic measurements of several of these molecules indicates spin-crossover events occurring at low temperatures.[228, 229] We would like to pair electronic absorption measurements to these reported spin crossover events. Additionally, the amide complexes (**II-6** and **II-10**) have not been explored like formamidinate or carboxylate complexes.

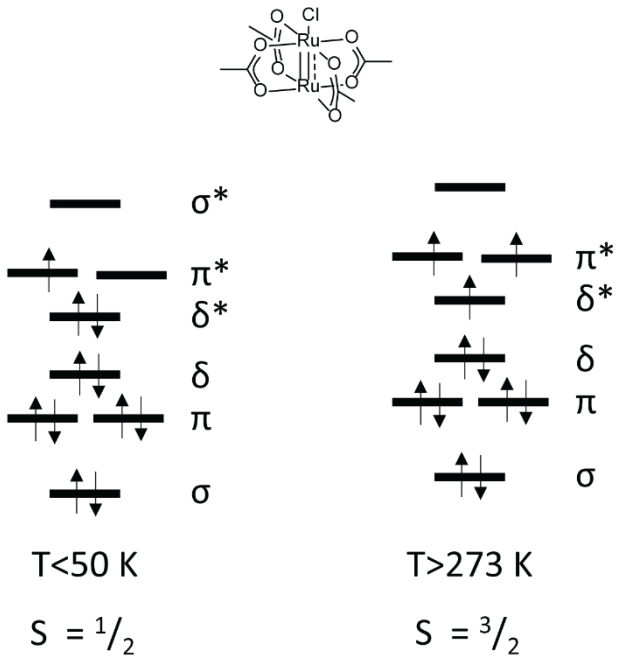

Figure III-14. Electronic configurations of Ru_2OAc_4Cl at low temperature and high temperature. Below 50 K, the molecule is S = ½, and above 273 K is S = $^3/_2$. The δ^* and π^* orbitals are close in energy, which enables spin crossover as a function of temperature.

III.5. Experimental Details

III.5.1 General Considerations

Materials

All reactions were carried out under ambient conditions unless stated otherwise. Solvents were obtained as ACS reagent grade. All chemicals and solvents were used as received unless noted otherwise. Glass slides were obtained from Environmental Monitoring Systems. Ruthenium chloride ($RuCl_3 \bullet xH_2O$) was obtained from Pressure Chemical. Acetic anhydride, toluene, tetrahydrofuran (THF), isobutyronitrile, n-butyl lithium, hexanes, methanol (MeOH), ethyl acetate (EtOAc), chloroform ($CHCl_3$), and acetic acid (AcOH) were obtained from Sigma Aldrich. Ethylene glycol and hydrochloric acid (HCl) were obtained from VWR. Pivalic acid,

tetrabutylammonium hydroxide (TBAOH, 37% in MeOH), bis(cyclopentadienyl) zirconium dichloride ($ZrCp_2Cl_2$), and lithium acetate were obtained from TCI. Platinum dioxide and trimethylsilyl azide ($TMSN_3$) were obtained from Alfa Aesar. Silver tetrafluoroborate ($AgBF_4$), triethyl amine (NEt_3), chlorobenzene, xylylene dibromide, and sodium azide (NaN_3) were obtained from Beantown Chemical. Silver trifluoromethanesulfonate (AgOTf) and furan-2,5-dicarboxylic acid (FDC) were obtained from Ambeed. *N*,*N*-dimethylacetamide (DMA) was obtained from Oakwood. Celite 545 and silica gel (0.060–0.200 mm, 60 Å for column chromatography) were obtained from Acros Organics. Diisopropylamine, was obtained from Fischer Scientific. Sodium hydroxide and sodium sulfate were obtained from EMD Millipore. Hydrogen gas was obtained from Airgas. NMR solvents were purchased from Cambridge Isotope Laboratories and were used as received. H_2ESP,[230] $Ru_2(OPiv)_4Cl$,[231] Ru_2BTC_4Cl (**III-6**)[117] and $[Zr_{12}(\mu_3\text{-}O)_4(\mu_2\text{-}OH)_{12}(Cp)_{12}(FDC)_6]OTf_4$ (**III-1**)[213] were prepared according to literature procedures.

Characterization Details

NMR spectra were recorded on a Bruker Ascend 400 operating at 400.13 MHz for ^1H and 376.36 MHz for ^{19}F or a Varian NMRS 500RM operating at 500.13 MHz for ^1H and 470.41 MHz for ^{19}F. Spectra were referenced against solvent signals: CD_3OD (3.31 ^1H), DMSO-d_6 (2.50 ppm, ^1H), and benzotrifluoride (–63.72ppm, ^{19}F).[177] ^1H and ^{19}F NMR data are reported as follows: chemical shift (δ, ppm), (multiplicity: s (singlet), d (doublet), t (triplet), m (multiplet), br (broad), integration). UV-vis spectra were recorded on a Shimadzu 2501PC spectrometer with DH UV-vis-NIR light source (190–900 nm). Scanning electron microscopy images were acquired using an Auriga 60 CrossBeam at 15kV. Film thickness measurements were obtained using either a KLA-Tencor P-6 Stylus profilometer or an Alpha-SE Ellipsometer equipped with 623.8nm laser. WDS measurements were obtained using a Cameca SXFive electron microprobe using a LaB_6 source.

Glass Slide Preparation

Glass slides were rinsed with DI H_2O followed by MeOH and dried with compressed air. Slides were then subjected to plasma treatment for 5 minutes using ATTO plasma cleaner (Diener Electronic). Glass slides were used immediately after plasma treatment.

Photochemistry Details

Samples were photolyzed under an N_2 atmosphere using an Ushio 100-watt Hg bulb with a Nikon HBO 100-watt power supply. Spectral output ranges from 320-800 nm; a 335 nm long pass filter from Thor Labs was used to filter the light source.

III.5.2 Synthesis and Characterization

Synthesis of III-1

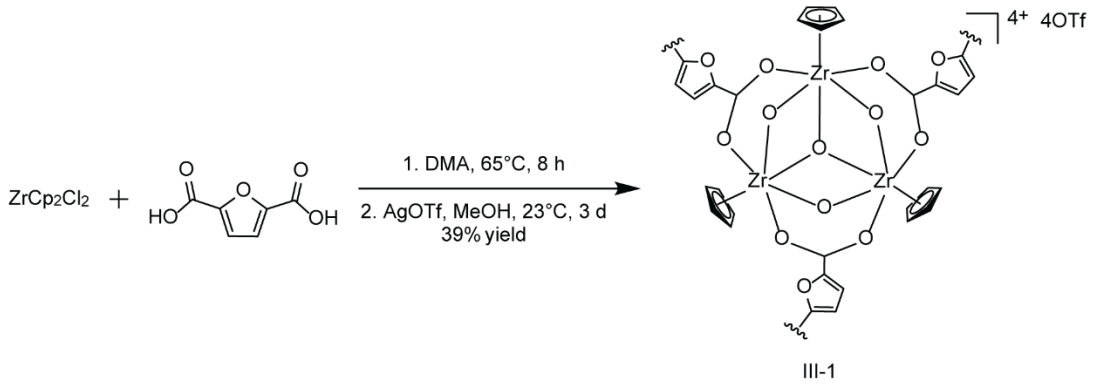

III-1

A 20-mL scintillation vial was charged with $ZrCp_2Cl_2$ (0.350 g, 1.20 mmol, 1.99 equiv), 2,5-furandicaboxylic acid (0.094 g, 0.60 mmol, 1.00 eq), and DMA (20 mL) and sonicated until dissolution. The resulting solution was split between two 20-mL scintillation vials, and water (0.3 mL) was added to each. The vials were submerged in a sand bath at 65 ºC for 8 h. The vials were cooled to 23 ºC. The observed white precipitate was isolated via centrifugation and washed with DMA (19 mL × 2). The obtained solid was solvent exchanged with 19 mL of $CHCl_3$ for 1 d, with fresh solvent replaced every 8 h. The solvent exchanged solid was dried *in vacuo* at 100 ºC to give ZrFDCCl as a white solid (0.132 g, 41% yield).

A 20 mL scintillation vial was charged with the activated solid (0.056 g, 0.017 mmol), AgOTf (0.016 g, 0.062 mmol, 3.6 equiv), and MeOH (20 mL). The reaction mixture was stirred in the dark at 23°C for 3 d. The liquid was isolated from the observed precipitate via centrifugation and concentrated *in vacuo* to give **III-1** as a white solid (0.054 g, 95% yield). ^{1}H NMR (δ, 23 °C, CD_3OD): 7.24 (br, 2H), 6.62 (br, 5H). ^{19}F NMR (δ, 23 °C, CD_3OD): –79.86 (s).

Synthesis of III-2-BF_4

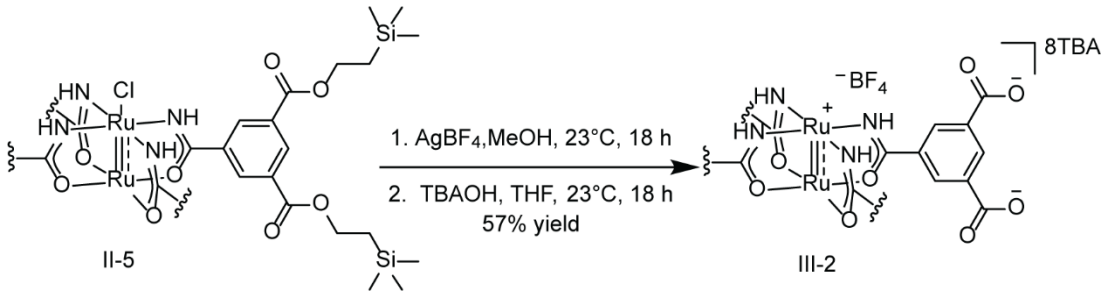

A 50-mL round-bottomed flask was charged with **II-5** (0.10 g, 0.053 mmol, 1.0 equiv), $AgBF_4$(0.011 g, 0.053 mmol, 1.0 equiv), and MeOH (20 mL). The reaction mixture was stirred at 23 ºC in the dark for 18 h. The resulting yellow solution was isolated via vacuum filtration and TBAF (1 M in THF, 0.11 mL, 0.11 mmol, 14 equiv) was added. The reaction mixture was stirred at 23 °C for 16 h. The obtained yellow solids were collected by vacuum filtration to yield **III-2** as a yellow solid (0.032 g, 57% yield). ^{19}F NMR (δ, 23 °C, DMSO-d_6): –148.33 (s).

Synthesis of Ru_2esp_2Cl

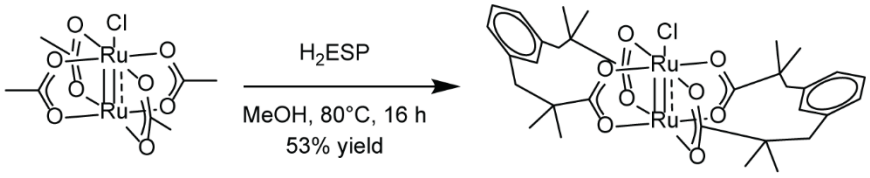

A 50-mL round-bottomed flask was charged with Ru_2OAc_4Cl (0.050 g, 0.11 mmol, 1.0 equiv), H_2esp (0.059 g, 0.21 mmol, 2.0 equiv), and chlorobenzene (20 mL). The reaction mixture was heated to 150 ºC for 16 h. The reaction mixture was concentrated *in vacuo,* and the purple residue was purified by SiO_2 gel column chromatography (1:3 EtOAc:Hex eluent) to afford Ru_2esp_2Cl as a red solid (0.041 g, 53% yield). ^{1}H NMR (δ, 23 °C, DMSO-d_6): 13.61, 13.59, 12.81, 12.32, 12.00, 11.89, 11.71, 10.85, 10.47, 2.08 ppm. All peaks are broad, preventing reliable integration, which is in agreement with reported literature.[232]

Synthesis of RuOAc (II,II)

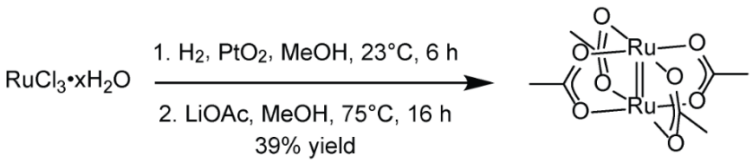

A 250-mL Schlenk flask was charged with $RuCl_3 \cdot xH_2O$ (4.0 g, 19 mmol, 1.0 equiv), PtO_2 (0.020 g, 0.088 mmol, 0.005 equiv), and MeOH (50 mL). The reaction mixture was degassed via three freeze-pump-thaw cycles and subsequently pressurized with 1 atm of H_2. The reaction mixture was stirred at 23 ºC for 6 h, during which the solution was observed to change colors from orange to blue. The reaction mixture was filtered using an air-free filtration frit. Under N_2. LiOAc (4.70 g, mmol, eq) was added to the solution and the reaction mixture was heated at 75 ºC for 16 h. The reaction mixture was cooled to 23 ºC and the observed orange precipitate was isolated via air-free filtration. The solid was dried *in vacuo* to give Ru_2OAc_4 (1.63 g, 39% yield) as an orange powder. UV-vis (THF, λ_{max} (nm)): 445. This data is well-matched with reported spectral data.[233]

Synthesis of III-5

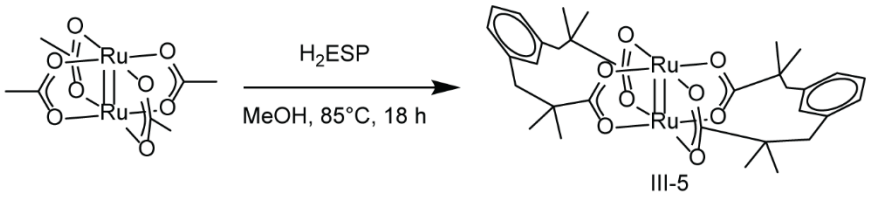

Under N_2, a 50-mL Schlenk flask was charged with Ru_2OAc_4 (0.045 g, 0.10 mmol, 1.0 equiv), H_2ESP (0.057 g, 0.21 mmol, 2.0 equiv), and degassed MeOH (20 mL). The reaction mixture was heated at 85 ºC for 18 h. Solvent was removed *in vacuo* to yield **III-5** as a red solid. **III-5** was used without further purification. ^{1}H NMR (δ, 23 °C, DMSO-d_6): 22.35, 13.45, 12.58, 12.44, 12.11, 11.80, 11.41, 10.57, 9.57, 6.55 ppm. All peaks are broad, preventing reliable integration. UV-vis (THF, λ_{max} (nm)): 300, 443.

Synthesis of Ru_2Piv_4Cl

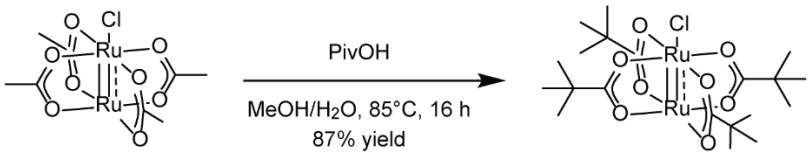

A 100-mL round-bottomed flask was charged with Ru_2OAc_4Cl (0.200 g, 0.422 mmol, 1.00 equiv), pivalic acid (0.700 g, 6.85 mmol, 16.2 equiv) and 1:1 MeOH/H_2O (30 mL). The reaction mixture was heated to 85 ºC for 16 h. The mixture was cooled to 23 ºC and the observed precipitate was isolated via vacuum filtration. The solid was washed extensively with H_2O and dried *in vacuo* to give Ru_2Piv_4Cl (0.235 g, 87% yield) as a red solid. ^{1}NMR (δ, 23 °C, DMSO-d_6): 12.25, 12.02, 11.76. All peaks are broad, preventing reliable integration.

Preparation of Thin Films

Thin films of III-2 were synthesized by hand via the following method: A treated glass slide was dipped into a 10 mg/mL solution of **III-1** in MeOH for 15 s. The slide was removed from solution and excess solution adhered to the surface was gently drained back into the parent solution. The slide was then dipped into a MeOH wash solution for 15 s, repeating the procedure to remove excess adhered solution. This process was then repeated with a 10 mg/mL solution of **III-2** and another wash solution. This process of four dips comprised one bilayer (BL). After 5 BL, the slide was allowed to air dry for 5 min. Every 25 BL the wash solutions were replaced with fresh MeOH.

Thin films of III-2 were synthesized by robot via the following method: A treated glass slide was attached to a Velmex Inc. BiSlide system. The slide was dipped into a 10 mg/mL solution of **III-1** in MeOH for 15 s. The slide was removed from solution and dried using filtered, compressed air. The slide was then dipped into a MeOH wash solution for 15 s, repeating the drying process.

This process was then repeated with a 10 mg/mL solution of **III-2** and another wash solution. This process of four dips comprised one bilayer (BL).

Azidation procedures

*Treatment of films of **III-2** with NaN_3*

A 20 mL scintillation vial was charged with a film of **III-2-Cl**, NaN_3 (0.050g, 0.77 mmol), and a solution of 1:1 H_2O/MeOH (20 mL). The reaction mixture was allowed to sit at 23 ºC for 12 h. The film was removed and assayed via UV-vis.

Treatment of III-2-BF_4 with $TMSN_3$

Under an atmosphere of N_2, a cuvette was charged with a film of **III-2-BF_4** and anhydrous THF (6 mL). To this was added $TMSN_3$ (100 μL) and the headspace of the cuvette was removed under vacuum to seal the sample. The reaction mixture was assayed via UV-vis at various time points as seen in Figure **III-8** at 23 ºC.

III.5.3 Photochemistry Details

General photolysis procedure for Ru_2esp_2Cl and Ru_2Piv_4Cl

Under an atmosphere of N_2, a cuvette was charged with 0.3 mg of solid and anhydrous THF (6 mL). The cuvette was sealed and photolyzed at 23 ºC using a 335 nm long pass filter, and assayed at various time points via UV-vis.

Photolysis procedure for thin films of III-2-N_3

Under an atmosphere of N_2, a cuvette was charged with the thin film. The headspace of the cuvette was removed under vacuum to seal the sample. The film was photolyzed at 23 ºC using a 335 nm long pass filter, and assayed at various time points via UV-vis.

Photolysis procedure for III-2-N_3

Under an atmosphere of N_2, a cuvette was charged with the thin film, anhydrous THF (6 mL), and $TMSN_3$ (100 μL). The headspace of the cuvette was removed under vacuum to seal the sample. The film was photolyzed at 23 ºC using a 335 nm long pass filter, and assayed at various time points via UV-vis.

Photolysis procedure for III-2-Cl

Under an atmosphere of N_2, a cuvette was charged with the thin film and anhydrous THF (6 mL). The headspace of the cuvette was removed under vacuum to seal the sample. The film was photolyzed at 23 ºC using a 335 nm long pass filter, and assayed at various time points via UV-vis.

NMR Spectra

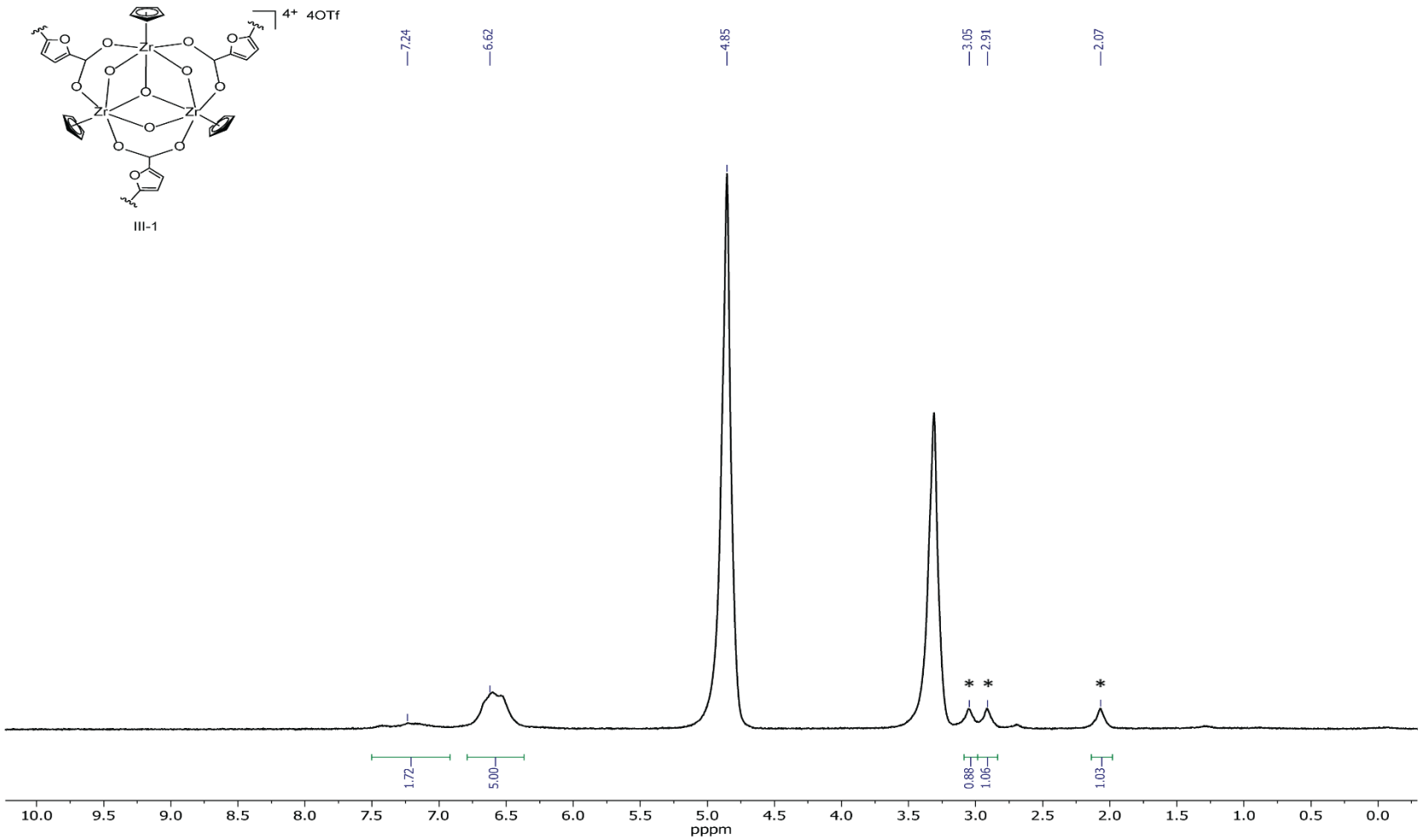

Figure III-15. ^{1}H NMR of III-1 in CD_3OD at 23 °C. * corresponds to peaks associated with DMA, hypothesized to be bound to Zr.

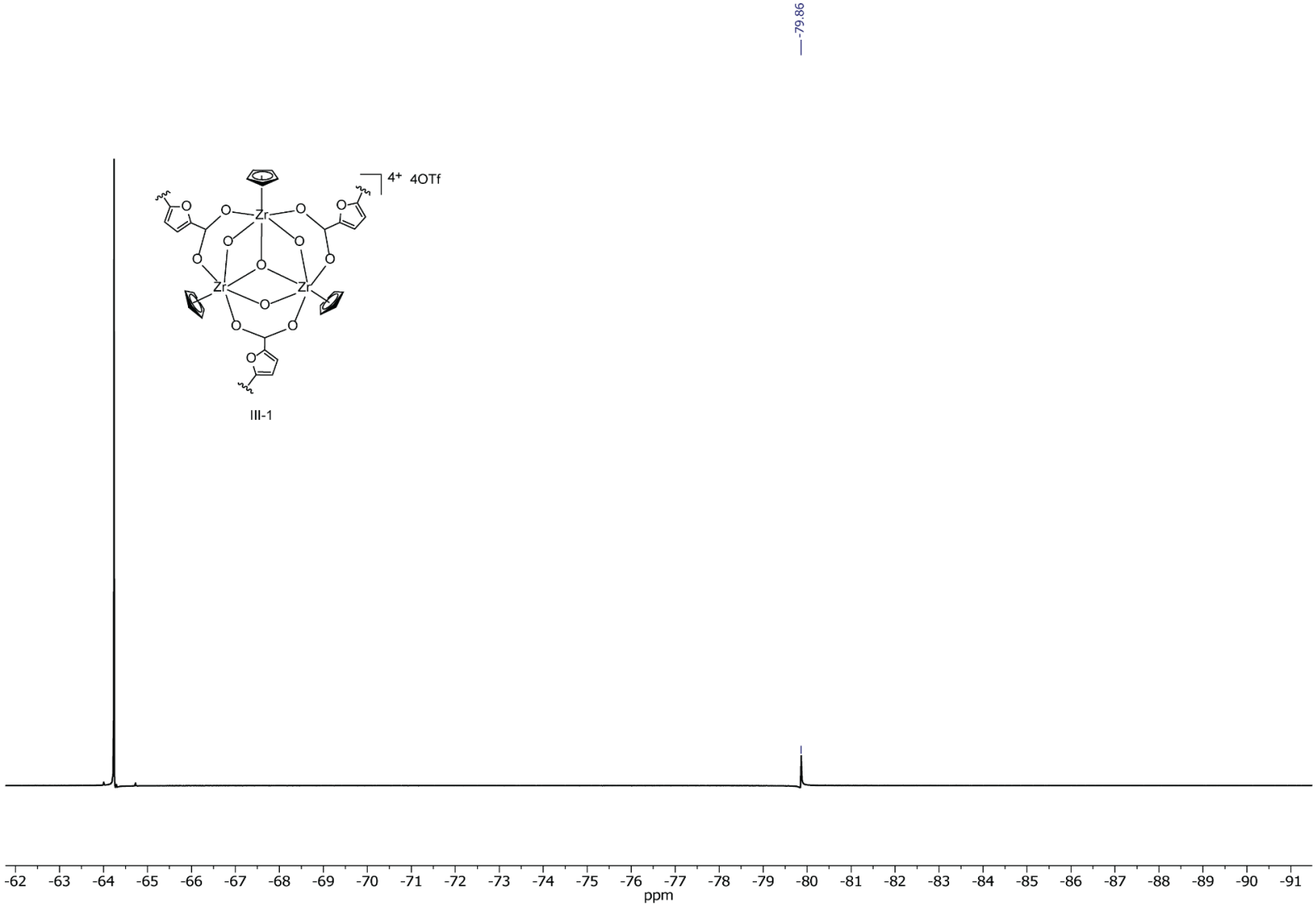

Figure III-16. ^{19}F NMR of III-1 in CD_3OD at 23 °C.

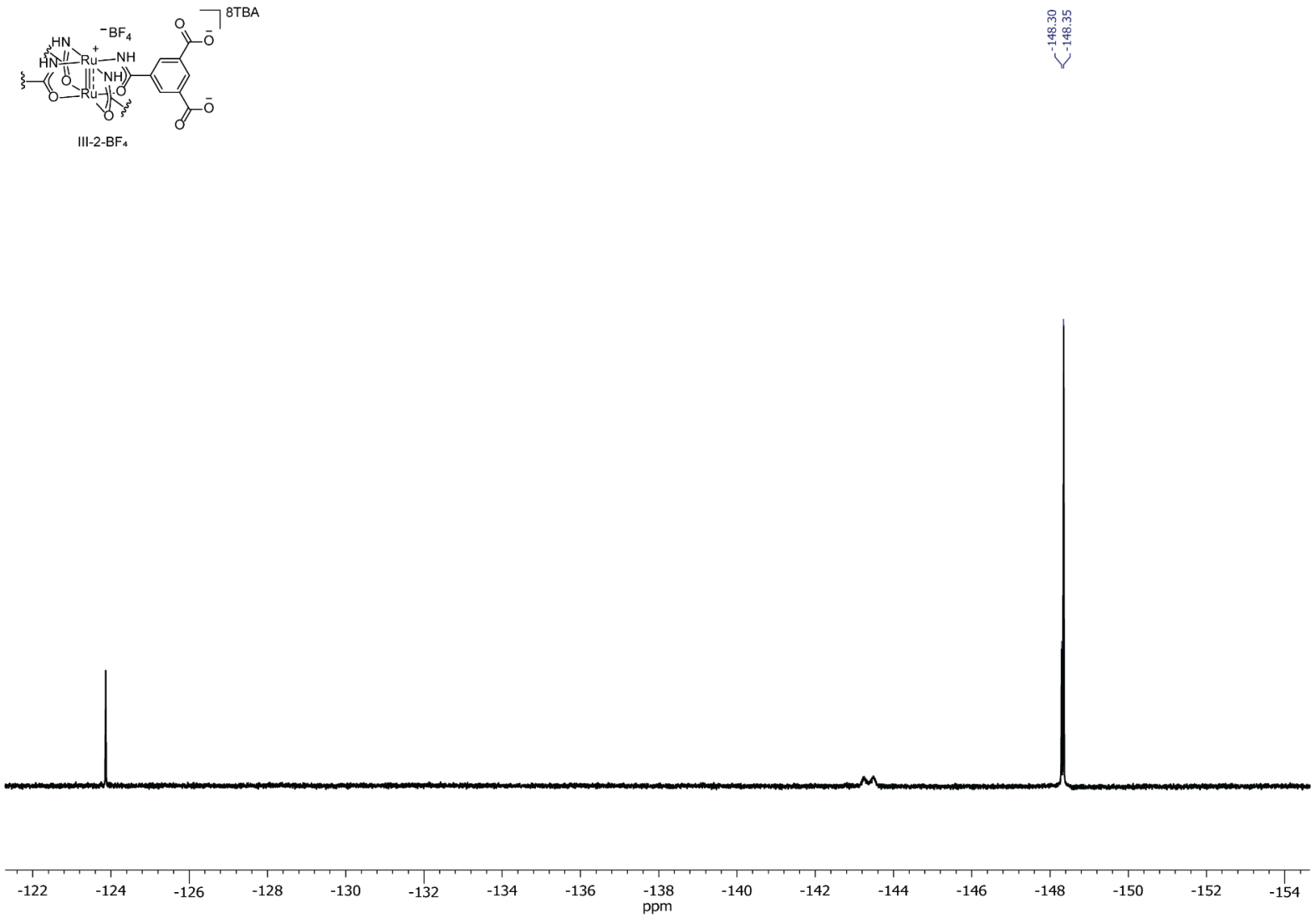

Figure III-17. ^{19}F NMR of III-2-BF$_4$ in DMSO-d$_6$ at 23 °C.

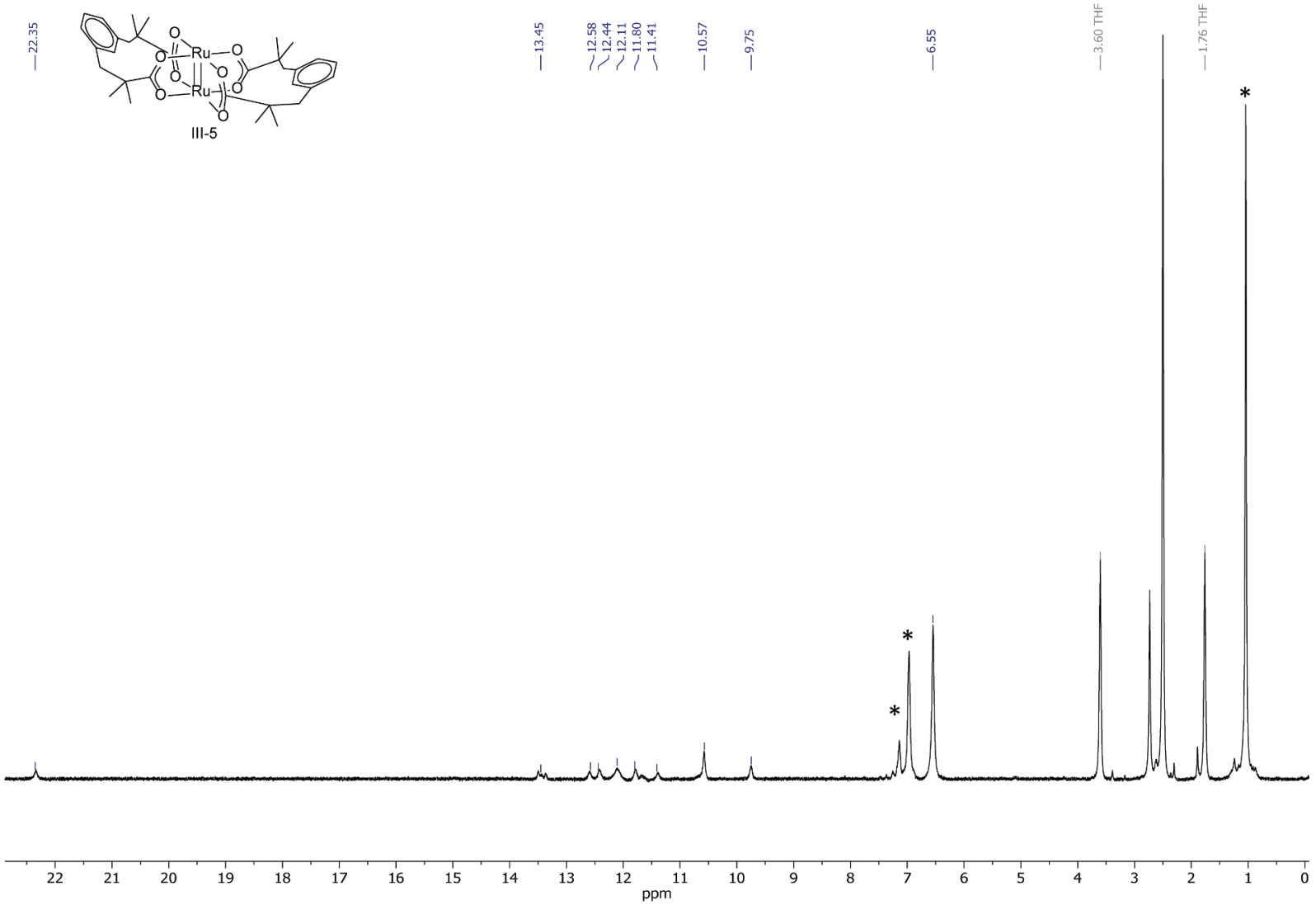

Figure III-18. ^{1}H NMR of III-5 in DMSO-d_6 at 23 °C. * corresponds to unreacted H_2esp ligand.

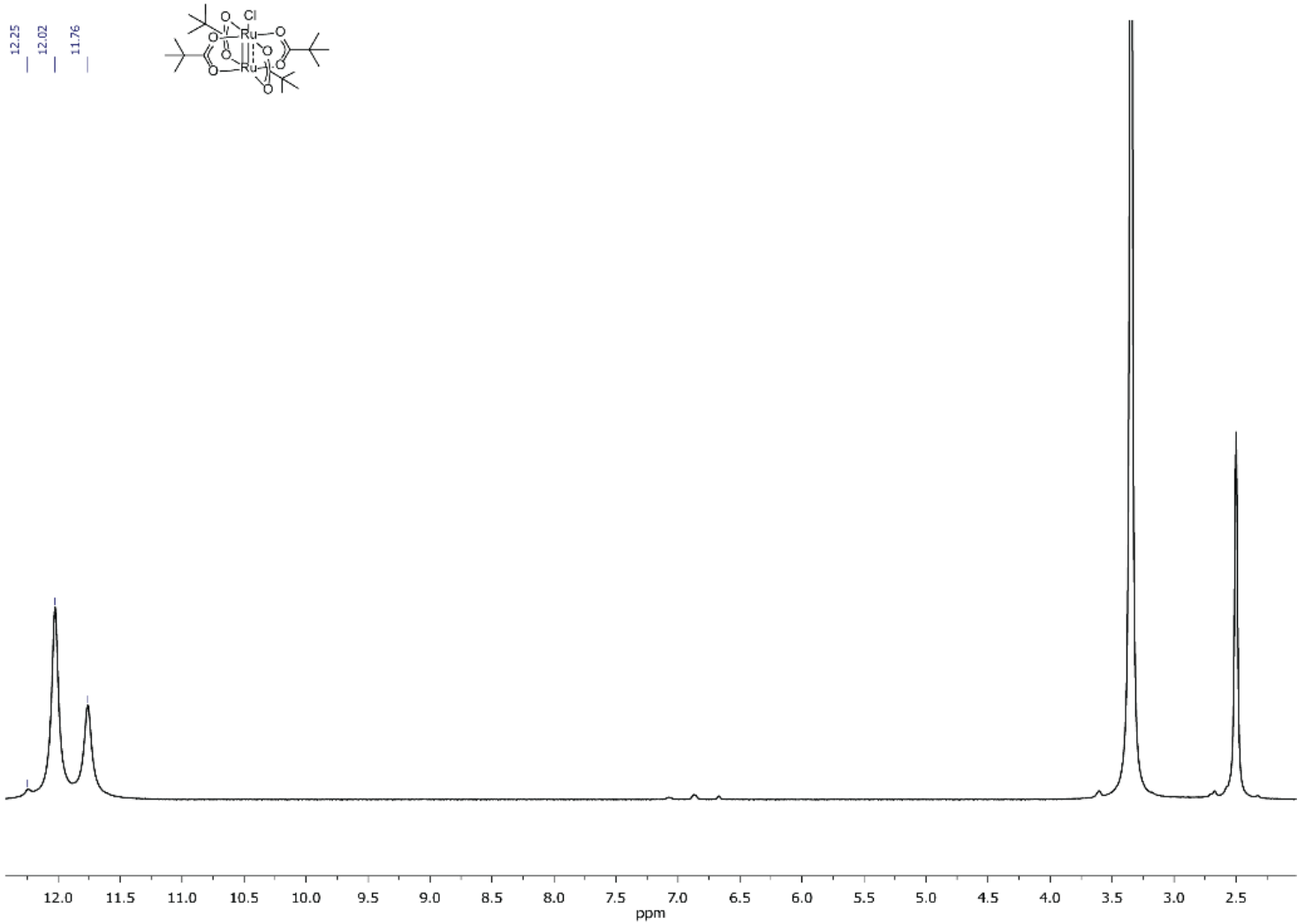

Figure III-19. ^{1}H NMR of Ru_2OPiv_4Cl in DMSO-d_6 at 23 °C.

CHAPTER IV

GROWTH MECHANISM AND CHARACTERIATION OF PORPHYRIN POLYELECTROLYTE FILMS

IV.1. Introduction

Porphyrins are a class of molecules which are ubiquitous across chemistry. They have been widely studied for their photochemical properties[234-237] and ability to form complexes with a variety of atoms.[238, 239] The high synthetic modularity of porphyrins make them attractive targets for materials chemistry and strong absorption in the visible region makes them particularly appealing for photochemical applications.[240-245]

As such, there is intense interest in synthetic methodologies to incorporate porphyrins into materials, particularly for photocatalysis or as photoresponsive sensors.[246-248] A wide body of literature exists predicated on the synthesis of thin films of porphyrins via methods discussed in the previous chapter, such as CVD or LbL.[249-253] These methods can be used to make films of varying thicknesses or have specific properties depending on the synthesis method.[254-257]

One relevant example is the synthesis of thin films of porphyrins and polyoxometallates (POM) via the LbL method.[258, 259] Ruhlmann and coworkers designed a system where the porphyrins perform photoreduction of a POM unit, which in turn reduces a substrate.[260, 261] The synthesized films were optically addressable and the thickness was tunable, which are the two main objectives we established in the previous chapter for our film systems. Ruhlmann and coworkers suggested that for their systems reduction of substrate occurs on the surface of the material. This would suggest a lack of porosity, which contrasts with our system based on **III-1.**

We sought to combine the optically transparent films platform we developed in the previous chapter with porphyrins to enable solid-state photochemistry, like the POM-porphyrin films previously discussed, but also porous. We initially targeted MnTCPPCl as the anionic component of our films as it had carboxylic acids (which are necessary for film construction) and easily differentiable oxidation states via UV-vis. Irradiation of a thin film of MnTCPPCl-**ZrFDC** with a 335 nm long pass filter in THF yields complete photoreduction (Figure IV-1), as evidenced by UV-vis. Mn(III)TCPPCl has its λ_{max} centered at 476 nm, while Mn(II)TCPP has its λ_{max} centered at 445 nm.

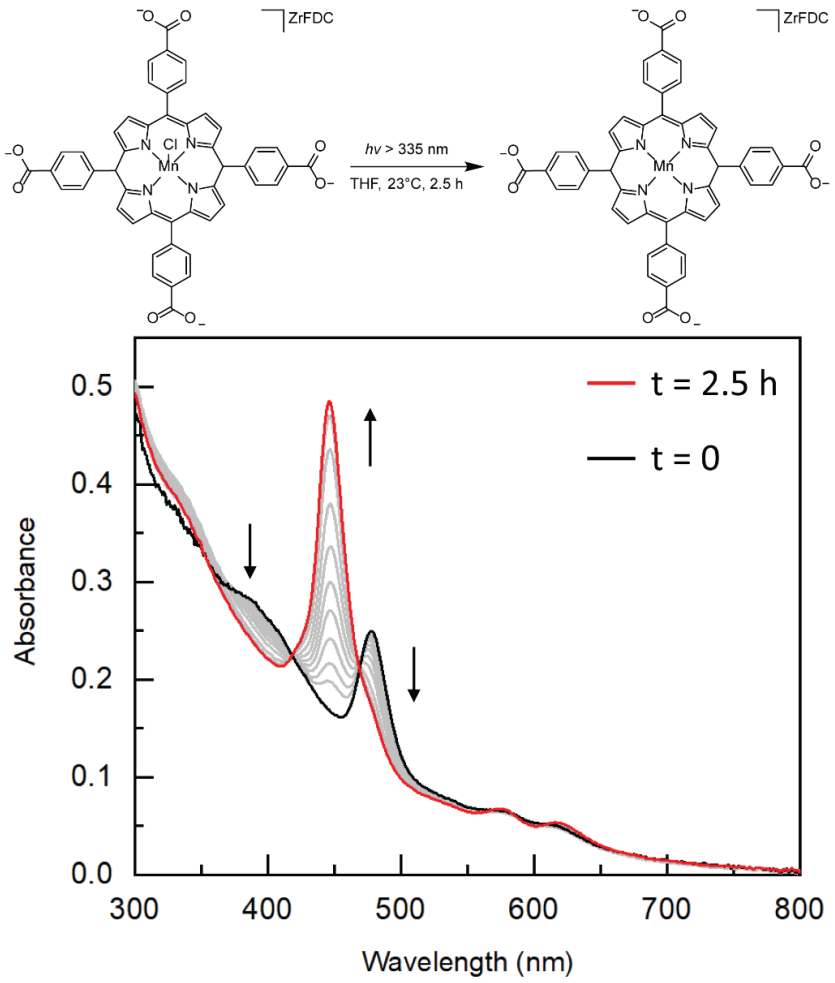

Figure IV-1. Photoreduction of a thin film of MnTCPPCl in THF using a 335 nm long pass filter. Complete conversion from Mn (III) to Mn (II) is obtained in 2.5 h.

To better design materials which we could leverage for solid-state photochemistry, we were interested in better understanding the growth mechanism of our films. The optical transparency of our films allowed us access to UV-vis as a tool for examining the growth mechanism, which is described in several models by Koenig and Martel and described herein.[262] There are several distinct growth mechanisms which manifest in the UV-vis as seen in Figure IV-2. Some key assumptions that are made when discussing the simplified mechanistic pictures presented are that scattering is negligible, only one component is absorbing light, and that Beer's Law is obeyed. The first mechanistic model (Figure IV-2a) corresponds to perfect layer coverage; each layer coats a surface evenly and completely in 2D and each subsequent dip builds up perfectly in 3D. The second model (Figure IV-2b) shows perfect layer by layer assembly but with incomplete surface coverage in 2D which results in the slope being depressed. There can also be a deviation from linearity at high bilayer count for denser materials and remains linear for less dense films. The third model (Figure IV-2c) corresponds to a pyramidal growth model, where growth in 2D is much greater than growth in 3D. The concave down shape may be a result of a change in growth mechanism to form a less dense phase.[263] The fourth model (Figure IV-2d) indicates lateral growth, when growth in 3D becomes greater than growth in 2D. The concave up shape of the graph corresponds to an increase in density.[264, 265] The fifth model (Figure IV-2e) represents a combination of pyramidal growth and lateral growth models which represents a more extreme version of that depicted in Figure IV-2d, which again indicates a change in density of layers to become more dense, thus yielding the curve seen.[266] It should be noted that in the initial number of bilayers for Figure IV-2d and 2e that the growth pattern initially appears to be linear – if the density is sufficiently low, or surface coverage is sufficiently low, the linear behavior of these

models would continue. The presented examples are extrapolated to show the extremes of the growth models for the purpose of differentiation.

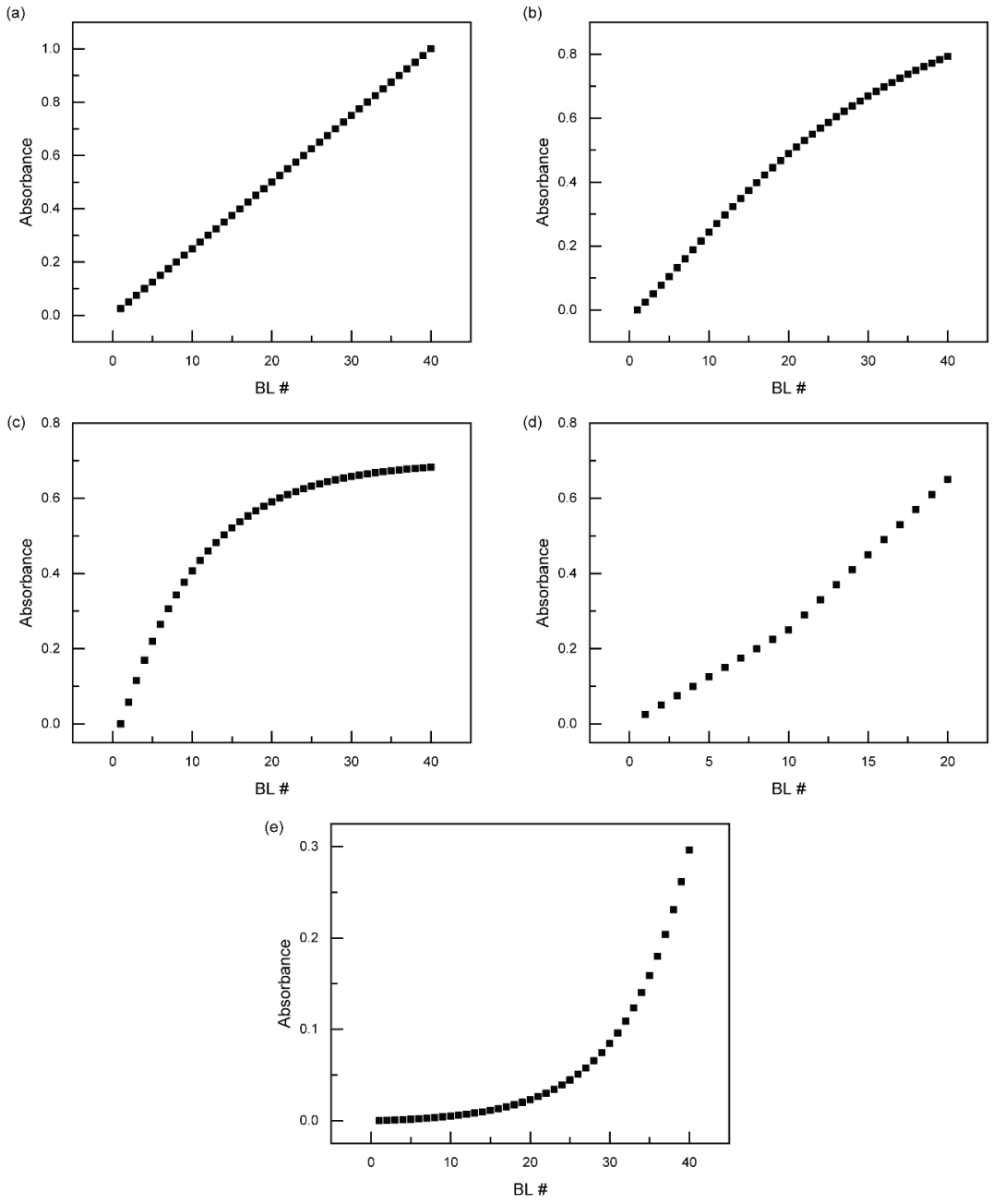

Figure IV-2. Simulated UV-vis spectra based on growth LbL growth model. (a) Perfect layer coverage. (b) Perfect LbL with incomplete surface coverage. (c) Pyramidal. (d) Lateral growth. (e) Pyramidal and lateral growth.

In this chapter, we discuss the synthesis of thin films comprised of either **IV-1** or **IV-2** (Figure IV-3**)** as the anionic component of a polyelectrolyte film, and **III-1** as the cationic component. Our desire to examine these substrates was two-fold: 1. We envisioned that the growth of **IV-1** based films would be transferrable to metalated analogs, giving us a base from which to explore future photochemical platforms without interrogating the minute details of film growth of each system and 2. Changing from **IV-1** to **IV-2** doubles the charge per molecule, and should correspond to a predictable change in mass and absorbance; this would enable programmable synthetic logic to be applied to the synthesis of thin films.

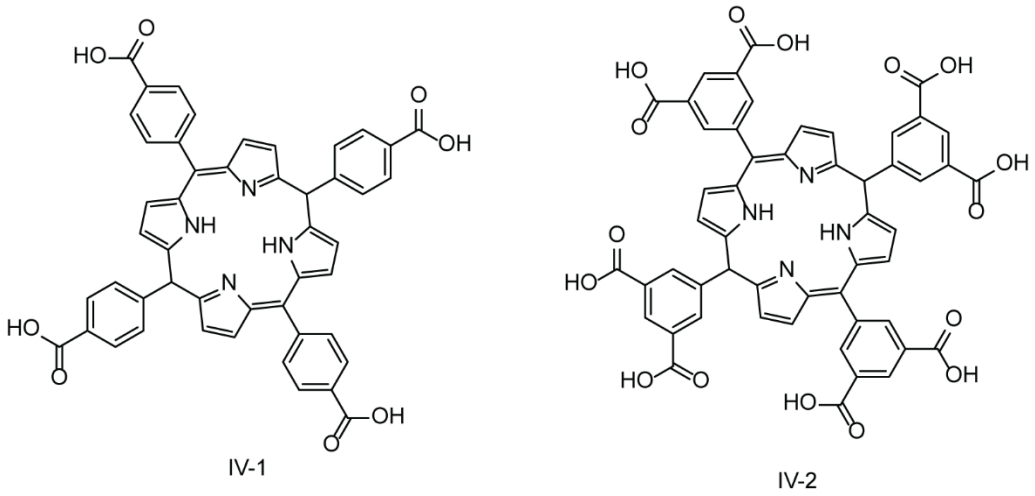

Figure IV-3. Porphyrins IV-1 and IV-2 used in this chapter for growth studies.

IV.2. Results and Discussion

In this section, we describe the synthesis and characterization of thin films of **IV-1** or **IV-2** and **III-1**. The growth mechanism of films of **IV-1** was examined by QCM and by UV-Vis. Additional thickness measurements and AFM images were obtained. The growth mechanism of films of **IV-2** was examined by UV-Vis.

*IV.2.1 Growth of **IV-1** based thin films*

Our initial efforts towards film growth of **IV-1** based films were focused on evaluating the impact of concentration and bilayer number on the growth curve behavior. Using UV-vis spectroscopy of the growing thin films, we produced growth curves of **IV-1** for four concentration regimes spanning 0.25 mg/mL to 2.5 mg/mL (Figure IV-4). Concentration plays a significant role in optical density (which we correlate to amount of **IV-1** deposited on the substrate): As concentration increases, the absorbance of the film increases. In Figure IV-4c and IV-4d, we observed that at and above 30 BL, there appears to be little difference in the absorbance of the 1 mg/mL and 2.5 mg/mL samples. This may indicate that there is a saturation limit of the effect concentration has on film thickness past a certain number of bilayers. Concentration is important however in the early BL phase to the amount of material deposited.

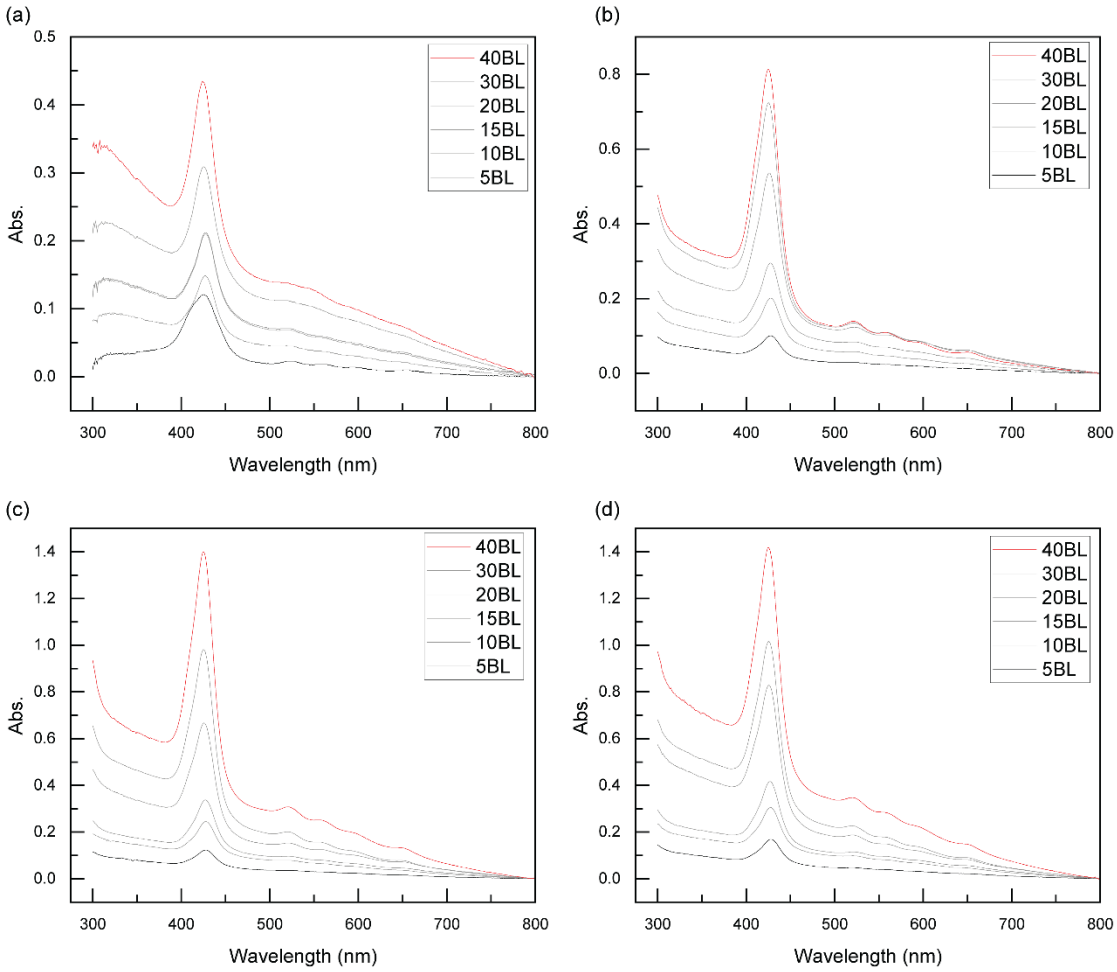

Figure IV-4. Growth curves represented via UV-vis absorbance for films of IV-1 and III-1 at (a) 0.25 mg/mL concentration. (b) 0.5 mg/mL concentration (c) 1 mg/mL concentration (d) 2.5 mg/mL concentration.

Figure IV-5 plots the absorbance of the Soret band vs. BL # for the different concentration regimes. Based on the UV-vis traces, there are two distinct linear regimes of growth for all the samples, with the change in growth regimes occurring between 15 and 20 BL. We rationalized this as a change during which no more nucleation is occurring, and we are in a layer-by-layer with incomplete surface coverage (Figure IV-2b).

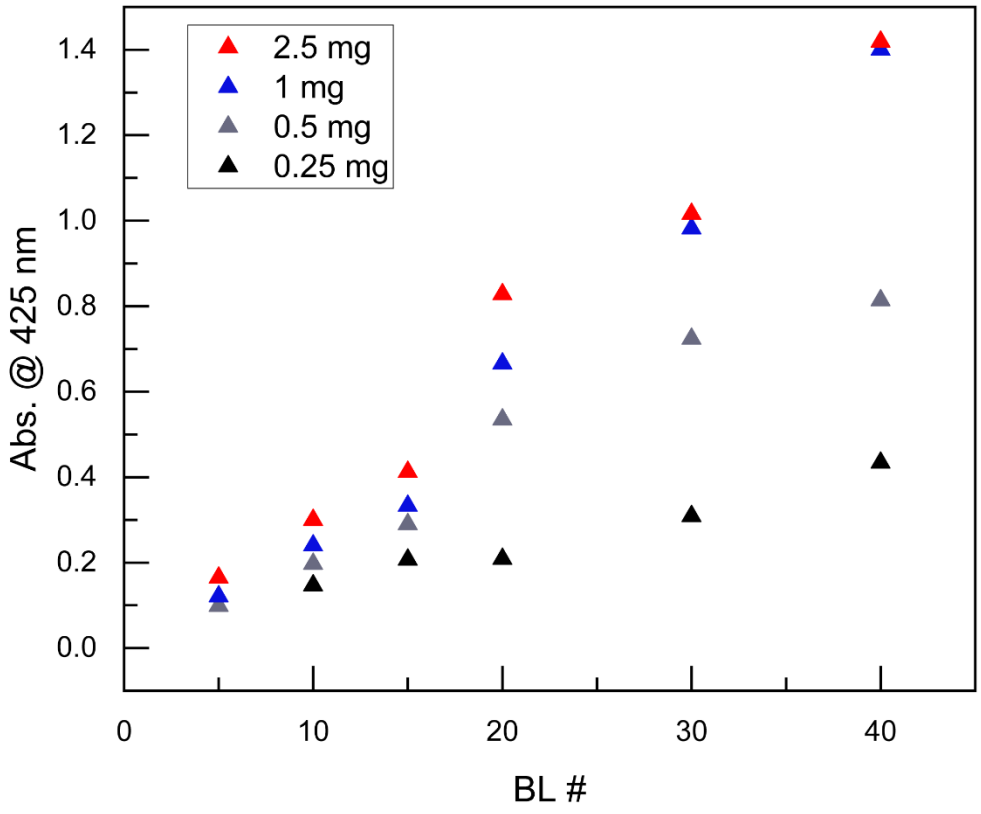

Figure IV-5. Growth curve based on absorbance at 425 nm for IV-1-III-1 in four different concentration regimes.

To gain further information about the growth mechanism, we performed quartz crystal microbalance measurements (QCM) at the 0.5 and 1 mg/mL concentrations (Figure IV-6). The difference in slopes indicates that concentration affects the rate of growth, which we hypothesized from the corresponding UV-vis data. Based on the UV-Vis data, we hypothesized that there might be two distinct growth regimes which transitions around 20 BL, but QCM indicates that there is only one, linear growth regime. Plotting the normalized absorbance and normalized mass *vs.* the number of bilayers (Figure IV-7) shows that the change in absorbance is well-matched to the change in mass in most cases.

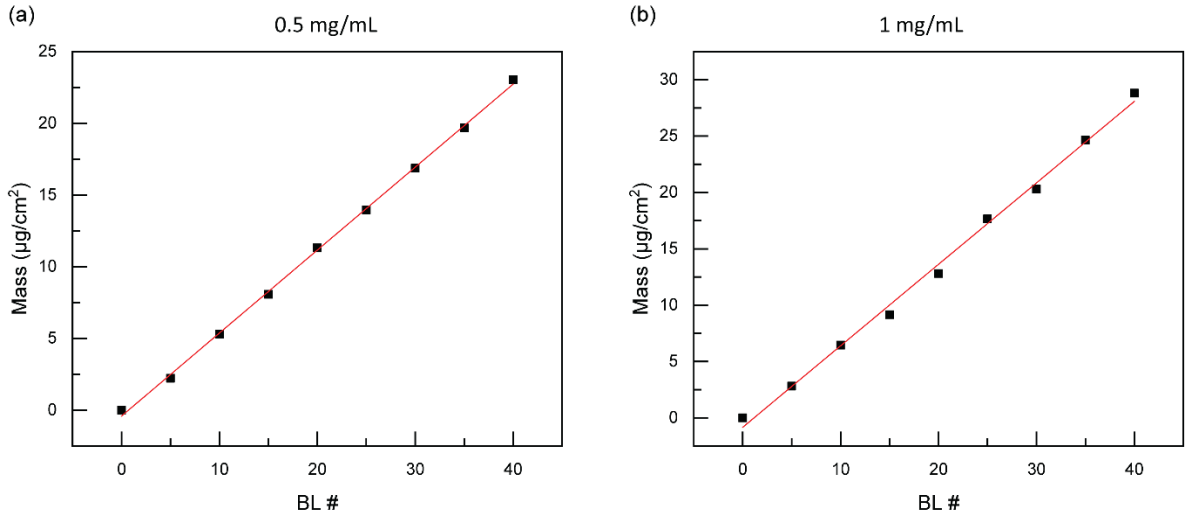

Figure IV-6. (a) QCM of 0.5 mg/mL concentration. Rate of growth is 0.58 µg cm^{-1} BL^{-1}, R^2 = 0.998. (b) QCM of 1 mg/mL concentration. Rate of growth is 0.72 µg cm^{-1} BL^{-1}, R^2 = 0.995.

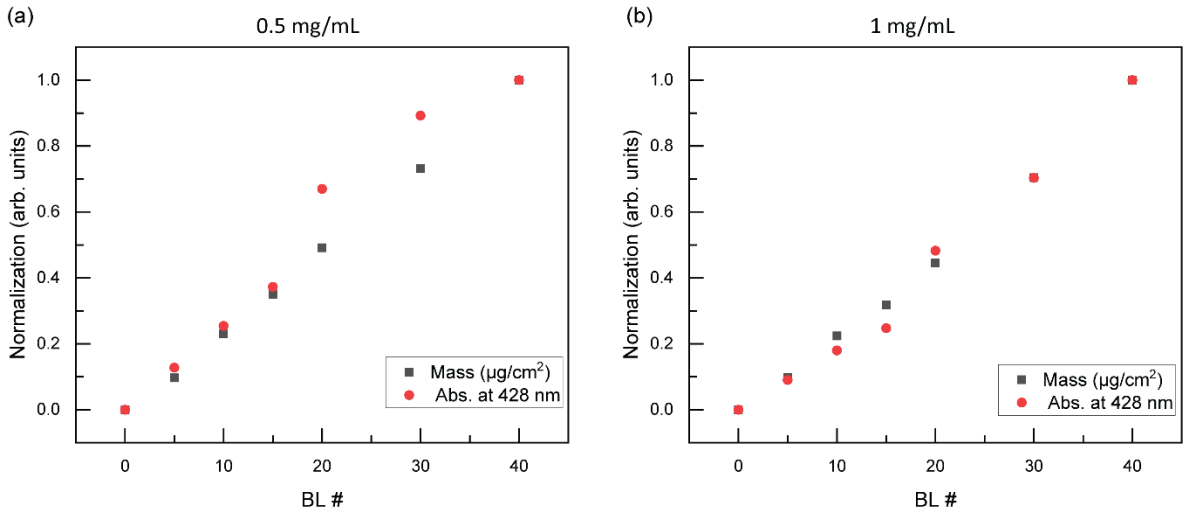

Figure IV-7. Normalized QCM and UV-vis absorbance at 428 nm for (a) 0.5 mg/mL concentration and (b) 1 mg/mL concentration.

We also sought to determine the reproducibility of our measurements. Figure IV-8 shows the successful replication of UV-vis data for three concentration regimes at 20 BL. We prepared three samples to evaluate the reproducibility of our synthetic protocol. In all figures, samples

labeled **I** were prepared first and represent the data presented in Figure IV-4. Samples labeled **II** were prepared from a fresh solution, while samples labeled **III** were prepared immediately after samples labeled **II**, and from the same parent solution. We initially hypothesized that solution depletion might be an issue for subsequent samples, but the QCM data presented in Figure IV-6 indicates that only 0.063% of the parent solution is plated out on film after 40 BL, and the UV-vis data indicates that there is no predictable change in UV-vis between samples **II** and **III**. Films prepared from higher concentrations were less reproducible than those prepared from lower concentrations.

Additionally, we attempted to prepare films from solutions that had been left to age under ambient conditions (Figure IV-9). We observed that after aging 4 days, film growth was much less efficient (as evaluated by the bilayer-dependent absorption spectra) and the results were outside the error bars indicated in Figure IV-8. To evaluate if the solutions underwent a reversible change, such as hydration under ambient conditions, the solutions were dried *in vacuo* at 60 °C and subsequently resolvated. Films grown from this procedure were labeled as "pump" in Figure IV-9 and showed almost no change in absorbance. Water exposure dramatically reduces the surface area of cage **III-1**, and using water washes instead of MeOH during the film making process leads to lower absorbances and no predictable growth pattern (*i.e.*, 10 BL samples had higher absorbance than 20 or 30 BL samples), which may suggest an irreversible reaction of **III-1** with water over time.

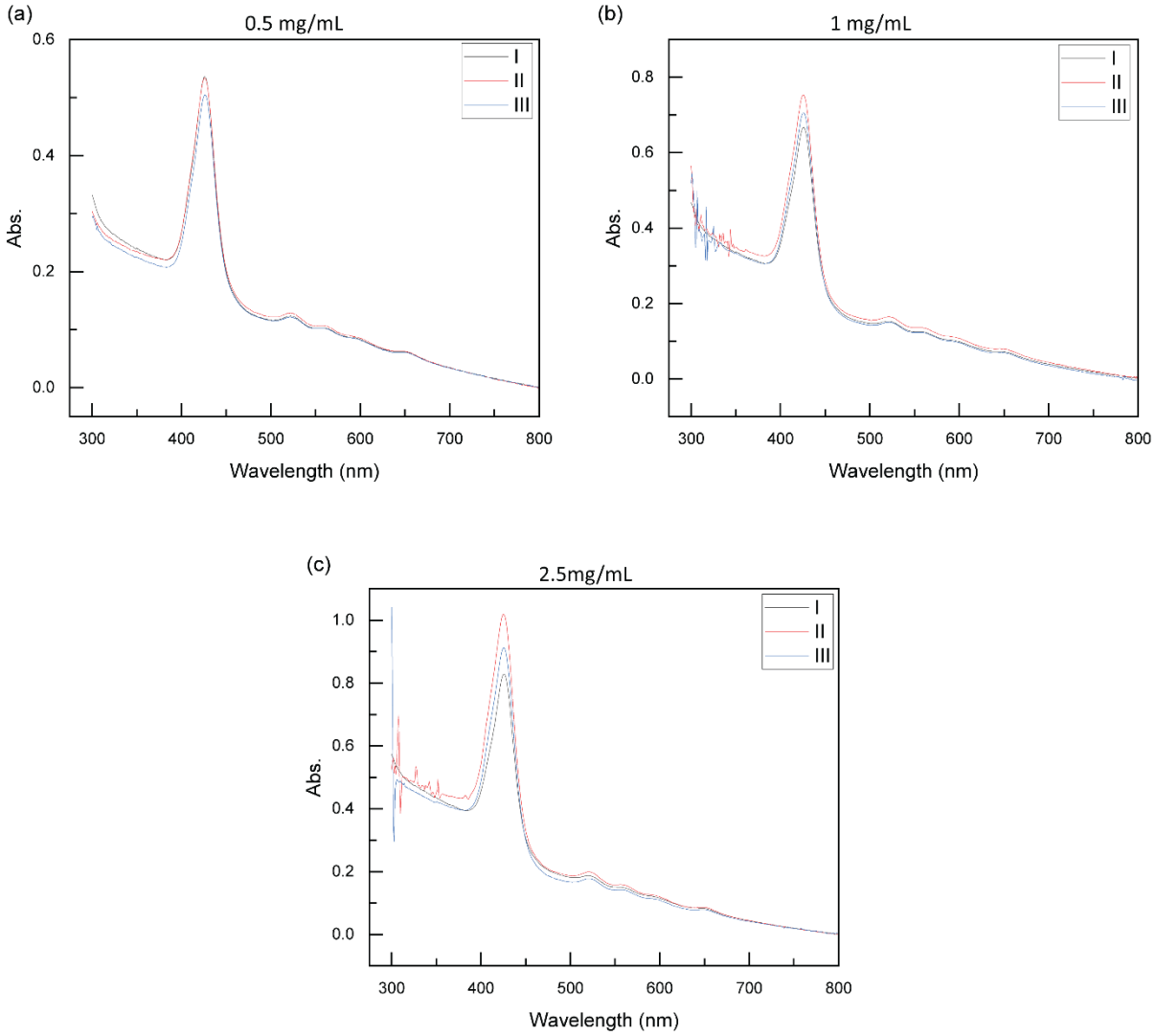

Figure IV-8. Replication at 20 BL for three concentration regimes (a) Average absorbance of 0.5 mg/mL film at 428 nm of 0.520 ± 0.020. (b) Average absorbance of 1 mg/mL film at 428 nm of 0.697 ± 0.052. (c) Average absorbance of 2.5 mg/mL film at 428 nm of 0.90 ± 0.11.

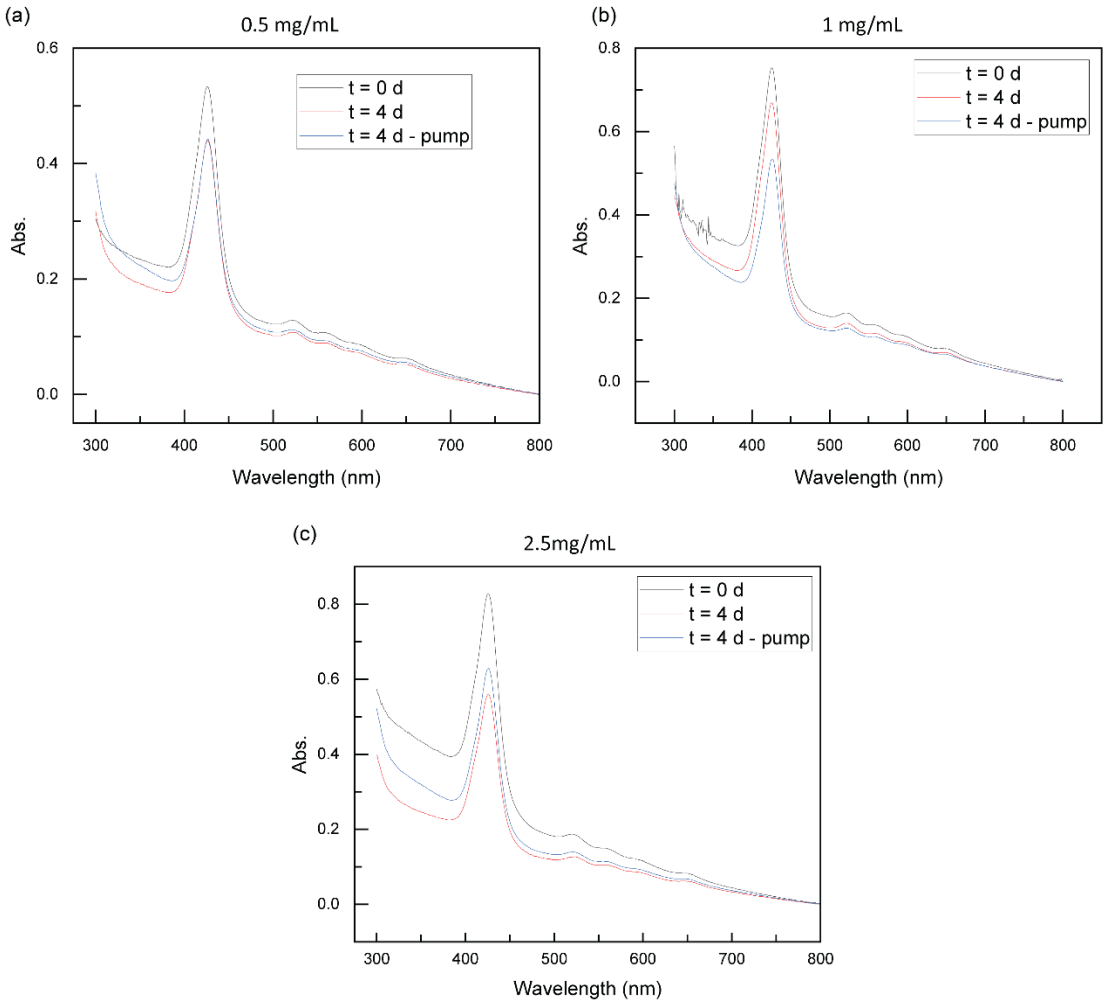

Figure IV-9. Solution aging experiments at 20 BL were conducted for three concentration regimes. Films were made from solutions at t = 0 days, then from solutions that have been aged for 4 days under ambient conditions. The aged solutions for dried in vacuo at 60°C, then resolvated with fresh MeOH and used to prepare another film. Aging leads to films with decreased absorbance values, indicating less electrolyte has been deposited. Drying solutions does not produce films with recovered absorbance values. (a) 0.5 mg/mL concentration. (b) 1 mg/mL concentration. (c) 2.5 mg/mL concentration.

Obtained profilometry data indicates increasing thickness with increasing bilayer number, with a roughly linear correlation until 40 BL (Table IV-1). Additionally, roughness increases with BL number, which is as expected. AFM images were obtained of the 1 mg/mL and 0.25 mg/mL films to interrogate surface roughness and obtain information about the growth mechanism (Figure IV-

10). We observed that for the 1 mg/mL samples, the surface is rather uniform which is consistent with a perfect layer by layer deposition. However, in the 0.25 mg/mL samples there are a large number of spots of greater vertical displacement, which might be indicative of growth from nucleation spots, growing in the z direction faster than the x and y directions, which is consistent with a pyramidal growth model.

Table IV-1. Thickness and roughness data values for 1 mg/mL concentration.

BL #	Thickness (nm)	Avg. Roughness (nm)
10	26	6
15	51	6
20	68	20
30	91	29
40	199	38

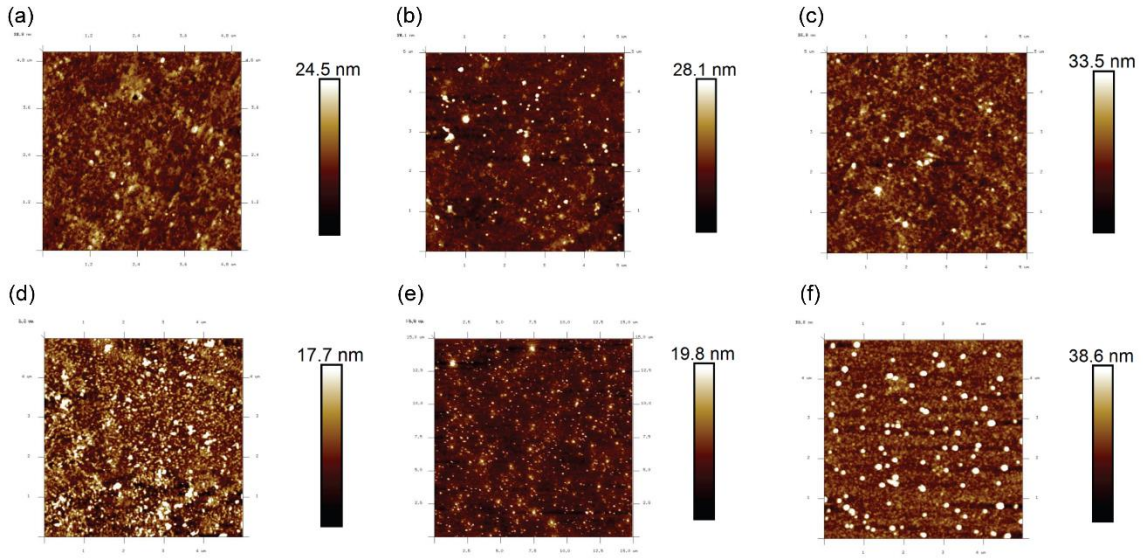

Figure IV-10. AFM images of films. All images taken are 5 x 5 µm. (a) 1 mg/mL 10 BL. (b) 1 mg/mL 20 BL. (c) 1 mg/mL 30 BL. (d) 0.25 mg/mL 5 BL. (e) 0.25 mg/mL 20 BL. (f) 0.25 mg/mL 30 BL.

*IV.2.2 Growth of **IV-**2 based thin films*

We also sought to make thin films based on **IV-2**. We chose this molecule as we rationalized that the molecule would pack similarly to **IV-1** and have similar optical properties, but also provide twice the charge density. This would allow us to examine the effect that charge has on the growth of our films, independent of concentration. Figure IV-11 shows the growth curves of films of **IV-2** at three concentration regimes: 0.5 mg/mL, 1 mg/mL, and 2.5 mg/mL. Even at low bilayer numbers, the absorbance of films of **IV-2** are much greater than that of **IV-1**. The absorbance for **IV-2** is much greater than **IV-1**, and also displays a strong solvatochromic response as solutions of **IV-2** are purple in color (the same as **IV-1**), but the films of **IV-2** are green in color (unlike **IV-1** which is still purple). Figure IV-12 displays the growth curves as a function of absorbance at 423 nm and reveals roughly linear trends.

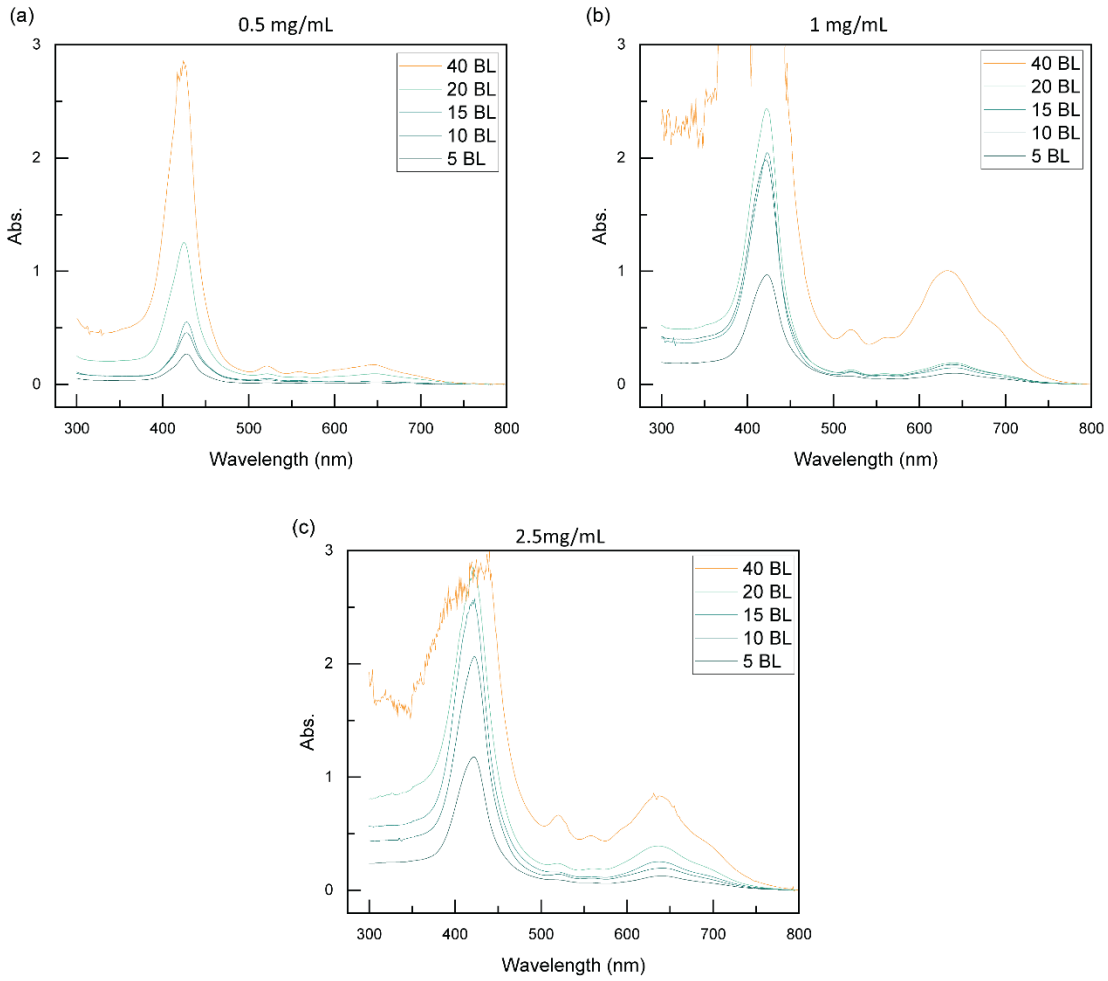

Figure IV-11. Growth curves for films of IV-2-III-1 for three different concentration regimes. (a) 0.5 mg/mL concentration. (b) 1 mg/mL concentration. (c) 2.5 mg/mL concentration.

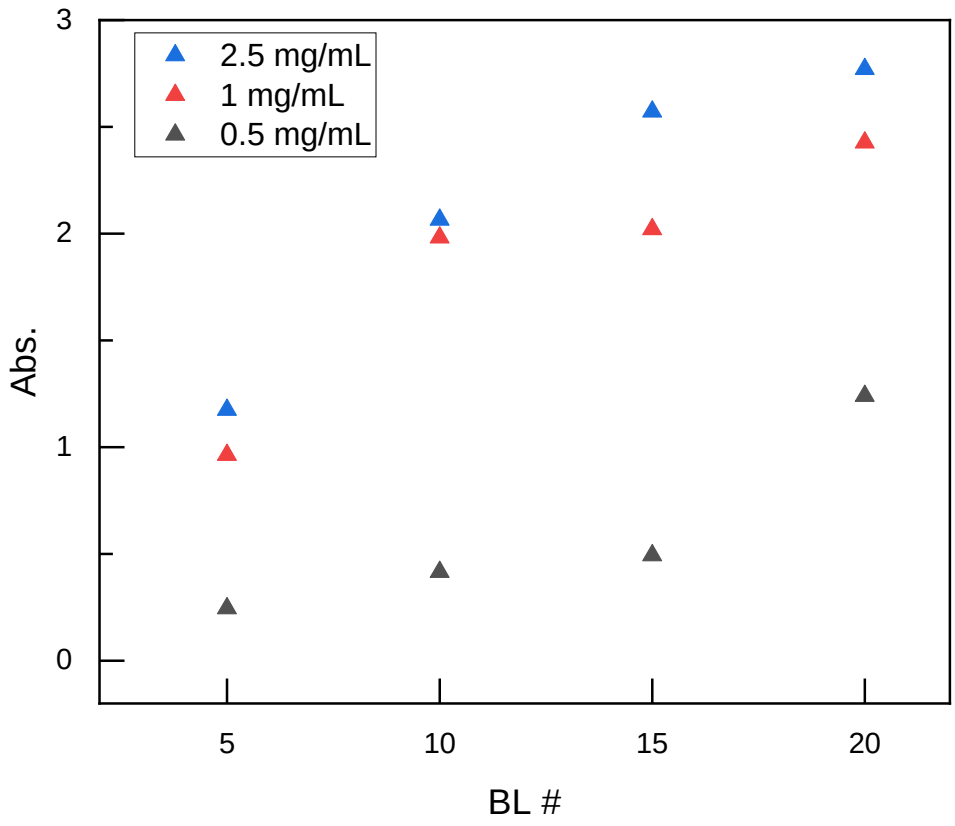

Figure IV-12. Growth curve based on absorbance at 423 nm for IV-2 in three different concentration regimes.

IV.3. Conclusion

In this chapter, we synthesized thin films based on **IV-1** and **IV-2** and examined the growth mechanisms of these films. Using QCM measurements, the films appear to follow a perfect LbL mechanism with incomplete surface coverage, with the concentration of the solution affecting the rate of growth. The UV-vis data also corroborates this growth mechanism. Surface characterization using AFM supports this conclusion for sample concentrations at 1 mg/mL but indicates that the growth mechanism for the 0.25 mg/mL concentration may be pyramidal.

Work is still underway to corroborate the growth mechanism of **IV-2** using QCM. Additionally, we are engaged in SEM-FIB experiments to determine the thickness of all samples,

and TOF-SIMS to probe the composition as a function of depth. For concentrations above 0.5 mg/mL we hypothesize that the ratio of porphyrin to cage will follow the charge ratio of the molecules.

We anticipate that this data will allow predictive synthesis of porphyrin-cage systems based on the relative charges of the molecules. We would like to examine several other variables and how they affect the growth mechanism, such as the dip time and the identity of the cage. Currently, we have only used **III-1** as the counterion, which features a +4 charge per molecule. We would like to extend to cages with higher charge, such as +12, and cages with different geometries.

IV.4. Experimental Details

IV.4.1 General Considerations

All reactions were carried out under ambient conditions unless stated otherwise. Solvents were obtained as ACS reagent grade. All chemicals and solvents were used as received unless noted otherwise. Glass slides were obtained from Environmental Monitoring Systems. EtOH (KOPTEC 200 proof) was purchased from Decon Labs. Tetrahydrofuran (THF), diethyl ether (Et_2O), hexanes, methanol (MeOH), ethyl acetate (EtOAc), dichloromethane (CH_2Cl_2), sodium borohydride, and acetic acid (AcOH) were obtained from Sigma Aldrich. Sulfuric acid (H_2SO_4) and hydrochloric acid (HCl) were obtained from VWR. 1H-pyrrole, sodium bicarbonate ($NaHCO_3$), potassium hydroxide (KOH), triethyl amine (NEt_3), and 2,3-dichloro-5,6-dicyano-1,4-benzoquinone (DDQ) were obtained from Oakwood Chemical. Propionic acid and 1,3,5-benzenetricarboxylic acid (trimesic acid) were obtained from Bean Town Chemical. 4-carboxybenzaldehyde and ceric ammonium nitrate (CAN) were obtained from Alfa Aesar. Boron trifluoride diethyl etherate ($BF_3{\cdot}OEt$) was obtained from Acros Organics. QCM crystals were

obtained from Inficon. Silica gel (0.063–0.200 mm, 60 Å for column chromatography) from EMD Millipore. NMR solvents were purchased from Cambridge Isotope Laboratories and were used as received. H_2TCPP[267] was prepared according to reported literature methods.

Characterization Details

NMR spectra were recorded on a Bruker Ascend 400 operating at 400.13 MHz for ^{1}H or a Varian NMRS 500RM operating at 500.13 MHz for ^{1}H. Spectra were referenced against solvent signals: $CDCl_3$ (7.26 ppm, ^{1}H) and DMSO-d_6 (2.50 ppm, ^{1}H). ^{1}H NMR data are reported as follows: chemical shift (δ, ppm), (multiplicity: s (singlet), d (doublet), t (triplet), q (quartet), m (multiplet), br (broad), integration). UV-vis spectra were recorded on a Shimadzu 2501PC spectrometer with DH UV-vis-NIR light source (190–900 nm). AFM images were obtained using a Bruker Dimension Icon AFM. Film thickness measurements were obtained using a KLA-Tencor P-6 Stylus profilometer. The mass of deposited layers was measured using a Maxtek RQCM.

Glass Slide Preparation

Glass slides were rinsed with DI H_2O followed by MeOH and dried with compressed air. Slides were then subjected to plasma treatment for 5 minutes using ATTO plasma cleaner (Diener Electronic). Glass slides were used immediately after plasma treatment.

IV.4.2 Synthesis and Characterization

Synthesis of IV-1 (TCPP)

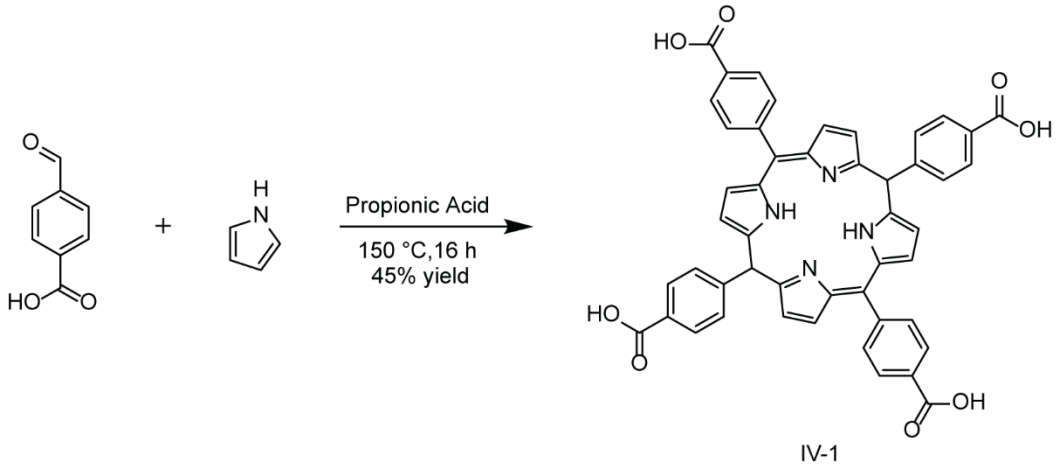

A 250-mL round-bottomed flask was charged with 4-carboxybenzaldehyde (1.56 g, 0.104 mol, 1.04 equiv.) and propionic acid (50 mL). The reaction mixture was heated at 80 ºC until the 4-carboxybenzaldehyde was completely dissolved. Freshly distilled 1H-pyrrole (0.70 mL, 0.010 mol, 1.0 equiv) was added to the reaction solution and heated to 150 ℃ for 16 h. The reaction mixture was cooled to 23 ºC and stored at –10℃ for several hours to induce precipitation. The precipitate was filtered and washed with CH_2Cl_2 (5 × 50 mL) and dried *in vacuo* to afford **IV-1** as a purple solid (0.89 g, 45% yield). ^{1}H NMR (δ, 23 °C, DMSO-d_6): 13.30 (s, 4H), 8.87 (s, 8H), 8.38 (q, J = 8 Hz, 16H), -2.94 (s, 2H).

Synthesis of IV-S1

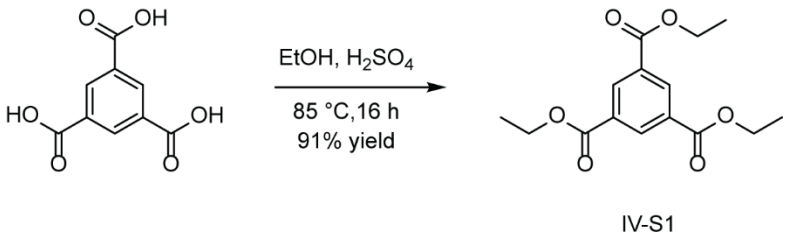

A 250-mL round-bottomed flask was charged with trimesic acid (5.00g, 23.8 mmol, 1.00 equiv), EtOH (125 mL), and H_2SO_4 (2 mL). The reaction mixture was heated at 85 °C for 16 h. The reaction mixture was cooled to 23 °C, the observed white precipitate was isolated via vacuum filtration and washed with H_2O (1 × 100 mL) and EtOH (2 × 75 mL) and dried *in vacuo* to afford **IV-S1** as a white solid (6.33g, 91% yield). ^{1}H NMR (δ, 23 °C, DMSO-d_6): 8.65 (s, 3H), 4.40 (q, J = 7 Hz, 8H), 1.36 (t, J = 7 Hz, 12H).

Synthesis of IV-S2

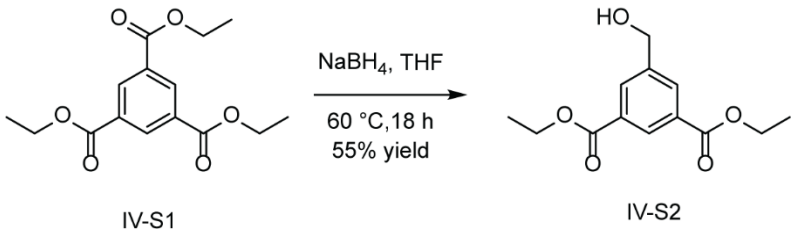

Under N_2, a 250-mL Schlenk flask was charged with **IV-S1** (4.64 g, 18.4 mmol, 1.00 equiv), $NaBH_4$ (0.574 g, 15.1 mmol, 0.821 equiv), and anhydrous THF (150 mL). The reaction mixture was heated to 60 °C for 18 h, during which time the solution turned red. The reaction mixture was cooled to –10 °C, and H_2O was added dropwise until bubbling ceased, after which 1 N HCl (10 mL) was added to give a clear solution. Solvent was removed *in vacuo* and the residue was partitioned between Et_2O (150 mL) and H_2O (100 mL). The organic phase was washed with brine (100 mL) and H_2O (100 mL). The organic phase was removed *in vacuo*, and EtOH (100 mL) was

added to the resulting white residue. The obtained suspension was filtered via vacuum filtration to remove unreacted starting material. Solvent was removed *in vacuo* and the resulting residue was purified by SiO_2 gel column chromatography (2:3 EtOAc/Hexanes, R_f = 0.45) to give **IV-S2** as a white solid (1.79 g, 55% yield). ^{1}H NMR (δ, 23 °C, $CDCl_3$): 8.59 (s, 1H), 8.22 (s, 2H), 4.81 (s, 2H), 4.41 (q, *J* = 7 Hz, 4H), 1.84 (br, 1 H), 1.41 (t, *J* = 7 Hz, 6H).

Synthesis of IV-S3 (Mono aldehyde)

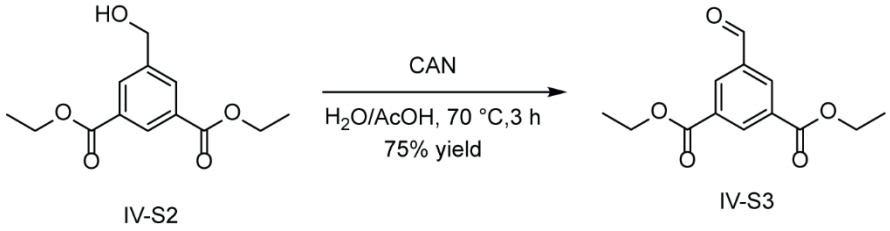

IV-S2 IV-S3

A 100-mL round-bottomed flask was charged with **IV-S2** (1.79 g, 7.10 mmol, 1.00 equiv) and AcOH (20 mL). Ceric ammonium nitrate (10.0 g, 18.2 mmol, 2.56 equiv) was dissolved in H_2O (20 mL) and added dropwise to the solution over 10 min. The reaction mixture was then heated to 70 °C for 3 h, during which the reaction mixture was observed to change colors from red to yellow. The reaction mixture was cooled to 23 °C and partitioned between Et_2O (150 mL) and water (150 mL). The aqueous phase was extracted with Et_2O (2 × 100 mL). The combined organic layers were washed with saturated $NaHCO_3$ (1 × 100 mL) and brine (1 × 100 mL). Solvent was removed *in vacuo* to give **IV-3** as a white solid (1.34 g, 75% yield). ^{1}H NMR (δ, 23 °C, $CDCl_3$): 10.14 (s, 1H), 8.92 (s, 2H), 8.71 (s, 2H), 4.46 (q, *J* = 7 Hz, 4H), 1.44 (t, *J* = 7 Hz, 6H).

Synthesis of IV-S4

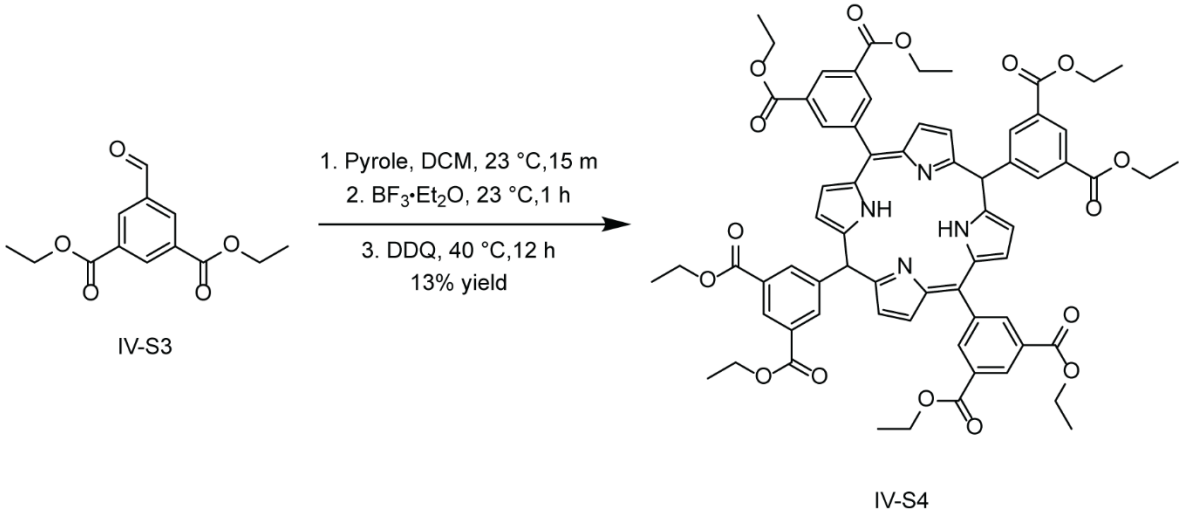

Under N_2, a 1-L three-necked round-bottomed flask was charged with **IV-S3** (1.34 g, 5.35 mmol, 1.00 equiv), freshly distilled 1H-pyrrole (0.36 mL, 5.3 mmol, 1.0 equiv), and degassed CH_2Cl_2 (500 mL). The reaction mixture was stirred at 23 °C for 15 min, after which time BF_3·OEt (0.12 mL, 0.97 mmol, 5.5 equiv) and the reaction vessel was moved to the dark. The reaction was stirred at 23 °C for 1 h, after which time DDQ (1.84 g, 8.11 mmol, 1.52 equiv) was added and the reaction was heated to 40 °C for 12 h. The reaction was cooled to 23°C and solvent was removed *in vacuo*. The resulting residue was purified by SiO_2 gel column chromatography (19:1 CH_2Cl_2/EtOAc) to give a dark red solid. This solid was further purified by SiO_2 gel column chromatography (49:1 CH_2Cl_2/EtOAc) to give **IV-S4** as a purple solid (0.41 g, 13% yield). ^{1}H NMR (δ, 23 °C, $CDCl_3$): 9.15 (s, 4H), 9.06 (s, 8H), 8.78 (s, 8H), 4.51 (q, *J* = 7 Hz, 16H), 1.43 (t, *J* = 7 Hz, 24H), –2.77 (br, 2H).

Synthesis of IV-2

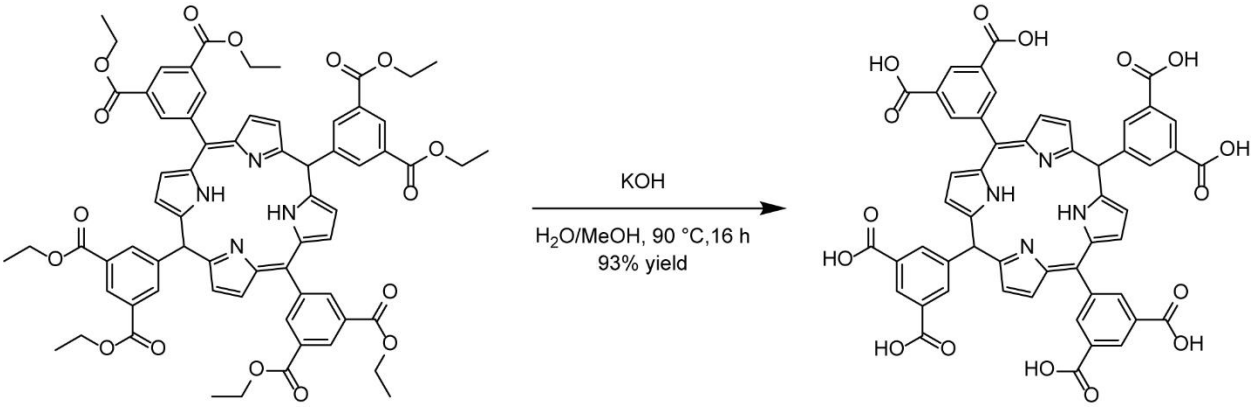

IV-S4 IV-2

A 100 mL round-bottomed flask was charged with **IV-S4** (0.400 g, 0.335 mmol, 1.00 equiv), KOH (2.00 g, 3.57 mmol, 10.7 equiv), H_2O (10 mL), and MeOH (60 mL). The reaction mixture was heated to 90 °C for 16 h. The reaction mixture was cooled to 23 °C and acidified using 1 M HCl (10 mL). The observed precipitate was isolated via vacuum filtration and washed with water (2 × 30 mL) to yield **IV-2** as a purple solid (0.302 g, 93% yield).

General Synthesis Procedure for Films

Solutions of **IV-1** or **I**V-**2** were prepared by charging a 40 mL scintillation vial with solid (10 mg for 0.25 mg/mL, 20 mg for 0.5 mg/mL, 40 mg for 1 mg/mL, 100 mg for 2.5 mg/mL), MeOH (5 mL), and triethylamine (1 mL). The reaction mixture was sonicated until dissolved, and solvent was removed *in vacuo*. MeOH (40 mL) was added to the residue to make solutions of the appropriate concentration. Solutions of **III-1** were prepared by charging a 40 mL scintillation vial with solid and MeOH (40 mL) and sonicated until dissolved.

A treated glass slide was attached to a Velmex inc. BiSlide system. The slide was dipped into a solution of **III-1** in MeOH (40 mL) for 1 min. The slide was removed from solution and dried using filtered, compressed air. The slide was then dipped into a MeOH wash solution for 1 min,

repeating the drying process. This process was then repeated with a solution of **IV-1** or **IV-2** and another wash solution. This process of four dips comprised one bilayer (BL). The wash solutions were replaced after every sample.

NMR Spectra

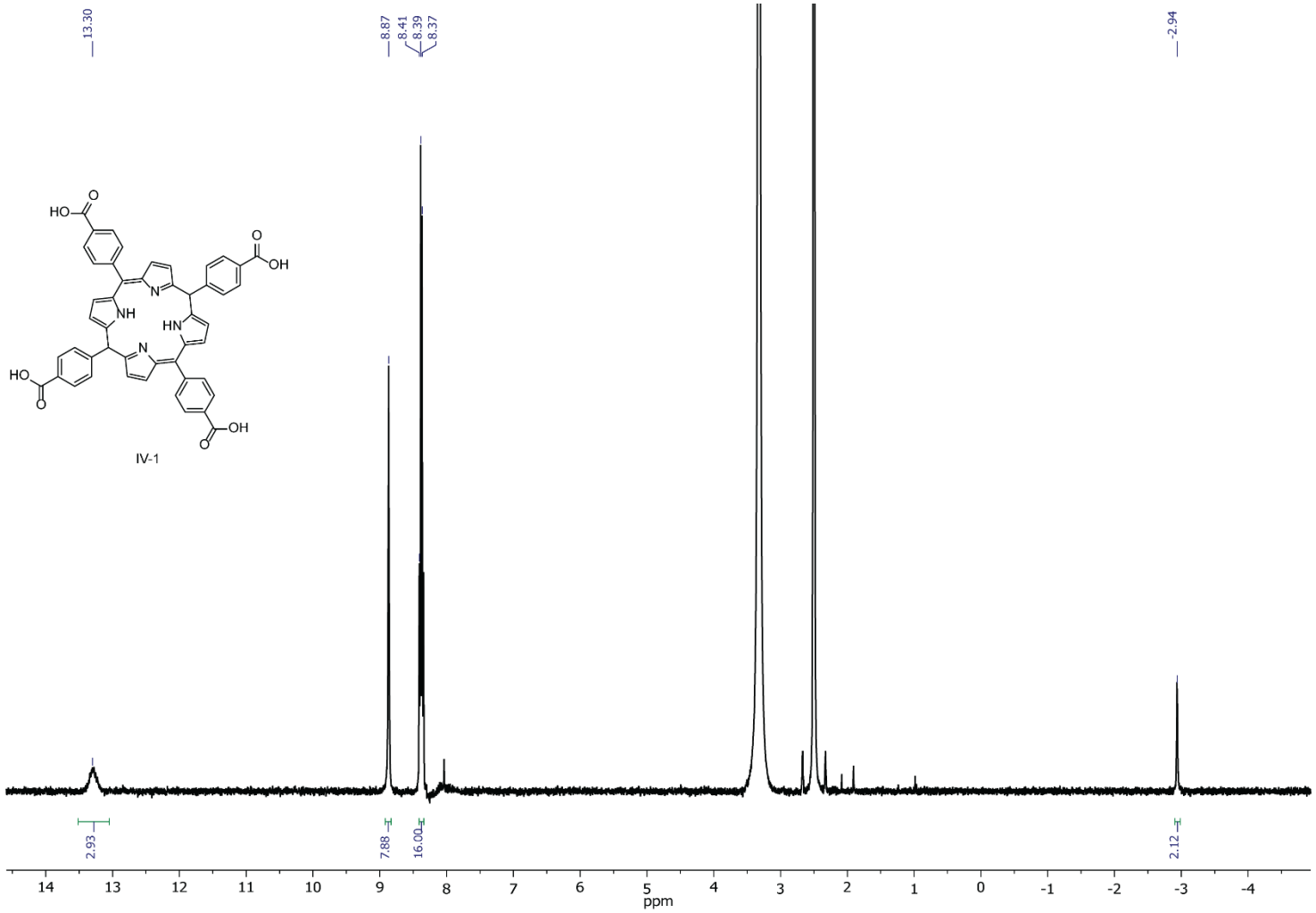

Figure IV-13. NMR of IV-1 in DMSO-d_6 at 23°C

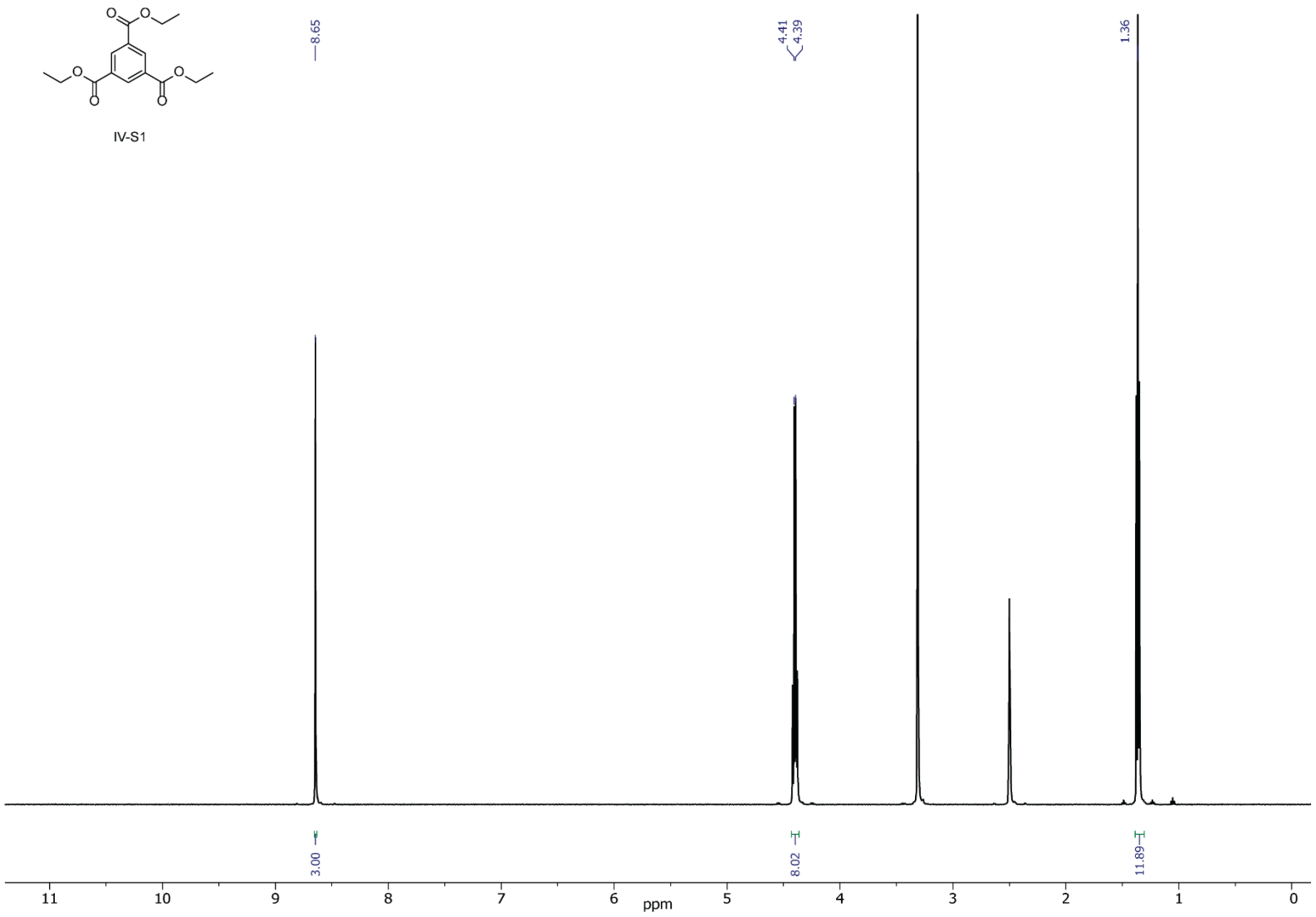

Figure IV-14. NMR of IV-S1 in DMSO-d_6 at 23°C.

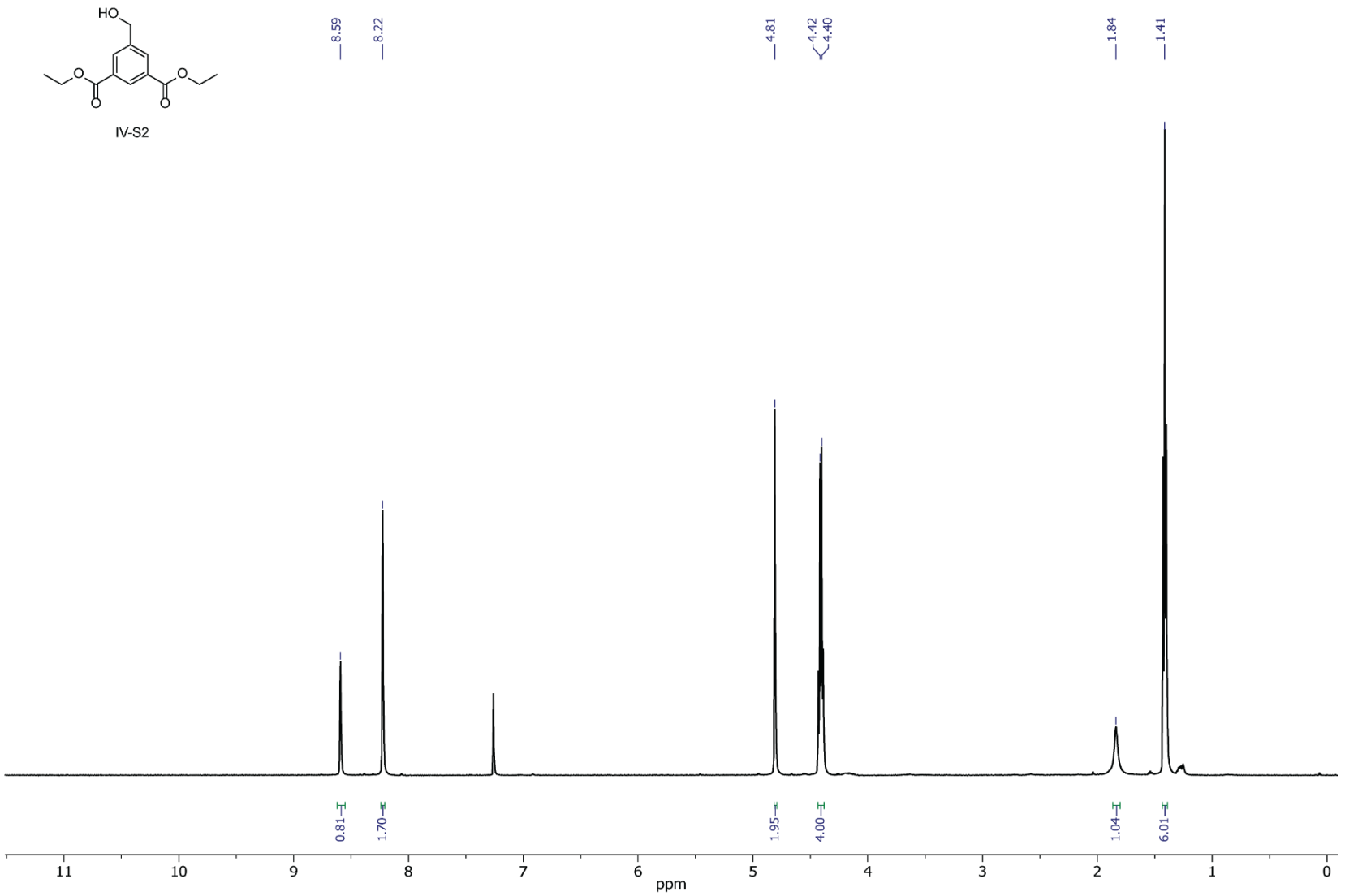

Figure IV-15. NMR of IV-S2 in $CDCl_3$ at 23°C.

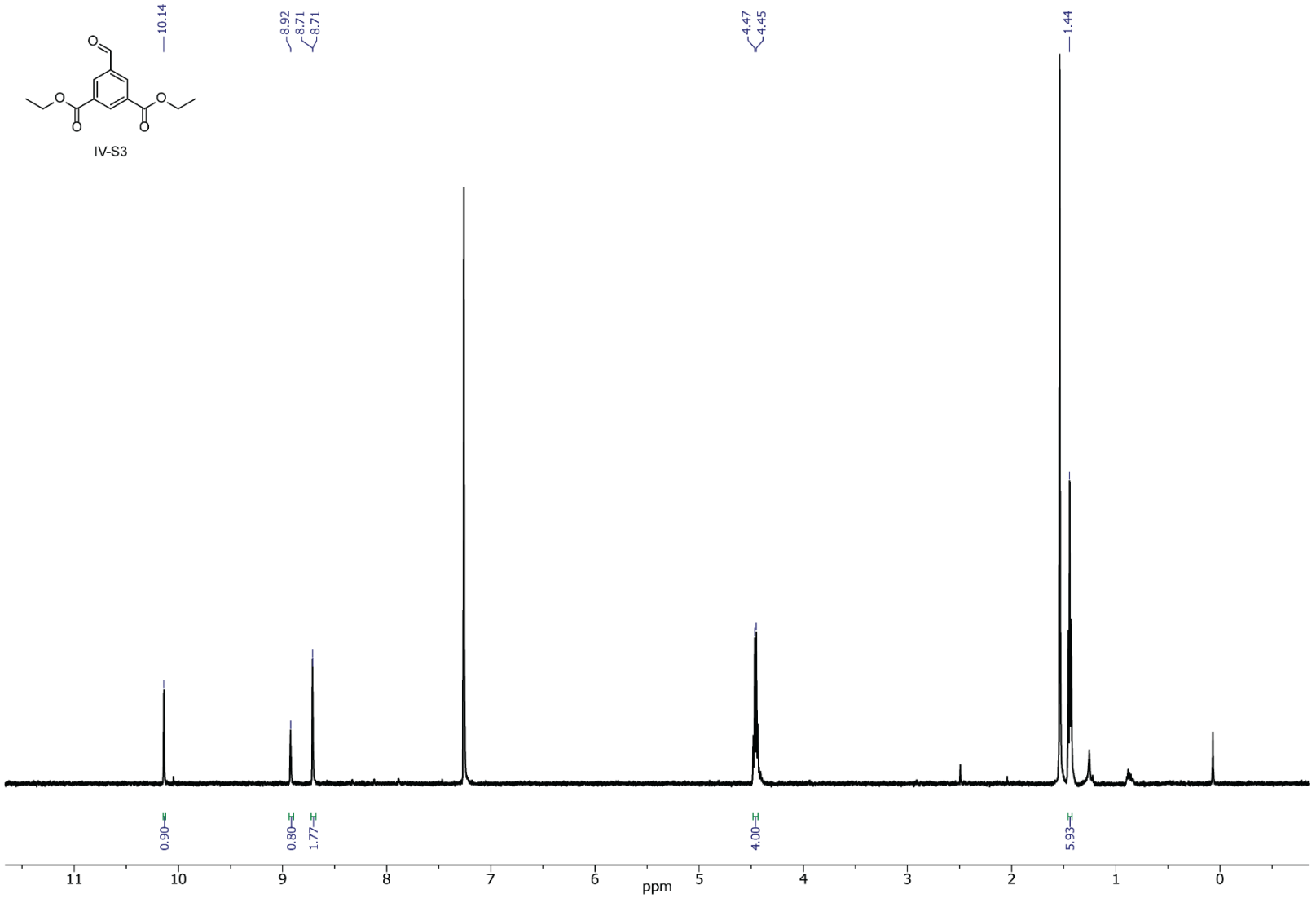

Figure IV-16. NMR of IV-S3 in $CDCl_3$ at 23°C.

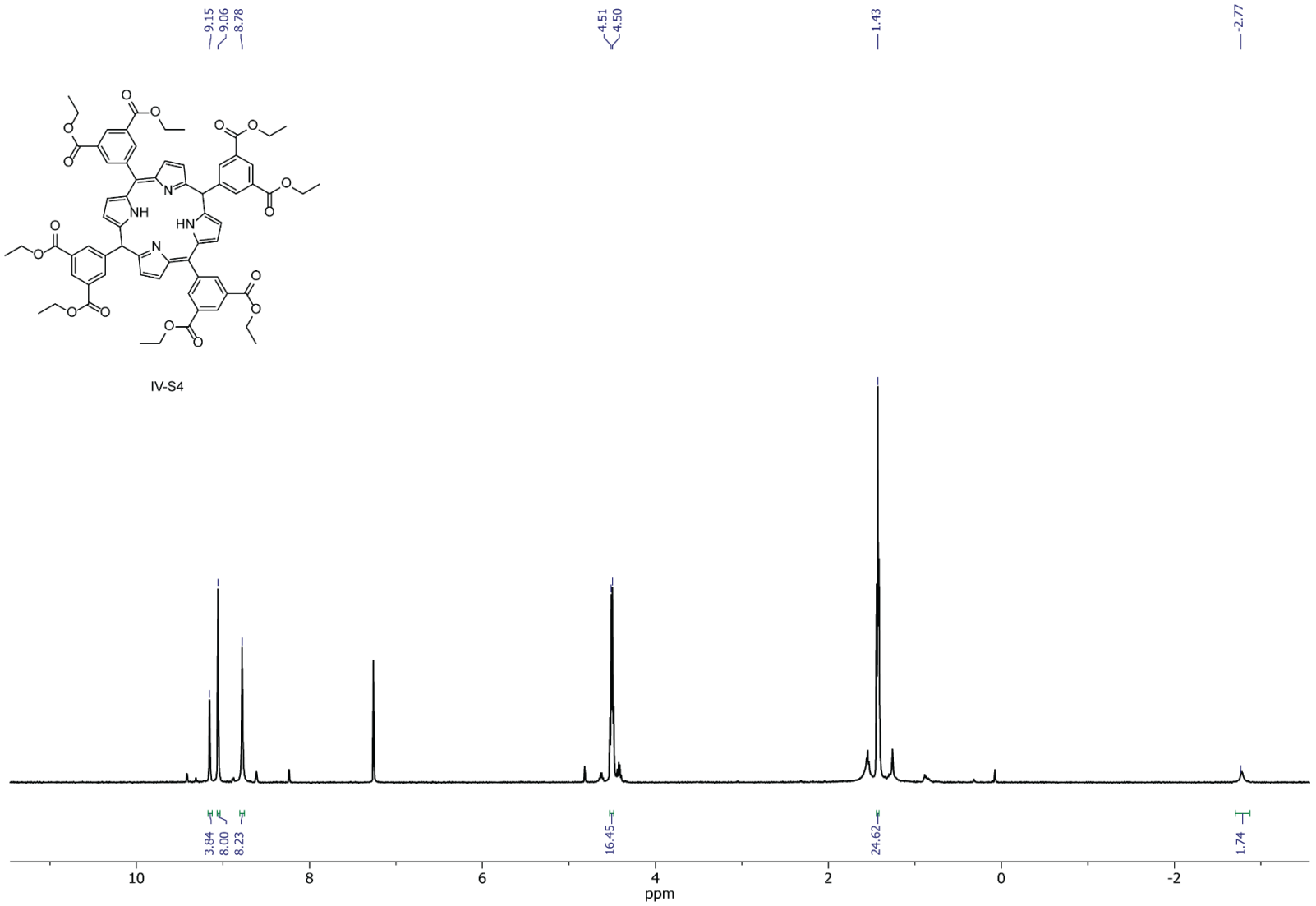

Figure IV-17. NMR of IV-S4 in $CDCl_3$ at 23°C

CHAPTER V

CONCLUDING REMARKS AND FUTURE DIRECTIONS

V.1. Summary

In the preceding chapters we have elaborated strategies to immobilize complexes that support reactive M–L multiply bonded species within porous architectures. We have pursued immobilization strategies in two classes of materials: MOFs and thin films. The MOF materials provide structural characterization via diffraction techniques but cannot be monitored *in operando* by optical methods because of opacity and the discrepancy between reactive intermediate lifetimes and measurement time. The thin films provide *in operando* capabilities but are non-crystalline and thus not amenable to diffraction-based structural characterization. As such, the two platforms are complimentary.

In Chapter II, we developed new materials based on new Ru_2 metalloligands with two different primary coordination sphere motifs, and two different peripheral functional group for post-synthetic polymerization. Metalloligands bearing carboxylate functional groups could only be subjected to ball-milling synthetic conditions because of competitive polymerization. Efforts to produce crystalline materials via ball-milling produced modest results, regardless of the material targeted. Metalloligands bearing amide functional groups could be subjected to solvothermal synthetic conditions, and yielded a crystalline, previously unknown material.

In Chapter III, we leveraged the metallomonomers synthesized in Chapter II to make optically transparent thin films with which we can affect photochemistry and potentially monitor reactive intermediates. By combining deprotonated versions of the complexes synthesized in Chapter II with Zr cage molecules, we prepared thin films with programmable thickness and

systematically modular composition. Photolysis of thin films yielded complete photoreduction, showcasing the photo addressability of our systems.

In Chapter IV we sought to better understand how to make thin films and examined the growth mechanism of films of porphyrin based thin films. We also examined how changes in the properties of the porphyrin affect the growth of thin films, and briefly introduced photochemistry we are exploring in porphyrin based thin film systems.

V.2. Future Directions

Our efforts toward synthesizing optically addressable thin films have yielded films with programmable thicknesses and which display photochemical activity. We view these as the key underpinnings for enabling *in operando* characterization and solid-state photochemistry potentially for a wide variety of systems. We have demonstrated that films can be made of **V-I** (Figure **V-I**). We hope that this platform will allow us to synthesize and study transient species confined in porous architectures such as Mn^{6+} nitrides.[268-271] We also envision these platforms being used to characterize reactive intermediates resulting from photochemistry.

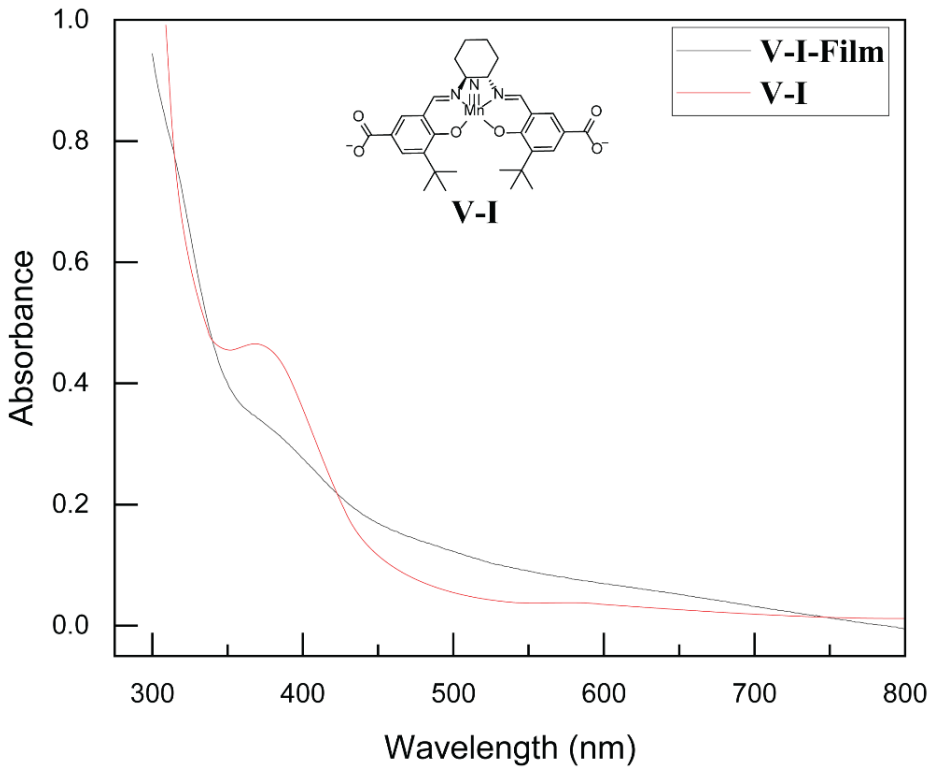

Figure V-1. UV-Vis of V-I molecule overlapped with the film of V-I and III-*1*. The spectral features are well matched.

Additionally, we view this technique as potentially applicable with oppositely charged counter ions as other cages are available.[213] This allows significant varieties of combinations with which to explore solid-state photochemistry as we can support any conceivable combination of functional groups which are commonly utilized in the coordination polymer literature.

REFERENCES

1. Hartwig, J. F., Palladium-Catalyzed Amination of Aryl Halides: Mechanism and Rational Catalyst Design. *Synlett* **1997,** *1997*, 329–340.

2. Sanford, M. S.; Love, J. A.; Grubbs, R. H., Mechanism and Activity of Ruthenium Olefin Metathesis Catalysts. *J. Am. Chem. Soc.* **2001,** *123*, 6543–6554.

3. De Rosa, C.; Di Girolamo, R.; Talarico, G., Expanding the Origin of Stereocontrol in Propene Polymerization Catalysis. *ACS Catal.* **2016,** *6*, 3767–3770.

4. Davies, H. M. L.; Liao, K., Dirhodium tetracarboxylates as catalysts for selective intermolecular C–H functionalization. *Nat. Rev. Chem.* **2019,** *3*, 347–360.

5. DiCiccio, A. M.; Longo, J. M.; Rodríguez-Calero, G. G.; Coates, G. W., Development of Highly Active and Regioselective Catalysts for the Copolymerization of Epoxides with Cyclic Anhydrides: An Unanticipated Effect of Electronic Variation. *J. Am. Chem. Soc.* **2016,** *138*, 7107–7113.

6. Hübner, S.; de Vries, J. G.; Farina, V., Why Does Industry Not Use Immobilized Transition Metal Complexes as Catalysts? *Adv. Synth. Catal.* **2016,** *358*, 3–25.

7. Li, Z.-X.; Xue, W.; Guan, B.-T.; Shi, F.-B.; Shi, Z.-J.; Jiang, H.; Yan, C.-H., A conceptual translation of homogeneous catalysis into heterogeneous catalysis: homogeneous-like heterogeneous gold nanoparticle catalyst induced by ceria supporter. *Nanoscale* **2013,** *5*, 1213–1220.

8. Taccardi, N.; Grabau, M.; Debuschewitz, J.; Distaso, M.; Brandl, M.; Hock, R.; Maier, F.; Papp, C.; Erhard, J.; Neiss, C.; Peukert, W.; Görling, A.; Steinrück, H. P.; Wasserscheid, P., Gallium-rich Pd–Ga phases as supported liquid metal catalysts. *Nat. Chem.* **2017,** *9*, 862–867.

9. De Clercq, B.; Lefebvre, F.; Verpoort, F., A new heterogeneous hybrid ruthenium catalyst being an eco-friendly option for the production of polymers and organic intermediates. *New. J. Chem.* **2002,** *26*, 1201–1208.

10. Jackson, M. N.; Surendranath, Y., Molecular Control of Heterogeneous Electrocatalysis through Graphite Conjugation. *Acc. Chem. Res.* **2019,** *52*, 3432–3441.

11. Weckhuysen, B. M.; Keller, D. E., Chemistry, spectroscopy and the role of supported vanadium oxides in heterogeneous catalysis. *Catal. Today* **2003,** *78*, 25–46.

12. Gross, E.; Liu, J. H.-C.; Toste, F. D.; Somorjai, G. A., Control of selectivity in heterogeneous catalysis by tuning nanoparticle properties and reactor residence time. *Nat. Chem.* **2012,** *4*, 947–952.

13. Kosinov, N.; Liu, C.; Hensen, E. J. M.; Pidko, E. A., Engineering of Transition Metal Catalysts Confined in Zeolites. *Chem. Mater.* **2018,** *30*, 3177–3198.

14. Shamzhy, M.; Opanasenko, M.; Concepción, P.; Martínez, A., New trends in tailoring active sites in zeolite-based catalysts. *Chem. Soc. Rev.* **2019,** *48*, 1095–1149.

15. Primo, A.; Garcia, H., Zeolites as catalysts in oil refining. *Chem. Soc. Rev.* **2014,** *43*, 7548–7561.

16. Smeets, P. J.; Woertink, J. S.; Sels, B. F.; Solomon, E. I.; Schoonheydt, R. A., Transition-Metal Ions in Zeolites: Coordination and Activation of Oxygen. *Inorg. Chem.* **2010,** *49*, 3573–3583.

17. Li, J.; Chang, H.; Ma, L.; Hao, J.; Yang, R. T., Low-temperature selective catalytic reduction of NOx with NH3 over metal oxide and zeolite catalysts—A review. *Catal. Today* **2011,** *175*, 147–156.

18. Yaghi, O. M.; O'Keeffe, M.; Ockwig, N. W.; Chae, H. K.; Eddaoudi, M.; Kim, J., Reticular synthesis and the design of new materials. *Nature* **2003,** *423*, 705–714.

19. Kalmutzki, M. J.; Hanikel, N.; Yaghi, O. M., Secondary building units as the turning point in the development of the reticular chemistry of MOFs. *Sci. Adv,* **2018,** *4* (10), eaat9180.

20. Pascanu, V.; González Miera, G.; Inge, A. K.; Martín-Matute, B., Metal–Organic Frameworks as Catalysts for Organic Synthesis: A Critical Perspective. *J. Am. Chem. Soc.* **2019,** *141*, 7223–7234.

21. Cheetham, A. K.; Kieslich, G.; Yeung, H. H. M., Thermodynamic and Kinetic Effects in the Crystallization of Metal–Organic Frameworks. *Acc. Chem. Res.* **2018,** *51*, 659–667.

22. Taube, H., Rates and Mechanisms of Substitution in Inorganic Complexes in Solution. *Chem. Rev.* **1952,** *50*, 69–126.

23. Richens, D. T., Ligand Substitution Reactions at Inorganic Centers. *Chem. Rev.* **2005,** *105*, 1961–2002.

24. Ding, M.; Cai, X.; Jiang, H.-L., Improving MOF stability: approaches and applications. *Chem. Sci.* **2019,** *10*, 10209–10230.

25. Bour, J. R.; Wright, A. M.; He, X.; Dincă, M., Bioinspired chemistry at MOF secondary building units. *Chem. Sci.* **2020,** *11*, 1728–1737.

26. Kumar, G.; Gupta, R., Molecularly designed architectures – the metalloligand way. *Chem. Soc. Rev.* **2013,** *42*, 9403–9453.

27. Song, F.; Wang, C.; Falkowski, J. M.; Ma, L.; Lin, W., Isoreticular Chiral Metal−Organic Frameworks for Asymmetric Alkene Epoxidation: Tuning Catalytic Activity by Controlling Framework Catenation and Varying Open Channel Sizes. *J. Am. Chem. Soc.* **2010,** *132*, 15390–15398.

28. Feng, X.; Chen, L.; Dong, Y.; Jiang, D., Porphyrin-based two-dimensional covalent organic frameworks: synchronized synthetic control of macroscopic structures and pore parameters. *Chem. Commun.* **2011,** *47*, 1979–1981.

29. Tanabe, K. K.; Cohen, S. M., Postsynthetic modification of metal–organic frameworks—a progress report. *Chem. Soc. Rev.* **2011,** *40*, 498–519.

30. Feng, D.; Gu, Z.-Y.; Li, J.-R.; Jiang, H.-L.; Wei, Z.; Zhou, H.-C., Zirconium-Metalloporphyrin PCN-222: Mesoporous Metal–Organic Frameworks with Ultrahigh Stability as Biomimetic Catalysts. *Angew. Chem. Int. Ed.* **2012,** *51*, 10307–10310.

31. Huh, S.; Kim, S.-J.; Kim, Y., Porphyrinic metal–organic frameworks from custom-designed porphyrins. *CrystEngComm* **2016,** *18*, 345–368.

32. Liao, H.; Wang, H.; Ding, H.; Meng, X.; Xu, H.; Wang, B.; Ai, X.; Wang, C., A 2D porous porphyrin-based covalent organic framework for sulfur storage in lithium–sulfur batteries. *J. Mater. Chem. A* **2016,** *4*, 7416–7421.

33. Jiang, W.; Yang, J.; Liu, Y.-Y.; Song, S.-Y.; Ma, J.-F., A Stable Porphyrin-Based Porous mog Metal–Organic Framework as an Efficient Solvent-Free Catalyst for C–C Bond Formation. *Inorg. Chem.* **2017,** *56*, 3036–3043.

34. Yuan, G.; Jiang, H.; Zhang, L.; Liu, Y.; Cui, Y., Metallosalen-based crystalline porous materials: Synthesis and property. *Coordin. Chem. Rev.* **2019,** *378*, 483–499.

35. Goldberg, I., Crystal engineering of porphyrin framework solids. *Chem. Commun.* **2005**, 1243–1254.

36. Cho, S.-H.; Ma, B.; Nguyen, S. T.; Hupp, J. T.; Albrecht-Schmitt, T. E., A metal–organic framework material that functions as an enantioselective catalyst for olefin epoxidation. *Chem. Commun.* **2006,** *24*, 2563–2565.

37. Gao, W.-Y.; Chrzanowski, M.; Ma, S., Metal–metalloporphyrin frameworks: a resurging class of functional materials. *Chem. Soc. Rev.* **2014,** *43*, 5841–5866.

38. Yang, X.-L.; Xie, M.-H.; Zou, C.; He, Y.; Chen, B.; O'Keeffe, M.; Wu, C.-D., Porous Metalloporphyrinic Frameworks Constructed from Metal 5,10,15,20-Tetrakis(3,5-biscarboxylphenyl)porphyrin for Highly Efficient and Selective Catalytic Oxidation of Alkylbenzenes. *J. Am. Chem. Soc.* **2012,** *134*, 10638–10645.

39. In *The Chemistry of Pincer Compounds*, Morales-Morales, D.; Jensen, C. M., Eds. Elsevier Science B.V.: Amsterdam, 2007; pp 1–450.

40. Peris, E.; Crabtree, R. H., Key factors in pincer ligand design. *Chem. Soc. Rev.* **2018,** *47*, 1959–1968.

41. Lawrence, M. A. W.; Green, K.-A.; Nelson, P. N.; Lorraine, S. C., Review: Pincer ligands—Tunable, versatile and applicable. *Polyhedron* **2018,** *143*, 11–27.

42. Alig, L.; Fritz, M.; Schneider, S., First-Row Transition Metal (De)Hydrogenation Catalysis Based On Functional Pincer Ligands. *Chem. Rev.* **2019,** *119* (4), 2681–2751.

43. He, J.; Waggoner, N. W.; Dunning, S. G.; Steiner, A.; Lynch, V. M.; Humphrey, S. M., A PCP Pincer Ligand for Coordination Polymers with Versatile Chemical Reactivity: Selective Activation of CO2 Gas over CO Gas in the Solid State. *Angew. Chem. Int. Ed.* **2016,** *55*, 12351–12355.

44. He, J.; Bohnsack, A. M.; Waggoner, N. W.; Dunning, S. G.; Lynch, V. M.; Kaska, W. C.; Humphrey, S. M., 1-D and 2-D phosphine coordination materials based on a palladium(II) PCP pincer metalloligand. *Polyhedron* **2018,** *143*, 149–156.

45. Burgess, S. A.; Kassie, A.; Baranowski, S. A.; Fritzsching, K. J.; Schmidt-Rohr, K.; Brown, C. M.; Wade, C. R., Improved Catalytic Activity and Stability of a Palladium Pincer

Complex by Incorporation into a Metal–Organic Framework. *J. Am. Chem. Soc.* **2016,** *138*, 1780–1783.

46. Kassie, A. A.; Duan, P.; Gray, M. B.; Schmidt-Rohr, K.; Woodward, P. M.; Wade, C. R., Synthesis and Reactivity of Zr MOFs Assembled from PNNNP-Ru Pincer Complexes. *Organometallics* **2019,** *38*, 3419–3428.

47. Wu, K.; Hu, J.; Shi, S.; Li, J.; Cheng, X., A thermal stable pincer-MOF with high selective and sensitive nitro explosive TNP, metal ion Fe3+ and pH sensing in aqueous solution. *Dyes Pigments* **2020,** *173*, 107993.

48. Zhang, Y.; Li, J.; Yang, X.; Zhang, P.; Pang, J.; Li, B.; Zhou, H.-C., A mesoporous NNN-pincer-based metal–organic framework scaffold for the preparation of noble-metal-free catalysts. *Chem. Commun.* **2019,** *55*, 2023–2026.

49. He, S.; Allemond, L. L.; Dunning, S. G.; Reynolds, J. E.; Lynch, V. M.; Humphrey, S. M., In situ formation and solid-state oxidation of a triselenane NSeN-pincer MOF. *Chem. Commun.* **2020,** *56*, 1286–1289.

50. Scattolin, T.; Nolan, S. P., Synthetic Routes to Late Transition Metal–NHC Complexes. *Trends in Chemistry* **2020,** *2*, 721–736.

51. Doddi, A.; Peters, M.; Tamm, M., N-Heterocyclic Carbene Adducts of Main Group Elements and Their Use as Ligands in Transition Metal Chemistry. *Chem. Rev.* **2019,** *119*, 6994–7112.

52. Froese, R. D. J.; Lombardi, C.; Pompeo, M.; Rucker, R. P.; Organ, M. G., Designing Pd–N-Heterocyclic Carbene Complexes for High Reactivity and Selectivity for Cross-Coupling Applications. *Acc. Chem. Res.* **2017,** *50*, 2244–2253.

53. Lei, P.; Meng, G.; Szostak, M., General Method for the Suzuki–Miyaura Cross-Coupling of Amides Using Commercially Available, Air- and Moisture-Stable Palladium/NHC (NHC = N-Heterocyclic Carbene) Complexes. *ACS Catal.* **2017,** *7*, 1960–1965.

54. Lalonde, M. B.; Farha, O. K.; Scheidt, K. A.; Hupp, J. T., N-Heterocyclic Carbene-Like Catalysis by a Metal–Organic Framework Material. *ACS Catal.* **2012,** *2*, 1550–1554.

55. Yuan, S.; Feng, L.; Wang, K.; Pang, J.; Bosch, M.; Lollar, C.; Sun, Y.; Qin, J.; Yang, X.; Zhang, P.; Wang, Q.; Zou, L.; Zhang, Y.; Zhang, L.; Fang, Y.; Li, J.; Zhou, H.-C., Stable Metal–Organic Frameworks: Design, Synthesis, and Applications. *Adv. Mater.* **2018,** *30*, 1704303.

56. Chun, J.; Jung, I. G.; Kim, H. J.; Park, M.; Lah, M. S.; Son, S. U., Concomitant Formation of N-Heterocyclic Carbene−Copper Complexes within a Supramolecular Network in the Self-Assembly of Imidazolium Dicarboxylate with Metal Ions. *Inorg. Chem.* **2009,** *48*, 6353–6355.

57. Burgun, A.; Crees, R. S.; Cole, M. L.; Doonan, C. J.; Sumby, C. J., A 3-D diamondoid MOF catalyst based on in situ generated [Cu(L)2] N-heterocyclic carbene (NHC) linkers: hydroboration of CO2. *Chem. Commun.* **2014,** *50*, 11760–11763.

58. Capon, P. K.; Burgun, A.; Coghlan, C. J.; Crees, R. S.; Doonan, C. J.; Sumby, C. J., Hydrogen adsorption in azolium and metalated N-heterocyclic carbene containing MOFs. *CrystEngComm* **2016,** *18*, 7003–7010.

59. Oisaki, K.; Li, Q.; Furukawa, H.; Czaja, A. U.; Yaghi, O. M., A Metal−Organic Framework with Covalently Bound Organometallic Complexes. *J. Am. Chem. Soc.* **2010,** *132*, 9262–9264.

60. Dong, Y.; Li, Y.; Wei, Y.-L.; Wang, J.-C.; Ma, J.-P.; Ji, J.; Yao, B.-J.; Dong, Y.-B., A N-heterocyclic tetracarbene Pd(ii) moiety containing a Pd(ii)–Pb(ii) bimetallic MOF for three-component cyclotrimerization via benzyne. *Chem. Commun.* **2016,** *52*, 10505–10508.

61. Kong, G.-Q.; Xu, X.; Zou, C.; Wu, C.-D., Two metal–organic frameworks based on a double azolium derivative: post-modification and catalytic activity. *Chem. Commun.* **2011,** *47*, 11005–11007.

62. Carson, F.; Martínez-Castro, E.; Marcos, R.; Miera, G. G.; Jansson, K.; Zou, X.; Martín-Matute, B., Effect of the functionalisation route on a Zr-MOF with an Ir–NHC complex for catalysis. *Chem. Commun.* **2015,** *51*, 10864–10867.

63. Ezugwu, C. I.; Mousavi, B.; Asrafa, M. A.; Mehta, A.; Vardhan, H.; Verpoort, F., An N-heterocyclic carbene based MOF catalyst for Sonogashira cross-coupling reaction. *Catal. Sci. Technol.* **2016,** *6*, 2050–2054.

64. Lee, H.-J.; Kwon, H.; Sim, J.; Song, D.; Kim, Y.; Kim, J.; Kim, K.; Lee, E., Synthetic control of coincidental formation of an N-heterocyclic carbene–copper(i) complex and imidazolium cations within metal–organic frameworks. *CrystEngComm* **2017,** *19*, 1528–1534.

65. Wang, Z.; Cohen, S. M., Postsynthetic modification of metal–organic frameworks. *Chem. Soc. Rev.* **2009,** *38*, 1315–1329.

66. Humphrey, S. M.; Allan, P. K.; Oungoulian, S. E.; Ironside, M. S.; Wise, E. R., Metal–organophosphine and metal–organophosphonium frameworks with layered honeycomb-like structures. *Dalton Trans.* **2009,** *13*, 2298–2305.

67. Dunning, S. G.; Nandra, G.; Conn, A. D.; Chai, W.; Sikma, R. E.; Lee, J. S.; Kunal, P.; Reynolds III, J. E.; Chang, J.-S.; Steiner, A.; Henkelman, G.; Humphrey, S. M., A Metal–Organic Framework with Cooperative Phosphines That Permit Post-Synthetic Installation of Open Metal Sites. *Angew. Chem. Int. Ed.* **2018,** *57*, 9295–9299.

68. Falkowski, J. M.; Sawano, T.; Zhang, T.; Tsun, G.; Chen, Y.; Lockard, J. V.; Lin, W., Privileged Phosphine-Based Metal–Organic Frameworks for Broad-Scope Asymmetric Catalysis. *J. Am. Chem. Soc.* **2014,** *136*, 5213–5216.

69. Wu, L.; Annibale, V. T.; Jiao, H.; Brookfield, A.; Collison, D.; Manners, I., Homo- and heterodehydrocoupling of phosphines mediated by alkali metal catalysts. *Nat. Commun.* **2019,** *10*, 2786.

70. Gao, W.-Y.; Ezazi, A. A.; Wang, C.-H.; Moon, J.; Abney, C.; Wright, J.; Powers, D. C., Metallopolymerization as a Strategy to Translate Ligand-Modulated Chemoselectivity to Porous Catalysts. *Organometallics* **2019,** *38*, 3436–3443.

71. Gao, W.-Y.; Van Trieste Iii, G. P.; Powers, D. C., Synthesis of atomically precise single-crystalline Ru2-based coordination polymers. *Dalton Trans.* **2020,** *49*, 16077–16081.

72. Kong, X.; Deng, H.; Yan, F.; Kim, J.; Swisher, J. A.; Smit, B.; Yaghi, O. M.; Reimer, J. A., Mapping of Functional Groups in Metal-Organic Frameworks. *Science* **2013,** *341*, 882–885.

73. Fukushima, T.; Horike, S.; Kobayashi, H.; Tsujimoto, M.; Isoda, S.; Foo, M. L.; Kubota, Y.; Takata, M.; Kitagawa, S., Modular Design of Domain Assembly in Porous Coordination Polymer Crystals via Reactivity-Directed Crystallization Process. *J. Am. Chem. Soc.* **2012,** *134*, 13341–13347.

74. Brozek, C. K.; Dincă, M., Cation exchange at the secondary building units of metal–organic frameworks. *Chem. Soc. Rev.* **2014,** *43*, 5456–5467.

75. Andreeva, A. B.; Le, K. N.; Chen, L.; Kellman, M. E.; Hendon, C. H.; Brozek, C. K., Soft Mode Metal-Linker Dynamics in Carboxylate MOFs Evidenced by Variable-Temperature Infrared Spectroscopy. *J. Am. Chem. Soc.* **2020,** *Just Accepted*.

76. Dincă, M.; Long, J. R., High-Enthalpy Hydrogen Adsorption in Cation-Exchanged Variants of the Microporous Metal−Organic Framework Mn3[(Mn4Cl)3(BTT)8(CH3OH)10]2. *J. Am. Chem. Soc.* **2007,** *129*, 11172–11176.

77. Botas, J. A.; Calleja, G.; Sánchez-Sánchez, M.; Orcajo, M. G., Cobalt Doping of the MOF-5 Framework and Its Effect on Gas-Adsorption Properties. *Langmuir* **2010,** *26*, 5300–5303.

78. Brozek, C. K.; Michaelis, V. K.; Ong, T.-C.; Bellarosa, L.; López, N.; Griffin, R. G.; Dincă, M., Dynamic DMF Binding in MOF-5 Enables the Formation of Metastable Cobalt-Substituted MOF-5 Analogues. *ACS Cent. Sci.* **2015,** *1*, 252–260.

79. Brozek, C. K.; Dincă, M., Ti3+-, V2+/3+-, Cr2+/3+-, Mn2+-, and Fe2+-Substituted MOF-5 and Redox Reactivity in Cr- and Fe-MOF-5. *J. Am. Chem. Soc.* **2013,** *135*, 12886–12891.

80. Stubbs, A. W.; Braglia, L.; Borfecchia, E.; Meyer, R. J.; Román- Leshkov, Y.; Lamberti, C.; Dincă, M., Selective Catalytic Olefin Epoxidation with MnII-Exchanged MOF-5. *ACS Catal.* **2018,** *8*, 596–601.

81. Park, H. D.; Comito, R. J.; Wu, Z.; Zhang, G.; Ricke, N.; Sun, C.; Van Voorhis, T.; Miller, J. T.; Román-Leshkov, Y.; Dincă, M., Gas-Phase Ethylene Polymerization by Single-Site Cr Centers in a Metal–Organic Framework. *ACS Catal.* **2020,** *10*, 3864–3870.

82. Stubbs, A. W.; Dincă, M., Selective Oxidation of C–H Bonds through a Manganese(III) Hydroperoxo in MnII-Exchanged CFA-1. *Inorg. Chem.* **2019,** *58*, 13221–13228.

83. Comito, R. J.; Fritzsching, K. J.; Sundell, B. J.; Schmidt-Rohr, K.; Dincă, M., Single-Site Heterogeneous Catalysts for Olefin Polymerization Enabled by Cation Exchange in a Metal-Organic Framework. *J. Am. Chem. Soc.* **2016,** *138*, 10232–10237.

84. Shultz, A. M.; Sarjeant, A. A.; Farha, O. K.; Hupp, J. T.; Nguyen, S. T., Post-Synthesis Modification of a Metal–Organic Framework To Form Metallosalen-Containing MOF Materials. *J. Am. Chem. Soc.* **2011,** *133*, 13252–13255.

85. Wang, X.-S.; Chrzanowski, M.; Wojtas, L.; Chen, Y.-S.; Ma, S., Formation of a Metalloporphyrin-Based Nanoreactor by Postsynthetic Metal–Ion Exchange of a Polyhedral-Cage Containing a Metal–Metalloporphyrin Framework. *Chem. Eur. J.* **2013,** *19*, 3297–3301.

86. Horváth, O.; Huszánk, R.; Valicsek, Z.; Lendvay, G., Photophysics and photochemistry of kinetically labile, water-soluble porphyrin complexes. *Coord. Chem. Rev.* **2006,** *250*, 1792–1803.

87. Brozek, C. K.; Bellarosa, L.; Soejima, T.; Clark, T. V.; López, N.; Dincă, M., Solvent-Dependent Cation Exchange in Metal–Organic Frameworks. *Chem. Eur. J.* **2014,** *20*, 6871–6874.

88. Brozek, C. K.; Dincă, M., Lattice-imposed geometry in metal–organic frameworks: lacunary Zn4O clusters in MOF-5 serve as tripodal chelating ligands for Ni2+. *Chem. Sci.* **2012,** *3*, 2110–2113.

89. Bellarosa, L.; Brozek, C. K.; García-Melchor, M.; Dincă, M.; López, N., When the Solvent Locks the Cage: Theoretical Insight into the Transmetalation of MOF-5 Lattices and Its Kinetic Limitations. *Chem. Mater.* **2015,** *27*, 3422–3429.

90. Wang, C.-H.; Gao, W.-Y.; Ma, Q.; Powers, D. C., Templating metastable Pd2 carboxylate aggregates. *Chem. Sci.* **2019,** *10*, 1823–1830.

91. Kim, H. K.; Yun, W. S.; Kim, M.-B.; Kim, J. Y.; Bae, Y.-S.; Lee, J.; Jeong, N. C., A Chemical Route to Activation of Open Metal Sites in the Copper-Based Metal–Organic Framework Materials HKUST-1 and Cu-MOF-2. *J. Am. Chem. Soc.* **2015,** *137*, 10009–10015.

92. Lian, X.; Feng, D.; Chen, Y.-P.; Liu, T.-F.; Wang, X.; Zhou, H.-C., The preparation of an ultrastable mesoporous Cr(iii)-MOF via reductive labilization. *Chem. Sci.* **2015,** *6*, 7044–7048.

93. Helm, L.; Merbach, A. E., Water exchange on metal ions: experiments and simulations. *Coordin. Chem. Rev.* **1999,** *187*, 151–181.

94. Li, W.-H.; Deng, W.-H.; Wang, G.-E.; Xu, G., Conductive MOFs. *EnergyChem* **2020,** *2*, 100029.

95. Yang, X.; Xu, Q., Bimetallic Metal–Organic Frameworks for Gas Storage and Separation. *Cryst. Growth Des.* **2017,** *17*, 1450–1455.

96. Wang, C.; An, B.; Lin, W., Metal–Organic Frameworks in Solid–Gas Phase Catalysis. *ACS Catal.* **2019,** *9*, 130–146.

97. Abednatanzi, S.; Gohari Derakhshandeh, P.; Depauw, H.; Coudert, F.-X.; Vrielinck, H.; Van Der Voort, P.; Leus, K., Mixed-metal metal–organic frameworks. *Chem. Soc. Rev.* **2019,** *48*, 2535–2565.

98. Masoomi, M. Y.; Morsali, A.; Dhakshinamoorthy, A.; Garcia, H., Mixed-Metal MOFs: Unique Opportunities in Metal–Organic Framework (MOF) Functionality and Design. *Angew. Chem. Int. Ed.* **2019,** *58*, 15188–15205.

99. Chen, L.; Wang, H.-F.; Li, C.; Xu, Q., Bimetallic metal–organic frameworks and their derivatives. *Chem. Sci.* **2020,** *11*, 5369–5403.

100. Boissonnault, J. A.; Wong-Foy, A. G.; Matzger, A. J., Core–Shell Structures Arise Naturally During Ligand Exchange in Metal–Organic Frameworks. *J. Am. Chem. Soc.* **2017,** *139*, 14841–14844.

101. Liu, Q.; Cong, H.; Deng, H., Deciphering the Spatial Arrangement of Metals and Correlation to Reactivity in Multivariate Metal–Organic Frameworks. *J. Am. Chem. Soc.* **2016,** *138*, 13822–13825.

102. Ji, Z.; Li, T.; Yaghi, O. M., Sequencing of metals in multivariate metal-organic frameworks. *Science* **2020,** *369*, 674–680.

103. Korzyński, M. D.; Braglia, L.; Borfecchia, E.; Lomachenko, K. A.; Baldansuren, A.; Hendon, C. H.; Lamberti, C.; Dincă, M., Quo vadis niobium? Divergent coordination behavior of early-transition metals towards MOF-5. *Chem. Sci.* **2019,** *10*, 5906–5910.

104. Song, Y.; Li, Z.; Ji, P.; Kaufmann, M.; Feng, X.; Chen, J. S.; Wang, C.; Lin, W., Metal–Organic Framework Nodes Support Single-Site Nickel(II) Hydride Catalysts for the Hydrogenolysis of Aryl Ethers. *ACS Catal.* **2019,** *9*, 1578–1583.

105. Bloch, E. D.; Britt, D.; Lee, C.; Doonan, C. J.; Uribe-Romo, F. J.; Furukawa, H.; Long, J. R.; Yaghi, O. M., Metal Insertion in a Microporous Metal−Organic Framework Lined with 2,2′-Bipyridine. *J. Am. Chem. Soc.* **2010,** *132*, 14382–14384.

106. Guo, W.; Xia, W.; Cai, K.; Wu, Y.; Qiu, B.; Liang, Z.; Qu, C.; Zou, R., Kinetic-Controlled Formation of Bimetallic Metal–Organic Framework Hybrid Structures. *Small* **2017,** *13*, 1702049.

107. Feng, D.; Wang, K.; Wei, Z.; Chen, Y.-P.; Simon, C. M.; Arvapally, R. K.; Martin, R. L.; Bosch, M.; Liu, T.-F.; Fordham, S.; Yuan, D.; Omary, M. A.; Haranczyk, M.; Smit, B.; Zhou, H.-C., Kinetically tuned dimensional augmentation as a versatile synthetic route towards robust metal–organic frameworks. *Nat. Commun.* **2014,** *5*, 5723.

108. Dong, L.-Z.; Zhang, L.; Liu, J.; Huang, Q.; Lu, M.; Ji, W.-X.; Lan, Y.-Q., Stable Heterometallic Cluster-Based Organic Framework Catalysts for Artificial Photosynthesis. *Angew. Chem. Int. Ed.* **2020,** *59*, 2659–2663.

109. Yuan, S.; Qin, J.-S.; Xu, H.-Q.; Su, J.; Rossi, D.; Chen, Y.; Zhang, L.; Lollar, C.; Wang, Q.; Jiang, H.-L.; Son, D. H.; Xu, H.; Huang, Z.; Zou, X.; Zhou, H.-C., [Ti8Zr2O12(COO)16] Cluster: An Ideal Inorganic Building Unit for Photoactive Metal–Organic Frameworks. *ACS Cent. Sci.* **2018,** *4*, 105–111.

110. Nguyen, H. L.; Gándara, F.; Furukawa, H.; Doan, T. L. H.; Cordova, K. E.; Yaghi, O. M., A Titanium–Organic Framework as an Exemplar of Combining the Chemistry of Metal– and Covalent–Organic Frameworks. *J. Am. Chem. Soc.* **2016,** *138*, 4330–4333.

111. Yuan, S.; Liu, T.-F.; Feng, D.; Tian, J.; Wang, K.; Qin, J.; Zhang, Q.; Chen, Y.-P.; Bosch, M.; Zou, L.; Teat, S. J.; Dalgarno, S. J.; Zhou, H.-C., A single crystalline porphyrinic titanium metal–organic framework. *Chem. Sci.* **2015,** *6*, 3926–3930.

112. Dan-Hardi, M.; Serre, C.; Frot, T.; Rozes, L.; Maurin, G.; Sanchez, C.; Férey, G., A New Photoactive Crystalline Highly Porous Titanium(IV) Dicarboxylate. *J. Am. Chem. Soc.* **2009,** *131*, 10857–10859.

113. Nickerl, G.; Stoeck, U.; Burkhardt, U.; Senkovska, I.; Kaskel, S., A catalytically active porous coordination polymer based on a dinuclear rhodium paddle-wheel unit. *J. Mater. Chem. A* **2014,** *2*, 144–148.

114. Kozachuk, O.; Yusenko, K.; Noei, H.; Wang, Y.; Walleck, S.; Glaser, T.; Fischer, R. A., Solvothermal growth of a ruthenium metal–organic framework featuring HKUST-1 structure type as thin films on oxide surfaces. *Chem. Commun.* **2011,** *47*, 8509–8511.

115. Heinz, W. R.; Kratky, T.; Drees, M.; Wimmer, A.; Tomanec, O.; Günther, S.; Schuster, M.; Fischer, R. A., Mixed precious-group metal–organic frameworks: a case study of the HKUST-1 analogue [RuxRh3−x(BTC)2]. *Dalton Trans.* **2019,** *48*, 12031–12039.

116. Han, Y.; Zheng, H.; Liu, K.; Wang, H.; Huang, H.; Xie, L.-H.; Wang, L.; Li, J.-R., In-Situ Ligand Formation-Driven Preparation of a Heterometallic Metal–Organic Framework for Highly Selective Separation of Light Hydrocarbons and Efficient Mercury Adsorption. *ACS Appl. Mater. Interfaces* **2016,** *8*, 23331–23337.

117. Gao, W.-Y.; Sur, A.; Wang, C.-H.; Lorzing, G. R.; Antonio, A. M.; Taggart, G. A.; Ezazi, A. A.; Bhuvanesh, N.; Bloch, E. D.; Powers, D. C., Atomically Precise Crystalline Materials Based on Kinetically Inert Metal Ions via Reticular Mechanopolymerization. *Angew. Chem. Int. Ed.* **2020,** *132*, 10970–10975.

118. Stolar, T.; Užarević, K., Mechanochemistry: an efficient and versatile toolbox for synthesis, transformation, and functionalization of porous metal–organic frameworks. *CrystEngComm* **2020,** *22*, 4511–4525.

119. Gotthardt, M. A.; Schoch, R.; Wolf, S.; Bauer, M.; Kleist, W., Synthesis and characterization of bimetallic metal–organic framework Cu–Ru-BTC with HKUST-1 structure. *Dalton Trans.* **2015,** *44*, 2052–2056.

120. Thiam, Z.; Abou-Hamad, E.; Dereli, B.; Liu, L.; Emwas, A.-H.; Ahmad, R.; Jiang, H.; Isah, A. A.; Ndiaye, P. B.; Taoufik, M.; Han, Y.; Cavallo, L.; Basset, J.-M.; Eddaoudi, M., Extension of Surface Organometallic Chemistry to Metal–Organic Frameworks: Development of a Well-Defined Single Site [(≡Zr–O−)W(═O)(CH2tBu)3] Olefin Metathesis Catalyst. *J. Am. Chem. Soc.* **2020,** *142*, 16690-16703.

121. Ahn, S.; Nauert, S. L.; Buru, C. T.; Rimoldi, M.; Choi, H.; Schweitzer, N. M.; Hupp, J. T.; Farha, O. K.; Notestein, J. M., Pushing the Limits on Metal–Organic Frameworks as a Catalyst Support: NU-1000 Supported Tungsten Catalysts for o-Xylene Isomerization and Disproportionation. *J. Am. Chem. Soc.* **2018,** *140*, 8535–8543.

122. Desai, S. P.; Ye, J.; Zheng, J.; Ferrandon, M. S.; Webber, T. E.; Platero-Prats, A. E.; Duan, J.; Garcia-Holley, P.; Camaioni, D. M.; Chapman, K. W.; Delferro, M.; Farha, O. K.; Fulton, J. L.; Gagliardi, L.; Lercher, J. A.; Penn, R. L.; Stein, A.; Lu, C. C., Well-Defined Rhodium–Gallium Catalytic Sites in a Metal–Organic Framework: Promoter-Controlled Selectivity in Alkyne Semihydrogenation to E-Alkenes. *J. Am. Chem. Soc.* **2018,** *140*, 15309–15318.

123. Ezazi, A. A.; Gao, W.-Y.; Powers, D. C., Leveraging Exchange Kinetics for the Synthesis of Atomically Precise Porous Catalysts. *ChemCatChem* **2021,** *13*, 2117–2131.

124. Park, Y.; Kim, Y.; Chang, S., Transition Metal-Catalyzed C–H Amination: Scope, Mechanism, and Applications. *Chem. Rev.* **2017,** *117*, 9247–9301.

125. Bollinger, J. M.; Broderick, J. B., Frontiers in enzymatic C–H-bond activation. *Curr. Opin. Chem. Biol.* **2009,** *13*, 51–57.

126. Rohde, J.-U.; In, J.-H.; Lim, M. H.; Brennessel, W. W.; Bukowski, M. R.; Stubna, A.; Münck, E.; Nam, W.; Que, L., Crystallographic and spectroscopic characterization of a nonheme Fe (IV)= O complex. *Science* **2003,** *299*, 1037–1039.

127. Pestovsky, O.; Bakac, A., Reactivity of aqueous Fe (IV) in hydride and hydrogen atom transfer reactions. *J. Am. Chem. Soc.* **2004,** *126*, 13757–13764.

128. Puri, M.; Que Jr, L., Toward the synthesis of more reactive S= 2 non-heme oxoiron (IV) complexes. *Acc. Chem. Res* **2015,** *48*, 2443–2452.

129. Aquino, M. A. S., Diruthenium and diosmium tetracarboxylates: synthesis, physical properties and applications. *Coord. Chem. Rev.* **1998,** *170*, 141–202.

130. Nakamura, E.; Yoshikai, N.; Yamanaka, M., Mechanism of C−H Bond Activation/C−C Bond Formation Reaction between Diazo Compound and Alkane Catalyzed by Dirhodium Tetracarboxylate. *J. Am. Chem. Soc.* **2002,** *124*, 7181–7192.

131. Das, A.; Reibenspies, J. H.; Chen, Y.-S.; Powers, D. C., Direct Characterization of a Reactive Lattice-Confined Ru2 Nitride by Photocrystallography. *J. Am. Chem. Soc.* **2017,** *139*, 2912–2915.

132. Corcos, A. R.; Long, A. K. M.; Guzei, I. A.; Berry, J. F., A Synthetic Cycle for Nitrogen Atom Transfer Featuring a Diruthenium Nitride Intermediate. *Eur. J. Inorg. Chem.* **2013,** *2013*, 3808–3811.

133. Zhao, X. S.; Bao, X. Y.; Guo, W.; Lee, F. Y., Immobilizing catalysts on porous materials. *Mater. Today* **2006,** (3), 32–39.

134. Grzech, A.; Yang, J.; Dingemans, T. J.; Srinivasan, S.; Magusin, P. C. M. M.; Mulder, F. M., Irreversible High-Temperature Hydrogen Interaction with the Metal Organic Framework Cu3(BTC)2. *J. Phys. Chem. C* **2011,** (43), 21521–21525.

135. Bennett, T. D.; Cheetham, A. K., Amorphous Metal–Organic Frameworks. *Acc. Chem. Res* **2014,** (5), 1555–1562.

136. Cohen, S. M.; Zhang, Z.; Boissonnault, J. A., Toward "metalloMOFzymes": Metal–Organic Frameworks with Single-Site Metal Catalysts for Small-Molecule Transformations. *Inorg. Chem.* **2016,** *55*, 7281–7290.

137. Klet, R. C.; Tussupbayev, S.; Borycz, J.; Gallagher, J. R.; Stalzer, M. M.; Miller, J. T.; Gagliardi, L.; Hupp, J. T.; Marks, T. J.; Cramer, C. J.; Delferro, M.; Farha, O. K., Single-Site

Organozirconium Catalyst Embedded in a Metal–Organic Framework. *J. Am. Chem. Soc.* **2015,** *137*, 15680–15683.

138. Cheetham, A. K.; Kieslich, G.; Yeung, H. H. M., Thermodynamic and Kinetic Effects in the Crystallization of Metal–Organic Frameworks. *Acc. Chem. Res* **2018,** *51*, 659–667.

139. Rieth, A. J.; Wright, A. M.; Dincă, M., Kinetic stability of metal–organic frameworks for corrosive and coordinating gas capture. *Nat. Rev. Mater.* **2019,** *4*, 708–725.

140. Van Vleet, M. J.; Weng, T.; Li, X.; Schmidt, J. R., In Situ, Time-Resolved, and Mechanistic Studies of Metal–Organic Framework Nucleation and Growth. *Chem. Rev.* **2018,** *118*, 3681–3721.

141. Cohen, S. M., The Postsynthetic Renaissance in Porous Solids. *J. Am. Chem. Soc.* **2017,** *139*, 2855-2863.

142. Kalaj, M.; Cohen, S. M., Postsynthetic Modification: An Enabling Technology for the Advancement of Metal–Organic Frameworks. *ACS Cent. Sci.* **2020,** *6*, 1046–1057.

143. Cohen, S. M., Postsynthetic Methods for the Functionalization of Metal–Organic Frameworks. *Chem. Rev.* **2012,** *112*, 970–1000.

144. Srivastava, S.; Gupta, R., Metalloligands to material: design strategies and network topologies. *CrystEngComm* **2016,** *18*, 9185–9208.

145. Bohnsack, A. M.; Ibarra, I. A.; Bakhmutov, V. I.; Lynch, V. M.; Humphrey, S. M., Rational Design of Porous Coordination Polymers Based on Bis(phosphine)MCl2 Complexes That Exhibit High-Temperature H2 Sorption and Chemical Reactivity. *Journal of the American Chemical Society* **2013,** *135*, 16038–16041.

146. Reiner, B. R.; Mucha, N. T.; Rothstein, A.; Temme, J. S.; Duan, P.; Schmidt-Rohr, K.; Foxman, B. M.; Wade, C. R., Zirconium Metal–Organic Frameworks Assembled from Pd and Pt

PNNNP Pincer Complexes: Synthesis, Postsynthetic Modification, and Lewis Acid Catalysis. *Inorg. Chem.* **2018,** *57*, 2663–2672.

147. Takamizawa, S.; Ohmura, T.; Yamaguchi, K.; Mori, W., Synthesis and gas-occlusion properties of ruthenium (II, III) dicarboxylates (fumarate, trans-trans-muconate and terephthalate) bridged by halogen atoms. *Mol. Cryst. Liq. Cryst. Sci. Technol., Sect. A* **2000,** *342*, 199–204.

148. Zhang, W.; Kozachuk, O.; Medishetty, R.; Schneemann, A.; Wagner, R.; Khaletskaya, K.; Epp, K.; Fischer, R. A., Controlled SBU Approaches to Isoreticular Metal-Organic Framework Ruthenium-Analogues of HKUST-1. *Eur. J. Inorg. Chem.* **2015,** *2015*, 3913–3920.

149. Elahi, S. M.; Lai, Q.-H.; Ren, M.; Bao, S.-S.; Kurmoo, M.; Zheng, L.-M., Two-and Three-Dimensional Heterometallic Ln [Ru2-α-Ammonium Diphosphonate] Nets: Structures, Porosity, Magnetism, and Proton Conductivity. *Inorganic Chemistry* **2019**.

150. Heinz, W. R.; Kratky, T.; Drees, M.; Wimmer, A.; Tomanec, O.; Guenther, S.; Schuster, M.; Fischer, R. A., Mixed Precious-Group Metal-Organic Frameworks: Case Study of the HKUST-1 Analogue [Ru x Rh 3-x (BTC) 2]. *Dalton Trans.* **2019**.

151. Miyasaka, H.; Izawa, T.; Takahashi, N.; Yamashita, M.; Dunbar, K. R., Long-range ordered magnet of a charge-transfer Ru24+/TCNQ two-dimensional network compound. *J. Am. Chem. Soc.* **2006,** *128*, 11358–11359.

152. Raghavan, A.; Mash, B. L.; Ren, T., Forging Ru–Csp2 Bonds in Paddlewheel Complexes Using the Lithium–Halogen Exchange Reaction. *Inorg. Chem.* **2019,** *58*, 2618–2626.

153. Furukawa, S.; Ohba, M.; Kitagawa, S., Rational synthesis of a two-dimensional honeycomb structure based on a paramagnetic paddlewheel diruthenium complex. *Chem. Comm.* **2005,** (7), 865–867.

154. Takamizawa, S.; Yamaguchi, K.; Mori, W., The gas-occlusion properties of dicarboxylate (fumarate, trans-trans-muconate and terephthalate) ruthenium(II,III) dinuclear complexes. *Inorg. Chem. Commun.* **1998,** *1*, 177–178.

155. Ribeiro, G.; Vichi, F. M.; de Oliveira Silva, D., Synthesis, characterization and adsorption properties of porous mixed valent diruthenium(II,III)-terephthalate and diruthenium(II,III)-adipate polymers. *J. Mol. Struct.* **2008,** *890*, 209–214.

156. Deegan, M. M.; Antonio, A. M.; Taggart, G. A.; Bloch, E. D., Manipulating solvent and solubility in the synthesis, activation, and modification of permanently porous coordination cages. *Coord. Chem. Rev.* **2021,** *430*, 213679.

157. Lundt, B. F.; Johansen, N. L.; Vølund, A.; Markussen, J., REMOVAL OF t-BUTYL AND t-BUTOXYCARBONYL PROTECTING GROUPS WITH TRIFLUOROACETIC ACID. *Int. J. Pept. Protein Res.* **1978,** *12*, 258–268.

158. Santos, R. L. S. R.; van Eldik, R.; de Oliveira Silva, D., Thermodynamics of Axial Substitution and Kinetics of Reactions with Amino Acids for the Paddlewheel Complex Tetrakis(acetato)chloridodiruthenium(II,III). *Inorg. Chem.* **2012,** *51*, 6615–6625.

159. Tolbatov, I.; Marrone, A., Kinetics of Reactions of Dirhodium and Diruthenium Paddlewheel Tetraacetate Complexes with Nucleophilic Protein Sites: Computational Insights. *Inorg. Chem.* **2022,** *61*, 16421–16429.

160. Matsunaga, S.; Hasada, K.-i.; Sugiura, K.; Kitamura, N.; Kudo, Y.; Endo, N.; Mori, W., Hetero Bi-Paddle-Wheel Coordination Networks: A New Synthetic Route to Rh-Containing Metal–Organic Frameworks. *Bull. Chem. Soc. J.* **2012,** *85*, 433–438.

161. Villalobos, L.; Cao, Z.; Fanwick, P. E.; Ren, T., Diruthenium(II,III) tetramidates as a new class of oxygenation catalysts. *Dalton. Trans.* **2012,** *41*, 644–650.

162. Friščić, T.; Trask, A. V.; Jones, W.; Motherwell, W. D. S., Screening for Inclusion Compounds and Systematic Construction of Three-Component Solids by Liquid-Assisted Grinding. *Angew. Chem. Int. Ed.* **2006,** *45*, 7546–7550.

163. Friščić, T.; Childs, S. L.; Rizvi, S. A. A.; Jones, W., The role of solvent in mechanochemical and sonochemical cocrystal formation: a solubility-based approach for predicting cocrystallisation outcome. *CrystEngComm* **2009,** *11*, 418–426.

164. Bowmaker, G. A., Solvent-assisted mechanochemistry. *Chem. Commun.* **2013,** *49*, 334–348.

165. Choi, J.; Gillan, E. G., Solvothermal Synthesis of Nanocrystalline Copper Nitride from an Energetically Unstable Copper Azide Precursor. *Inorg. Chem.* **2005,** *44*, 7385–7393.

166. Wang, Z.; Bilegsaikhan, A.; Jerozal, R. T.; Pitt, T. A.; Milner, P. J., Evaluating the Robustness of Metal–Organic Frameworks for Synthetic Chemistry. *ACS Appl. Mater. Interfaces* **2021,** *13*, 17517–17531.

167. Karadeniz, B.; Žilić, D.; Huskić, I.; Germann, L. S.; Fidelli, A. M.; Muratović, S.; Lončarić, I.; Etter, M.; Dinnebier, R. E.; Barišić, D.; Cindro, N.; Islamoglu, T.; Farha, O. K.; Friščić, T.; Užarević, K., Controlling the Polymorphism and Topology Transformation in Porphyrinic Zirconium Metal–Organic Frameworks via Mechanochemistry. *J. Am. Chem. Soc.* **2019,** *141*, 19214–19220.

168. Karadeniz, B.; Howarth, A. J.; Stolar, T.; Islamoglu, T.; Dejanović, I.; Tireli, M.; Wasson, M. C.; Moon, S.-Y.; Farha, O. K.; Friščić, T.; Užarević, K., Benign by Design: Green and Scalable Synthesis of Zirconium UiO-Metal–Organic Frameworks by Water-Assisted Mechanochemistry. *ACS Sustainable Chem. Eng.* **2018,** *6*, 15841–15849.

169. Fidelli, A. M.; Karadeniz, B.; Howarth, A. J.; Huskić, I.; Germann, L. S.; Halasz, I.; Etter, M.; Moon, S.-Y.; Dinnebier, R. E.; Stilinović, V.; Farha, O. K.; Friščić, T.; Užarević, K., Green and rapid mechanosynthesis of high-porosity NU- and UiO-type metal–organic frameworks. *Chem. Commun.* **2018,** *54*, 6999–7002.

170. Feng, D.; Gu, Z. Y.; Li, J. R.; Jiang, H. L.; Wei, Z.; Zhou, H. C., Zirconium-metalloporphyrin PCN-222: mesoporous metal–organic frameworks with ultrahigh stability as biomimetic catalysts. *Angew. Chem. Int. Ed. Engl.* **2012,** *51*, 10307–10310.

171. Feng, D.; Chung, W.-C.; Wei, Z.; Gu, Z.-Y.; Jiang, H.-L.; Chen, Y.-P.; Darensbourg, D. J.; Zhou, H.-C., Construction of Ultrastable Porphyrin Zr Metal–Organic Frameworks through Linker Elimination. *J. Am. Chem. Soc.* **2013,** *135*, 17105–17110.

172. Furukawa, H.; Gándara, F.; Zhang, Y.-B.; Jiang, J.; Queen, W. L.; Hudson, M. R.; Yaghi, O. M., Water Adsorption in Porous Metal–Organic Frameworks and Related Materials. *J. Am. Chem. Soc.* **2014,** *136*, 4369–4381.

173. Nateghi, B.; Boldog, I.; Domasevitch, K. V.; Janiak, C., More versatility than thought: large {Zr26} oxocarboxylate cluster by corner-sharing of standard octahedral subunits. *CrystEngComm* **2018,** *20*, 5132–5136.

174. Lu, Z.; Liu, J.; Zhang, X.; Liao, Y.; Wang, R.; Zhang, K.; Lyu, J.; Farha, O. K.; Hupp, J. T., Node-Accessible Zirconium MOFs. *J. Am. Chem. Soc.* **2020,** *142*, 21110–21121.

175. Cavka, J. H.; Jakobsen, S.; Olsbye, U.; Guillou, N.; Lamberti, C.; Bordiga, S.; Lillerud, K. P., A New Zirconium Inorganic Building Brick Forming Metal Organic Frameworks with Exceptional Stability. *J. Am. Chem. Soc.* **2008,** *130*, 13850–13851.

176. Choi, J. I.; Chun, H.; Lah, M. S., Zirconium-Formate Macrocycles and Supercage: Molecular Packing versus MOF-like Network for Water Vapor Sorption. *J. Am. Chem. Soc.* **2018,** *140*, 10915–10920.

177. Rosenau, C. P.; Jelier, B. J.; Gossert, A. D.; Togni, A., Exposing the Origins of Irreproducibility in Fluorine NMR Spectroscopy. *Angew. Chem. Int. Ed.* **2018,** *57*, 9528–9533.

178. Macrae, C. F.; Edgington, P. R.; McCabe, P.; Pidcock, E.; Shields, G. P.; Taylor, R.; Towler, M.; van de Streek, J., Mercury: visualization and analysis of crystal structures. *J. Appl. Cryst.* **2006,** *39*, 453–457.

179. Graffner-Nordberg, M.; Marelius, J.; Ohlsson, S.; Persson, Å.; Swedberg, G.; Andersson, P.; Andersson, S. E.; Åqvist, J.; Hallberg, A., Computational Predictions of Binding Affinities to Dihydrofolate Reductase: Synthesis and Biological Evaluation of Methotrexate Analogues. *J. Med. Chem.* **2000,** *43*, 3852–3861.

180. Wang, C. H.; Das, A.; Gao, W. Y.; Powers, D. C., Probing Substrate Diffusion in Interstitial MOF Chemistry with Kinetic Isotope Effects. *Angew. Chem. Int. Ed. Engl.* **2018,** *130*, 3738–3743.

181. Puchberger, M.; Kogler, F. R.; Jupa, M.; Gross, S.; Fric, H.; Kickelbick, G.; Schubert, U., Can the Clusters Zr6O4(OH)4(OOCR)12 and [Zr6O4(OH)4(OOCR)12]2 Be Converted into Each Other? *Eur. J. Inorg. Chem.* **2006,** *2006*, 3283–3293.

182. Kickelbick, G.; Wiede, P.; Schubert, U., Variations in capping the Zr6O4(OH)4 cluster core: X-ray structure analyses of [Zr6(OH)4O4(OOC–CH□CH2)10]2(μ-OOC–CH□CH2)4 and Zr6(OH)4O4(OOCR)12(PrOH) (R=Ph, CMe=CH2). *Inorg. Chim. Acta* **1999,** *284*, 1–7.

183. Carsch, K. M.; DiMucci, I. M.; Iovan, D. A.; Li, A.; Zheng, S.-L.; Titus, C. J.; Lee, S. J.; Irwin, K. D.; Nordlund, D.; Lancaster, K. M.; Betley, T. A., Synthesis of a copper-supported triplet nitrene complex pertinent to copper-catalyzed amination. *Science* **2019,** *365*, 1138–1143.

184. Reid, K. A.; Powers, D. C., In crystallo organometallic chemistry. *Chem. Commun.* **2021,** *57*, 4993–5003.

185. Wang, C.-H.; Gao, W.-Y.; Powers, D. C., Measuring and Modulating Substrate Confinement during Nitrogen-Atom Transfer in a Ru2-Based Metal-Organic Framework. *J. Am. Chem. Soc.* **2019,** *141*, 19203–19207.

186. Wang, C.-H.; Das, A.; Gao, W.-Y.; Powers, D. C., Probing Substrate Diffusion in Interstitial MOF Chemistry with Kinetic Isotope Effects. *Angewandte Chemie International Edition* **2018,** *57* (14), 3676-3681.

187. Brozek, C. K.; Miller, J. T.; Stoian, S. A.; Dincă, M., NO Disproportionation at a Mononuclear Site-Isolated Fe2+ Center in Fe2+-MOF-5. *J. Am. Chem. Soc.* **2015,** *137*, 7495–7501.

188. Jover, J.; Brozek, C. K.; Dincă, M.; López, N., Computational Exploration of NO Single-Site Disproportionation on Fe-MOF-5. *Chem. Mater.* **2019,** *31*, 8875–8885.

189. Oelkrug, D.; Brun, M.; Rebner, K.; Boldrini, B.; Kessler, R., Penetration of Light into Multiple Scattering Media: Model Calculations and Reflectance Experiments. Part I: The Axial Transfer. *Appl. Spectrosc.* **2012,** *66*, 934–943.

190. Kubelka, P., New Contributions to the Optics of Intensely Light-Scattering Materials. Part I. *J. Opt. Soc. Am.* **1948,** *38*, 448–457.

191. Ash, C.; Dubec, M.; Donne, K.; Bashford, T., Effect of wavelength and beam width on penetration in light-tissue interaction using computational methods. *Lasers Med. Sci.* **2017,** *32*, 1909–1918.

192. Jellison, G. E.; Boatner, L. A., Optical functions of uniaxial ZnO determined by generalized ellipsometry. *Phys. Rev. B* **1998,** *58*, 3586–3589.

193. Paulauskas, I. E.; Jellison, G. E.; Boatner, L. A.; Brown, G. M., Photoelectrochemical Stability and Alteration Products of n-Type Single-Crystal ZnO Photoanodes. *Int. J. Electrochem.* **2011,** *2011*, 563427.

194. Mirabella, F. M., *Modern Techniques in Applied Molecular Spectroscopy*. John Wiley & Sons Inc.: New York, 1998; p 185–219.

195. Hanna, L.; Lockard, J. V., From IR to x-rays: gaining molecular level insights on metal-organic frameworks through spectroscopy. *J. Phys.: Condens. Matter* **2019,** *31*, 483001.

196. Fabbri, E.; Abbott, D. F.; Nachtegaal, M.; Schmidt, T. J., Operando X-ray absorption spectroscopy: A powerful tool toward water splitting catalyst development. *Curr. Opin. Electrochem.* **2017,** *5*, 20–26.

197. Choe, M.; Koo, J. Y.; Park, I.; Ohtsu, H.; Shim, J. H.; Choi, H. C.; Park, S. S., Chemical Vapor Deposition of Edge-on Oriented 2D Conductive Metal–Organic Framework Thin Films. *J. Am. Chem. Soc.* **2022,** *144*, 16726–16731.

198. Salmi, L. D.; Heikkilä, M. J.; Puukilainen, E.; Sajavaara, T.; Grosso, D.; Ritala, M., Studies on atomic layer deposition of MOF-5 thin films. *Micropor. Mesopor. Mat.* **2013,** *182*, 147–154.

199. Ahvenniemi, E.; Karppinen, M., Atomic/molecular layer deposition: a direct gas-phase route to crystalline metal–organic framework thin films. *Chem. Commun.* **2016,** *52*, 1139–1142.

200. Claire, F. J.; Solomos, M. A.; Kim, J.; Wang, G.; Siegler, M. A.; Crommie, M. F.; Kempa, T. J., Structural and electronic switching of a single crystal 2D metal-organic framework prepared by chemical vapor deposition. *Nat. Commun.* **2020,** *11*, 5524.

201. Choe, M.; Kim, S.; Choi, H. C., Smooth and large scale organometallic complex film by vapor-phase ligand exchange reaction. *RSC Adv.* **2020,** *10*, 9536–9538.

202. Lausund, K. B.; Nilsen, O., All-gas-phase synthesis of UiO-66 through modulated atomic layer deposition. *Nat. Commun.* **2016,** *7*, 13578.

203. Lan, G.; Quan, Y.; Wang, M.; Nash, G. T.; You, E.; Song, Y.; Veroneau, S. S.; Jiang, X.; Lin, W., Metal–Organic Layers as Multifunctional Two-Dimensional Nanomaterials for Enhanced Photoredox Catalysis. *J. Am. Chem. Soc.* **2019,** *141*, 15767–15772.

204. Cao, L.; Wang, C., Metal–Organic Layers for Electrocatalysis and Photocatalysis. *ACS Cent. Sci.* **2020,** *6*, 2149–2158.

205. Chen, P.; Liu, Y.; Hu, X.; Liu, X.; You, E.-M.; Qian, X.; Chen, J.; Xiao, L.; Cao, L.; Peng, X.; Zeng, Z.; Jiang, Y.; Ding, S.-Y.; Liao, H.; Wang, Z.; Zhou, D.; Wang, C., Probing surface structure on two-dimensional metal-organic layers to understand suppressed interlayer packing. *Nano Res.* **2020,** *13*, 3151–3156.

206. Zacher, D.; Shekhah, O.; Wöll, C.; Fischer, R. A., Thin films of metal–organic frameworks. *Chem. Soc. Rev.* **2009,** *38*, 1418–1429.

207. Mandemaker, L. D. B.; Rivera-Torrente, M.; Geitner, R.; Vis, C. M.; Weckhuysen, B. M., In Situ Spectroscopy of Calcium Fluoride Anchored Metal–Organic Framework Thin Films during Gas Sorption. *Angew. Chem. Int. Ed.* **2020,** *59*, 19545–19552.

208. Zhuang, J.-L.; Kind, M.; Grytz, C. M.; Farr, F.; Diefenbach, M.; Tussupbayev, S.; Holthausen, M. C.; Terfort, A., Insight into the Oriented Growth of Surface-Attached Metal–

Organic Frameworks: Surface Functionality, Deposition Temperature, and First Layer Order. *J. Am. Chem. Soc.* **2015,** *137*, 8237–8243.

209. Hempenius, M. A.; Robins, N. S.; Lammertink, R. G. H.; Vancso, G. J., Organometallic Polyelectrolytes: Synthesis, Characterization and Layer-By-Layer Deposition of Cationic Poly(ferrocenyl(3-ammoniumpropyl)-methylsilane). *Macromol. Rapid Commun.* **2001,** *22*, 30–33.

210. Decher, G., Fuzzy Nanoassemblies: Toward Layered Polymeric Multicomposites. *Science* **1997,** *277*, 1232–1237.

211. Liu, S.; Kurth, D. G.; Bredenkötter, B.; Volkmer, D., The Structure of Self-Assembled Multilayers with Polyoxometalate Nanoclusters. *J. Am. Chem. Soc.* **2002,** *124*, 12279–12287.

212. Zhang, J.; Gong, C.; Zeng, X.; Shu, J.; Xiao, P.; Xie, J., Fabrication of crystalline porphyrinic polyoxometalate cluster with high thermal stability and exploration of its photocatalytic activity. *Polyhedron* **2017,** *121*, 95–100.

213. Gosselin, A. J.; Antonio, A. M.; Korman, K. J.; Deegan, M. M.; Yap, G. P. A.; Bloch, E. D., Elaboration of Porous Salts. *J. Am. Chem. Soc.* **2021,** *143*, 14956–14961.

214. Chen, W.; McCarthy, T. J., Layer-by-Layer Deposition: A Tool for Polymer Surface Modification. *Macromolecules* **1997,** *30*, 78–86.

215. Kolasinska, M.; Krastev, R.; Gutberlet, T.; Warszynski, P., Layer-by-Layer Deposition of Polyelectrolytes. Dipping versus Spraying. *Langmuir* **2009,** *25*, 1224–1232.

216. Homola, T.; Matoušek, J.; Kormunda, M.; Wu, L. Y. L.; Černák, M., Plasma Treatment of Glass Surfaces Using Diffuse Coplanar Surface Barrier Discharge in Ambient Air. *Plasma Chem. Plasma Process.* **2013,** *33*, 881–894.

217. Liston, E. M., Plasma Treatment for Improved Bonding: A Review. *J. Adhes.* **1989,** *30*, 199–218.

218. Buček, A.; Brablec, A.; Kováčik, D.; Sťahel, P.; Černák, M., Glass bond adhesive strength improvement by DCSBD atmospheric-pressure plasma treatment. *Int. J. Adhes. Adhes.* **2017,** *78*, 1–3.

219. Murthy, V. S. M. D.; Vaidya, U., Improving the adhesion of glass/polypropylene (glass-PP) and high-density polyethylene (HDPE) surfaces by open air plasma treatment. *Int. J. Adhes. Adhes.* **2019,** *95*, 102435.

220. Bagiatis, V.; Critchlow, G. W.; Price, D.; Wang, S., The effect of atmospheric pressure plasma treatment (APPT) on the adhesive bonding of poly(methyl methacrylate) (PMMA)-to-glass using a polydimethylsiloxane (PDMS)-based adhesive. *Int. J. Adhes. Adhes.* **2019,** *95*, 102405.

221. So, L.; Ng, N.; Bilek, M.; Pigram, P. J.; Brack, N., X-ray photoelectron spectroscopic study of the surface chemistry of soda-lime glass in vacuum. *Surf. Interface Anal.* **2006,** *38*, 648–651.

222. Terpilowski, K.; Rymuszka, D., Surface properties of glass plates activated by air, oxygen, nitrogen and argon plasma. *Glass Phys. Chem.* **2016,** *42*, 535–541.

223. Jang, W.-S.; Grunlan, J. C., Robotic dipping system for layer-by-layer assembly of multifunctional thin films. *Rev. Sci. Instrum.* **2005,** *76*, 103904.

224. Rio, E.; Boulogne, F., Withdrawing a solid from a bath: How much liquid is coated? *Adv. Colloid Interface Sci*, **2017,** *247*, 100–114.

225. Delen, G.; Ristanović, Z.; Mandemaker, L. D. B.; Weckhuysen, B. M., Mechanistic Insights into Growth of Surface-Mounted Metal-Organic Framework Films Resolved by Infrared (Nano-) Spectroscopy. *Chem. Eur. J.* **2018,** *24*, 187–195.

226. Podsiadlo, P.; Michel, M.; Lee, J.; Verploegen, E.; Wong Shi Kam, N.; Ball, V.; Lee, J.; Qi, Y.; Hart, A. J.; Hammond, P. T.; Kotov, N. A., Exponential Growth of LBL Films with Incorporated Inorganic Sheets. *Nano Let.* **2008,** *8*, 1762–1770.

227. Zhang, L.; Liu, H.; Zhao, E.; Qiu, L.; Sun, J.; Shen, J., Drying and Nondrying Layer-by-Layer Assembly for the Fabrication of Sodium Silicate/TiO2 Nanoparticle Composite Films. *Langmuir* **2012,** *28*, 1816–1823.

228. Yamashita, M.; Inoue, K.; Ohishi, T.; Takeuchi, T.; Yosida, T.; Mori, W., Low-Dimensional Magnetic Systems With S=1, 3/2 and 2. *Mol. Cryst. Liq. Cryst. Sci. Technol., Sect. A* **1995,** *274*, 25–32.

229. Angaridis, P.; Cotton, F. A.; Murillo, C. A.; Villagrán, D.; Wang, X., Structural and Magnetic Evidence Concerning Spin Crossover in Formamidinate Compounds with Ru25+ Cores. *J. Am. Chem. Soc.* **2005,** *127*, 5008–5009.

230. Das, A.; Maher, A. G.; Telser, J.; Powers, D. C., Observation of a Photogenerated Rh2 Nitrenoid Intermediate in C–H Amination. *J. Am. Chem. Soc.* **2018,** *140*, 10412–10415.

231. Barral, M. C.; Jiménez-Aparicio, R.; Priego, J. L.; Royer, E. C.; Saucedo, M. J.; Urbanos, F. A.; Amador, U., Non-polymeric diruthenium(II,III) carboxylates. Crystal structures of [Ru2Cl(μ-O2CCMe3)4(H2O)] and [Ru2Cl(μ-O2CCHMe2)4(thf)](thf = tetrahydrofuran). *J. Chem. Soc., Dalton Trans.* **1995,** *13*, 2183–2187.

232. Harvey, M. E.; Musaev, D. G.; Du Bois, J., A Diruthenium Catalyst for Selective, Intramolecular Allylic C–H Amination: Reaction Development and Mechanistic Insight Gained through Experiment and Theory. *J. Am. Chem. Soc.* **2011,** *133*, 17207–17216.

233. Lindsay, A. J.; Wilkinson, G.; Motevalli, M.; Hursthouse, M. B., The synthesis, magnetic, electrochemical, and spectroscopic properties of diruthenium(II,II) tetra-μ-carboxylates and their

adducts. X-Ray structures of Ru2(O2CR)4L2(R = Me, L = H2O or tetrahydrofuran; R = Et, L = Me2CO). *J. Chem. Soc., Dalton Trans.* **1985,** *11*, 2321–2326.

234. Whitten, D. G., Photochemistry of porphyrins and their metal complexes in solution and organized media. *Rev. Chem. Intermed.* **1978,** *2*, 107–138.

235. Sekhar, A. R.; Chitose, Y.; Janoš, J.; Dangoor, S. I.; Ramundo, A.; Satchi-Fainaro, R.; Slavíček, P.; Klán, P.; Weinstain, R., Porphyrin as a versatile visible-light-activatable organic/metal hybrid photoremovable protecting group. *Nat. Commun.* **2022,** *13*, 3614.

236. Roundhill, D. M., Photochemistry and Photophysics of Metal Porphyrins, Phthalocyanins, and Metal Ions in Supramolecular Systems. In *Photochemistry and Photophysics of Metal Complexes*, Roundhill, D. M., Ed. Springer US: Boston, MA, 1994; pp 321–340.

237. Rybicka-Jasińska, K.; König, B.; Gryko, D., Porphyrin-Catalyzed Photochemical C–H Arylation of Heteroarenes. *Eur. J. Org. Chem.* **2017,** *2017*, 2104–2107.

238. Mironov, A., 85 Transition Metal Complexes of Porphyrins and Porphyrinoids. In *Handbook of Porphyrin Science*, 2012; pp 303–413.

239. Lemon, C. M.; Brothers, P. J.; Boitrel, B., Porphyrin complexes of the period 6 main group and late transition metals. *Dalton Trans.* **2011,** *40*, 6591–6609.

240. Zhang, X.; Wasson, M. C.; Shayan, M.; Berdichevsky, E. K.; Ricardo-Noordberg, J.; Singh, Z.; Papazyan, E. K.; Castro, A. J.; Marino, P.; Ajoyan, Z.; Chen, Z.; Islamoglu, T.; Howarth, A. J.; Liu, Y.; Majewski, M. B.; Katz, M. J.; Mondloch, J. E.; Farha, O. K., A historical perspective on porphyrin-based metal–organic frameworks and their applications. *Coord. Chem. Rev.* **2021,** *429*, 213615.

241. Van Trieste III, G. P.; Reid, K. A.; Hicks, M. H.; Das, A.; Figgins, M. T.; Bhuvanesh, N.; Ozarowski, A.; Telser, J.; Powers, D. C., Nitrene Photochemistry of Manganese N-Haloamides**. *Angew. Chem. Int. Ed.* **2021,** *60*, 26647–26655.

242. Suslick, K. S. W., R. A., The Photochemsitry of Chromium, Manganese, and Iron Porphyrin Complexes. *New J. Chem.* **1992,** *16*, 633–642.

243. Hendrickson, D. N.; Kinnaird, M. G.; Suslick, K. S., Photochemistry of (5,10,15,20-tetraphenylporphyrinato)iron(III) halide complexes, Fe(TPP)(X). *J. Am. Chem. Soc.* **1987,** *109*, 1243–1244.

244. Suslick, K. S.; Bautista, J. F.; Watson, R. A., Metalloporphyrin photochemistry with matrix isolation. *J. Am. Chem. Soc.* **1991,** *113*, 6111–6114.

245. Takagi, S.; Eguchi, M.; Tryk, D. A.; Inoue, H., Porphyrin photochemistry in inorganic/organic hybrid materials: Clays, layered semiconductors, nanotubes, and mesoporous materials. *J. Photochem. Photobiol. C* **2006,** *7*, 104–126.

246. Paolesse, R.; Nardis, S.; Monti, D.; Stefanelli, M.; Di Natale, C., Porphyrinoids for Chemical Sensor Applications. *Chem. Rev.* **2017,** *117*, 2517–2583.

247. Norvaiša, K.; Kielmann, M.; Senge, M. O., Porphyrins as Colorimetric and Photometric Biosensors in Modern Bioanalytical Systems. *ChemBioChem* **2020,** *21*, 1793–1807.

248. Ishihara, S.; Labuta, J.; Van Rossom, W.; Ishikawa, D.; Minami, K.; Hill, J. P.; Ariga, K., Porphyrin-based sensor nanoarchitectonics in diverse physical detection modes. *Phys. Chem. Chem. Phys.* **2014,** *16*, 9713–9746.

249. Bélanger, S.; Keefe, M. H.; Welch, J. L.; Hupp, J. T., Rapid derivatization of mesoporous thin-film materials based on Re(I) zinc-porphyrin ‘molecular squares’: selective modification of

mesopore size and shape by binding of aromatic nitrogen donor ligands. *Coord. Chem. Rev.* **1999,** *190*, 29–45.

250. Makiura, R.; Kitagawa, H., Porous Porphyrin Nanoarchitectures on Surfaces. *Eur. J. Inorg. Chem.* **2010,** *2010*, 3715–3724.

251. Makiura, R., Creation of metal–organic framework nanosheets by the Langmuir-Blodgett technique. *Coord. Chem. Rev.* **2022,** *469*, 214650.

252. Li, D.; Swanson, B. I.; Robinson, J. M.; Hoffbauer, M. A., Porphyrin based self-assembled monolayer thin films: synthesis and characterization. *J. Am. Chem. Soc.* **1993,** *115*, 6975–6980.

253. Baba, K.; Bengasi, G.; Loyer, F.; Fernandes, J. P. C.; El Assad, D.; De Castro, O.; Boscher, N. D., Fused Metalloporphyrin Thin Film with Tunable Porosity via Chemical Vapor Deposition. *ACS Appl. Mater. Interfaces* **2020,** *12*, 37732–37740.

254. Ding, G.; Han, S.-T.; Kuo, C.-C.; Roy, V. A. L.; Zhou, Y., Porphyrin-Based Metal–Organic Frameworks for Neuromorphic Electronics. *Small Struct* **2023,** *4*, 2200150.

255. Gottfried, J. M., Surface chemistry of porphyrins and phthalocyanines. *Surf. Sci. Rep.* **2015,** *70*, 259–379.

256. Giancane, G.; Valli, L., State of art in porphyrin Langmuir–Blodgett films as chemical sensors. *Adv. Colloid Interface Sci.* **2012,** *171*, 17–35.

257. Lin, J.; Shi, D., Photothermal and photovoltaic properties of transparent thin films of porphyrin compounds for energy applications. *Appl. Phys. Rev.* **2021,** *8*, 011302.

258. Bazzan, G.; Smith, W.; Francesconi, L. C.; Drain, C. M., Electrostatic Self-Organization of Robust Porphyrin−Polyoxometalate Films. *Langmuir* **2008,** *24*, 3244–3249.

259. García, M.; Honores, J.; Quezada, D.; Díaz, C.; Dreyse, P.; Celis, F.; Kubiak, C. P.; Canzi, G.; Guzmán, F.; Aguirre, M. J.; Isaacs, M., Nitrite reduction on a multimetallic

porphyrin/polyoxotungstate layer-by-layer modified electrodes. *Electrochim. Acta* **2016,** *192*, 61–71.

260. Costa-Coquelard, C.; Sorgues, S.; Ruhlmann, L., Photocatalysis with Polyoxometalates Associated to Porphyrins under Visible Light: An Application of Charge Transfer in Electrostatic Complexes. *J. Phys. Chem. A* **2010,** *114*, 6394–6400.

261. Schaming, D.; Farha, R.; Xu, H.; Goldmann, M.; Ruhlmann, L., Formation and Photocatalytic Properties of Nanocomposite Films Containing Both Tetracobalt Dawson-Derived Sandwich Polyanions and Tetracationic Porphyrins. *Langmuir* **2011,** *27*, 132–143.

262. Koenig, J.-F.; Martel, D., Applying UV–Vis spectroscopy to step-by-step molecular self assembly on surface: Does it bring pertinent information? *Thin Solid Films* **2008,** *516*, 3865–3872.

263. Shen, Y.; Liu, J.; Jiang, J.; Liu, B.; Dong, S., Fabrication of Metalloporphyrin-Polyoxometalyte Hybrid Film by Layer-by-Layer Method and Its Catalysis for Dioxygen Reduction. *Electroanalysis* **2002,** *14*, 1557–1563.

264. Shen, Y.; Liu, J.; Jiang, J.; Liu, B.; Dong, S., Fabrication of a Metalloporphyrin−Polyoxometalate Hybrid Film by a Layer-by-Layer Method and Its Catalysis for Hydrogen Evolution and Dioxygen Reduction. *J. Phys. Chem. B* **2003,** *107*, 9744–9748.

265. Pyrasch, M.; Toutianoush, A.; Jin, W.; Schnepf, J.; Tieke, B., Self-assembled Films of Prussian Blue and Analogues: Optical and Electrochemical Properties and Application as Ion-Sieving Membranes. *Chem. Mater.* **2003,** *15*, 245–254.

266. Zhang, G.; Chen, Z.; He, T.; Ke, H.; Ma, Y.; Shao, K.; Yang, W.; Yao, J., Construction of Self-Assembled Ultrathin Polyoxometalate/1,10-Decanediamine Photochromic Films. *J. Phys. Chem. B* **2004,** *108*, 6944–6948.

267. Cardenal, A. D.; Jeong Park, H.; Chalker, C. J.; Ortiz, K. G.; Powers, D. C., cis-Decalin oxidation as a stereochemical probe of in-MOF versus on-MOF catalysis. *Chem. Commun.* **2017,** *53*, 7377–7380.

268. Clarke, R. M.; Storr, T., Tuning Electronic Structure To Control Manganese Nitride Activation. *J. Am. Chem. Soc.* **2016,** *138*, 15299–15302.

269. Hein, N. M.; MacNeil, G. A.; Storr, T., Elaboration on the Electronics of Salen Manganese Nitrides: Investigations into Alkoxy-Substituted Ligand Scaffolds. *Inorg. Chem.* **2021,** *60*, 16895–16905.

270. Shi, H.; Lee, H. K.; Pan, Y.; Lau, K.-C.; Yiu, S.-M.; Lam, W. W. Y.; Man, W.-L.; Lau, T.-C., Structure and Reactivity of a Manganese(VI) Nitrido Complex Bearing a Tetraamido Macrocyclic Ligand. *J. Am. Chem. Soc.* **2021,** *143*, 15863–15872.

271. Chantarojsiri, T.; Reath, A. H.; Yang, J. Y., Cationic Charges Leading to an Inverse Free-Energy Relationship for N−N Bond Formation by MnVI Nitrides. *Angew. Chem. Int. Ed.* **2018,** *57*, 14037–14042.